Aus dem Deutschen Krebsforschungszentrum Heidelberg
(Wissenschaftlicher Vorstand: Prof. Dr. Michael Baumann)
Abteilung für Medizinische Physik in der Strahlentherapie
(Abteilungsleiter: Prof. Dr. Oliver Jäkel)

Carbon-ion radiotherapy monitoring in depth using secondary-ion tracking

Inauguraldissertation
zur Erlangung des Doctor scientiarum humanarum (Dr.sc.hum.)
an der
Medizinischen Fakultät Heidelberg
der
Ruprecht-KarlsUniversität.

vorgelegt von
Laura Marie Hélène, Ghesquière-Diérickx

aus
Versailles, France

2021

Dekan:	Herr Prof. Dr. Hans-Georg Kräusslich
Doktorvater:	Herr Prof. Dr. Oliver Jäkel

Table of Content

Abbreviations

- 2D two dimensional
- 3D three dimensional
- BP Bragg peak
- C12 carbon-ion
- CiRT carbon-ion radiotherapy
- CMOS complementary-metal-oxide-semiconductor
- CT computed tomography
- CTV clinical target volume
- fToA fast-time-of-arrival
- GTV gross tumor volume
- Gy gray
- GyE/Gy(E) gray equivalent
- Gy (RBE) gray RBE
- H1 proton
- HIT Heidelberg ion therapy center, Germany
- HLUT Hounsfield look-up table
- H&N or HN head and neck cancer
- HU Hounsfield units
- IES iso-energetic slice
- IGRT image guided radiotherapy
- IMRT intensity-modulated radiotherapy
- IVI interaction vertex imaging
- LEM local effect model
- LET linear energy transfer
- MCS multiple coulomb scattering
- OAR organ at risk
- PB pencil beam
- PET positron emitters tomography
- PT particle therapy
- PTV planning target volume
- RBE relative biological effectiveness
- RSP relative stopping power
- RT radiotherapy
- SOBP spread out Bragg peak
- ToA time-of-arrival
- ToT time-over-threshold
- VMAT volumetric modulated arc therapy
- WET water equivalent thickness

1. Introduction

1.1 Role and benefits of carbon-ion radiotherapy

As first suggested by R. Wilson in 1946 (Wilson 1946), particle therapy, which includes proton and carbon-ion radiotherapy, offers several advantages when compared to other conventional photons radiotherapy techniques such as VMAT, IMRT, IGRT, SBRT, etc. (Sakthivel et al. 2019). Currently, more than a hundred centers worldwide treat patients with particle therapy using either protons or carbon ions (PTCOG 2021a). Among the main advantages of proton and carbon-ion radiotherapies over conventional radiotherapy belong the physical benefits of charged particles, which include their finite range inside the tissue, and the associated increasing dose deposition towards the end of their range (the so-called Bragg-peak or BP). This characteristic dose profile improves sparing of the surrounding tissues and thus allows dose escalation within the tumor. Which is especially of interest for deep seated tumors. Additionally, heavy charged particles also exhibit biological benefits characterized through an enhanced relative biological effectiveness (RBE) in the Bragg-peak compared to photons, which allows to better control radio-resistant tumors. Given all of this, particle therapy using proton and carbon ion beams is seen as an attractive tool to treat deep-seated, radio-resistant cancers, while keeping the dose delivered to the healthy organs within limits (Rackwitz et al. 2019).

Within particle radiotherapy modalities, carbon-ion radiotherapy offers further advantages compared to proton radiotherapy in terms of additional physical and biological advantages. The higher mass of carbon ions compared to protons leads to their lower scattering in tissue and thus narrower lateral penumbra of the carbon-ion beams. The higher RBE of carbon ions towards the end of their range compared to the plateau leads to more unrepairable carbon-ion induced DNA damages in tumor cells per unit dose in comparison to protons (Combs et al. 2012). Additionally, carbon ions are seen to be more effective in hypoxic tumors compared to protons (Mohamad et al. 2017). These benefits of particle therapy are of special interest when aiming to reduce the risk of secondary radiation-induced tumors for young patients (Combs et al. 2012) or patients with tumors in the close vicinity of organs at risk (Rackwitz et al. 2019).

Today, carbon-ion radiotherapy has gained a lot of interest and is used in twelve centers located across five countries, including Austria, China, Germany, Italy, and Japan (PTCOG 2021a) and six more carbon-ion radiotherapy sites are under construction in China, Japan, France, South Korea, and Taiwan (PTCOG 2021b).

1.2 Limitations of carbon-ion radiotherapy

The steep dose deposition profile of the Bragg peak makes carbon-ion radiotherapy more sensitive to the treatment delivery uncertainties (Paganetti 2012). In particular variations in the dose distribution due to geometrical changes of the patient's anatomy can lead to undesirable under-dosage of the tumor tissues or over-dosage of the healthy tissues (Fattori et al. 2014). These treatment delivery uncertainties can be divided into systematic or random uncertainties (ICRU 93 2016).

Systematic uncertainties of carbon-ion radiotherapy affect in the same way all repeated irradiations of the same patient treatment. They stem, among others, from treatment planning uncertainties including wrong relation between CT and range in the calculation of the physical dose distribution or uncertainties of the biological dose calculation.
On the contrary, random uncertainties of the carbon-ion radiotherapy are randomly distributed over the entire treatment course and separately affecting each repeated irradiation of patient treatment. They arise from daily beam delivery changes, inter-fractional changes (patient positioning uncertainties, swelling, weight loss, tumor volume changes), and intra-fractional changes (such as heartbeat, organ, or respiratory motions).
To counteract these effects, larger safety margins are currently applied around targeted tumor volumes in patients treated with particle therapy (up to 3.5 % + 3 mm for proton therapy (Paganetti 2012) and 2 to 3 mm for carbon ions in the head (Fattori et al. 2014; Jäkel, Krämer, et al. 2001). However, as safety margins are defined around the tumor volume directly in healthy tissue, larger margins immediately lead to more healthy tissue being irradiated.

1.3 Techniques for monitoring of carbon-ion radiotherapy delivery

Due to the above-mentioned reasons, monitoring methods of the treatment dose delivery within the patient are of great importance for carbon-ion beam radiotherapy. This is necessary to properly follow possible under- or over-dosage in the patient, and, eventually, to control them, and thus reduce the tumor safety margins applied around targeted tumor volumes and decrease the overall dose delivered in healthy tissues.
Over the years, several non-invasive in-vivo ion-beam monitoring methods have been developed, as summarized in (Kraan 2015; Parodi 2016; Parodi et al. 2018). Most of these methods are based on the detection of secondary radiations (such as β+ emitters, prompt gammas, or prompt charged nuclear fragments) which are emitted from a patient during the particle therapy delivery. As these secondary radiations are the results of nuclear interactions of the primary irradiation beam with the nuclei of the crossed tissue, they carry valuable information regarding the primary radiation beam such as the carbon-ion range and beam position, in the patient.
Each ion-beam monitoring technique offers different advantages and has certain limitations as detailed in section (§2.3.2.). Although PET-based monitoring techniques were up to now the only technique implemented in clinics (Parodi 2016; Shakirin et al. 2011), these PET-based monitoring techniques are still limited by β+ emitter ranges in tissue, long acquisition times, or physiological wash-out. On the contrary, other monitoring techniques such as the prompt secondary-ion-based techniques offer fast and direct measurements of the carbon-ions of secondary radiations in the patient (Muraro et al. 2016) without the need for additional time, nonetheless with large enough detection yields. These secondary-ion-based monitoring techniques, thus appear to be an interesting tool for non-invasive in-vivo carbon-ion beam monitoring.

1.4 Study aim

This thesis **aims** at investigating and further developing a monitoring method based on secondary-ion tracking to estimate the carbon-ion pencil beam stopping positions inside a patient's head and under clinical conditions (i.e. using clinical treatment beam energies, doses, and dose rates). This is considered to essentially contribute to visualize and quantify inter-fractional anatomical changes that might occur between two irradiation fractions.

This thesis is based on the previous research and development of (Félix-Bautista 2017; Gaa et al. 2017; Gwosch et al. 2013; Martišíková et al. 2012; Reimold 2018; Reinhart et al. 2017). The main difference to the previous studies resides in the investigation of full clinic-like treatment plans, composed of thousands of single pencil beams including those with low numbers of primary-ions, instead of single pencil beams with significantly higher fluences (Reimold 2018).

The **final purpose** of this thesis is to demonstrate the applicability of the monitoring of carbon-ion pencil beam delivery in real patient treatment by designing a patient-friendly measurement setup, integrating it into a clinical workflow, and performing first patient measurements for carbon-ion pencil beam monitoring using secondary-ion tracking.

1.5 Thesis structure

The thesis report is structured as follows: the next Chapter 2 gives a global overview of the thesis framework which includes medical and physical bases necessary to understand the context within which the thesis was conducted. Chapter 3 details the methods, experimental configurations, and data analysis developed for the pre-clinical and clinical measurements performed within the frame of the thesis. Chapter 4 summarizes the thesis results. These results comprise five main investigations:

(1) A general analysis of the secondary-ions track distributions along the beam axis.
(2) An analysis of the measured secondary-ion emission profiles (single feature analysis) to detect inter-fractional surface and internal changes, including the detectability and localization of the anatomical changes.
(3) An investigation of the ideal mini-tracker position.
(4) An analysis of the measured secondary ion cluster and track parameters (multi-feature analysis) was developed to evaluate the potential of the method to detect small inter-fractional surface changes.
(5) A first clinical application the proposed monitoring methodology during a patient treatment delivery.

Chapter 5 proposes an overall discussion of the thesis towards essential future investigations. Chapter 6 offers a summary and conclusions regarding the performed work. Bachelor (A. Schlechter) and Master (N. Abbani) students were supervised during this thesis. Part of the presented results regarding the ideal mini-tracker angle analysis was based on the analysis developed by (Schlechter 2021), see section (§4.3.3.). Part of the simulation presented in (§4.1.1.), was based on the simulations developed by (Abbani 2020; Schlechter 2021).

2. Medical, physical, & biological backgrounds of ion-beam radiotherapy

The first mention of the clinical advantages of particle therapy can be traced back to Robert Wilson in 1946 (Wilson 1946). Since then, more than a hundred centers have treated patients with particle therapy using either protons or carbon ions. Carbon-ion radiotherapy (CiRT) in particular, is used today in twelve centers located across five countries, including Austria, China, Germany, Italy, and Japan and six more CiRT sites are under construction in China, Japan, France, South Korea, and Taiwan, (PTCOG 2021b). In Germany, at the Heidelberg Ion Therapy center, HIT, see section (§3.1.), between 2009 and 2017, approximately 2800 patients were treated with CiRT (PTCOG 2017, 2019). Currently, the global interest in using carbon-ion radiotherapy for clinical applications is growing, but what makes carbon ions such an interesting therapeutic tool?

In this chapter, the medical, physical, and biological backgrounds relevant to this thesis are described. First, a short medical background will be detailed in section (§2.1.), with a focus on head-and-neck, brain, and skull base tumors. Carbon-ion radiotherapy is one of the many treatment modalities for such tumors. Therefore, the general physical and biological properties of ions and, in particular carbon ions, will be detailed (§2.2.). A special emphasis will be then given to carbon-ion beam radiotherapy in section (§2.3.) where a list of its advantages but also its limitations will be detailed. This last section will then conclude on the current state of the art of treatment monitoring techniques for carbon-ion radiotherapy.

2.1. Medical background

2.1.1 Definition of cancer and tumor types

A *tumor*, also known as a *neoplasm*, can either be benign or malignant. *Cancer* is a generic term which regroups malignant tumor diseases. A tumor is defined as *malignant*, and thus cancerous, when it exhibits several key hallmarks as summarized in (Hanahan et al. 2000, 2011). Cancer is mostly characterized by a fast proliferation of abnormal cells which is based on diverse genome instabilities and mutations. In 134 countries out of 183 ones, cancer is either the first or the second main cause of premature death (death between 30 and 69 years). Cancer also ranks third or fourth in an additional 45 countries (Wild et al. 2020). It can affect any type of cell, in any organ, at any time. Its causes are many and mostly depend on the cancer type and/or the cancer location. Cancer types are defined by the International Statistical Classification of Diseases and Related Health Problems of WHO using the following codes (C00-C97) (WHO 2019):

- Primary cancer types (C00-75) of the:
  - Lip, oral cavity, and pharynx (C00-C14)
  - Digestive organs (C15-C26)
  - Respiratory system and intrathoracic organs (C30-C39)
  - Bones, joints, and articular cartilage (C40-41)
  - Melanoma and skin (C43-44)
  - Mesothelia and soft tissue (C45-49)
  - Breast (C50)
  - Female genital organs (C51-C58)
  - Male genital organs (C60-C63)
  - Urinary track (C64-C68)
  - Eye, brain, and central nervous system (C69-72)
  - Thyroid and endocrine glands (C73-75)
- Ill-defined sites, secondary sites, and unspecified sites (C76-80)
- Lymphoid and hematopoietic sites (C81-C96)
- Independent multiple sites (C97)

2.1.2 Tumor types of interest

The treated tumors at the Heidelberg Ion Therapy Center (HIT) facility in Germany are, among others: salivary gland carcinoma (C08), chordo-/chondrosarcoma (C41), meningioma (C70), glioma (C71), astrocytoma (C71), medulloblastoma (C71), and, pituitary adenoma (C75), and craniopharyngioma (C75) (UniversitätsKlinikum Heidelberg 2021b). In this thesis, a focus was given to brain and central nervous system (CNS) tumors (C69-71), as well as to head and neck (HN) tumors (C00-14), and skull base tumors (C40). Each of these tumor types will be shortly described in the following three paragraphs. For some of these tumor types, and especially for brain tumors, conventional radiotherapy has been shown to significantly improve local control and to prolong patient survival (Rieken et al. 2012). Nonetheless, the treatment of such tumors is challenging and calls for precaution when using conventional radiotherapy, thus carbon-ion radiotherapy is of interest for such tumors (Rieken et al. 2012). This is mostly because of their location and their proximity to known sensitive organs at risk (OARs), such as optic nerves, spinal cord, salivary glands, or mucous glands.

Brain or CNS tumors are a relatively broad term that is used to describe tumors affecting brain cells. A distinction should be made between primary and secondary (metastatic) brain tumors, and between adults and child brain tumors. Brain cancer is the 13th most common cancer in men and the 14th most common in women (Wild et al. 2020). Overall, a total of approximately 297 000 new brain and CNS cancer cases were found worldwide in 2018 (Bray et al. 2018). Brain cancer causes are not clear yet and the only known cause for brain and CNS tumors is X-radiation and γ-radiation exposure (Wild et al. 2020). The most common types of primary brain tumors for adults are gliomas and meningiomas (skull base tumors), see Figure 2.1-a)-b) for an example. Gliomas arise from glial cells and account for 78 % of malignant brain tumors. Gliomas include astrocytoma, glioblastoma, and medulloblastoma (the most frequent tumor in children) (Moini et al. 2020). Meningiomas, on the other hand, arise from the meninges, the membrane surrounding the brain and spinal cord (WHO report 2020).

Head and neck (HN or H&N) tumors cover a wide range of tumor types and locations. They can be located in the oral cavity (50 %), the pharynx (34 %, including 10 % oropharynx, 14 % nasopharynx, and 10 % hypopharynx), the larynx (20 %), the nasal cavity/paranasal sinuses, or the salivary glands (WHO report 2020). Head and neck cancer is the 7th most common cancer type with a total of approximately 888 000 new cancer cases found in 2018 (Bray et al. 2018). The causes of head and neck cancers are many, among them, one can cite: tobacco smoking, alcohol consumption, and certain human papillomaviruses (HPVs) (WHO report 2020).
Other cancer types that are of relevance for this thesis are not strictly speaking classified as brain cancers (C69-71), nor head and neck cancers (C00-14). These additional cancer types are mostly cancers of the bones of the skull and face (C40), located within the skull area and surrounded by OARs, as shown in Figure 2.2. Of these cancers, skull base chordoma/chondrosarcoma and skull base osteosarcoma are of interest.

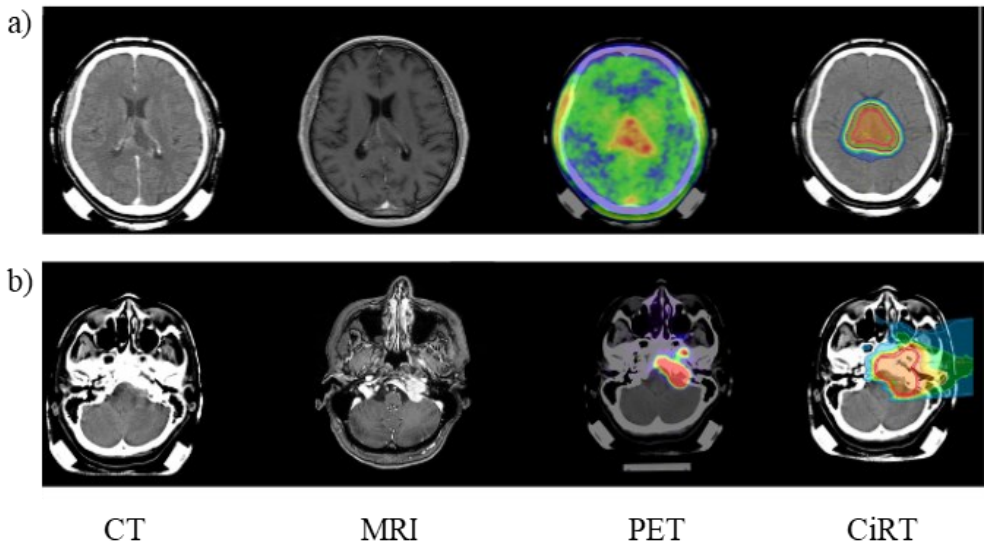

Figure 2.1: Clinical CT, MRI, PET, and CT+ treatment plans images of typical primary brain tumors treated with carbon-ion radiotherapy (CiRT) at the HIT facility: (a) glioblastoma multiform and (b) atypical meningioma. Both tumors were treated with carbon-ion radiotherapy using two treatment fields. Reprinted from (Rieken et al. 2012).

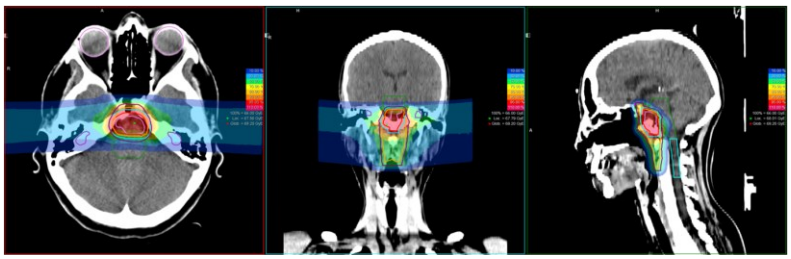

Figure 2.2: Clinical carbon-ion radiotherapy treatment plan of a skull base clival chordoma overlaid with clinical CT images of the patient. Reprinted from (Vogin et al. 2019).

At the HIT facility, in 2009, among the 80 first-treated patients, 36 % of the treated tumors were HN tumors (salivary glands), and 13 % were brain tumors, including low-grade gliomas (< 1 %), astrocytoma + glioblastoma (10 %). The remaining 36% of the first treated tumors were other skull base tumors, which included chordoma (11%), skull base chondrosarcoma (22 %), and skull base osteosarcoma (3 %) (Combs, Ellerbrock, et al. 2010).
Moreover, among the first 36 children and young adults treated with particle therapy (protons or carbon ions) at the HIT facility in 2009, 28 % of the treated tumor were primary brain tumors, 28 % were skull base chordoma/chondrosarcoma, and 8 % were skull base osteosarcoma (Combs et al. 2012).
Additionally, at the HIT facility, 260 patients with brain and skull base tumors were treated between 2009 and 2013. Among them, 107 had meningioma, 55 had high-grade gliomas, 51 had low-grade gliomas, 14 had pituitary adenomas, and 5 had craniopharyngioma. Of these 260 brain cancer patients, 84 patients were treated specifically with carbon-ion radiotherapy (Combs et al. 2013).

2.2. Physical and radiobiological backgrounds of particle therapy

Particle therapy, also known as ion-beam therapy or hadron therapy, was implemented in clinics based on the physical properties of ions and their interactions in matter. In this section the physical and radiobiological bases of charged particles, also called ions, are detailed. This section will present first the physics processes that ions, and in particular carbon ions, undergo in matter. In a second section, the radiobiology of ions will be detailed.

2.2.1 Physics of particle therapy

2.2.1.1 Interactions of charged particles with matter

The linear stopping power, *S*, of a charged particle, e.g. a carbon ion, in matter is defined as its energy loss, *dE*, per unit path length, *dl*, (ICRU 93 2016):

$$S\,[MeV/cm] = mean\left(-\frac{dE}{dl}\right) \qquad \text{(Eq.2.1)}$$

In principle, *S* can be divided into several independent components for the electronic, radiative, and nuclear effects (ICRU 93 2016):

$$S = S_{el} + S_{nuc} + S_{rad} \qquad \text{(Eq.2.2)}$$

The electronic stopping power, S_{el}, is caused by inelastic Coulomb scattering leading to the ionization of matter. The nuclear stopping power, S_{nuc}, is due to elastic Coulomb scattering on target nuclei, which is dominant at low energies (< 10 - 100 keV/u) (Bimbot et al. 2005). And the radiative stopping power, S_{rad}, is due to the emission of radiation during the acceleration of the charged particle in the Coulomb field of the target nuclei (Bremsstrahlung) and may be neglected as compared to the other contributions. Figure 2.3 shows the contribution of S_{el} and

S_{nuc} in water for carbon ions (ICRU 93 2016). For therapeutic protons and carbon ions, S_{el} is the dominant part of S in tissue:

$$S \sim S_{el} \qquad \text{(Eq.2.3)}$$

S_{el} of a charged particle is usually described by the relativistic Bethe-Bloch formula (Bethe 1932; Bloch 1933; Fano 1963):

$$S \sim -\left(\frac{dE}{dl}\right)_{el} = \rho_{med} 4\pi N_A r_e^2 m_e c^2 \frac{Z_{med}}{A_{med}} \frac{z_p^2}{\beta^2} \left(ln\left(\frac{2m_e c^2 \beta^2}{I_{med}\,(1-\beta^2)} \right) - \beta^2 - \frac{C}{Z_{med}} - \frac{\delta}{2} \right) \qquad \text{(Eq.2.4)}$$

where N_A is the Avogadro number (N_A = 6.022 × 10^{23} atoms/g-atom), r_e is the electron radius (r_e = 2.82 fm), m_e is the electron rest mass (m_e = 0.5110 MeV/c²), and c is the speed of light (c = ~3 × 10^8 m/s). Z_{med} represents the charge number of the medium, A_{med} its atomic mass number, ρ_{med} its mass density, and I_{med} is the mean excitation potential of the medium's atoms. β represents the normalized particle velocity ($\beta = v/c$) and z_p its charge number ($z_{p(12C)}$ = +6). The last two terms are correction terms: the shell correction (C/Z_{med}), to describe electron capture that may occur for a charged particle with a velocity comparable to the electron orbital velocity, and the density correction ($\delta/2$), which considers the dielectric polarization in the medium through the electric field of the charged particle crossing it. For therapeutic carbon ions, the polarization correction is of minor importance (Schlegel et al. 2002).

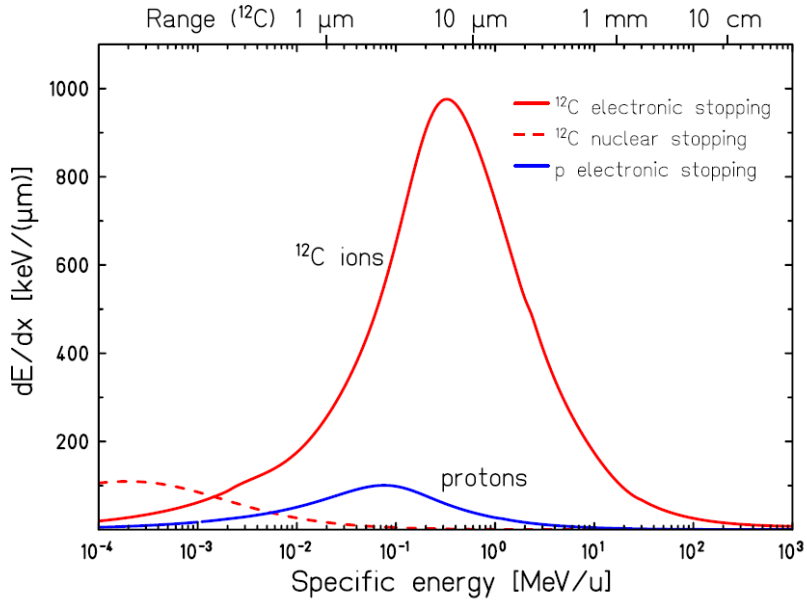

Figure 2.3: Contributions of the energy loss per unit path length S in water for carbon ions and protons. The top axis illustrates the corresponding carbon-ion range in water. Reprinted from (Schardt et al. 2010).

At non-relativistic energies, the electronic stopping power, S_{el}, from (Eq.2.4) is dominated by the factor $1/\beta^2$. Therefore, the particle energy loss increases with decreasing particle velocity. It is known that when penetrating a certain medium, charged particles such as protons or carbon ions slowly slow down, depositing little energy to the medium in a so-called *dose plateau*. Once their entire kinetic energy is almost depleted, there is an increased peak in energy deposited to the medium, followed by a particle stop at a well-defined range. This precise energy deposition of particles in matter is called the *Bragg peak* (or BP) (Bragg et al. 1904), as seen in Figure 2.4.

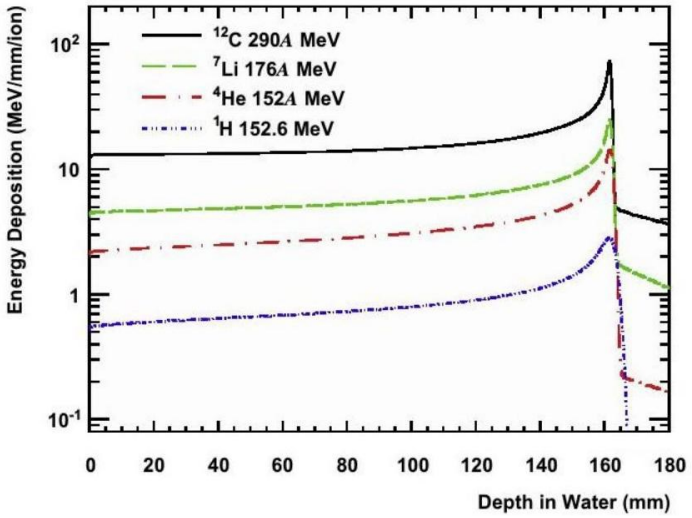

Figure 2.4: Calculated depth-dose profiles for different ion beams with energy that corresponds to a BP located at a depth of 161.6 mm. Reprinted from (Burigo et al. 2014).

Additionally, if both correction factors in (Eq.2.4) are neglected and considering the following approximation:

$$\beta^2 \approx \frac{2E}{A_{proj}\, m_{nuc}\, c^2} \qquad \text{(Eq.2.5)}$$

with A_{proj} as the atomic mass of the projectile and m_{nuc} as the nucleon mass.
Then, the stopping power, $S_{heavy\text{-}ion}$, of a heavy ion can be approximated from the stopping power, S_{proton}, of a proton (Schlegel et al. 2002):

$$S_{heavy-ion} \approx Z^2_{heavy-ion} \times S_{proton}\left(\frac{E}{A_{heavy-ion}}\right) \qquad \text{(Eq.2.6)}$$

with $Z_{heavy\text{-}ion}$ the atomic number and $A_{heavy\text{-}ion}$ the atomic mass number of the heavy-ion. Considering (Eq.2.6) and as seen in Figure 2.5, the stopping power, $S_{carbon\text{-}ion}$, of a carbon ion is thus 36 times greater than the stopping power, S_{proton}, of a proton of the same energy per nucleon.

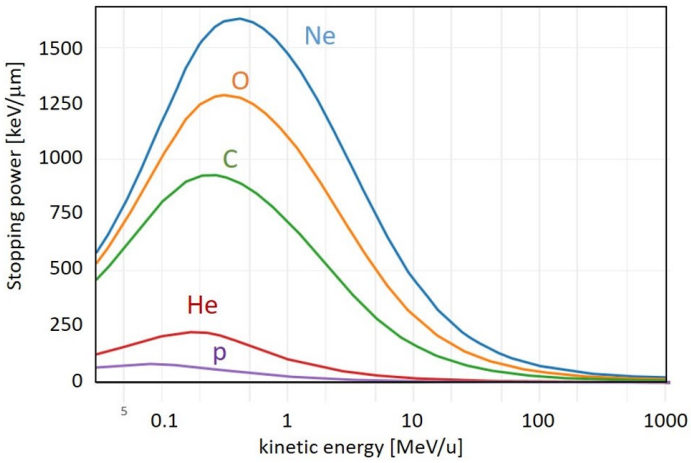

Figure 2.5: Linear stopping power S of several ions as a function of their kinetic energy (logarithmic scale). Reprinted from (Jäkel 2020).

The mass stopping power, S_{MASS}, is defined as the linear stopping power of a charged particle, S, divided by the medium density, ρ (ICRU 93 2016):

$$S_{MASS}\,[MeV \cdot cm^2/g] = (S/\rho)_{tot} \qquad \text{(Eq.2.7)}$$

The linear energy transfer, LET, of a charged particle to a medium is a measure of the energy locally transferred, dE, by the particle per path length, dl. The local aspect of the LET is defined as follows: the *restricted* LET_{Δ} with $\boldsymbol{\Delta}$ being the maximum energy up to which the energy loss is counted. In its unrestricted form, LET_{inf} is equal to mass stopping power, S, (ICRU 85 2011):

$$LET_{\Delta}\left[\frac{J}{m} or \frac{keV}{\mu m}\right] = \frac{dE_{\Delta}}{dl} \qquad \text{(Eq.2.8)}$$

$$LET_{inf} = S \qquad \text{(Eq.2.9)}$$

The LET of a charged particle is a common measure for local biological effects induced by the charged particle to the crossed medium. It is thus used for characterizing the ionization density of different charged particle types. A distinction is made between high and low-LET radiation, where high-LET corresponds to high doses locally deposited. A detailed explanation of high and low LET will be given later in section (§2.2.2.1.).

2.2.1.2 Physical dose

In radiotherapy, the physical or absorbed dose, D, describes the mean energy, $d\bar{\varepsilon}$, macroscopically deposited in a medium by an ionizing radiation per unit mass, dm:

$$D\left[1\,Gy = 1\,\frac{J}{kg}\right] = \frac{d\bar{\varepsilon}}{dm} \qquad \text{(Eq.2.10)}$$

The physical dose, D, is given in [Gray (Gy)] and used to be expressed in the old unit [rad] (where 1 Gy = 100 rad). D should not be confused with the biological dose, D_{RBE} in [Gy (RBE)], nor with the Exposure, X, or the Equivalent Dose $H\ [Sv] = D \times w_R$.
The physical dose, D, of charged particles in a medium is also connected to the stopping power S or mass stopping power $(S/\rho)_{tot}$ by (Schardt et al. 2010):

$$D\ [Gy] = 1.602 \times 10^{-9} \times\ F \times \left(\frac{dE}{dl}\frac{1}{\rho}\right) \qquad \text{(Eq.2.11)}$$

where F represents the particle fluence cm^{-2}, ρ is the medium density expressed in g/cm^3, and $(dE/dl)/\rho$) is the mass stopping power in keV/µm.

2.2.1.3 Range of charged particles in matter

The range, R, of a particle beam in a medium is defined as the depth at which 50 % of the primary particles have stopped (if nuclear interactions are neglected). This depth depends on the particle type, its energy, and the medium material. For mono-energetic protons, the depth at which half of the protons have stopped coincides with the distal point at which 80 % of the maximum dose is reached, i.e. 80 % of the Bragg peak (Paganetti 2012):

$$R = d_{80} \qquad \text{(Eq.2.12)}$$

The stopping power, S, of a charged particle in a medium can also be used to calculate the particle mean total path length (or range, if the path is assumed to be straight) R by using the so-called continuous slowing down approximation (CSDA). R_{CSDA} of a charged particle is then given then by the integration of the inverse stopping power S of the particle from the initial particle kinetic energy $E_{initial}$ until zero (ICRU 93 2016):

$$R_{CSDA}(E_{initial}) = \int_{E_{initial}}^{0} \frac{1}{S(E)}\,dE = -\int_{0}^{E_{initial}} \left(\frac{dE}{dl}\right)^{-1} dE \qquad \text{(Eq.2.13)}$$

Using the approximation (Eq.2.6), the mean range of a heavy ion $R_{heavy\text{-}ion}$ can be calculated from the range of a proton R_{proton} of the same energy per nucleon (ICRU 93 2016):

$$R_{heavy-ion}(E_{initial}) \approx -\frac{A_{heavy-ion}}{Z^2_{heavy-ion}}\, R_{proton}(E_{initial}) \qquad \text{(Eq.2.14)}$$

The mean range of mono-energetic carbon ions, $R_{carbon\text{-}ion}$, is thus a third of the range of proton ions, R_{proton}, of the same energy per nucleon. Figure 2.6 shows the mean ranges in water for different charged particles.

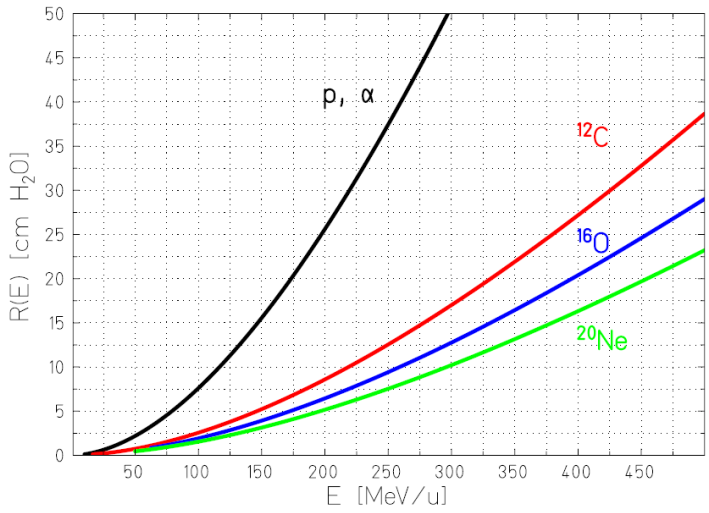

Figure 2.6: Mean range R in water per for several heavy ions as a function of their energy per nucleon as reprinted from (Schardt et al. 2010).

2.2.1.4 Range straggling

The *range straggling* is defined as the range difference that is seen between particles with identical initial energy. Both energy-loss straggling and lateral straggling directly contribute to the range straggling. As in Figure 2.7, the standard deviation σ_R of a range distribution R in water (in cm) due to the range straggling of ions with the atomic number $A_{heavy\text{-}ion}$ can be approximated as a function of the depth, x, (Chu et al. 1993):

$$\sigma_R = \frac{0.012 \times x^{0.951}}{\sqrt{A_{heavy\ ion}}} \qquad \text{(Eq.2.15)}$$

During the energy-loss process, as seen in Figure 2.8, the energy loss statistically fluctuates due to the number of collisions and the energy transferred in each collision. This effect is called *energy-loss straggling* and is one of the reasons for the broadening of the Bragg peak.
When charged particles pass through matter, they also experience repeated elastic scattering caused by the Coulomb field of the target medium nuclei. This process leads to many small angular deflections and results in a lateral scattering of the charged particles. The summation of all these small angles is called multiple Coulomb scattering (MCS). MCS is described by the Molière distribution(Bethe 1953; Moliere 1948). .For larger deflection angles, the resulting angular distribution is obtained from Rutherford scattering. For small deflection angles, the angular distribution is approximated by a Gaussian function (Highland 1975). For charged particles of the same speed the root-mean-square angle θ_0 of multiple Coulomb scattering is (ICRU 93 2016):

$$\theta_0 \propto \frac{Z_{ion}}{A_{ion}} \qquad \text{(Eq.2.16)}$$

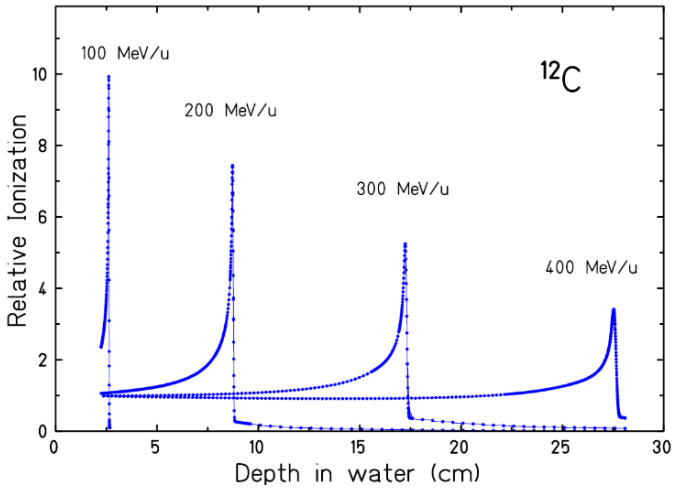

Figure 2.7: Impact of the range straggling on the broadening of the Bragg peaks as a function of the carbon-ion range in water as reprinted from (Schardt et al. 2010).

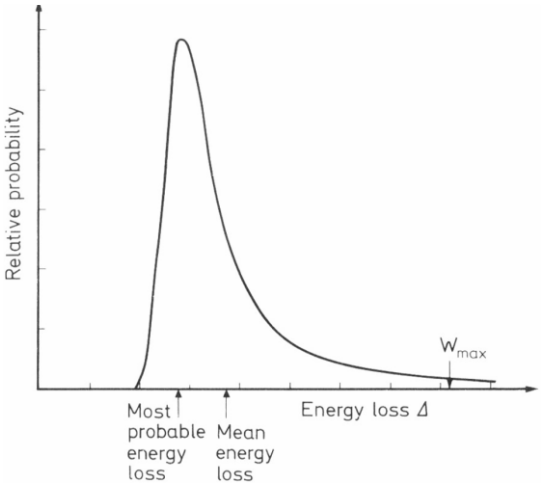

Figure 2.8: The Landau distribution representing the energy loss probability as a function of the energy loss Δ, this phenomenon is the energy-loss straggling. Reprinted from (Leo et al. 1990).

2.2.1.5 Relative stopping power of a material

The linear stopping power of a medium is directly used to express the relative stopping power, *RSP*, of a medium, also called water equivalent path length, *WEPL*. It defined is by the ratio between the linear stopping power S_{medium} of the medium, as defined as in (Eq.2.1), and the linear stopping power of water S_{water}. Therefore, by definition, $RSP_{water} = 1$.

$$RSP = WEPL = \frac{S_{medium}}{S_{water}} \qquad \text{(Eq.2.17)}$$

The water equivalent thickness, *WET*, of an object, is the integrated *RSP* (or *WEPL*) of the medium along the charged particle beam path. In other words, the *WET* of an object characterizes the thickness of a water body that has the same effect as the object on the particle range:

$$WET_{object} = \int_0^L WEPL \; dl = RSP \; L \qquad \text{(Eq.2.18)}$$

The knowledge of the RSP values in a patient is crucial for particle therapy planning. Those values are obtained from Computed Tomography (CT) images. However, CT images measure X-ray attenuation in matter. The measured attenuation $\bar{\mu}$ is expressed in Hounsfield Units [HU] as:

$$H\,[HU] = \left(\frac{\bar{\mu}}{\bar{\mu}_{H2O}} - 1\right)1000 \qquad \text{(Eq.2.19)}$$

(Schneider et al. 2000) proposed to retrieve the mass density and chemical composition of human tissues using measured CT HUs and stoichiometric calibration curves. So-called Hounsfield Look-Up Tables (HLUT) have thus been made for different radiation types, allowing integrated carbon ion stopping powers to be extrapolated from measured CT HUs. For this, measured HUs were correlated to measured *RSP* (Jäkel, Jacob, et al. 2001; Rietzel et al. 2007) leading to the following calibration function (see Figure 2.9):

$$RSP = \begin{cases} HU\,(9.41 \pm 0.08)10^{-4} + 1.0: & HU < 0 \\ HU\,(4.35 \pm 0.12)10^{-4} + 1.0: & HU \geq 0 \end{cases} \qquad \text{(Eq.2.20)}$$

The uncertainties of the stopping power conversion are found to be 2 % to 3 % for carbon ions in water (Jäkel, Jacob, et al. 2001).

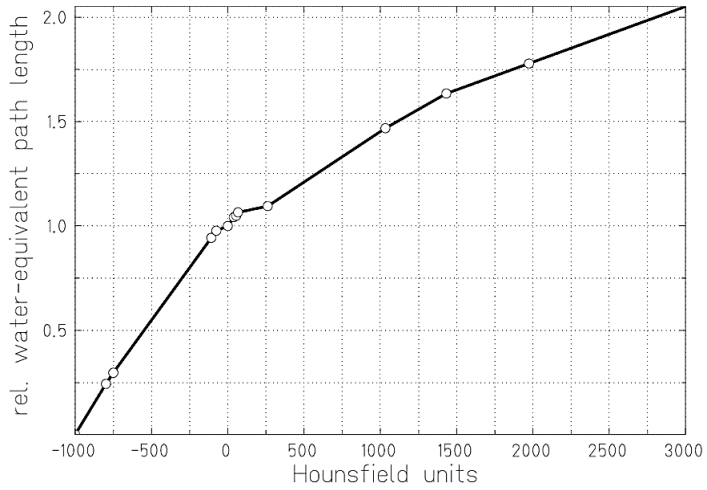

Figure 2.9: Comparison of the measured HUs to measured RSP (or WEPL) values (retrieved from measured carbon-ion residual ranges) for different tissue samples. Reprinted from (Rietzel et al. 2007) using data from (Jäkel, Jacob, et al. 2001).

2.2.1.6 Nuclear fragmentation

When crossing a medium, heavy ions experience hard nucleus-nucleus interactions. These so-called nuclear fragmentations lead to a decrease of the primary-ion fluence and a production (build-up) of light fragments (secondary, tertiary, etc. ions).

The nuclear fragmentation of an ion is described in a two-step process by the abrasion-ablation model (Serber 1947) as shown in Figure 2.10. First, target and projectile nuclei collide, and a fireball is produced from the shredded off nucleons in the overlapping region of the target and projectile (abrasion step within 10^{-23} s). Second, the de-excitation of the produced target and projectile fragments, as well as the fireball, happens, leading to the emission of nucleons and prompt gammas (ablation step within 10^{-21} s to 10^{-16} s).

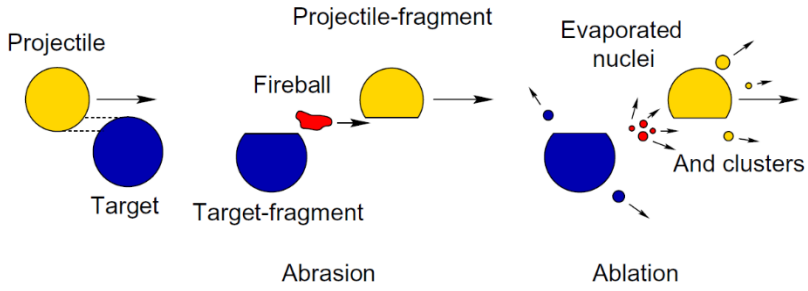

Figure 2.10: Abrasion-ablation model describing the nuclear fragmentation of high-energy projectile nuclei (yellow) and target nuclei (blue). Reprinted from (Gunzert-Marx et al. 2008).

The produced target fragments are considered at rest, while the projectile fragments continue to cross the material in a forward peaked direction with a velocity similar to the projectile. As the projectile fragments have a lower mass and charge than the projectiles themselves, these fragments exhibit longer ranges in the medium than the projectiles. The produced secondary fragments directly contribute to the dose deposited in the medium. Thus, the energy of target fragments can be deposited downstream of the Bragg peak in a characteristic *fragmentation dose tail* as seen in Figure 2.11.

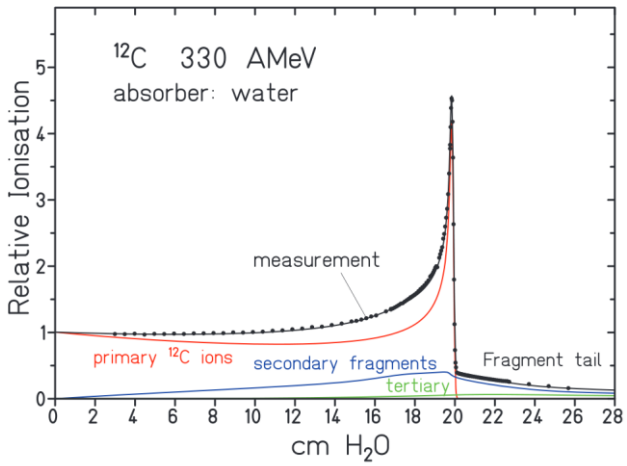

Figure 2.11: Depth-dose profile by carbon ions of 330 MeV/u in water as measured at GSI. Contribution from the produced secondary and tertiary fragments is visible in the so-called fragment tail downstream of the Bragg peak. Reprinted from (Schardt 2007).

2.2.2. Radiobiology of ion beam therapy

2.2.2.1 Effect of radiation in cells

When radiation penetrates a medium, energy is transferred to the medium as described by the LET defined in (Eq.2.8) in section (§2.2.1.1.). LET is also an important parameter to quantify locally the radiobiological effect of ion beams since it is linked to the Relative Biological Effectiveness (RBE) and the oxygen enhancing ratio (OER) of ions as presented in the next paragraphs. A distinction is made between non-ionizing radiations and ionizing radiations.
Within the ionizing radiations, one distinguishes between (Lomax et al. 2013; Mohamad et al. 2017):

- indirect ionizing radiation, such as photons (X-rays and γ-rays) or neutrons, that are generally considered to be low-LET. This low-LET radiation mostly leads to simple DNA damages, such as single-strand breaks (SSB), or simple double-strand breaks (simple DSB). Only 30 % of the energy deposited by low-LET radiation induces clustered or multiple damage sites.

- direct ionizing radiation, such as electrons, protons, charged particles, or heavy ions, leading to high-LET. This high-LET radiation mostly leads to complex multiple DNA damage, including complex double-strand breaks (complex DSBs). 90 % of the energy deposited by high-LET radiation induces clustered or multiple damage sites (Lomax et al. 2013; Mohamad et al. 2017).

Two examples of the deposited energy distribution for high- and low-LET radiations are shown in Figure 2.12. Since this thesis focuses on carbon-ion radiotherapy, a special interest is given to direct high-LET ionizing radiation.
Radiation-induced DSBs can be repaired using non-homologous end joining (NHEJ), alternative end-joining (Alt-EJ or A-EJ), or homologous recombination (HR). As shown in Figure 2.13, low-LET radiation-induced DSBs are repaired by NHEJ or a combination of NHEJ/HR. However, because of the more complex nature of the DNA damage induced by high-LET radiation, less efficient DNA repair mechanisms follow high-LET radiation exposure (HR repair mechanism only). This leads to DNA being unrepaired for a longer time, which promotes genome instability and eventually leads to cell death. (Lomax et al. 2013).

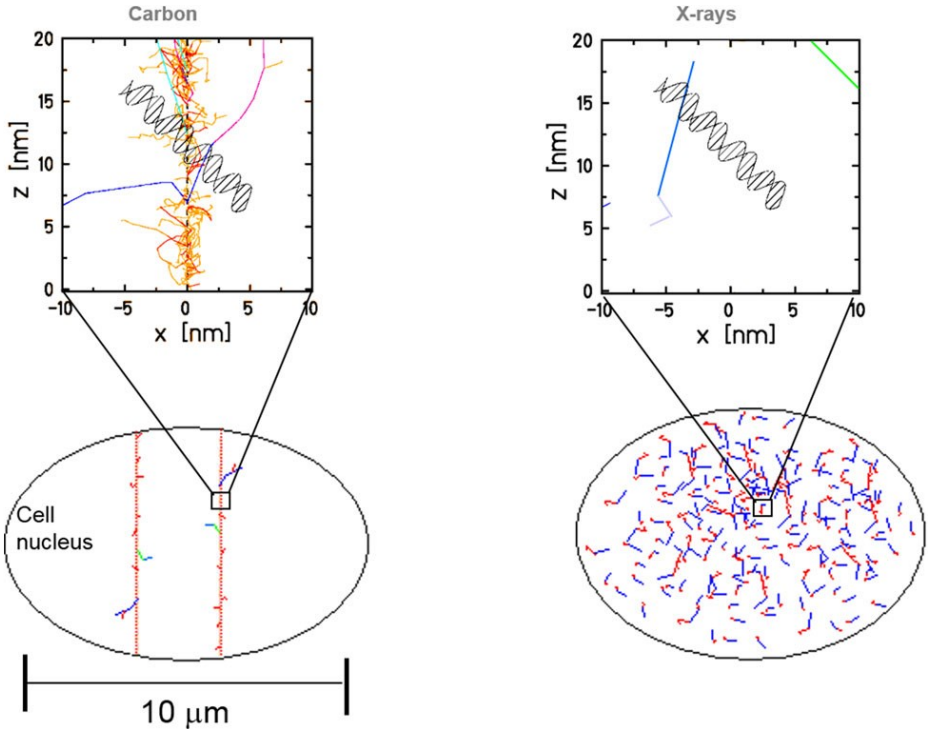

Figure 2.12: Different track structures of carbon ions and photons in a cell nucleus and comparison with the DNA size. The deposited energy distribution is localized along the trajectory of the high-LET carbon ion, but it is randomly distributed for low-LET photons (X-rays) (reprinted from (ICRU 93 2016)).

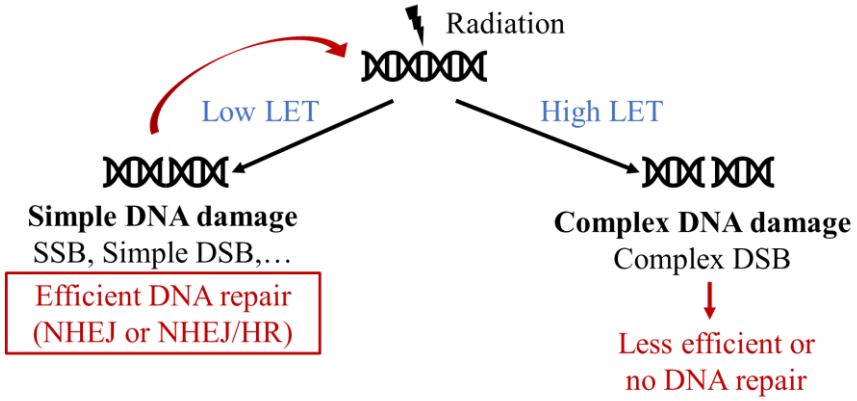

Figure 2.13: Repair of radiation-induced DNA damage from high- and low-LET radiation. Simple DNA damage is repaired by NHEJ or a combination of NHEJ/HR. More complex DNA damage is repaired by less efficient repair mechanisms. Adapted from (Mohamad et al. 2017).

2.2.2.2 Cell survival fraction

The effect of a certain radiation dose, *D*, in a cell population is quantified by the survival fraction, *SF*, of the irradiated cells. This *SF* is a measurable quantity that can be described as a function of the delivered dose, *D*, by linear quadratic curve (Podgorsak 2005):

$$SF(D) = e^{-(\alpha D + \beta D^2)} \qquad \text{(Eq.2.21)}$$

From this linear quadratic fit, cell-specific parameters can be retrieved: the parameter α (in Gy^{-1}) represents the single hits contribution, and β (in Gy^{-2}) represents the double hits contribution. From these cell-specific parameters, an *α/β-ratio* (in Gy) is defined. This ratio describes the extent of the *SF* curve shoulder, see Figure 2.14-a). A small *α/β-ratio*, seen as almost no *SF* curve shoulder, corresponds to a large cell repair capacity, while a large *α/β-ratio*, seen as a large *SF* curve shoulder, correlates with small cell repair capacity.

The shape of the cell-specific *SF* curve and the corresponding *α/β-ratio* play an important role when treating cancer patients. Indeed, radiotherapy uses the differences in radiation sensitivity and repair capacity of healthy and cancerous cells to disproportionally affect tumor cells. This is done in the following way, as seen in Figure 2.14-b): the total dose to be delivered to a tumor is split up into several irradiations (called *fractions*) which are spread over several days. The time between each fraction allows the healthy cells (usually exhibiting a small *α/β-ratio*) to repair their radiation-induced DNA damage, while tumor cells (usually exhibiting large *α/β-ratio*) cannot do this to the same extent.

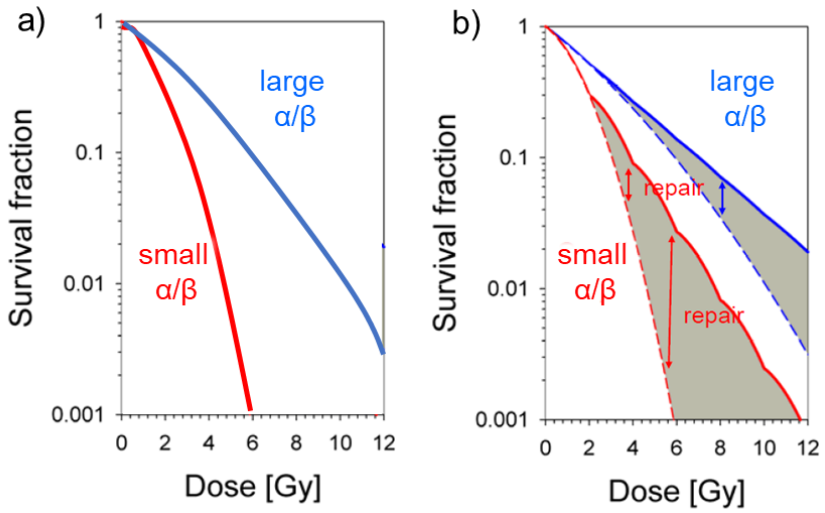

Figure 2.14: a) Two linear quadratic curves corresponding to two survival fraction curves after irradiation for cells exhibiting small and large α/β. b) Repeated irradiations (fractionation) allow bettering healthy cells sparing (small α/β) compared to tumor cells (large α/β). Adapted from (Karger 2021).

2.2.2.3 Relative Biological Effectiveness

The Relative Biological Effectiveness, *RBE*, of a charged particle in a medium is defined as the ratio between the iso-effective absorbed doses of X-rays and that of particles (ICRU 93 2016):

$$RBE = \frac{D_{X-rays}}{D_{ions}}\Big|_{iso-effective} \qquad \text{(Eq.2.22)}$$

A difference in the quality between the two radiation types thus leads to an $RBE \neq 1$. The *RBE* also depends on the biological endpoint (e.g. cell survival level) used for its calculation; see Figure 2.15.

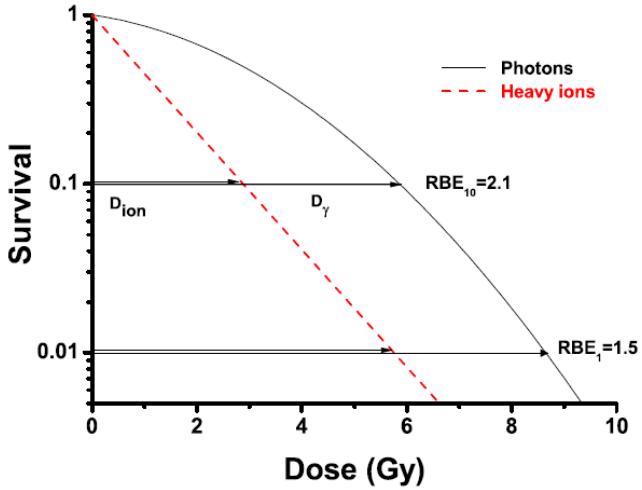

Figure 2.15: Survival fraction curves as a function of dose for photons and ions. RBE_{10} and RBE_1 are calculated at a cell survival of 10 % and 1 %, respectively. Reprinted from (Schardt et al. 2010).

Usually, the *RBE* of charged particles varies as a function of tissue type and fraction dose, but it is conventionally accepted that:

$$RBE_{proton} = 1.1 \text{ and } RBE_{carbon\text{-}ion} \sim 1.5 \text{ to } 3$$

The $RBE_{carbon\text{-ion}}$ is given for a typical clinical dose range, target organs, and tumors (Mein et al. 2020). It can be determined experimentally or approximated by models such as the Local Effect Model (LEM I/IV) or the modified Microdosimetric Kinetic Model (MKM). At the Heidelberg Ion Therapy Center (HIT), carbon-ion treatment planning with $RBE_{carbon\text{-ion}}$ is based on the Local Effect Model (LEM1) (Scholz et al 1997). For intracranial lesions, a constant tissue fractionation parameter $(\alpha/\beta)_x$ of 2 Gy is used (Combs et al. 2013).
The *RBE* is a complex entity and is, among other factors, correlated with particle energy, the *LET*, the cell type, etc. The main dependency of RBE is with LET and dose: *RBE* increases with the *LET* until the overkill effect is reached (as seen in Figure 2.16-a)-b)).

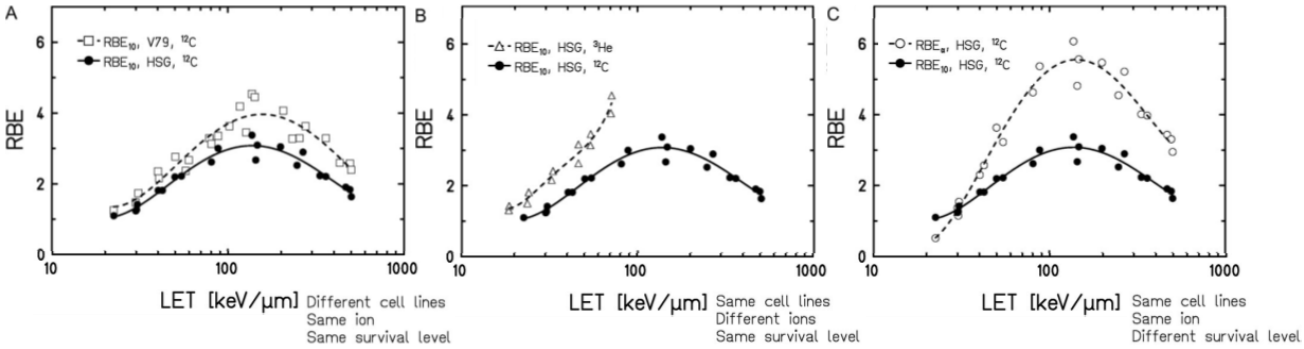

Figure 2.16: a) Dependencies between *RBE* and *LET* for different cell lines (a), ions (b), and survival level (c). The decrease in *RBE* at high-LET is due to the overkill effect. Reprinted from (ICRU 93 2016) using data from (Furusawa et al. 2000).

2.2.2.4 Oxygen Enhancement Ratio

The oxygen enhancement ratio, *OER*, is defined as the ratio between iso-effective absorbed doses under hypoxic and under oxic conditions (ICRU 93 2016):

$$OER = \frac{D_{hypoxic}}{D_{oxic}}\Big|_{iso-effective} \qquad \text{(Eq.2.23)}$$

As seen in Figure 2.17, the *OER* is *LET* dependent: for high-LET radiation, the *OER* is seen to be smaller. In other words, high-LET radiation leads to the same damage under hypoxic or oxic conditions. Thus high-LET radiation is efficient against radio-resistant hypoxic cells.

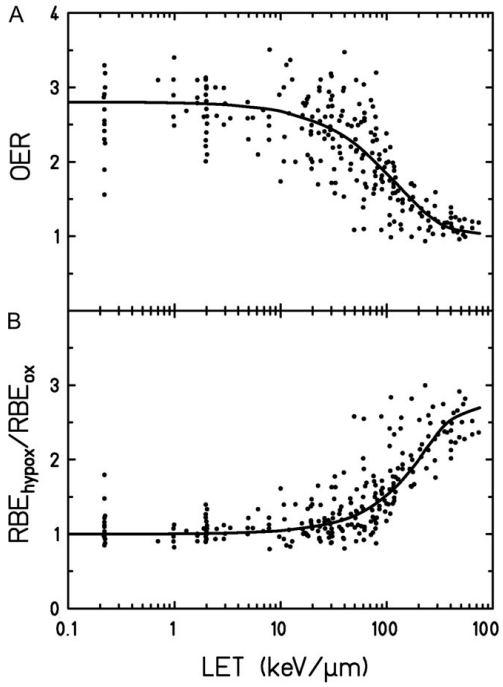

Figure 2.17: Relationship between *OER*, *RBE* and *LET* as measured for a large variety of ion types. Reprinted from (ICRU 93 2016) using data from (Wenzl and Wilkens, 2011).

2.2.2.5 Prescribed dose

In ion beam therapy, the dose is prescribed in RBE-weighted dose, $D_{RBE,}$ (ICRU 93 2016):

$$D_{RBE}[Gy\ (RBE)] = RBE\ \times D \qquad \text{(Eq.2.24)}$$

The unit of the D_{RBE} is Gy (RBE). In the particle community, RBE-weighted dose is also termed "biological effective dose" or "biological dose" (GyE, Gy(E), Gye, Gy (RBE), and CGE). Individual carbon-ion pencil beams show a Bragg peak that is too sharp for the treatment of typical tumors, see Figure 2.18. Therefore, pencil beams of different ranges, i.e. of different beam energies, are combined in a so-called *spread-out Bragg peak* (SOBP) as seen in Figure 2.19.

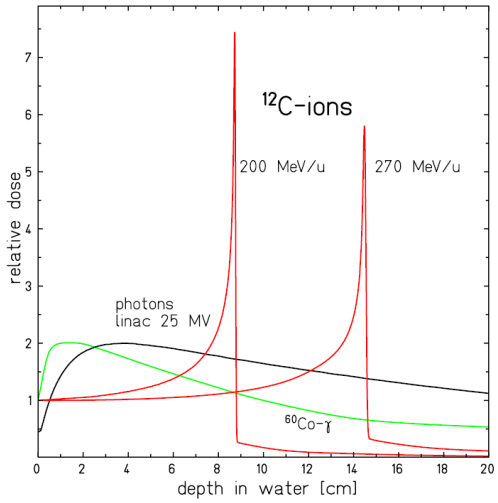

Figure 2.18: Relative dose deposition curves in water for mono-energetic 200 MeV/u and 270 MeV/u carbon ions compared with 25 MV photons, and ^{60}Co gamma radiation. The sharp energy deposition of carbon ions in matter shows a visible Bragg peak at the end of the ion range. Reprinted from (Schardt et al. 2010).

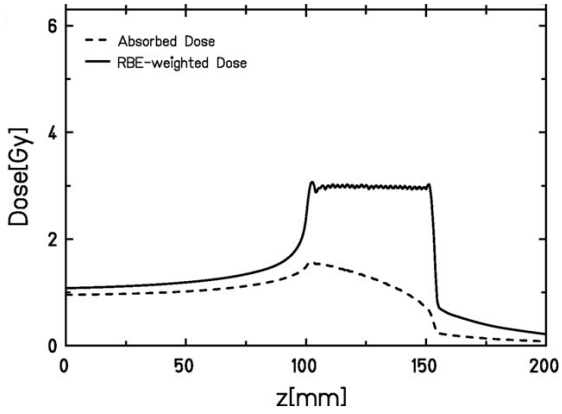

Figure 2.19: Schematic difference between physical and RBE-weighted doses for a biologically optimized SOBP. Adapted from (ICRU 93 2016).

2.3. Carbon-ion radiotherapy

2.3.1 Theoretical advantages of carbon-ion radiotherapy

The theoretical advantages of carbon-ion radiotherapy over photon and proton radiotherapy are directly related to the intrinsic physical and radio-biological properties of carbon ions. A detailed list of carbon-ion advantages can be found in (Mohamad et al. 2017).

First, as seen in Figure 2.18, when comparing the dose deposition curve of ions in water with one of the photons, carbon ions and protons allow to better spare healthy tissues in their dose plateau regions and to deliver more dose to the tumor using the Brag-peak. This effect is even stronger when delivering doses using SOBPs. Though, as seen in (Eq.2.15), the range straggling of carbon ions is seen to be $1/\sqrt{12} \sim 3.5$ times smaller than for protons of the same range. An even sharper Bragg peak is thus expected for carbon ions than for protons. Carbon-ion radiotherapy should, thus, lead to a better dose conformation in the longitudinal dimension compared to photon and even proton radiotherapy.

Moreover, the MCS and the lateral beam spread associated with particle beams is reduced for carbon ions compared with protons, as seen in (Eq.2.16) and Figure 2.20. Carbon-ion radiotherapy should, thus, also lead to a better dose conformation in the lateral dimensions compared to proton or photon radiotherapy.

Additionally, as seen in Figure 2.16, the direct damage of high-LET radiation such as carbon ions has a higher biological effect than that of low-LET radiation such as X-rays and protons. Thus, carbon ions exhibit a higher *RBE* than photons and protons.

Lastly, as seen in Figure 2.17, the *OER* is seen to be smaller for high-LET radiations. Hence, high-LET carbon ions lead to the same damage under hypoxic or oxic conditions. Carbon-ion radiotherapy should, thus, be more efficient against radio-resistant hypoxic cells compared to proton or photon radiotherapy.

In conclusion, given all the aforementioned physical advantages of carbon ions (which include sharper dose profile, lower lateral penumbra, and/or smaller scattering) and considering the precision reached with carbon-ion beam delivery using magnetic steering (raster scanning beams), it is clear that carbon-ion radiotherapy is of interest compared to photon and even to proton radiotherapy. Overall, carbon-ion radiotherapy offers the possibility to design dose distributions of superior dose conformity compared with X-rays and protons, allowing to theoretically better spare healthy tissues and organs at risk (OARs) from radiation damage.

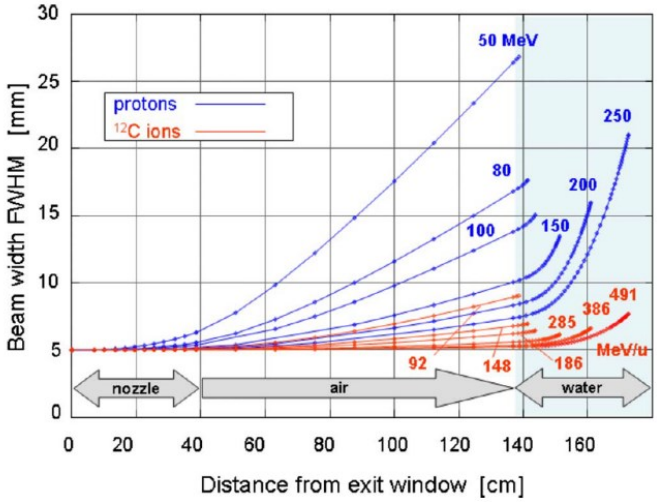

Figure 2.20: Calculated lateral spread for carbon ions and protons beams in a beam nozzle, in air, and water. Reprinted from (Weber et al. 2009)

Current clinical trials

The inherent physical and biological properties of protons and carbon ions suggest that particle therapy is a great tool to treat challenging tumors such as deep-seated tumors of the brain and the HN (surgery, photon 3DCRT, IMRT, VMAT, etc.). These benefits have been verified for several tumor types such as skull base chordoma (Takagi et al. 2018), meningiomas (El Shafie et al. 2018), resistant adenoid cystic carcinomas (Schulz-Ertner et al. 2005), and pediatric tumors (Sakthivel et al. 2019). However, within particle therapy, the theoretical benefit of carbon-ion radiotherapy over protons radiotherapy is still under investigation (Rackwitz et al. 2019).

To prove and support the theoretical benefits of carbon ions over protons, several clinical trials have been initiated at the Heidelberg Ion Therapy Center (HIT) (UniversitätsKlinikum Heidelberg 2021c). Table 2.1 summarizes the current clinical trials at the HIT facility that compare carbon-ion radiotherapy treatments of CNS and HN tumors with other treatment modalities (such as photon or proton radiotherapies, with or without boost, etc.). More clinical trials evaluating carbon-ion radiotherapy can also be found in (Malouff et al. 2020).

From these trials, numerous metrics, such as treatment overall survival, long-term survival, tumor control, acute and late toxicities, can be used to evaluate the potential benefits of carbon-ion radiotherapy over proton or photon radiotherapies. As an example, the CINDERELLA trial showed that re-irradiation of patients with recurrent gliomas with 10 to 16 fractions of 3 Gy (RBE) is safe: it was found that carbon-ion radiotherapy leads to no dose-limiting toxicities and a higher median overall survival of approximately one year in comparison to fractionated stereotactic radiotherapy (Combs, Burkholder, et al. 2010).

However, even though the benefits of particle therapy shown in some of these trials are promising, it is difficult to conclude the general effectiveness of carbon-ion radiotherapy for an individual patient. Indeed, the lack of standardization in between treatments sites, the different dose effectiveness in between the radiation types, the different learning curves and training levels of operating teams, the years-long follow-up times, and the randomization issues that are linked to such clinical trials are some of the limiting points impeding further conclusions on the general effectiveness of carbon-ion radiotherapy (Rackwitz et al. 2019).

Table 2.1: Carbon-ion radiotherapy clinical trials for brain and HN tumors at the HIT facility.

Status	Closed	Recruiting	Evaluating	Published
Brain tumors		**MARCIE** atypical meningiomas II A: photon + C12 boost (Combs, Edler, et al. 2010)	**CLEOPATRA** primary glioblastoma A: chemo. + H1 boost B: chemo. + C12 boost (Combs, Kieser, et al. 2010) **CINDERELLA** recurrent glioblastoma A: CiRT vs B: FSRT (Combs, Burkholder, et al. 2010)	
HN tumors	**TPF-C-HIT** throat H&N cancer A: radioimmunotherapy + C12 + IMRT (Jensen, Krauss, et al. 2011)	**ACCO** adenoid cystic carcinoma A: C12 only vs B: IMRT + C12 boost (UniversitätsKlinikum Heidelberg 2021a) **ACCEPT** adenoid cystic carcinoma A: IMRT + C12 boost (Adeberg et al. 2020) **IMRT-HIT-SNT** sinu-nasal cancer A: IMRT + C12 boost (Jensen, Nikoghosyan, et al. 2011)		**COSMIC** salivary glands A: IMRT + C12 boost (Jensen et al. 2015)
Skull base chordoma/sarcoma		**ISAC** sacrococcygeal chordoma A: H1 vs B: CiRT (Uhl et al. 2014). **Skull base chordoma III HIT-1** A: CiRT vs B: H1 (Nikoghosyan, Karapanagiotou-Schenkel, et al. 2010). **Skull base chondrosarcomas III CSP12C**: A: CiRT vs B: H1 (Nikoghosyan, Rauch, et al. 2010) **OSCAR** inoperable osteosarcoma A: H1 + 12C boost (UniversitätsKlinikum Heidelberg 2021e)		

2.3.2 Disadvantages of carbon-ion radiotherapy

Opposite of the theoretical advantages of carbon-ion radiotherapy over photon and proton radiotherapy, carbon-ion radiotherapy also exhibits theoretical disadvantages and limitations. These disadvantages are detailed in the following section.

2.3.2.1 Fragmentation dose tail

First, as seen in Figure 2.4, a characteristic fragmentation dose tail is visible in the dose deposition curve downstream of the Bragg peak due to the contribution of produced light secondary fragments from carbon-ion beams. Due to the Z^2/A energy-loss dependence of these secondary fragments (ICRU 93 2016), this fragmentation dose tail is bigger for carbon ions compared to protons. Protons, however, do not undergo nuclear fragmentation and deliver virtually no dose behind the Bragg peak (neglecting the production of neutral particles). The limitations introduced by the fragmentation tail can be mitigated by avoiding carbon-ion beam directions that make ions stop directly in front of organs at risk (OAR).

2.3.2.2 Systematic and statistical uncertainties

The more conformal dose delivery of ions, achieved thanks to their steeper dose profile, is also more impacted by treatment uncertainties (Fattori et al. 2014). These uncertainties can be separated into systematic and random (statistical) uncertainties. A summary of these systematic and random uncertainties are presented in Table 2.2 and the following two paragraphs.

Systematic uncertainties affect all fractions of patient treatment in the same way. These uncertainties, see Figure 2.21, can arise from the treatment planning uncertainties, uncertainties from conversion from CT HU to WET, the uncertainties from RBE-weighted dose calculation, or the patient immobilization setup uncertainties.

- Systematic treatment planning uncertainties mostly come from the planning CT uncertainties (affected by the CT imaging accuracy and CT reconstruction artifacts), the delineation variability of the tumor volume (Jäkel et al. 2000).
- Empirical uncertainties in the CT HU conversion into particle stopping power lead to systematic uncertainties of the order of 1 mm for carbon-ion radiotherapy (Rietzel et al. 2007). The combined uncertainty of stopping-power ratios derived from CT HU conversion is around 2-3 % (Jäkel, Jacob, et al. 2001) but can increase to 6.3 % for head and neck treatments from (ICRU 93 2016).
- RBE prediction uncertainties directly transfer into a systematic uncertainty of the biological RBE-weighed dose (Böhlen et al. 2012). The RBE is, among others, particle-type-specific, tumor-specific, and patient-specific. Hence, complex radiobiological models have been developed over the years to predict the RBE of carbon ions in matter. However, the employed RBE models differ significantly between Europe (LEM I/IV) and Japan (MKM). This results in RBE prediction uncertainties of up to 20 - 30 % (Fossati et al. 2012). In a recent in-silico patient study, these uncertainties lead to RBE-weighted dose prediction variations of up to ~ 40 % (Mein et al. 2020).
- Systematic patient immobilization uncertainties are directly linked to the accuracy of the robotic treatment couch position (below 0.2 mm ± 0.2 mm std at the HIT facility (Jensen et al. 2012)) and the accuracy of the patient correction imaging system, such as

in-room orthogonal X-rays (0.2 mm ± 0.1 mm std at the HIT facility (Jensen et al. 2012)).

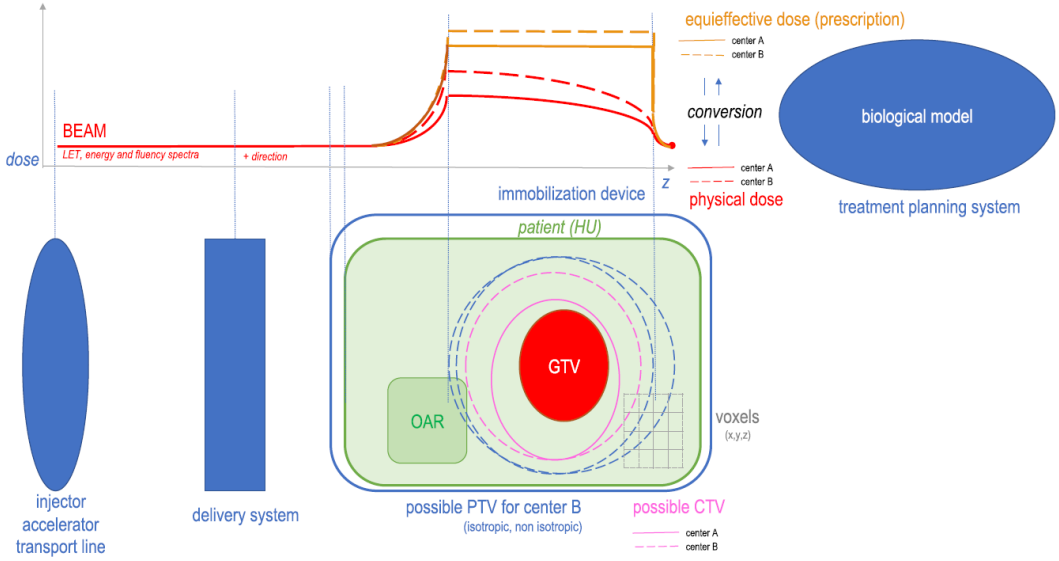

Figure 2.21: Global overview of the systematic uncertainties directly affecting dose deposition during the carbon-ion radiotherapy treatment planning process. Reprinted from (Vogin et al. 2019).

Random uncertainties, on the other hand, randomly affect each fraction of patient treatment. They can arise from intra-fractional changes, happening within a treatment fraction, or from inter-fractional changes, happening between two treatment fractions.

- Intra-fractional changes can arise from organ or respiratory motion, or even heartbeat.
- Inter-factional changes can come from random uncertainties in:
    - Inter-fractional patient positioning setup error, which is expected to be ±1.0 mm and ±1.0° for cranial treatments (Fattori et al. 2014).
    - Inter-fractional anatomical changes, as seen in Figure 2.22. Changes in the patient anatomy can arise from inflammation, weight loss ((Bhandari et al. 2014) found weight loss up to 10 % (3 to 8 kg weight loss) in studied HN cancer patients), or tumor volume shrinkage among others (mean PTV shrinkage of 149.83 cm^3 for HN tumor treated with IMRT (Bhandari et al. 2014)).

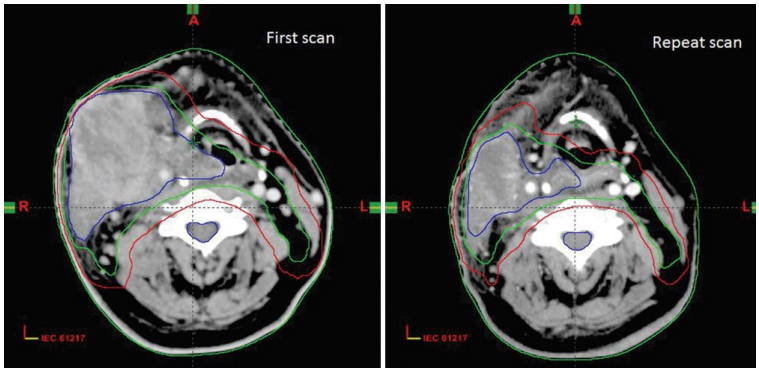

Figure 2.22: Tumor volume shrinkage between the first and a repeated CT scan for an HN tumor treated with IMRT. Reprinted from (Bhandari et al. 2014).

Table 2.2: Overview of uncertainty sources in CiRT (adapted from (ICRU 93 2016)). Systematic uncertainties are marked by * and random uncertainties by ▼.

	Uncertainty sources	Uncertainty deviations in delivered dose
Intrinsic patient parameters * ▼	α/β-ratio tissue parameters *	> 10%
	Patient individual radiation sensitivity *	> 10%
	Anatomical changes during radiotherapy (e.g. tumor growth/shrinkage, weight loss, re-oxygenation...) ▼	Strongly dependent on delivery and organ site
	Inter- and intra- fractional organ motion ▼	Strongly dependent on delivery and organ site
Treatment planning *	Data base for TPS*	< 3%
	Planning imaging (distortion, geometrical uncert., image resolution, HU) *	< 3% for CT, and between 3 - 10% for MR
	Image registration*	Motion dependent (< 3% for rigid areas, between 3-10% for deformable)
	Segmentation, contouring, target definition*	< 3% for normal tissue, > 10% for target
	Dose calculation model (scattering, fragmentation...) *	< 3% and between 3 - 10% (heterogeneities)
	Range uncertainties*	< 3% and between 3 - 10%
	Uncertainty in RBE*	> 10%
	Calculation of control parameters*	< 3%
Beam delivery* ▼	Design and location of passive beam line elements (collimators, vacuum window, monitor system, ripple filter...) *	< 3%
	Changes of beam parameters (purity, position, energy, size, intensity...) * ▼	< 3% and between 3 - 10% (for beam size)
	Calibration of dose or particle monitors *▼	< 3%
	Absorbed dose measurement *	< 3%
	Delivery uncertainties (control system and tolerances) * ▼	< 3%
Patient immobilization and setup * ▼	Reproducibility of immobilization and alignment procedures▼	Strongly dependent on device and tumor site
	Positioning devices (lasers, table) * ▼	< 3%
	In-room imaging systems (orthogonal X-rays, CT, optical systems) * ▼	< 3%
	Accuracy of position corrections (registration algorithms) * ▼	< 3%

2.3.2.3 Planned tumor volume margins

The above-mentioned uncertainties and their impact on the dose distribution are accounted for by adding safety margins around the tumor volume (Paganetti 2012).

The ICRU 93 defines several volumes and margins to which strict RBE-weighted dose constraints are applied during radiotherapy from (ICRU 93 2016). These volumes are separated into oncological, anatomical, planned, and treated tumor volumes. The anatomical gross tumor volume (GTV) refers to the known oncological tumor volume. This GTV is then extrapolated into a clinical target volume (CTV) including probable microscopic tumor infiltrations and organs at risk (OARs) surrounding the CTV. The treatment planning aims to find an optimum compromise between high RBE-weighted dose conformation to the CTV and low dose conformation to the OARs. However, the CTV irradiation is subject to geometrical uncertainties, such as organ motion, patient misalignment, inter and intra-fractional changes, or setup uncertainties. For this, a planning target volume (PTV) is created. This PTV includes the

CTV and the internal target volume (ITV), which accounts for tumor motion within the patient, plus some additional margins that account for all external treatment uncertainties. The PTV is dependent on the tumor location, tumor type, and treatment modality. The actual treated volume (TV), which received the RBE-weighted dose, might differ from the PTV.
As seen in Figure 2.23, most carbon-ion facilities apply a 2 to 3 mm CTV-to-PTV safety margin (Fattori et al. 2014; Jäkel et al. 2000).
However, applying such margins directly leads to a larger irradiated volume of healthy tissue. Even with a 2 mm CTV-to-PTV margin, random uncertainties in scanned beams can lead to heterogeneities in the delivered dose with hot and cold spots in the OARs and CTV (Fattori et al. 2014).

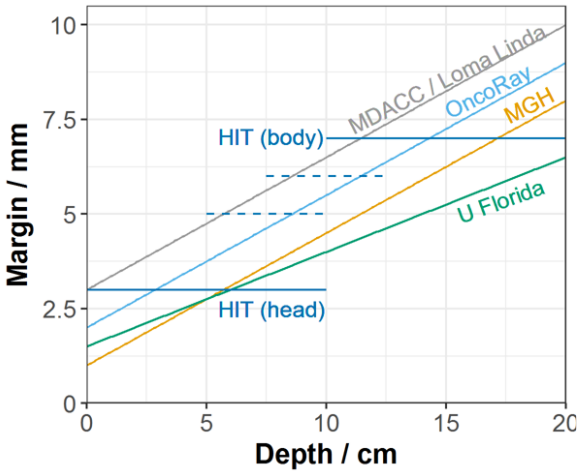

Figure 2.23: Applied margins around the CTV for different carbon-ion beam facilities. Reprinted from (Greilich 2017).

2.3.3 Overview of non-invasive carbon-ion radiotherapy monitoring techniques

It is thus of utmost interest to track and monitor any of the inter- and intra-fractional changes that directly impact the carbon-ion radiotherapy delivery. The monitoring of such treatment is especially relevant along the longitudinal coordinate (depth) as the dose distribution in the patient is very sensitive to the carbon-ion stopping positions. Therefore, methods to monitor the carbon-ion radiotherapy delivery in depth and to track potential anatomical changes during or after irradiation were developed. Such monitoring methods should ideally be non-invasive, time-resolved and in real-time (Parodi 2016).
Most of the developed methods for carbon-ion radiotherapy monitoring are based on the detection of direct and indirect nuclear reaction products such as radioactive nuclei (like β+ emitters, followed by a decay process that is slow with half-lives in the order of seconds to hours), de-excitation radiation (leading to the emission of prompt gammas, in a fast process in order of ~ 10^{-12}s) and evaporated light ions (such as protons, neutrons, and alphas, in a very fast process in order of ~ 10^{-12}s).
A detailed overview of monitoring methods for carbon-ion radiotherapy can be found in (Parodi 2016) or (Parodi et al. 2018). Some of the monitoring methods of carbon-ion radiotherapy will be detailed in the following paragraphs.

2.3.3.1 Positron Emission Tomography - based monitoring

Carbon-ion radiotherapy can be monitored in depth using Positron Emission Tomography (PET). Several PET-based monitoring methods have been developed over the years as summarized in (Shakirin et al. 2011) and in (Parodi 2016). The isotopes which are produced by the nuclear fragmentation of the carbon-ion beam in the target decay and emit positrons (β+). PET is based on the detection of pairs of annihilation photons that are emitted during the annihilation of these β+ with the tissue electrons. Measuring the annihilation-photons allows the carbon ion beam path in the patient to be reconstructed. PET-based monitoring of carbon ion beams has the advantage (compared with proton beams) that positron emitters are not only generated from target fragments but also from projectile fragments such as ^{11}C, ^{10}C ^{13}N, or ^{15}O, which correlate well with the ion beam range in a patient.

PET-based data acquisition can be performed online in-spill or inter-spill during the treatment delivery (in-beam PET) (Enghardt et al. 2004), shortly after irradiation (in-room PET) (Nishio et al. 2006), or outside the treatment room later after the irradiation (offline PET) (Parodi et al. 2007). In-room and offline PET monitoring can be operated with conventional clinical PET or PET-CT scanners, in-beam PET monitoring needs a dedicated scanner such as in (Ferrero et al. 2018).

PET-based monitoring methods highly depend on the half-lives of the produced isotopes, which range from a few seconds $t_{1/2}(^{10}C) = 20$ s to a few minutes $t_{1/2}(^{11}C) = 20.4$ min. They therefore directly suffer from both fast signal decay due to the short half-lives of some of the created isotopes, and from long acquisition times due to the low induced activity and long half-lives of other isotopes (Enghardt et al. 2004). PET-based monitoring methods are consequently impacted by physiological washout happening within a few minutes after the irradiation. Other performance-limiting factors of PET-based monitoring are the poor count statistics, the high background, the partial volume effect due to PET's limited spatial resolution which can lead to underestimation of activity concentrations, and the positron range in tissue after the beta decay. Additionally, PET-based monitoring does not directly measure the dose distribution and therefore requires the distribution of the produced positron emitters to be predicted e.g. via Monte Carlo simulations (Shakirin et al. 2011).

2.3.3.2 Prompt gamma-based monitoring

Carbon-ion radiotherapy can also be monitored in depth using the detection of prompt gamma rays that are emitted in the prompt de-excitation processes of the excited nuclei created in nuclear reactions induced by the carbon-ion beam. These prompt gammas are emitted on a prompt time scale of less than 10^{-16} s (Serber 1947). Over the years, several prompt-gamma-based monitoring techniques have been developed using either mechanical collimation (Min et al. 2006) or electronic collimation (Compton camera) (Everett et al. 1977), as well as un-collimated systems such as prompt gamma timing (PGT) (Golnik et al. 2014) and prompt gamma peak integral (PGPI) (Krimmer et al. 2017) based on TOF information. Clinical prototypes of prompt-gamma-based monitoring techniques are being implemented by several research groups such as (Draeger et al. 2018; Hueso-González et al. 2018). A detailed overview of prompt-gamma-based monitoring can be found in (Krimmer et al. 2018).

Prompt-gamma-based monitoring offers several advantages: unlike PET-based monitoring methods, which rely on the minute-long lifetimes of β+ emitters, prompt-gamma-based

monitoring methods allow real-time measurements during patient irradiations. Moreover, prompt gammas offer a better correlation between the distal dose and the activity falloff than PET-based monitoring (Kurosawa et al. 2012; Min et al. 2006), do not suffer from any biological washout, and allow both carbon-ion and proton beams to be monitored. Additionally, the spectrum of emitted gammas can also be used to determine the composition of the target tissues (Dal Bello et al. 2020). However, prompt-gamma-based monitoring methods still suffer from several limiting factors in the detection of high-energetic gammas rays. Among these challenges are the Compton scattering of prompt gammas, the large radiation background from neutrons, light fragments, and scattered photons as well as the limited detection efficiency, all of which affect the overall quantity and quality of measured gammas.

2.3.3.3 Secondary-ion-based monitoring

Carbon-ion radiotherapy can also be monitored in depth using the detection of promptly charged particles. During the nuclear reaction of the carbon-ion beam, prompt secondary ions are created from the fragmentation of the projectile nuclei. These secondary ions are emitted on a prompt time scale of less than 10^{-16} s and are predominantly emitted in a forward-peaked direction. Secondary-ion-based monitoring methods were first described by (Dauvergne et al. 2009) interaction vertex imaging (IVI) (Amaldi et al. 2010) and simulated in Geant 4 Monte Carlo study by (Henriquet et al. 2012). Up to now, fundamental research using secondary-ion-based monitoring methods was investigated based on secondary ion fluxes, energy spectra, emission profiles, and identification exclusively on PMMA targets and at relatively large detection angles with respect to the beam axis (60° and 90°). A detailed overview of monitoring of ion beam treatments using charged particles can be found in (Muraro et al. 2016). A first clinical implementation of such a monitoring method is described in (Fischetti et al. 2020). Detection and tracking of secondary ions can be performed using either drift chambers (DC) with lutetium–yttrium oxyorthosilicate scintillator crystals LYSO (Mattei, Battistoni, et al. 2017; Piersanti et al. 2014), scintillating fiber (Traini et al. 2017), hybrid pixelized silicon semiconductor (Gaa et al. 2017; Reimold 2018), or monolithic active pixel detectors (Reidel et al. 2019).

Compared to PET-based monitoring techniques, secondary-ion-based monitoring methods offer the same advantages as prompt-gamma-based monitoring methods, by allowing the measurement to be performed in real-time during patient irradiations. Additionally, simultaneous information on the lateral position of the carbon-ion beams can also be retrieved by monitoring these methods (Félix-Bautista et al. 2019; Félix-Bautista et al. 2021).

Compared to prompt-gamma-based monitoring methods, secondary-ion-based monitoring methods offer superior detection efficiency and a better signal-to-noise ratio, since there exist no alternative production channels for charged fragments than projectile fragmentation. However, secondary-ion-based monitoring methods are only applicable for beam monitoring of ions heavier than protons because protons do not undergo nuclear fragmentation. Moreover, and in contrast to prompt gamma rays, charged fragments undergo MCS, which limits the imaging resolution. The spatial resolution along the longitudinal coordinate is further reduced because of the forward-peaked emission of nuclear fragments: the non-isotropic emission prevents the detection system to be placed at the optimum angle of 90 degrees to the longitudinal axis.

Table 2.3: Overview of the leading three carbon-ion radiotherapy monitoring methods

	PET-based	Prompt-gamma-based	Secondary-ion-based
Process speed	Slow decay seconds to hours	Prompt de-excitation 10^{-12} [2] s	Prompt emission 10^{-12} s
Online / real-time	☒	☑	☑
Acquisition time	5 – 30 min	< 1 min	< 1 min
Carbon detection	Indirect	Indirect	Indirect
Invasive	☒	☒	☒
Visualization	3D	3D	3D
Anatomical location	All	All	All
Expected spatial resolution	2-10 mm	~2 mm	~2 mm
Production rate		70 x higher production rate than β+	High in the forward direction, low at large angles
Detection yield	Low detection efficiency, High background	Low detection efficiency, High background	High detection efficiency, low noise
Disadvantages	• PET simulation needed (bad correlation with dose) • Biological washout (20 min)	• Collimators needed for non-Compton cameras • No tracking, • low detection yield, • high background	• Low spatial resolution, • high attenuation, • low correlation with dose

3. Materials and Methods

The work of this thesis is based on the detection and tracking of secondary ions produced during irradiations of carbon-ion radiotherapy treatments. In this chapter, the materials and methods used for the thesis are summarized.

3.1. Heidelberg Ion-Beam Therapy Center

3.1.1 Facility overview

The experiments performed in this thesis were carried out at the Heidelberg Ion Therapy Center (HIT), in Germany. The HIT facility is composed of nine main elements, all of which are depicted in Figure 3.1. The HIT facility offers several ion types from different ion sources: two ion types for clinical purposes (protons ^{1}H, and carbon ions ^{12}C) and two ion types for research purposes (helium ions ^{4}He, and oxygen ions ^{16}O). A stage linear accelerator followed by a synchrotron allow for ions to be accelerated to up to 75 % of the speed of light. Afterward, the synchrotron keeps the ion beam in a circular path. The ion beam is then guided and bundled by additional magnets towards the treatment delivery rooms. At HIT, three treatment rooms are available: one ion-Gantry room (rotating 360°, with a weight of 670 T) and two horizontal treatment rooms, called H1 and H2 rooms. Additionally, an experimental room, mimicking the irradiation conditions of the horizontal treatment rooms, is available for experimental work. Most of the experimental work in this thesis was performed in this last experimental room.

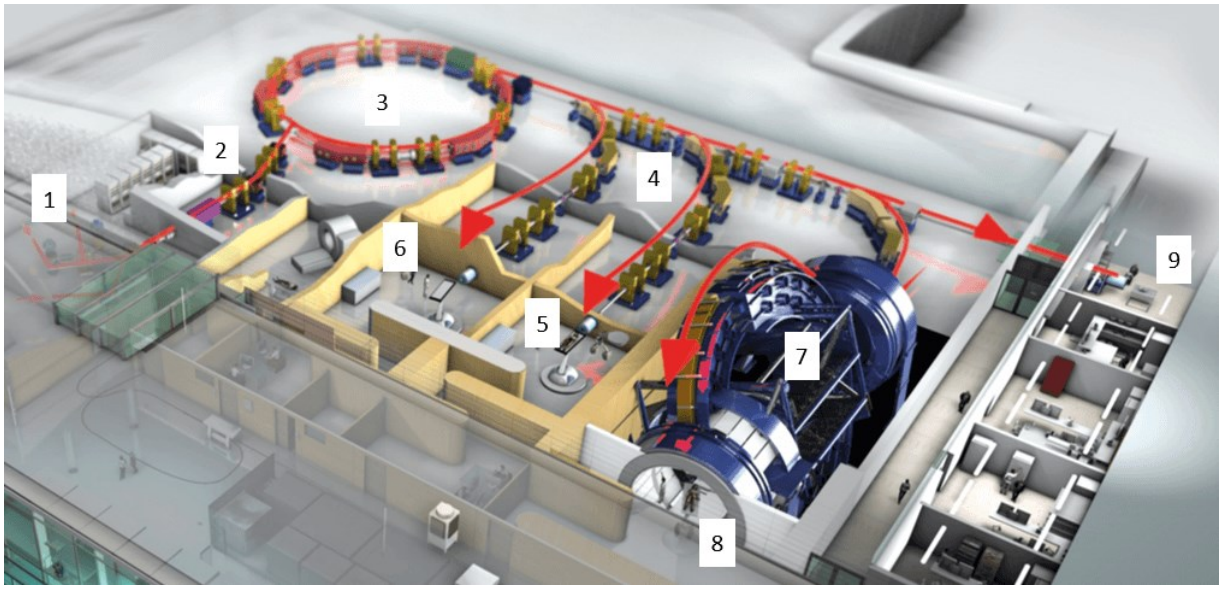

Figure 3.1: Overview of the HIT facility. (1) ion sources, (2) linear accelerator, (3) synchrotron, (4) magnets, (5-6) two horizontal treatment rooms, (7) one gantry, and (8) gantry treatment room, and (9) one experimental treatment room. Picture reprinted from (UniversitätsKlinikum Heidelberg 2021d)

The experimental work of this thesis was only performed with carbon-ion beams. The HIT facility offers carbon-ion beams energy values ranging from 88.83 to 430.10 MeV/u (LIBC library). This corresponds to ranges in water from 20 to 300 mm with range increments of 1.0 mm for low beam energies and 1.5 mm for higher beam energies of carbon ion beams. The full width at half maximum of the carbon-ion beam ranges from 3.4 mm to 13.4 mm (FWHM).

3.1.2 Active raster scanning technique

At the HIT facility, beam delivery is based on the active intensity-modulated raster scanning method (Haberer et al. 1993). This allows for an active variation of the carbon-ion beam's focus size, the number of particles, and beam energy for each irradiation point, also called raster points. The term "pencil beam" often refers to the carbon-ion beam covering a certain irradiation point. With this raster scanning method, the tumor volume is sliced longitudinally into iso-energetic slices (IES) as shown in Figure 3.2. The continuous beam is actively deflected and focused using fast dipole magnets to irradiate laterally each IES of the tumor volume. At the HIT facility, shallow IESs are irradiated first with low beam energies. Deeper IESs are irradiated later with higher beam energies. Treated lateral field sizes at the room isocenter can be up to 20 cm × 20 cm at the HIT facility (Combs, Jäkel, et al. 2010).

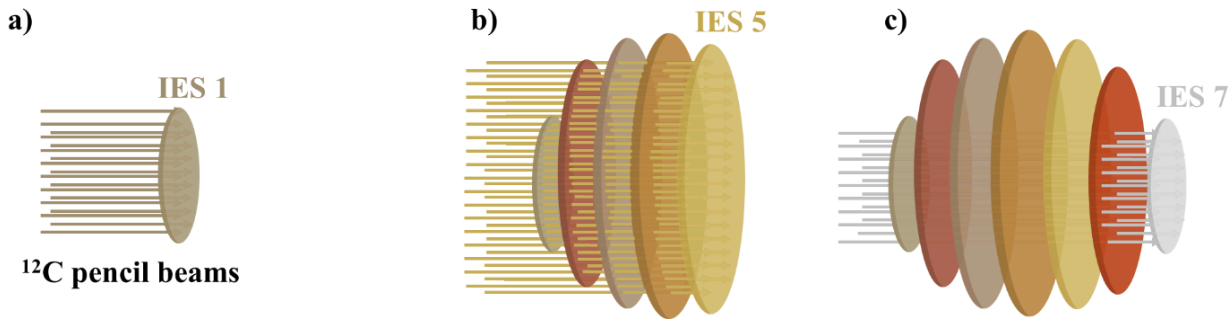

Figure 3.2: Each iso-energetic slice (IES) of a tumor volume by a continuous pencil beam that is actively deflected to cover all lateral pencil beam positions. At the HIT facility, shallow IESs are irradiated first (IES1) and deeper IESs are irradiated later (IES7).

3.1.3 Accelerator beamline

At HIT the beam nozzle is located approximately 1.12 meters upstream of the room isocenter with which the patient is aligned. As depicted in Figure 3.3, the beam nozzle contains several elements that are important for patient irradiation. First, ripple filters of either 3 or 4 mm can be mounted in the beam nozzle. Ripple filters are used with carbon-ion beams to broaden the beam energies distribution and, thus, to reduce the number of ion beam energy steps required to achieve a smooth spread-out Bragg Peak in the tumor volume (Weber et al. 1999). Additionally, an online beam feedback system, called beam monitoring system (BAMS) is mounted at HIT in the beam nozzle. The BAMS allows for an active beam position feedback, as well as feedback concerning the number of carbon ions. The lateral beam spot positions are measured in the beam nozzle by two multi-wire proportional chambers (MWPC 1 and 2) and the number of particles per pencil beam is measured by three ionization chambers (IC1, 2, and

3). A schematic representation of the HIT beam nozzle, including the BAMS with its MWPCs and ICs, is depicted in Figure 3.3. The beam information measured by the BAMS inside the nozzle is then extrapolated to the room isocenter to approximate the ion beam delivery parameters inside the patient. Log files of the beam positions, energies, focus sizes, and the number of particles as measured over time by the BAMS in the nozzle are produced and stored during each performed irradiation.

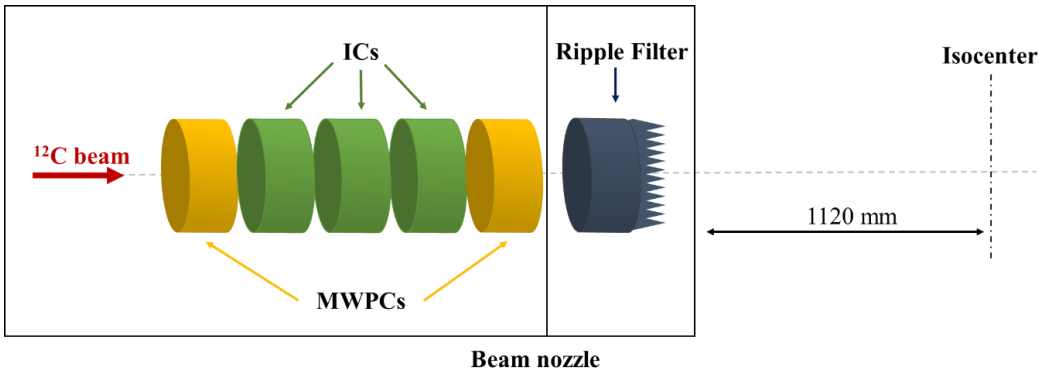

Figure 3.3: Schematic representation of the HIT beam nozzle. It is composed of two multi-wire proportional chambers (MWPC 1 and 2), three ionization chambers (IC, IC2, IC3), and a ripple filter, placed 1120 mm upstream of the room isocenter. An additional MWPC 3 can be placed at the isocenter for quality assurance purposes. Adapted from (Parodi et al. 2012).

3.1.4 Treatment planning for carbon-ion radiotherapy

At the HIT facility, clinical CT images of the patients are made on a SIEMENS Sensation Open device, using head clinical protocols. Conversion of HU values of these CT images to WET is done using calibration functions, see (Eq.3.34) and (Jäkel, Jacob, et al. 2001; Rietzel et al. 2007). From these quantitative patient images, carbon-ion treatment plans are designed on the Siemens "Syngo RT Planning system" (Siemens Healthcare GmbH, Erlangen, Germany), using LEM1 for biological plan optimization (Combs, Jäkel, et al. 2010).

Within this thesis, three clinical carbon-ion treatment plans were used. Snapshots of the three carbon-ion treatment plans and their clinical CT images are shown in Figure 3.4. Details of the three treatment plans are summarized in Table 3.1. The three plans were designed for pre-clinical experiments on an anthropomorphic and a homogeneous head model, as well as for a first clinical application of the method on a real patient.

For the pre-clinical experiments in this thesis, two treatment plans of spherical tumor volumes treated with prescribed fraction doses of 3 Gy (RBE) were used. A 100-cm^3 sphere was defined in the anthropomorphic head model and a 70-cm^3 sphere was defined in the homogeneous head model. Both tumor volumes were centered in the head models and both treatment plans consisted of one single field.

For the first clinical application, a clinical patient treatment plan of a non-spherical tumor volume of 73.85 cm^3 treated with a prescribed fraction dose of 3 Gy (RBE) was used. This clinical treatment plan consisted of two fields (5° and 330°). Only the first 5° treatment field was measured in this thesis, corresponding to a maximum biological dose of 0.84 Gy (RBE).

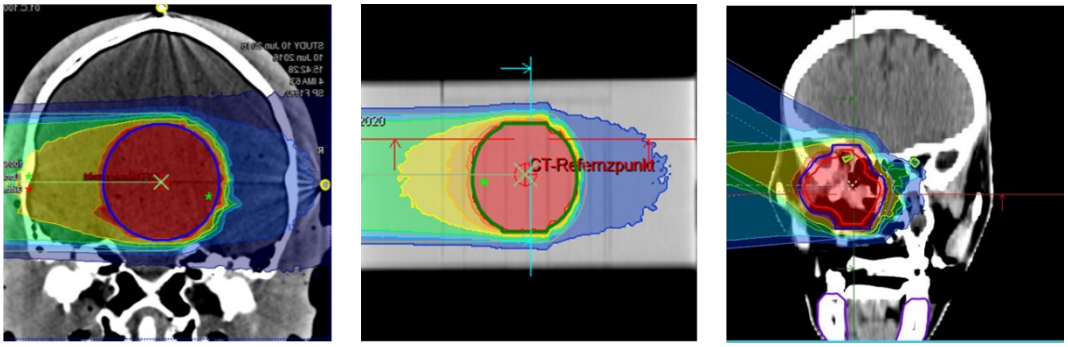

Figure 3.4: Coronal views of the three clinic-like treatment plans as designed in the Siemens syngo RT Planning system overlaid with CT images for the anthropomorphic Alderson head model (left), the homogeneous cylindrical head model (center), and patient head (right). The green line delineates GTV (center) and the blue line PTV (left and right). Courtesy of Dr. M. Ellerbrock, and Dr. M. Winter.

Table 3.1: Carbon-ion treatment plan parameters

	Homogeneous head model	**Alderson head model**	**Patient 1**
PTV (cm^3)	70.06	100.01	73.85
Beam Modifier	Ripple Filter 3mm	Ripple Filter 3mm	Ripple Filter 3mm
Treatment field number	1	1	2 (5° and 330°)
Fraction dose (Gy (RBE))	3	3	3 for total fraction 0.84 (*)
Scan grid lat. dist X/Y (mm)	2.0/2.0	2.0/2.0	2.0/2.0
Scan grid long. dist Z (mm)	3	3	3
Number of energy slices	19	22	23 (*)
Min energy (Mev/u)	167.66	163.09	95.67 (*)
Max energy (Mev/u)	239.45	246.57	204.27 (*)
Spot positions	8356	10218	5735 (*)
Total primary ion number	$5.69.\ 10^8$	$7.06.\ 10^8$	$3.31.\ 10^8$ (*)
Pencil beams FWHM (mm)	6	6	6

(*) for the measured field

3.2. Secondary ion tracking system: mini-tracker

3.2.1 Hybrid semiconductor pixel detector

In this thesis, a mini-tracker was used to detect and track the secondary ions produced and departing from the irradiated head models. This mini-tracker consists of two hybrid semiconductor pixel detectors.

Semiconductor detector refers to detectors that are made of semiconductor crystals, such as silicon or germanium. Semiconductors exhibit different conductivity depending on the concentration of impurity they contain. This conductivity is defined in a so-called doping process and can lead to different p- or n-types of materials depending on the atomic number of the used dopant. P-N junctions can be formed within a semiconductor crystal. A depleted region of the semiconductor can be created at the p-n junctions by applying an external voltage on both sides of the junction. The depletion width, W, for n-type semiconductor detectors with pn-junctions is defined as a function of the applied bias voltage Vb (Spieler, 2005, p.65):

$$W = \sqrt{\frac{2\varepsilon_s}{q}\left(\frac{V_0 + V_b}{N_D}\right)} \qquad \text{(Eq.3.1)}$$

with $q = 1.602\times10^{-19}$ C as the unit of the electric charge in Coulomb, $\varepsilon_s = 1.0536\times10^{-12}$ F/cm as the silicon electric permittivity (see Table 3.2), $N_D = 1.005\times10^{12}$ cm^{-3} intrinsic carrier doping concentration of donors or impurity concentration[1], and V_b the applied bias voltage in volt. $V_0 \approx 0.63$ V is the build-in voltage which is negligible when approximated by (Spieler, 2005, p.61):

$$V_0 = \frac{k_b\, T}{q}\, log\left(\frac{N_A N_D}{{n_i}^2}\right) \qquad \text{(Eq.3.2)}$$

with $N_A = 1\times10^{19}$ cm^{-3} as the intrinsic carrier doping concentration of acceptors[1], $k_b = 1.38066 \times 10^{-23}$ J/K the Boltzmann's constant, T the temperature in Kelvin $T = 300$ K, and $n_i = 9.65\times10^{9}$ cm^{-3} being the intrinsic silicon carrier concentration at 300 K. Table 3.3 summarizes the depletion width W of the mini-tracker silicon sensors for the different bias voltages applied in this thesis.

When a charged particle crosses a partially (or fully) depleted semiconductor sensor, it triggers the creation of charged electron-hole pairs along its path. These created pairs travel the sensor and produce a signal current that is then read by the detector electronics, as seen in Figure 3.5-b).

Semiconductor detectors are said to be "pixelized" when they have a 2D surface segmentation as seen in Figure 3.5-a) in contrast to, for example, other 1D strip semiconductor detectors. Pixel semiconductor detectors are said to be "hybrid" when they have miniaturized electronics, where each sensor pixel has its own readout channel connected via bump bound to the detector electronics, as seen in Figure 3.5-b).

[1] N_D and N_A from Advacam s.r.o. personal conversation

Table 3.2: Silicon properties at room temperature (300 K) from (Spieler 2005; Sze et al. 2007).

Properties	**Silicon**
Atomic density [cm^{-3}]	5.02×10^{22}
Atomic weight A	28.09
Density ρ [g/cm]	2.329
Dielectric constant $\varepsilon_s / \varepsilon_0$	11.9
Electric permittivity ε_s [F/cm]	1.0536×10^{-12}
Electron affinity χ [V]	4.05
Energy gap / Bandgap [eV]	1.12 (indirect)
Intrinsic carrier concentration n_i [cm^{-3}]	1.45×10^{10}
Mobility [cm^2/V-s]	Electrons $\mu_e = 1.450$
	Holes $\mu_h = 500$

Table 3.3: Calculated depletion width of detector sensor in mini-tracker per applied bias voltages

Bias Voltage [V]	**Depletion width [µm]**
10	118
30	200
40	231
80	325*
100	363*

* fully depleted 300 µm sensor

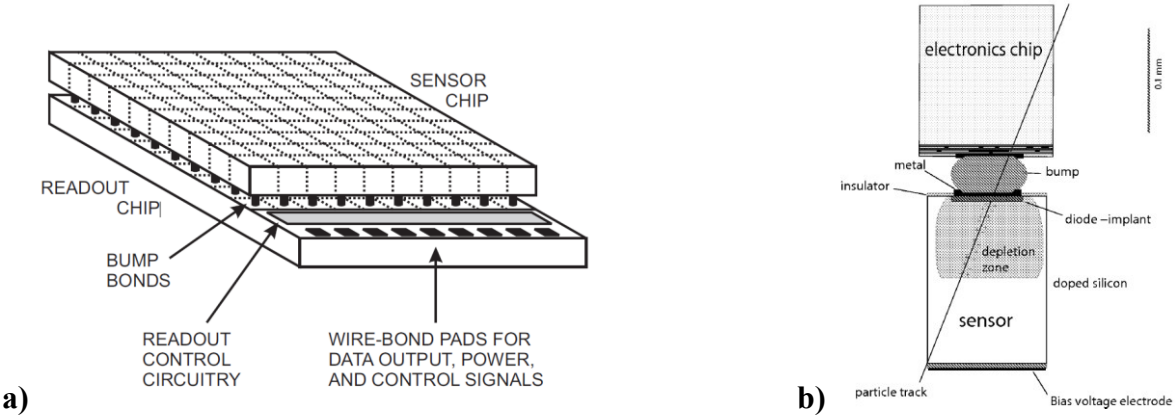

Figure 3.5: Hybrid pixel semiconductor detector (a) and zoom on its bump-bonded region (b). The charged particle generates electron-hole pairs (+ and -) while crossing the depleted zone of the sensor. The signal is then acquired by the electronics of the detector. a) is reprinted from (Rossi et al. 2005) and b) is reprinted from (Spieler 2005).

3.2.2 AdvaPIX TPX3 modules

The mini-tracker consists of two parallel AdvaPIX TPX3 modules[2]. Each of the AdvaPIX TPX3 modules contains a Timepix3 detector.

Timepix3 is a compact hybrid semiconductor pixel detector that was developed by the Medipix3 Collaboration at CERN. Timepix3 detector has ultra-fast sparse data readout that allows acquiring up to 40-million-pixel hits per second. Each pixel is bump-bonded to the read-out chip. In this work, the Timepix3 sensitive area is around 2 mm², divided into 256 x 256 pixels (pixel pitch of 55 µm), with a silicon sensor thickness of 300 µm.

Compared to the previous generation of mini-trackers, using Advacam TPX modules with the Timepix detector, (as in Gwosch et al. 2013, Reinhart et al. 2017 and Gaa et al. 2017), the new AdvaPIX TPX3 modules with Timepix3 detector allow for simultaneous measurement of position, energy, and time-of-arrival of single ions with a better time resolution (1.56 ns) and no deadtime.

Detailed characteristics of a single AdvaPIX TPX3 module are presented in Table 3.4 and Figure 3.6. During experimental and clinical measurements, the two AdvaPIX TPX3 modules of the mini-tracker were operated in synchronization, with a 3 keV pixel energy threshold. They were connected with a 5 V power supply and a USB 3.0 communication to a standard mini-PC notebook which assured continuous fast data-driven read-out of the acquired data. The two layers of the module sensor were partially depleted at a low bias voltage of 10 V, which corresponds to a depletion depth of the detector of about 100 µm (as calculated from (Eq.3.1) and (Eq.3.2)).

The two parallel AdvaPIX TPX3 modules of the mini-tracker can be operated in several pixel acquisition modes (Llopart 2014):

- in Time-of-Arrival mode only (ToA mode)
- in Time-of-Arrival and Time-over-Threshold mode (ToA/ToT mode)
- in event counting and integral Time-over-Threshold (event count and iToT)

In this thesis, the two AdvaPIX TPX3 modules were operated in the ToA/ToT mode and the measured raw data was exported in ASCII files in a .t3pa file format, see section (§3.5.1.) for more details. The two parallel AdvaPIX TPX3 modules of the mini-tracker were also operated in synchronization, where the first module, i.e. the closest to the tumor center, was set to be the "Master" device and the other module was set to be the "Slave". Measurements were started and stopped by the hardware trigger of the Master device.

Additionally, an offline synchronization with the beam record was implemented, allowing to distinguish from which pencil beam the measured tracks were coming.

[2] ADVACAM s.r.o. Prague

Table 3.4: AdvaPIX TPX3 module characteristics

Characteristics	Values
Sensor Material	Silicon (Si)
Sensor Thickness (µm)	300
Sensitive Area (mm x mm)	14 x 14
Time Resolution (ns)	1.6
Readout Speed (Mhits/s)	40
Number of Pixels	256 x 256
Pixel Pitch (µm)	55
Energy Resolution (keV):	1
Weight (g)	503
Dimensions (mm)	125 x 79 x 25.5
Software	Pixet Pro (v. 1.6.5.778)

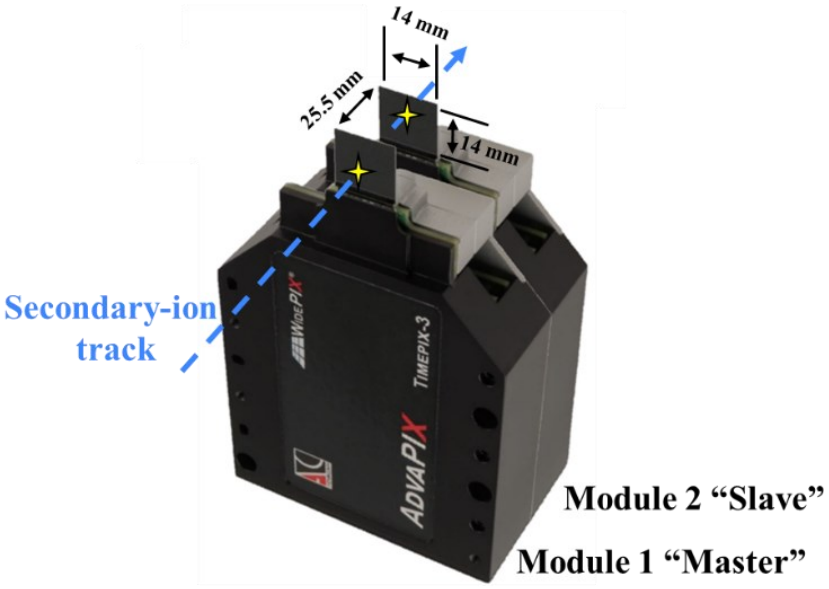

Figure 3.6: Two parallel AdvaPIX TPX3 modules of the mini-tracker crossed by a secondary ion. The secondary ion track is represented by the dashed blue line, the ion hits on the sensor layers are represented by the yellow crosses. Module picture adapted from AdvaPIX TPX3's datasheet.

.

3.3. Pre-clinical and clinical measurement setups

3.3.1. Pre-clinical measurements

To mimic a clinical treatment, single carbon-ion treatment plan deliveries corresponding to a single fraction were performed in the experimental room of the HIT facility.

3.3.1.1 Head model targets

Two head model types were irradiated with carbon-ion treatment plans: either a homogeneous cylindrical head model or an anthropomorphic Alderson head model. Internal changes were aimed to be detected in the homogeneous head model, while only surface changes were feasible in the anthropomorphic one.

The homogeneous cylindrical head model was a homogeneous polymethyl methacrylate (PMMA) cylinder of 90 mm height and 80 mm radius as shown in Figure 3.7-a). Several geometrical shapes of different thicknesses could be inserted inside this cylinder as shown in Figure 3.7-b). The homogeneous cylindrical head model shape was chosen to investigate the secondary ion emission due to the carbon-ion beams in a simplified homogeneous medium with an RSP similar to soft human tissues and dimensions comparable to a real human head. The cylinder had an RSP (or WEPL) of 1,163 while soft human tissues have an RSP close to 1. This cylinder contained eight interchangeable 80 x 80 mm PMMA slabs of different thicknesses with an RSP of 1,151. The RSPs of these different elements of the cylindrical head model were measured with the PTW Peakfinder Water Column mounted with a thin T34080 Bragg Peak chamber and read out by a TANDEM XDR electrometer via the PTW Peakscan software (v.1.1).

The heterogeneous anthropomorphic Alderson head model, on the other hand, contained a real human skull, filled with homogeneous soft tissue-equivalent material (Alderson, 1962). It was irradiated in a standing upwards position (see Figure 3.7-c)) for easy reproducibility of the positioning in repeated experiments.

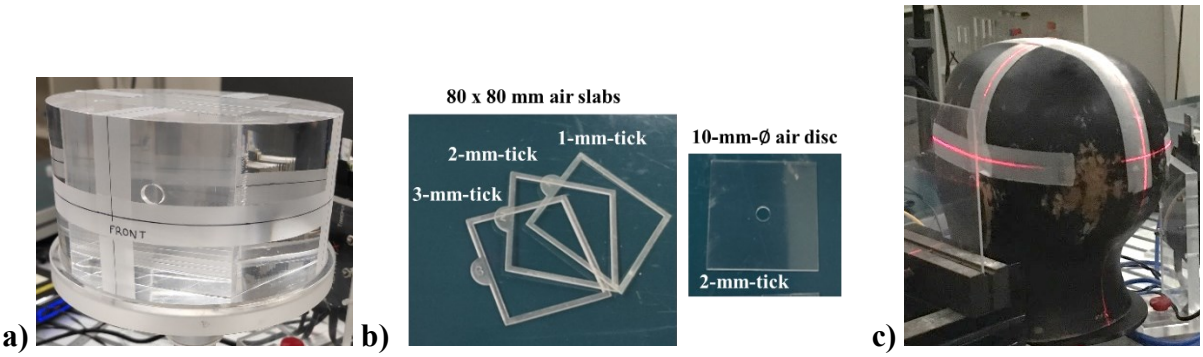

Figure 3.7: a) Homogeneous cylindrical head model, with an inserted PMMA slab containing a small 2-mm-tick 10-mm-Ø air disc. b) shows other possible insert shapes such as 80 x 80 mm air slabs or discs of thinner thicknesses. c) Alderson head model irradiated in a standing upwards position.

3.3.1.2 Experimental setups

The two homogeneous and anthropomorphic head models were placed with their tumor center coinciding with the center of the experimental room (room isocenter). As depicted in Figure 3.8, secondary ions exiting the head models were detected using the mini-tracker placed behind the targets at a distance *d* from the room isocenter (usually *d* = 120 mm) with an angle α with respect to the beam axis (usually *α* = 30 degrees). The distance *d* was defined between the head-model center and the center of the mini-tracker's first sensitive layer, i.e. placed the closest to the head model. The angle *α* is defined between the beam axis and the normal of the mini-tracker's first sensitive layer. The two sensitive layers of the mini-tracker were separated by a distance of 25.5 mm, which is the thickness of the AdvapixTPX3 readout interfaces.

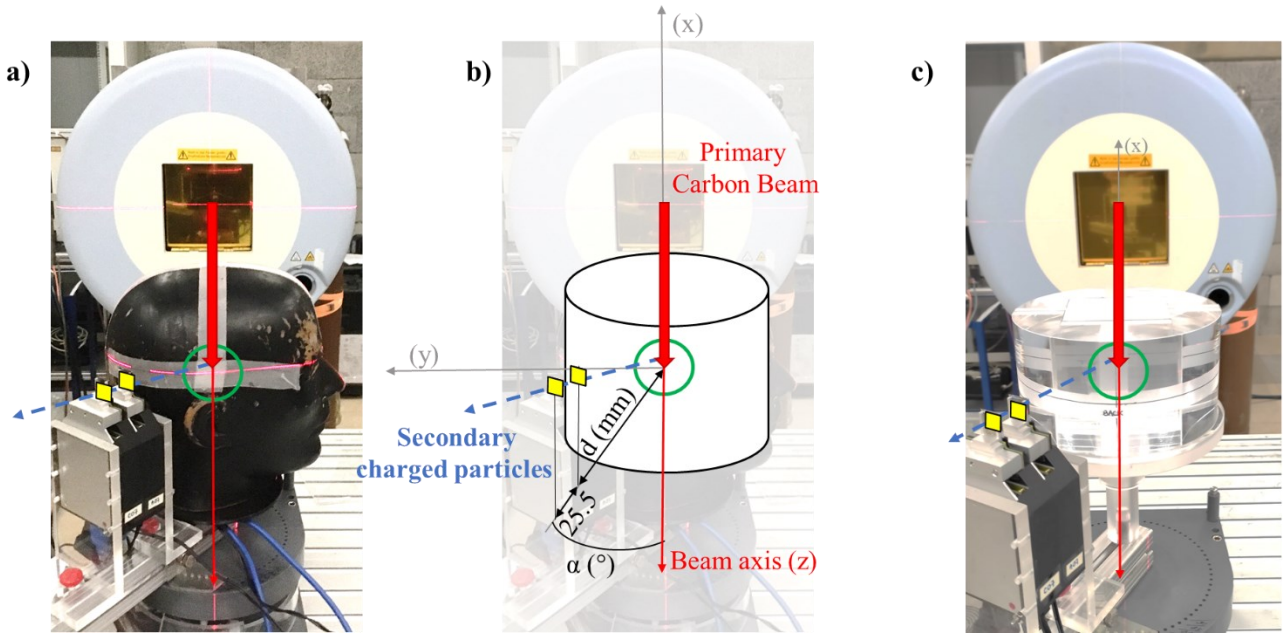

Figure 3.8: Experimental setup with (a) Alderson head model or (c) PMMA cylinder. The mini-tracker sensitive areas are represented by the yellow squares, the targeted tumor volume is represented by the green circle. The carbon ion beam axis is represented by the red arrow. Definitions of the distance d (mm) and angle α (°) of the mini-tracker with respect to the head model are indicated with arrows in (b).

Using this experimental setup, different anatomical changes were investigated in front or inside of the head models. For this, several small geometrical heterogeneity shapes were used:

- 1-, 2-mm, or 3-mm-thick PMMA slabs placed in front of the anatomical head model
- 2-mm-thick (80 x 80 mm) air slabs placed inside the homogeneous head model
- 2-mm-thick (10-mm-Ø) air disk placed inside the homogeneous head model

Figure 3.9-a)-d) show the different experimental setups, as used during the measurements in this thesis. Measurements were either performed once or repeated eight times to acquire enough data to be equivalent to having 8 mini-trackers. The latter constitutes a setup similar to a setup that will be used in the near future for a clinical trial with a larger patient cohort.

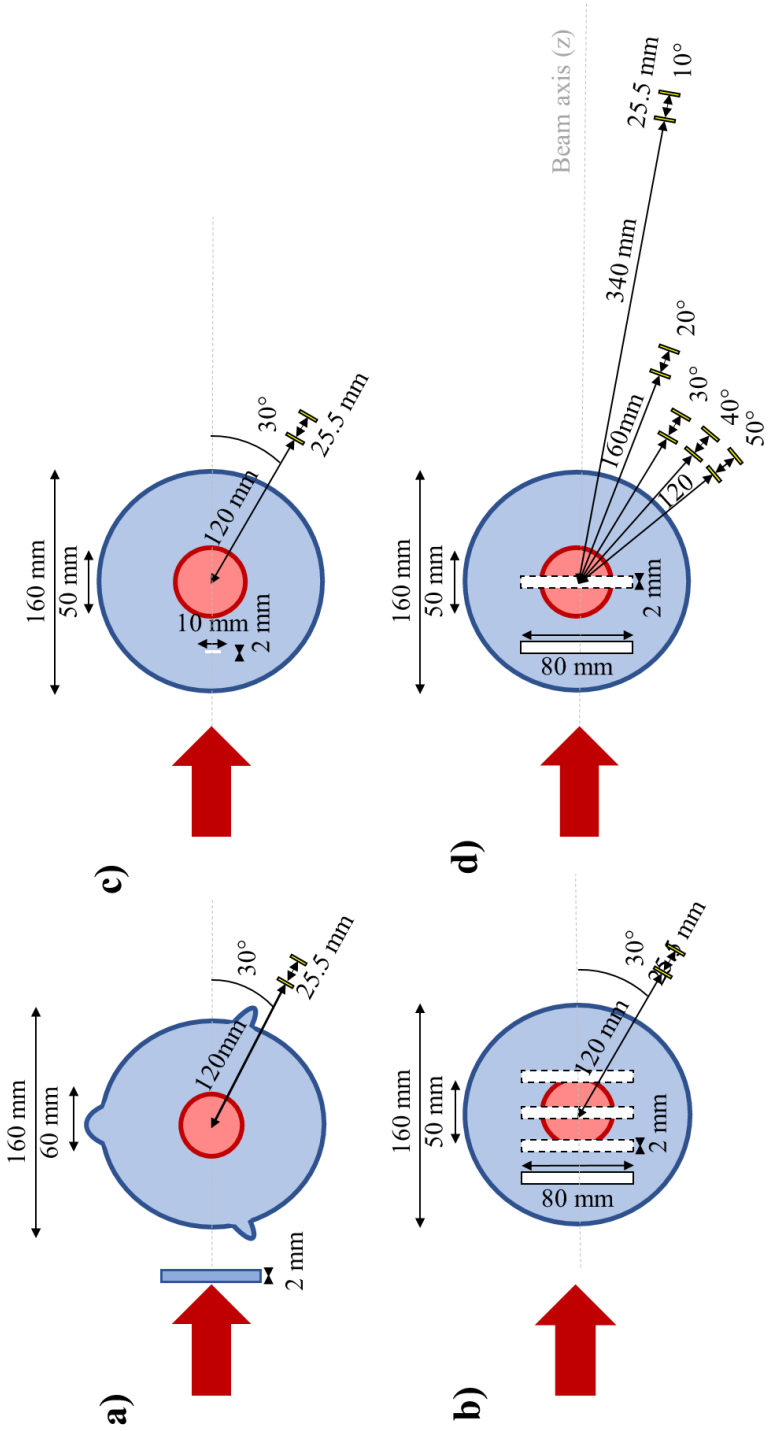

Figure 3.9: Experimental setup with (a) anthropomorphic or (b-c-d) homogeneous head models standing in an upward position (blue volumes). The mini-tracker, represented by the yellow squares, was mostly positioned at 120 mm and 30° (a-b-c). Other mini-tracker positions were studied in (d). Several heterogeneities were introduced at different depths with respect to the tumor center: -a) PMMA slab (blue strip) placed -200 mm upstream of the center; -b) 2-mm-thick 80 mm x 8 mm 0 air slabs (white strips) centered at a depth of – 40, -22, 0, or +18 mm; -c) 2-mm-thick air disk of 10 mm diameter (small white strip) centered at a depth of -40 mm; and -d) 2-mm-thick 80 mm x 80 mm air slabs (white strips) centered at a depth of – 40 or +0 mm. The minus sign indicates upstream of the center. The carbon ion beam is represented by the red arrow. The targeted tumor volume is represented by the red circle.

3.3.2. Clinical measurement

The clinical measurement was performed in the H2 horizontal patient room at the HIT facility where data of a single fraction of a clinical carbon-ion treatment were acquired to verify the applicability of the monitoring method to clinics.

3.3.2.1 Patient positioning

The patient was positioned on the robotic rotating table also called "treatment couch", which allowed the tumor center to be aligned with the isocenter of the horizontal treatment room. This table has a position accuracy below 0.2 mm ± 0.2 mm std (Jensen et al. 2012). The patient was immobilized in a supine position with a standard head-rest pillow and a custom-made thermoplastic head mask (HeadSTEP IT-V), see Figure 3.10-b).

Additional patient position control was done using an orthogonal planar x-ray system mounted on a robotic C-arm. This C-arm has a radial position accuracy of 0.2 mm ± 0.1 mm std (Jensen et al. 2012). It is used to generate patient positioning images before the irradiation which are then compared to the CT images from irradiation planning (Combs et al. 2012). Daily position corrections can subsequently be performed.

Overall the robotic treatment table, thermoplastic masks, orthogonal x-ray, and daily position corrections permit to limit patient positioning uncertainties of to 1 to 4 mm for extracranial HN targets (Jensen et al. 2012). Smaller uncertainties are expected with the subject patient of this thesis as the target was located inside the patient's head.

3.3.2.2 Clinical setup of the mini-tracker

The mini-tracker was placed behind the patient's head at a distance d = 160 mm from the center of the tumor with an angle α = 30 degrees with respect to the beam axis as seen in Figure 3.10-a). The distance d was bigger for this clinical measurement than for the experimental measurement due to the patient geometry (shallow tumor) and to avoid any contact between the mini-tracker and the patient's head.

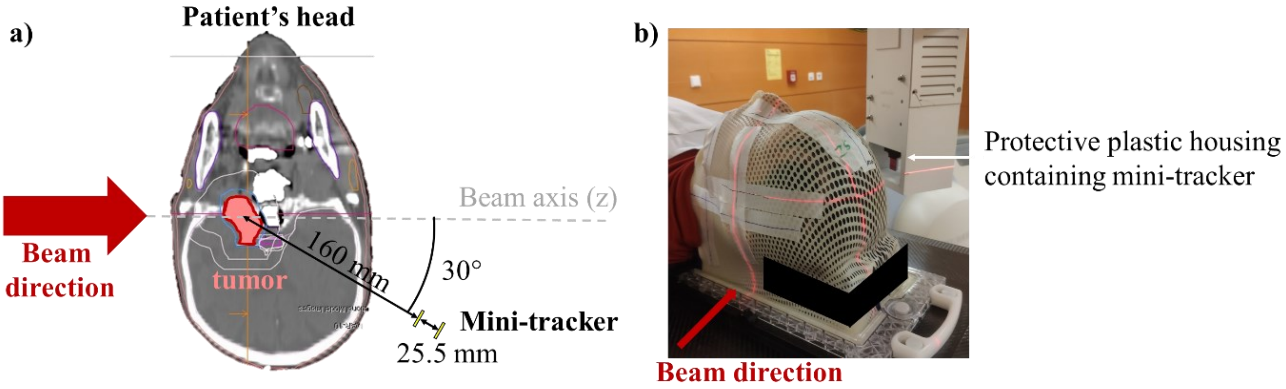

Figure 3.10: a) Clinical setup for patient measurement with mini-tracker placed at a distance d = 160mm from the tumor center and at a detection angle of 30° with respect to the beam axis. The mini-tracker is represented by the two yellow rectangles, the tumor volume is shown in pink. b) The patient's head was immobilized to the table with a custom-made thermoplastic head mask, the mini-tracker was placed in a housing to protect the detector sensitive areas.

3.3.2.3 Patient monitoring system

To evaluate the performance of this monitoring method in clinics, an entire patient monitoring system, containing the mini-tracker, was designed and developed during this thesis in collaboration with G. Echner and (Félix-Bautista 2021). Detailed pictures of the patient monitoring system can be found in Figure 3.10 and Figure 3.11.

The monitoring system consists of the same mini-tracker as for the preclinical experiments and is explained in section (§3.2.), as well as in Table 3.4. As seen in Figure 3.11-a), the mini-tracker was additionally covered by a protective housing, positioned at the end of an aluminum arm which allowed the tracker sensor to be placed next to the patient's head while keeping the rest of the equipment far from it. The Mini PC for the detector steering and data acquisition, as well as the power supplies, were stored in the drawer compartment of a Siemens medical trolley. All cables connecting to the mini-tracker were mounted inside the aluminum arm. The power supply of the trolley was connected to the HIT power system via an isolating transformer (polytronik Medical Isolating Transformer polyMIT from Sedlbauer) to avoid electric shock to the patient and isolate the monitoring system from the patient room electrical circuit. The Mini PC was connected to the HIT network via an Ethernet cable and a galvanic Ethernet insulator for medical appliances (MI 1005 from Baaske Medical GmbH 1 Co. KG). The alignment system of the entire patient monitoring system consisted of three plastic indicators used to align the medical chart with respect to the laser system inside the treatment room as shown in Figure 3.11-a) and Figure 3.11-c). The height of the detector sensitive layers' center was set to correspond to the fixed room isocenter.

3.3.2.4 Medical regulations compliance in the patient room

To guarantee the safe operation of the monitoring system inside the patient room, several medical safety regulations need to be fulfilled to ensure that no electrical interference with treatment delivery and no additional risk for the patient exists. These medical regulations were fulfilled considering that the AdvaPIX TPX3 modules of the mini-tracker are CE labeled, compatible with EN 61000-6-2 (2005), EN 61000-6-4 (2007), and EN 61010-1 (2010) standards. The mini-tracker and NUC Mini PC were operated at low voltage, thus fulfilling the low voltage directive (as from their CE labels). These two devices were connected to the two insulating units: the polyMIT transformer and the MI 1005 ethernet insulator. The PolyMIT transformer follows the IEC 60601-1:2005 3rd Edition and the EN 60601-1-2 standards, while the MI 1005 insulator is following IEC/EN 60601-1 and IEC/EN 6061-1-2 standards. Thus, there were no additional risks of electric shocks for the patient and the monitoring system was isolated from the patient room electrical circuit.

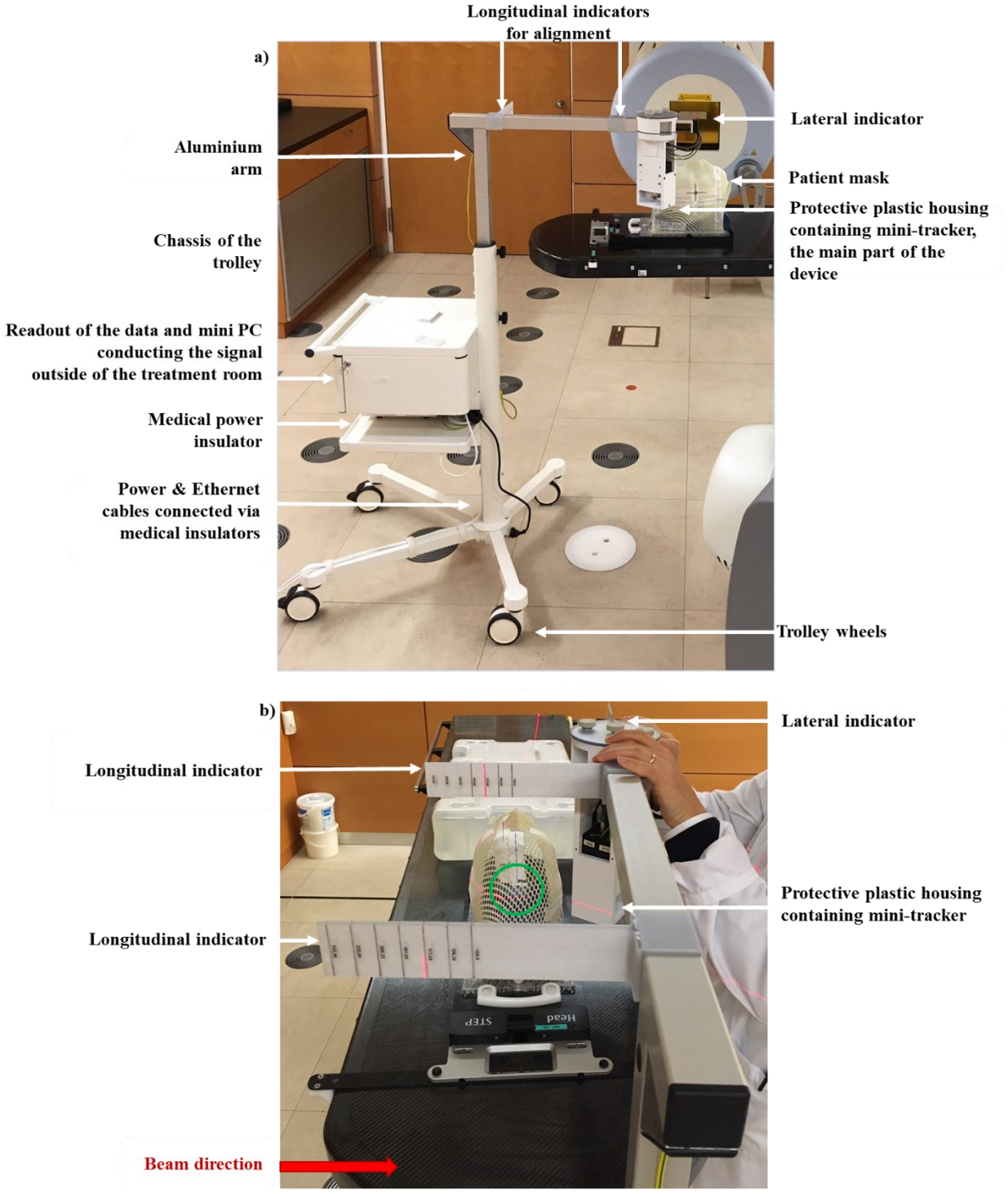

Figure 3.11: a) Patient monitoring system positioned with respect to the patient head and beam nozzle. The mini-tracker was placed in a protective housing at the end of a long aluminum arm. Mini PC, power supply, medical power insulator, Ethernet cable, and medical Ethernet insulator were placed in the drawer of a medical trolley. b) Indicator used to align the trolley with respect to the room isocenter via the room laser system.

3.4. Monte Carlo simulations

3.4.1 FLUKA and FLAIR

Monte Carlo (MC) simulations were performed to investigate the performance of the method with respect to the simulated true fragmentation origin positions. For this, an MC code using FLUKA (version 2011.2.8) (Battistoni et al. 2007, 2017; Böhlen et al. 2014; Ferrari et al. 2005) and the Flair graphical user interface (version 2.3-0) (Vlachoudis 2009) were used to simulate the true secondary-ion origin positions in different head models.

The physical parameters used in the MC simulation were defined from the built-in FLUKA HADROTHErapy parameter set. In addition, two Fortran sub-routine templates (source.f and mgdraw.f) were adapted and compiled using Flair to implement additional features (FLUKA 2018) as indicated in Table 3.5.

Table 3.5: The adapted Fortran sub-routines as used in this thesis for Monte Carlo simulations

Sub-routine	Activated by	Purpose
source.f	FLUKA SOURCE	To mimic an entire clinic-like treatment plan of the homogeneous head model. It simulated multiple carbon-ion pencil beams per simulation, with specific beam energy, position, FWHW, and the number of primary ions per pencil beam.
mgdraw.f	FLUKA USERDUMP	To score carbon-ion fragmentation positions: • Cartesian coordinates of the fragmentation position of the primary carbon-ions were scored as “true fragmentation origins”. • Cartesian coordinates of every fragment (secondary, tertiary ions, etc.) crossing the mini-tracker scored as “measured tracks”.

3.4.2 Simulated elements

3.4.2.1 Simulated head models

Two main simulations were performed using both anthropomorphic and homogeneous head models. These simulations were based on the Master thesis of M. Reimold. Within this project, the Master's thesis of N. Abbani and the Bachelor's thesis of A. Schlechter allowed simulating the anthropomorphic and homogeneous head models, respectively. Figure 3.12 shows both simulated head models.

The homogeneous cylindrical head model was implemented in FLUKA as a PMMA cylinder of 160 mm diameter and 10 mm height, as described in (§3.3.1.1.), to investigate the performance of the monitoring at different detection angles and to compare the track origins, obtained with the same method as in the measured data, to the true fragmentation origins.

To investigate the performance of the monitoring for different mini-tracker sizes or positions, and for different target change complexities, the anthropomorphic Alderson head model was implemented in FLUKA as described in (Abbani 2020). For this, CT DICOM images, acquired using the clinically used SIEMENS Sensation Open scanner of the anthropomorphic head model were imported into the Flair interface. The Schneider parametrization was used to segment the CT images into different materials according to the Hounsfield Unit (HU) value of its voxels and to assign a nominal predefined mean density to each segmented material (Jiang et al. 2004; Parodi et al. 2012; Schneider et al. 2000).

3.4.2.2 Simulated mini-trackers

As depicted in Figure 3.13, the mini-tracker, composed of two Timepix3 detectors, was implemented in FLUKA by the following elements:

- Two silicon sensor layers of 14 mm x 14 mm width and 300 µm thickness.
- Two silicon read-out chip layers of 14 mm x 14 mm width and 700 µm thickness.
- Four aluminum sensor chip supports of 2.35 mm x 2.35 mm x 14 mm
- 256 x 256 bump-bonds placed between the sensor and read-out layer, represented by small cuboids of 25 µm x 25 µm width and 12.5 µm thickness, made of 63 % tin and 37 % lead alloy (mass fraction).

3.4.2.3 Accelerator beamline

The accelerator beamline, as described in (§3.1.1.) was implemented in FLUKA using the following two elements, as seen in Figure 3.14:

- a water insert of 1.47 mm thickness (Parodi et al. 2012) to approximate the beam energy loss induced by the beam delivery monitoring system (BAMS) in the beam nozzle.
- a PMMA ripple filter of 3 mm thickness (Parodi et al. 2012) is used at the HIT facility to increase the energy spread of the primary beam to achieve a flattening of the Spread-Out Bragg Peak in carbon-ion treatments.

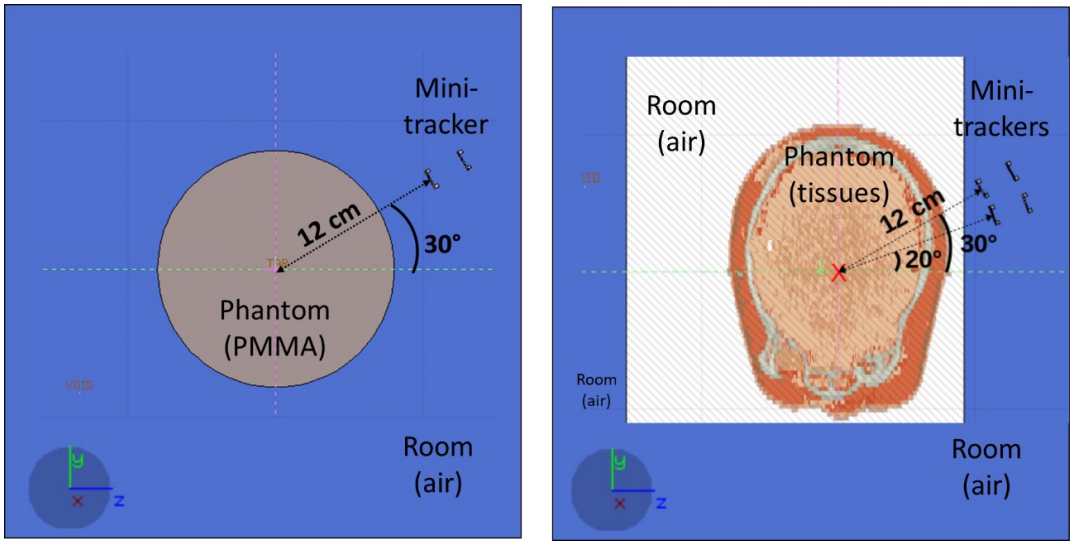

Figure 3.12: Top view of the FLAIR geometrical rendering of the two head models as implemented in FLUKA. The homogeneous cylinder is seen on the

left. The anthropomorphic Alderson head model adapted from (Abbani 2020) is seen on the right.

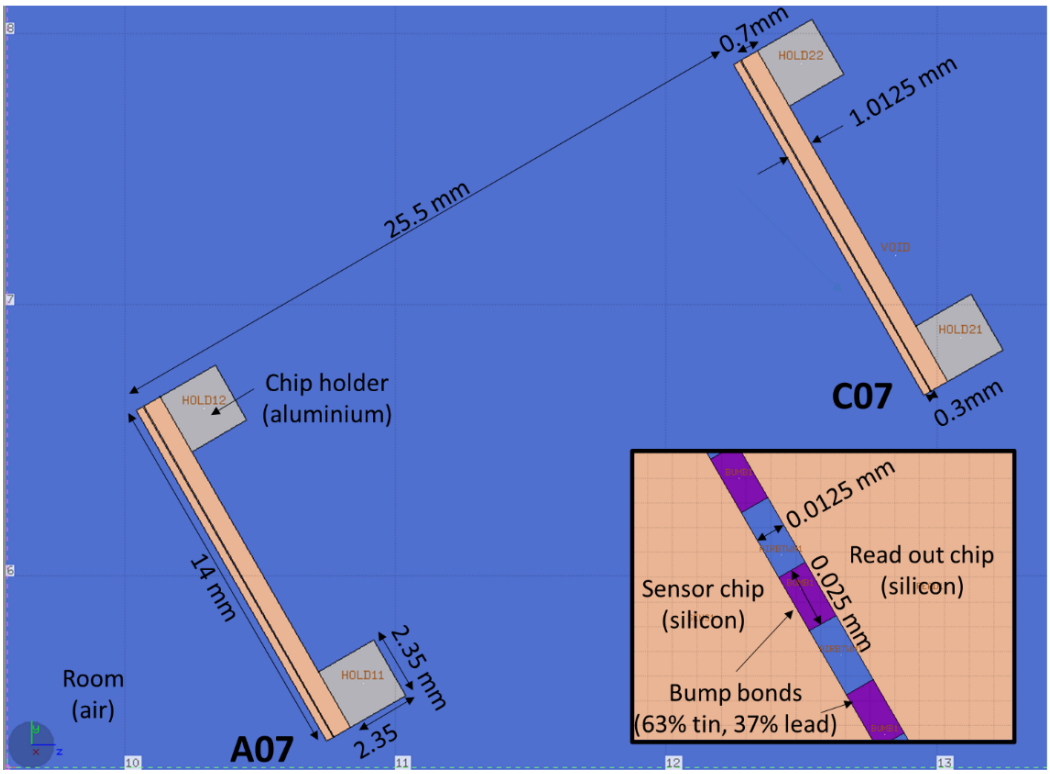

Figure 3.13: Top view of the FLAIR geometrical rendering of the mini-tracker as implemented in FLUKA. The mini-tracker is made of two parallel Timepix3 detectors, separated by a distance of 25.5 mm. Zoom is made on the bump bonds between the detection layer (sensor chip) and the read-out chip.

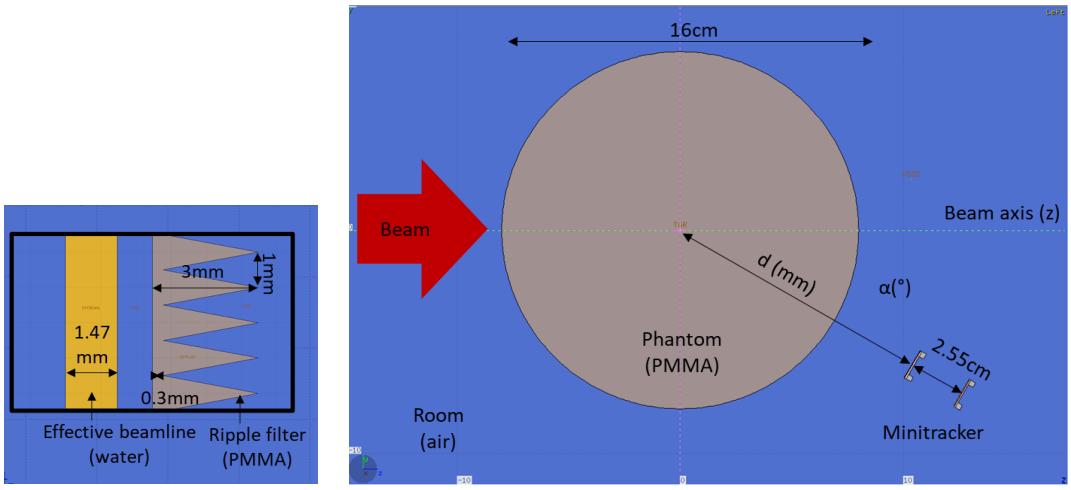

Figure 3.14: Top view of the FLAIR geometrical rendering of accelerator beam (left) and experimental setup (right) as implemented in FLUKA. The HIT facility beamline, visualized on the left of the figure, is composed here of a 3-mm-thick ripple filter and a BAMS represented by a water-effective beamline.

3.4.3 Simulated setups

The entire geometry of the experimental setup was reproduced in FLUKA, as shown in Figure 3.14. The experimental setup included the mini-tracker (with all its components as shown in Figure 3.13), one of the head models (either homogeneous or anthropomorphic, as shown in Figure 3.12), and the accelerator beamline (including the ripple filter, as shown in Figure 3.14). The head model was modified in different simulation runs using 2-mm-thick air slabs of 80 mm x 80 mm lateral surface, as seen in Figure 3.15.

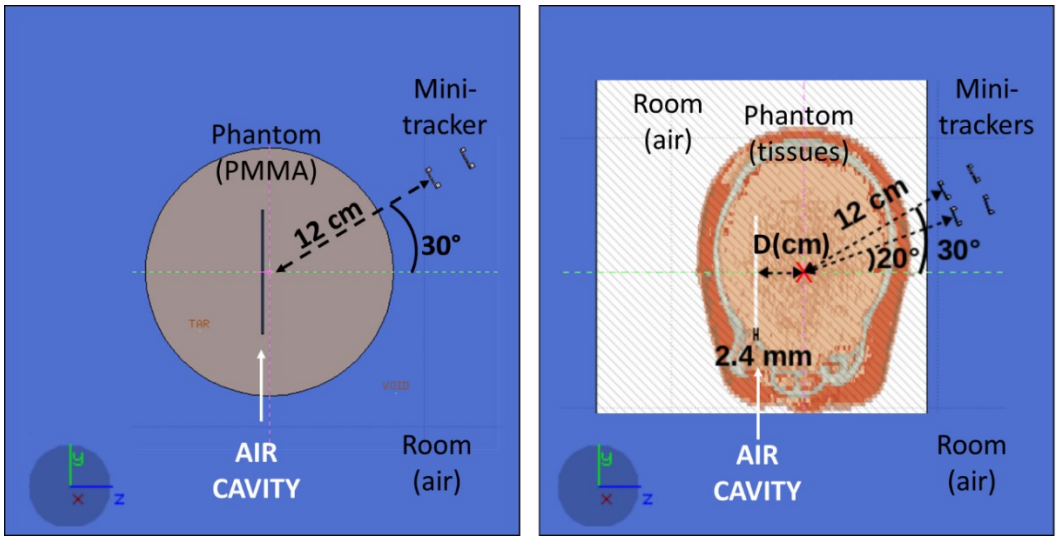

Figure 3.15: Top view of the FLAIR geometrical rendering of the two head models with air cavities implemented in FLUKA. The homogeneous cylinder is seen on the left. The anthropomorphic Alderson head model adapted from (Abbani 2020) is seen on the right.

3.5. Data post-processing

Pixel information of single-ion hits measured by the mini-tracker was post-processed and analyzed using C++ and MATLAB codes. See the following paragraphs for details on each process and Figure 3.16 for an overview of the data post-processing.

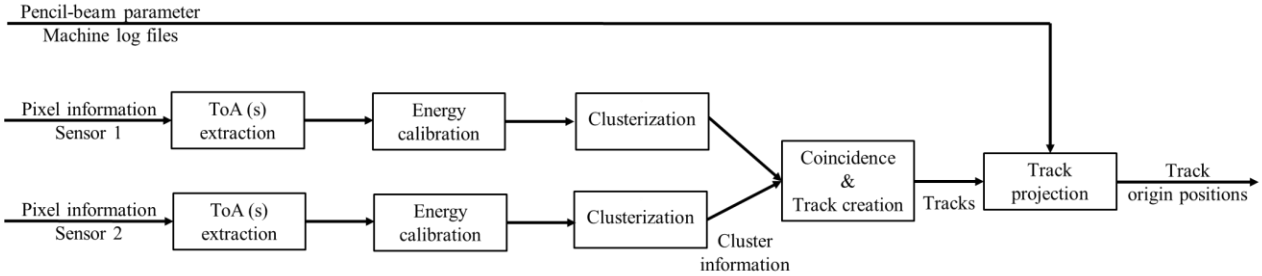

Figure 3.16: Flowchart of the data post-processing from the pixel information acquisition of single ion hits by the sensor 1 and 2 of the mini-tracker, until the extraction of measured secondary-ion track and estimation of the track origin positions in the target. Each process is detailed in the following paragraphs.

3.5.1. Pixel data acquisition

During all measurements, the raw data acquired by the mini-tracker operated at 10 V bias voltage in ToA/ToT mode allows for the extraction of four main information for each detector pixel that was hit by a single ion where the signal rose above the 3 keV threshold:

- pixel coordinates (X, Y)
- time-of-arrival (ToA)
- fast time-off-arrival (fToA)
- time-over-threshold (ToT)

3.5.1.1 Pixel time of arrival extraction

Pixel signal arrival time, t_{ToA}, is calculated using both the resolution of the fast clock (1.56 ns) and the resolution of the slow clock (25 ns):

$$t_{ToA}\,[ns] = ToA \times 25\,ns - fToA \times 1.56\,ns \qquad \text{(Eq.3.3)}$$

3.5.1.2 Pixel energy calibration

Due to inherent differences in the read-out circuit characteristics of each individual pixel, an energy calibration needed to be performed for all 256 x 256 pixels of each detector. The calibration curves were parameterized by the following function:

$$ToT(E) = a\,E + b - \frac{c}{E - t} \qquad \text{(Eq.3.4)}$$

where *a*; *b*; *c* and *i* parameters were obtained for each detector pixel from a detector calibration procedure developed by (Jakubek 2009a, 2011; Jakubek et al. 2008) as shown in Figure 3.17. This calibration procedure uses discrete X-ray fluorescence and γ- radiation of known energies and is performed for each pixel individually. The AdvaPIX TPX3 modules used in this thesis were calibrated by ADVACAM s.r.o. in Prague.

The energy *E* deposited in a given pixel was thus calculated for the measured *ToT* using:

$$E\,[keV] = \frac{at + ToT - b + \sqrt{(b + at - ToT)^2 + 4ac}}{2a} \qquad \text{(Eq.3.5)}$$

with *a, b, c,* and *t* are the pixel parameters determined by the aforementioned calibration procedure of (Eq.3.4).

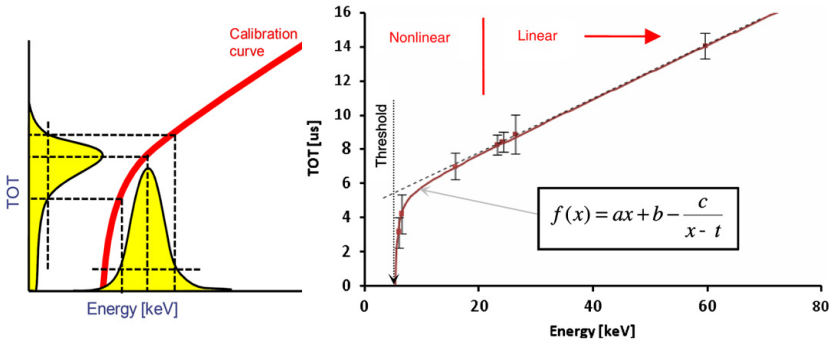

Figure 3.17: ToT as a function of the deposited energy in AdvaPIX TPX3 sensor layer, reprinted from (Jakubek 2011). The calibration curve f(x), on the right, composed of linear and nonlinear parts, permits the retrieval of pixel-specific calibration parameters a, b, c, and t for each detector using (Eq.3.5).

3.5.1.3 Charge sharing by neighboring pixels

When an ion impinges the sensitive area of the detector, its deposited energy can be collected over several neighboring pixels in a so-called charge sharing effect (Jakůbek 2009), as shown in Figure 3.18. The lateral spread of the collected charge of an ion is based on the diffusion of the created electron-hole pairs along the path of the ion in the silicon detector. Adjacent pixels that have collected the charge of the same ion will be referred to as *cluster* pixels. They together represent a single ion hit.

The magnitude of the charge sharing effect and the size of the resulting cluster depend on the energy deposited by the impinging ion and the bias voltage applied to the sensor. In this thesis, the bias voltage *Vb* was set to 10 V to improve the energy deposition accuracy for ion measurements (Gehrke et al. 2017). After performing time conversion and energy calibration, an example of the measured time t_{TOA} and energy *E* pixel information of several neighboring pixels corresponding to a single ion hit are shown in Figure 3.19.

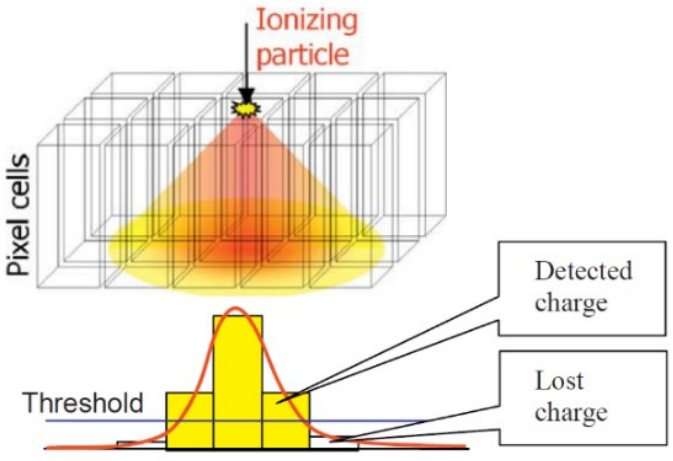

Figure 3.18: Charge sharing effect on neighboring pixels, reprinted from (Jakubek 2009b).

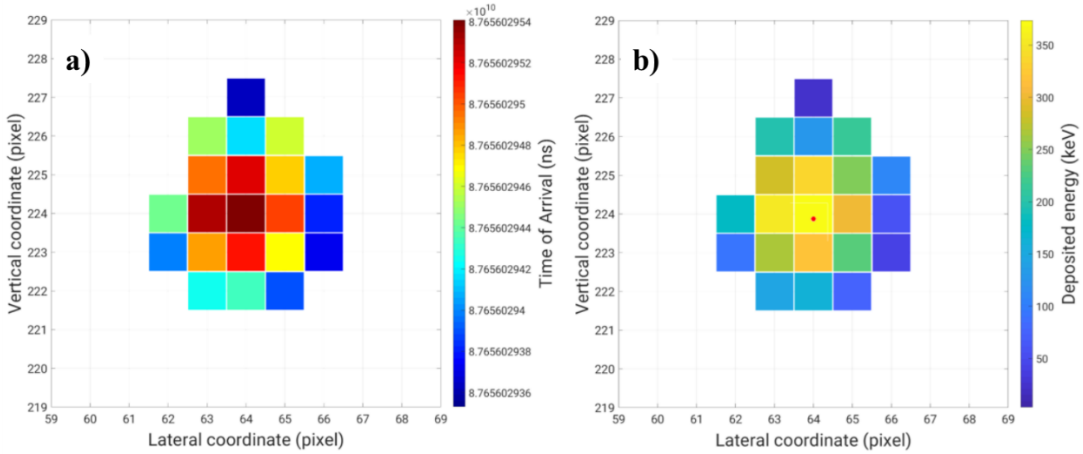

Figure 3.19: Cluster of pixels representing the hit of a single secondary ion in terms of a) time of arrival and b) time-over-threshold information as measured with a mini-tracker placed at 0° with respect to the beam axis. The red point represents the energy-weighted center of mass of the cluster of pixels. Reprinted from (Félix-Bautista 2021).

3.5.2. Clusterization

During the off-line data processing, quasi-simultaneous hits detected by neighboring pixels in a detector were grouped to form a so-called '*cluster*'. A clusterization time window, $\Delta T_{Clusterization}$, of 150 nanoseconds was defined on the t_{TOA} of the measured pixels, see (Eq.3.3), to group these pixels while accounting for the charge collection time of an ion hit on the sensor (~ 10 ns). This charge collection time depends on the applied bias voltage, here 10 V. Figure 3.20 shows typical ToA-color-coded pixel information as measured during a 5 ms acquisition.

$$|t_{TOA\,2} - t_{TOA\,1}| \leq \Delta T_{Clusterization} = 150\ ns \qquad \text{(Eq.3.6)}$$

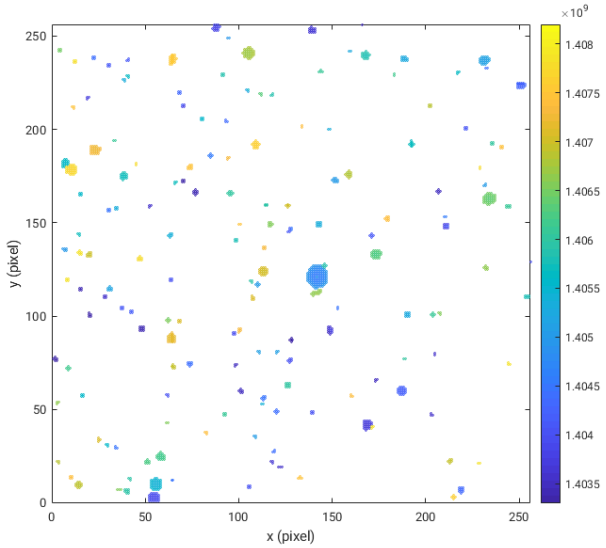

Figure 3.20: ToA-color-coded pixel information scored by one of the mini-tracker sensor layers during a 5 ms time frame. Pixels are grouped in a cluster when their t_{ToA} difference is $\leq \Delta T_{Clusterization}$ =150 ns.

3.5.2.1 Main cluster features

A group of N_{pix} pixels representing a single detected secondary ion in one of the sensor layers, i.e. labeled as a cluster, was characterized by four main features: the time of arrival (T_C) of the entire cluster, the size (S_C) of the cluster in terms of the number of pixels, the energy-weighted center of mass position (X_C, Y_C) of the cluster, and the total deposited energy (E_{sum}) measured for that particular cluster. Each feature is defined as follow:

- Cluster time of arrival (T_C):

$$T_C\ [ns] = min\left(t_{TOA\,i} \,\middle|\, i \in N_{pix} \right) \quad \text{(Eq.3.7)}$$

Cluster size (S_C), with a minimum cluster size of 2 pixels to neglect photons and electrons hits:

$$S_C\ [px] = N_{pix} \quad \text{(Eq.3.8)}$$

- Energy-weighted center of mass position of the cluster (X_C, Y_C):

$$X_c\ [px] = \frac{\sum_{i=1}^{Npix} X_i E_i}{\sum_{i=1}^{Npix} E_i}$$

$$Y_c\ [px] = \frac{\sum_{i=1}^{Npix} Y_i E_i}{\sum_{i=1}^{Npix} E_i} \quad \text{(Eq.3.9)}$$

X_c and Y_c [px] can then be converted into Cartesian coordinates [mm] with respect to the experimental room.

- Total deposited energy within the cluster (E_{sum})

$$E_{sum}\ [keV] = \sum_{i=1}^{Npix} E_i \quad \text{(Eq.3.10)}$$

3.5.2.2 Additional morphological features of the cluster

From these four main cluster features (T_C, S_C, $[X_C, Y_C]$, and E_{sum}), several additional morphological features of the cluster can be derived as detailed in (Marek 2020): optimal polar angle (α_p) that minimizes the momentum inertia along the x-axis, weighted standard deviations for new (X'', Y'') coordinate system, cluster linearity, count of the border and the inner pixels, cluster thinness, cluster thickness, cluster curliness, cluster roundness, and cluster length. These additional morphological features can be used to differentiate between multi-coincident clusters when looking for two coincident particle hits on both sensor layers.

3.5.3. Coincident clusters finding and secondary-ion track reconstruction

If an ion crosses both sensor layers of the mini-tracker, it quasi-simultaneously generates a cluster in both layers. By finding such coincident clusters in both sensor layers, one can retrieve the two clusters created by the same ion. The trajectory of the ion in-between the two sensor layers can then be determined using the information of the impact position of the ion on the two detector layers, as detailed below.

3.5.3.1 Time-based coincidence

Two detected clusters C1 and C2 were defined as *coincident* when the difference between the cluster times was less than a certain coincidence time window, $\Delta T_{coincidence}$. This window was large enough to cover the uncertainties due to several 25 ns clock ticks caused by possible delayed cluster times in either the first or the second sensor layer.

$$|T_{C1} - T_{C2}| \leq \Delta T_{coincidence} = \pm 75\ ns \qquad \text{(Eq.3.11)}$$

with T_{C1} the cluster time of C1 in the first sensor layer of the mini-tracker and T_{C2} the cluster time of C2 in the second one as defined in (Eq.3.7).

When exactly two coincident clusters were found within $\Delta T_{coincidence}$ these clusters were referred to as *single coincidence clusters*. When three or more coincident clusters were found within $\Delta T_{coincidence}$ these clusters were referred to as *multi-coincidence clusters.* Less than 10 % of the measured clusters are multi-coincident. Additional dissimilarity-based analysis of multi-coincidence clusters was needed to resolve these clusters.

3.5.3.2 Dissimilarity-based anticoincidence

When three or more multi-coincident clusters were found, the dissimilarity (*DIS*) of the different cluster features was computed for each pair of the multi-coincident cluster as detailed in (Marek 2020). In the case of three multi-coincident clusters, the dissimilarity *DIS(cluster1,cluster2)* was compared to *DIS(cluster1,cluster3)* and to *DIS(cluster2,cluster3).* The two clusters with the lowest dissimilarity value were kept. With this method, approximately 97 % of the multi-coincidence clusters could be resolved Additionally, a maximum dissimilarity constraint of 2σ(*DIS*) was applied for single coincidence clusters.
The features used for the dissimilarity-based analysis were the following ones: the total deposited energy in the cluster (E_{sum}), the energy-weighted cluster center (X_C, Y_C), the maximum energy within one pixel (E_{max}), the α axis and polar angle, the cluster linearity, the number of the border and the inner pixels, the cluster thickness, its thinness, its linearity, its curliness, its roundness, and its length. For definition see (Marek 2020).

3.5.3.3 Reconstruction of the secondary-ion tracks

Following the coincidence process, track reconstruction of the measured secondary ions was carried out. As shown in Figure 3.21, the straight *ion-track* which was followed by a detected secondary ion to travel from the first detector sensor layer to the second one was defined as the straight line connecting the energy-weighted center of mass positions (X_{C1}, Y_{C1}) and (X_{C2}, Y_{C2}) of two coincident clusters C1 and C2 in each detector.

3.5.4. Back-projections of secondary-ion tracks

The next step in the data analysis was to find the best approximation of the origin of the measured secondary ions. This was accomplished by a back-projection of the measured ion tracks to the head model volume.

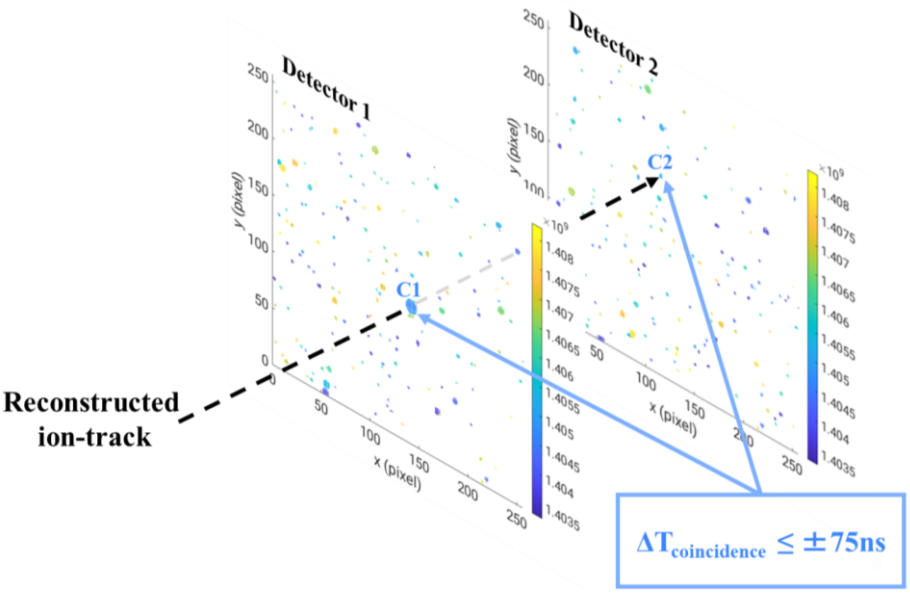

Figure 3.21: Ion track reconstructed between two clusters: C1, detected in detector 1, and C2, in detector 2 using time-based cluster coincidence of (Eq.3.11) and energy-weighted center of mass positions (X_{C1}, Y_{C1}) and (X_{C2}, Y_{C2}) as defined in (Eq.3.9).

In this thesis, the depth of the secondary ion production site along the beam direction is of the highest interest, to estimate this depth three track-projection methods were investigated. This secondary ion production site is referred to as the *origin* along the beam axis and can be approximated using either a 2D, a time-dependent 2D+, or a time-dependent 3D+ projection method, as seen in Figure 3.22

Figure 3.22.The secondary-ion origin along the beam axis in the head model was defined in the **2D projection method** as the crossing point between the straight line representing the detected secondary-ion track and the constant plane longitudinal to the beam axis located at the center of the tumor, i.e. at the center of the head model, see Figure 3.22-a) – as used before in (Gwosch et al. 2013).

The secondary-ion origin along the beam axis in the head model was defined in the **time-dependent 2D+ projection method** as the crossing point between the straight line representing detected a secondary-ion track and the plane longitudinal to the beam axis that contains the carbon-ion pencil beam at the time of the secondary ion detection, see Figure 3.22-b).

The secondary-ion origin along the beam axis in the head model was defined in the **time-dependent 3D+ projection method** as the middle of the minimum distance in three-dimensional space between the straight line representing the detected secondary-ion track and the straight line representing the axis of the primary carbon-ion pencil beam at the time of the secondary ion detection, see Figure 3.22-c).

For the two time-dependent projection methods, information regarding the primary carbon-ion pencil beam was retrieved from the beam records of the irradiation. A time re-alignment of a few milliseconds between the beam record and the measured data was required.

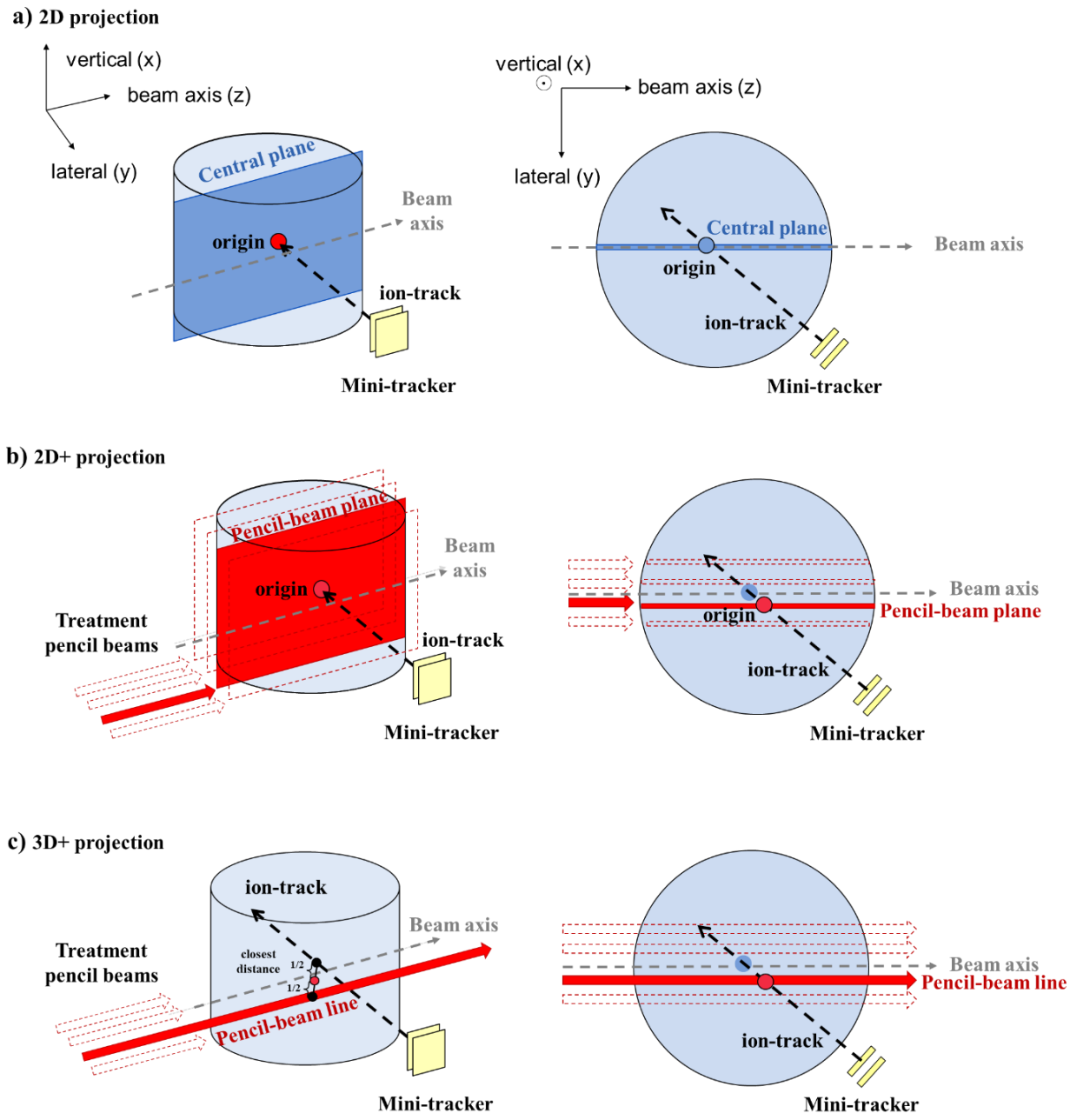

Figure 3.22: Representation of the three track-projection methods a) 2D projection, b) 2D+ projection and c) 3D+ projection, as used to find the secondary-ion origin coordinate along the beam axis in the head model from the detected secondary-ion track. The head model is represented here by a blue cylinder, the detected ion track by the dashed black line, and the approximated ion origin position by the red dot. Only the depth of the origin-position is of relevance for this thesis.

During an entire fraction delivery, a distribution of the secondary-ion origin positions along the beam axis could be extrapolated from the measured secondary ion tracks, as shown in Figure 3.23. The uncertainty evaluation of each bin, *N*, of this secondary-ion emission profile was defined based on a Poisson distribution, using:

$$\sigma(N) = \sqrt{N} \qquad \text{(Eq.3.12)}$$

This secondary-ion origin distribution, also known as secondary-ion emission profile, carries information about the production of the secondary ions in the targeted head model during the treatment fraction delivery. Ideally, by comparing several secondary-ion origin profiles measured during different treatment fraction deliveries, internal changes inside the head model can be tracked.

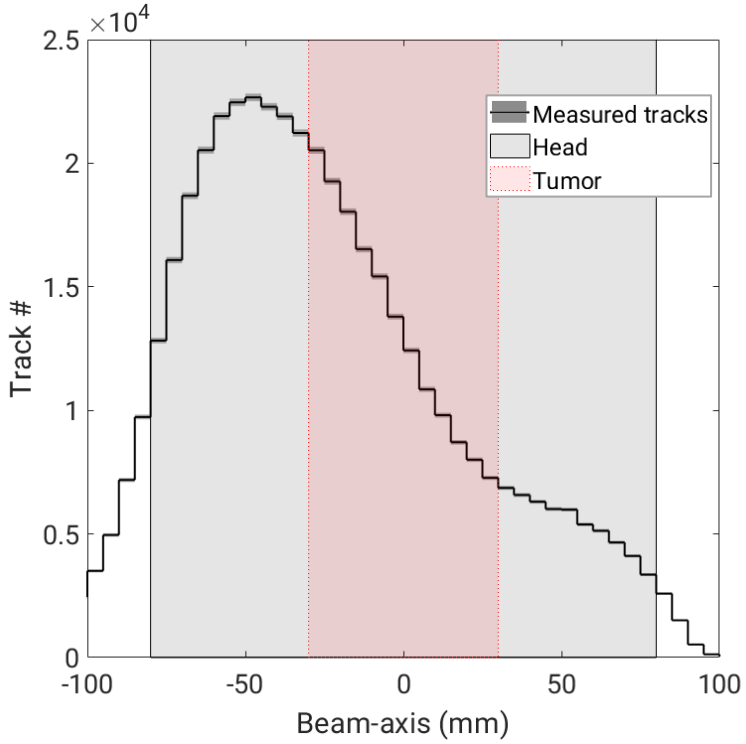

Figure 3.23: Secondary-ion emission profile plotted along the beam axis with a bin size of 5 mm. The profile is retrieved here using the 3D+ projection method applied to the secondary-ion tracks measured from the anthropomorphic head model. Corresponding statistical uncertainties *σ(N)* are plotted as barely visible error bands.

3.6. Performances of the tracker

3.6.1. Energy deposition analysis

The energy deposited per unit path length by a secondary ion in a sensor layer (*dE/dl*) was defined from E_{sum}, see (Eq.3.10), using:

$$\frac{dE}{dl}\left[\frac{MeV}{mm}\right] = \frac{E_{sum}}{dl} = \frac{\sum_{i=1}^{Npix} E_i\,[keV]}{dl\,[mm]}\,0.001 \qquad \text{(Eq.3.13)}$$

and the path of the ion, *dl*, in each mini-tracker layer is given by:

$$dl\,[mm] = \sqrt{dx^2 + dy^2 + dz^2} \qquad \text{(Eq.3.14)}$$

with *dx, dy,* and *dz*, as the distance traveled in the x, y, and z directions by the detected ion in the depleted region of the sensor layer. Here dz corresponds to the depleted depth of the sensor layer which depends on the applied bias voltage. The two sensors were 0.3 mm thick depleted with a bias voltage of 10 V. This results in a depleted depth of approximately 0.118 mm as seen in Table 3.3 from equations (Eq.3.1) and (Eq.3.2).In this thesis, the mini-tracker was composed of two detector layers, hence dE_1/dl and dE_2/dl were defined to describe the energy deposited per unit path length in the first and second sensor layer respectively, as seen in Figure 3.24.

3.6.2. Detection yield of secondary-ion tracks

The detection yield of the secondary-ion tracks was defined as the ratio between the number of detected secondary-ion tracks and the number of incident carbon-ion primaries:

$$Yield = \frac{N_{secondary\ ion\ track}}{N_{primary\ ion}} \qquad \text{(Eq.3.15)}$$

Additionally, the track yield can be defined per solid angle, Ω, in [sr^{-1} per incident carbon ion] as used in previous studies (Finck et al. 2017; Gunzert-Marx et al. 2008; Mattei, Bini, et al. 2017; Piersanti et al. 2014; Rucinski et al. 2018).

$$Yield_{\Omega}[sr^{-1}\ per\ incident\ carbon\ ion] = \frac{\frac{N_{secondary\ ion\ track}}{N_{primary\ ion}}}{\Omega} \qquad \text{(Eq.3.16)}$$

Even though the secondary-ion emission is not isotropic, the solid angle Ω allow to estimate the impact of the distance of the mini-tracker on the detection of secondary-ion tracks. The solid angle (Ω [sr]) of an on-axis rectangle of size *a* by *b* placed at a distance *d* was calculated using two cone parameters $\alpha = \frac{a}{2d}$ and $\beta = \frac{b}{2d}$, following the equation:

$$\Omega\,[sr] = 4\,\cos^{-1}\sqrt{\frac{1 + \alpha^2 + \beta^2}{(1 + \alpha^2)(1 + \beta^2)}} \qquad \text{(Eq.3.17)}$$

Table 3.6 presents the solid angle (Ω) calculated for a 14 x 14 mm rectangular plate placed at different distances *d,* as used in this thesis.

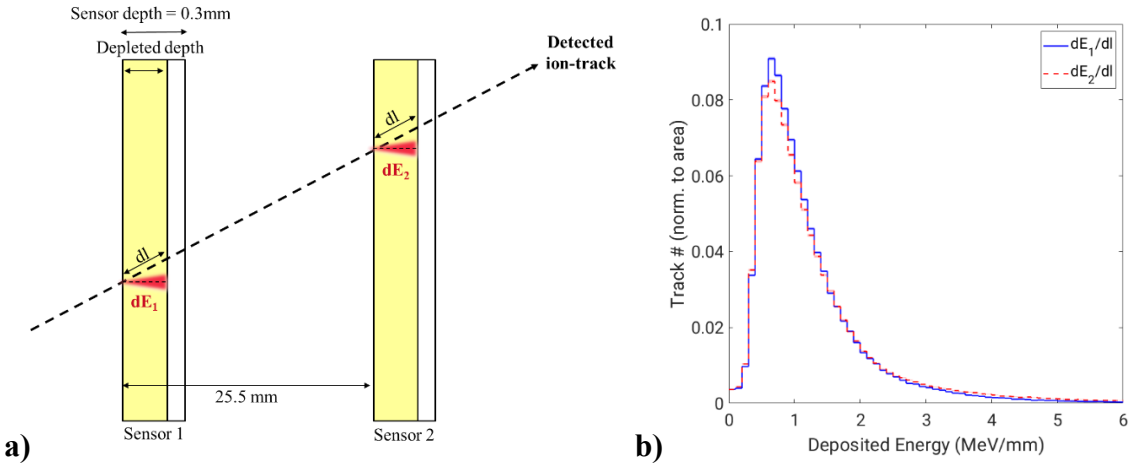

Figure 3.24: a): Lateral visualization of the two sensor layers of the mini-tracker and their corresponding dE_1/dl and dE_2/dl. b) dE/dl spectra from both sensor layers.

Table 3.6: Solid angle of a 14 mm x 14 mm rectangular plate (representing the first sensitive layer of the tracker) placed at different distances d from the target center:

Distance d (mm)	**Ω (msr = 10^{-3} sr)**
120	13.6
160	7.6
340	1.7

3.7. Analysis of the measured secondary-ion emission profiles

In this thesis, different methods of analysis of the measured emission profiles of secondary ion tracks were employed, such as single-feature analysis, secondary ion grouping, and multi-feature analysis. The single-feature analysis aimed to detect and localize inter-fractional changes inserted in the head model using the measured emission profiles of secondary ion tracks. The secondary ion grouping aimed to improve the performances of the single-feature analysis by grouping measured tracks according to their corresponding pencil beam properties. The multi-feature analysis aimed to improve the performance of the single-feature analysis (using only secondary-ion emission profiles information) with additional track parameters information.

3.7.1. Detection & localization of anatomical changes using secondary-ion emission profiles

To investigate if any structural changes in the irradiated targeted volume can be detected in the global shape of the secondary-ion emission profile, the shape of the profile (Z) was investigated in a so-called *single-feature analysis*. For this analysis, several tools were utilized to analyze the shape of the emission profile.

3.7.1.1 Maximum value

The maximum value of the secondary-ion emission profile was defined as the average of the profile's highest bin value and its two adjacent bins (Abbani 2020; Gwosch et al. 2013). An example is plotted in Figure 3.25.

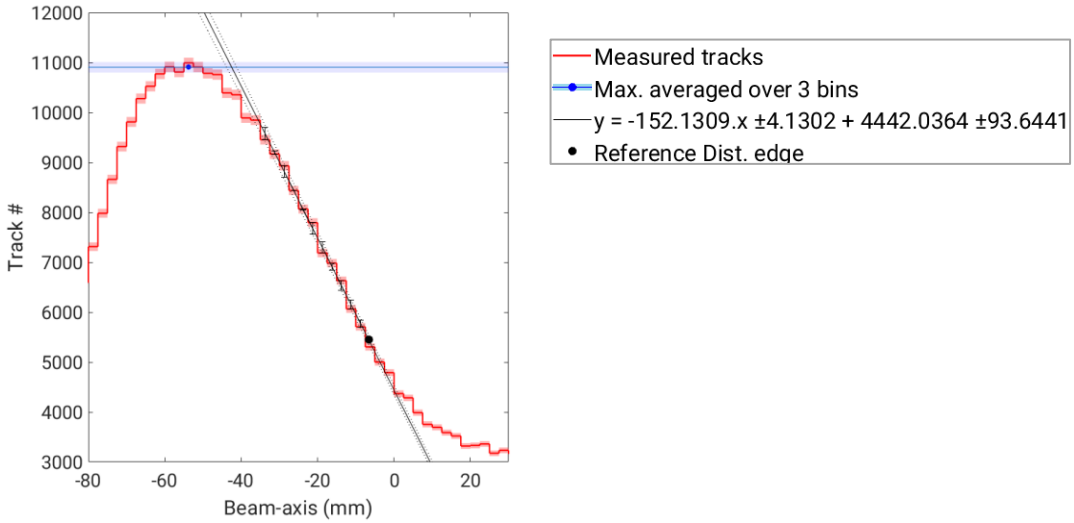

Figure 3.25: Secondary-ion emission profile along the beam axis as measured for the homogeneous head model at 30° from the beam axis, and 120 mm from the tumor center. Corresponding statistical uncertainties $\sigma(N)$ of the measured track are plotted as error bands. The entire treatment fraction was irradiated with beam energies from 167.66 to 239.45 MeV/n. The maximum value is represented by the blue dot and line, the blue band indicates the uncertainties on the maximum. The linear fit y_{fit}, performed between 50 % and 90 % of the profile's maximum, is plotted using the black line, its uncertainties $y_{uncertainties}$ are plotted using the black dotted lines (see (Eq.3.20)). The distance from the fit and each bin used for the fit are shown with the black error bars.

3.7.1.2 Linear fit of the distal falloff of the emission profile

To estimate the range of the primary ion beam in the head model, a linear fit (y_{fit}) of the secondary-ion emission profile's distal falloff, i.e. the falloff located the deepest into the dead model, was defined as:

$$y_{fit} = (a \pm \sigma_a)\, x + (b \pm \sigma_b) \qquad \text{(Eq.3.18)}$$

with

$$\sigma_{fit} = \sqrt{{\sigma_a}^2 x^2 + {\sigma_b}^2} \qquad \text{(Eq.3.19)}$$

$$y_{uncertainties} = y_{fit} \pm \sigma_{fit} \qquad \text{(Eq.3.20)}$$

The a and b coefficients of the linear fit and their uncertainties σ_a and σ_b were based on a 1σ confidence level. Due to the broader shape of the profile measured from a full treatment plan compared to from a single pencil beam, the linear fit was performed between 50 % - 90 % of the profile's maximum as opposed to the 25 % -75 % used in (Abbani 2020; Gwosch et al. 2013). An example is plotted in Figure 3.25.

3.7.1.3 Detection of the position of a change in the irradiated volume

The discrepancy in the secondary-ion emission profiles between a reference and a follow-up fraction was searched by using the **ratio** between two measured profiles as defined on a bin-basis by:

$$N_{ratio} = N_{follow-up} / N_{ref} \quad \text{(Eq.3.21)}$$

and

$$\sigma(N_{ratio}) = N_{ratio} \sqrt{\left(\frac{\sigma(N_{follow-up})}{N_{follow-up}}\right)^2 + \left(\frac{\sigma(N_{ref})}{N_{ref}}\right)^2} \quad \text{(Eq.3.22)}$$

with N_{ref} as the number of track origins in the bins of the profile of the reference fraction, $N_{follow-up}$ as in the bins of the profile of a follow-up fraction, and with $\sigma(N) = \sqrt{N}$ as defined in (Eq.3.12).

To detect the position of the internal change in the irradiated volume, the air cavity position was assumed to be located at the minimum of the two profiles' ratio and to correspond to the maximum of the signal reduction. The N_{ratio} curved was smoothed by its nearest neighbor as defined for each bin i by:

$$N_{ratio-smoothed}(i) = \frac{N_{ratio}(i-1) + N_{ratio}(i) + N_{ratio}(i+1)}{3} \quad \text{(Eq.3.23)}$$

The position $Z_{MIN\text{-}RATIO}$ of the minimum ratio value was defined as the mean of the three-bin positions z_1, z_2, z_3 of the three minimal bin values of the smoothed ratio $N_{ratio\text{-}smoothed}$, weighted by their corresponding N_{ratio} heights $N_{ratio}(z_1)$, $N_{ratio}(z_2)$, $N_{ratio}(z_3)$. This accounts for a potential asymmetry of the minimum. The statistical uncertainty on this $Z_{MIN\text{-}RATIO}$ was estimated to be at maximum of the order of the bin size, i.e. 5 mm.

$$Z_{MIN-RATIO} = \frac{N_{ratio}(z_1) \times z_1 + N_{ratio}(z_2) \times z_2 + N_{ratio}(z_3) \times z_3}{N_{ratio}(z_1) + N_{ratio}(z_2) + N_{ratio}(z_3)} \quad \text{(Eq.3.24)}$$

with $N_{ratio}(z)$ being the bin height of the profile of the ratio between the reference fraction and follow-up fraction at the position "z", and z_1, z_2, and z_3 the bin positions along the beam axis of the three minimal values of the smoothed profile of the ratio. Figure 3.26-a) shows two secondary-ion emission profiles. Their ratio and the corresponding position $Z_{MIN\text{-}RATIO}$ of the maximum of the signal reduction are shown in Figure 3.26-b).

Parallel to this relative comparison of the secondary-ion emission profiles, an absolute comparison was performed. To do so, the **difference** between two secondary-ion emission profiles along the beam axis measured during a reference and a follow up fraction was defined on a bin-basis as:

$$N_{diff} = N_{follow-up} - N_{ref} \quad \text{(Eq.3.25)}$$

and

$$\sigma(N_{diff}) = \sqrt{\sigma(N_{follow-up})^2 + \sigma(N_{ref})^2} = \sqrt{N_{follow-up} + N_{ref}} \quad \text{(Eq.3.26)}$$

with N_{ref} as the number of track origins in the bins of the profile of the reference fraction, $N_{follow-up}$ as the number of track origins in the bins of the profile of a follow-up fraction, and with $\sigma(N) = \sqrt{N}$, as seen in (Eq.3.12).

To detect the position of the internal change in the irradiated volume, the air cavity position was assumed to be located at the minimum of the two profiles' difference. The N_{diff} curve was smoothed by its nearest neighbor as defined for each bin *i* by:

$$N_{diff-smoothed}(i) = \frac{N_{diff}(i-1) + N_{diff}(i) + N_{diff}(i+1)}{3} \quad \text{(Eq.3.27)}$$

The position $Z_{MIN-DIFF}$ of the minimum value was defined as the mean position of the three-bin positions z_1, z_2, z_3 of the three minimal bin values of the smoothed difference $N_{diff-smoothed}$, weighted by their corresponding N_{diff} heights: $N_{diff}(z_1)$, $N_{diff}(z_2)$, $N_{diff}(z_3)$. This accounts for a potential asymmetry of the minimum. The statistical uncertainty on this $Z_{MIN-DIFF}$ was estimated to be at maximum of the order of the bin size, i.e. 5 mm.

$$Z_{MIN-DIFF} = \frac{N_{diff}(z_1) \times z_1 + N_{diff}(z_2) \times z_2 + N_{diff}(z_3) \times z_3}{N_{diff}(z_1) + N_{diff}(z_2) + N_{diff}(z_3)} \quad \text{(Eq.3.28)}$$

with $N_{diff}(z)$ the bin height of the profile of the difference between the reference fraction and follow-up fraction at the position "z", and z_1, z_2, and z_3 the bin positions along the beam axis of the three minimal values of the smoothed profile of the difference. Figure 3.27-a) shows two secondary-ion emission profiles and their difference and the corresponding position $Z_{MIN-DIFF}$ is shown in Figure 3.27-b).

Ratio

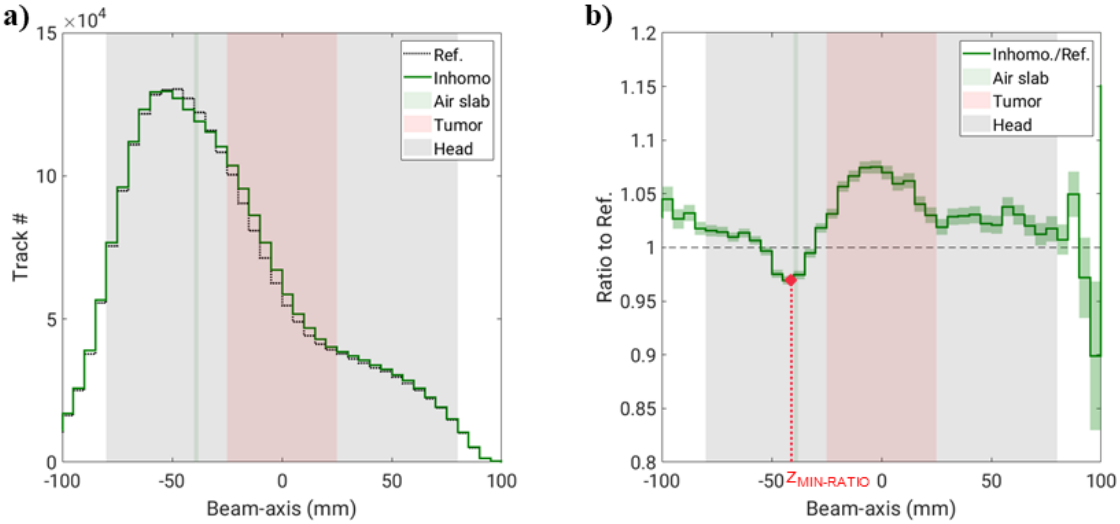

Figure 3.26: a) Secondary-ion emission profiles along the beam axis as measured in the homogeneous head model at 30° from the beam axis, and 120 mm from the tumor center for a reference and a follow-up fraction including a cavity. b) Their ratio. Statistical uncertainties corresponding to an 8-fold sensitive mini-tracker area are plotted as error bands.

Difference

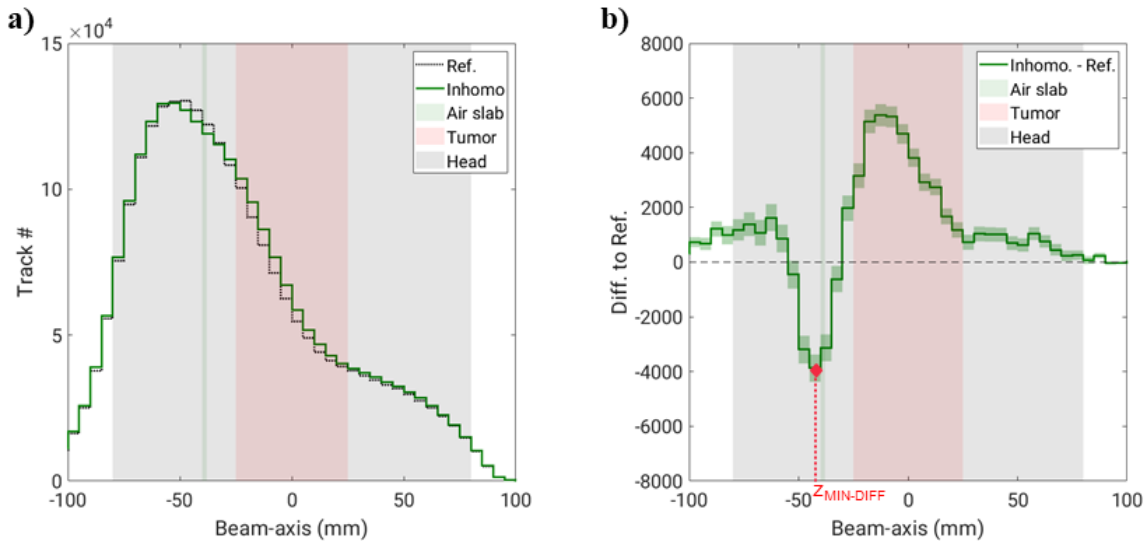

Figure 3.27: a) Secondary-ion emission profiles along the beam axis as measured in the homogeneous head model at 30° from the beam axis, and 120 mm from the tumor center for a reference and a follow-up fraction including a cavity. b) Their difference. Statistical uncertainties corresponding to an 8-fold sensitive mini-tracker area are plotted as error bands.

3.7.1.4 Magnitude of the internal change and its significance

To evaluate the magnitude of the internal change and its significance with respect to an un-altered fraction, several D- and D/σ(D)-values were defined based on the absolute difference ($N_{abs\ diff}$) between the two follow-up fractions (the un-altered one and the one with a change) and the same reference fraction. The absolute difference ($N_{abs\ diff}$) between two emission profiles (see Figure 3.28), measured during a reference and a follow-up fraction, is defined by:

$$N_{abs\ diff} = |N_{diff}| = |N_{follow-up} - N_{ref}| \quad \text{(Eq.3.29)}$$

and

$$\sigma(N_{abs\ diff}) = \sigma(N_{diff}) = \sqrt{N_{follow-up} + N_{ref}} \quad \text{(Eq.3.30)}$$

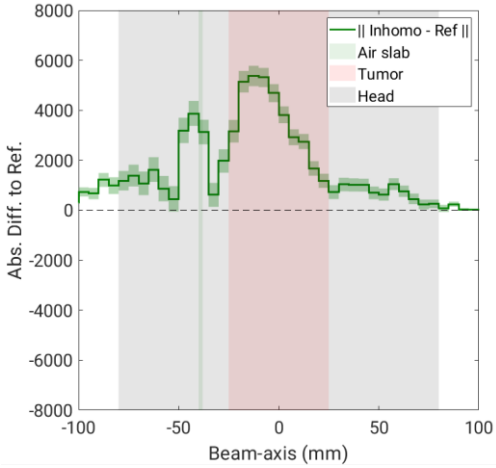

Figure 3.28: Absolute difference between the secondary-ion emission profiles along the beam axis as measured in the homogeneous head model at 30° from the beam axis, and 120 mm from the tumor center for a reference and a follow-up heterogeneous fraction. Statistical uncertainties corresponding to an 8-fold sensitive detector area are plotted as error bands.

The integral values integrated along the head-model depth $I_{|N_{follow-up1} - N_{ref}|}$ and $I_{|N_{follow-up2} - N_{ref}|}$ of the absolute difference between two follow-up fractions and the same reference fraction were compared using *D* and *D/σ(D)* values. Two fractions were assumed to be different from each other if their *D*-value is large. The *D*-value was defined as:

$$D = I_{|N_{followup2} - N_{ref}|} - I_{|N_{followup1} - N_{ref}|} \quad \text{(Eq.3.31)}$$

with

$$\sigma(D) = \sqrt{\sigma(I_{|N_{followup2} - N_{ref}|})^2 + \sigma(I_{|N_{followup1} - N_{ref}|})^2} \quad \text{(Eq.3.32)}$$

Detection of an air cavity was assumed to be significant if the *D/σ(D)*-value between the fraction with the air cavity and the fraction without is *D/σ(D)* > 1, with:

$$\frac{D}{\sigma(D)} \quad \text{(Eq.3.33)}$$

3.7.2. Detection of small changes

To better detect small anatomical changes that only affect part of the pencil beams, the measured secondary ion tracks can be separated according to the pencil beams they originate from. This is possible due to the offline synchronization of the pencil beam delivery as measured by the BAMS and the corresponding secondary ion tracks detected. In this thesis, the separation was performed according to two characteristics:

- the pencil-beam lateral positions (X_{PB}, Y_{PB})
- the expected pencil-beam stopping position along the beam axis (Z_{EXP}).

As seen in Table 3.1, the entire fraction irradiation of a 25-mm-radius tumor placed in the homogeneous head model contains 8356 different pencil beams. Each carbon-ion pencil beam was assumed to be parallel to the beam axis (0, 0, $\vec{z}$) and was characterized by its initial lateral position (X_{PB}, Y_{PB}) scored by machine beam records, its beam energy (E_{PB}), and its primary ion number.

3.7.2.1 Lateral separation in horizontal and vertical pencil beam positions

Several lateral regions can be defined to cover the lateral dimensions of a tumor (XY plane). As it can be seen in Figure 3.29 and Figure 3.30, nine lateral regions were defined to cover the lateral dimensions of an entire 25-mm-radius tumor centered on the axis of the treatment field (X = 0 and Y = 0). Each carbon-ion pencil beam used during the treatment plan irradiation was assigned to one of these nine defined regions depending on their lateral position.

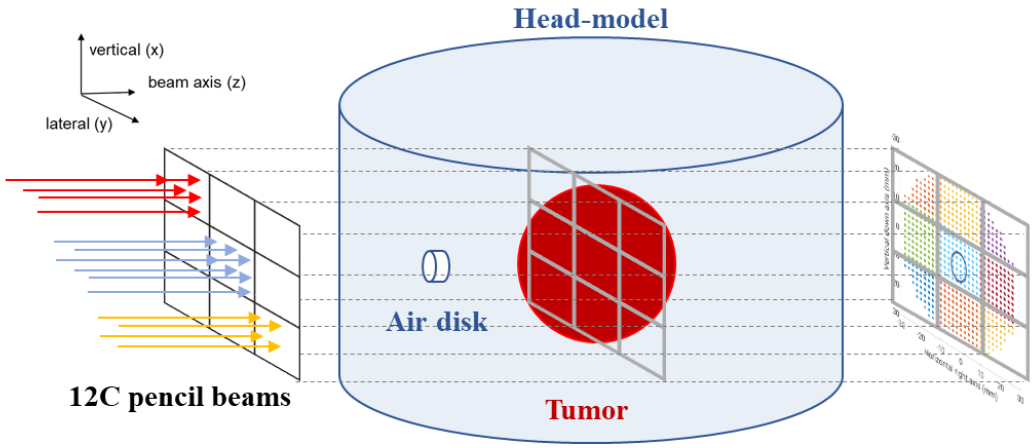

Figure 3.29: Schematic representation of the homogeneous head model (blue cylinder), tumor volume (red sphere), and inserted air disk of 2-mm-thick and 10-mm-diameter (white disk). Some of the treatment pencil beams used for the irradiation of the tumor volume are represented by the horizontal arrows upstream of the head model. The pencil beams are grouped in nine regions according to their lateral positions.

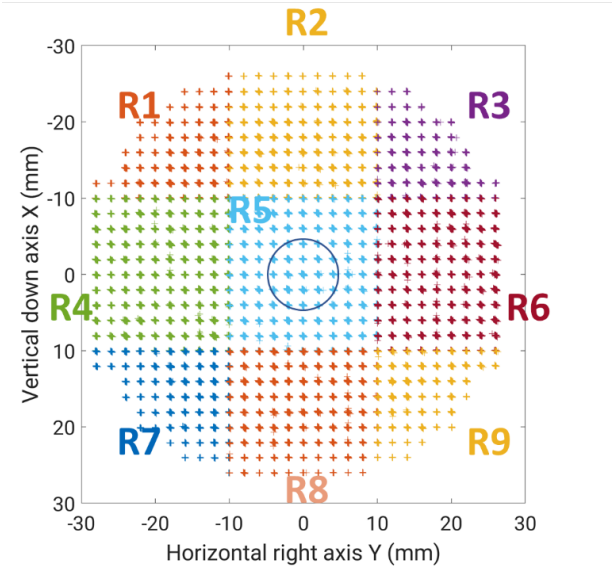

Figure 3.30: Lateral visualizations (beam eye view) of the nine 20 mm x 20 mm lateral regions defined to cover the entire lateral dimensions of the 25-mm-radius tumor. Each point represents a raster point position of the used treatment plan. Regions are numbered in the beam eye view from the top right (R1 red) to the bottom left (R9 yellow). Mini-tracker is positioned on the right side of the head model, closer to region 6 (R6). Region R5 ranges from X = [-10 mm; +10 mm] and Y = [-10 mm; +10 mm] and cover potentially affected pencil beams due to the inserted 10-mm-diameter air-disk (blue circle). A coordinated system is defined with the tumor center located at the room isocenter at (X, Y) = (0 mm, 0 mm).

As the measured secondary-ion tracks were resolved on a single pencil beam-basis, each of the measured ion tracks could be assigned to one of the nine defined regions depending on the primary pencil beam they came from.

3.7.2.2 Longitudinal separation of pencil beams according to the expected stopping positions

Following the lateral separation of pencil beams, longitudinal separation can also be performed. To do so, longitudinal regions can be defined along the beam axis to cover the longitudinal dimension of a tumor (Z_{EXP}). This is especially of interest in the case of a heterogeneous environment, e.g. a real patient head, as the expected stopping position Z_{EXP} along the beam axis of carbon ion pencil beams for the same beam energy can spread over several centimeters depending on the water-equivalent thickness (WET) of the crossed material for different lateral positions of the treatment pencil beams. For example, in the real patient treatment (see Figure 3.33), the pencil beams of the IES20 of energy E_{PB} = 192.13 MeV/u have expected stopping positions that spread over more than 29 mm in depth.

To calculate these expected stopping positions Z_{EXP}, carbon-ion ranges in water (R_{WATER}) were extracted for typical beam energies of carbon-ion beams using the Electronic Stopping Power mobile application (Electronic Stopping Power (Aarhus Particle Therapy Group); Lühr et al., 2012; Toftegaard et al., 2014).

The *WET* of a crossed material *i* in a voxel was extracted from:

$$WET_i = RSP_i \times T_i \quad \text{(Eq.3.34)}$$

with T_i being the geometrical thickness and RSP_i the relative stopping power of a traversed object of material *i*. In this work, the following RSP were assumed:

- $RSP_{water} = 1$,
- $RSP_{air} \approx 0.00089$ (Jäkel, Jacob, et al. 2001).
- $RSP_{PMMA} = 1.163$ for the cylinder, and $RSP_{PMMA} = 1.151$ for the inserted slabs in the cylinder measured as described in section (§3.3.1.1.).

WETs of the different patient head materials were extracted on a voxel-basis from the HU of clinical CT images using the matRad toolkit and a specific matRad base data of the HIT facility. MatRad is a radiation treatment planning software for intensity-modulated proton and carbon-ion radiotherapy (Bangert et al. 2020; Wieser et al. 2017).
The matRad toolkit was used to define an axis of each treatment pencil beam, also known as "*rays"*. From the treatment of the patient tumor, 736 treatment rays were extracted from all treatment pencil beams. The matRad toolkit was then adapted to retrieve cumulative WET_{cum} for each of the treatment rays. This cumulative $WET_{cum(z)}$ along a treatment ray was defined as the cumulative sum until the depth *z* of the *WET* of all voxels that were crossed by the treatment ray. A schematic representation of such a cumulative *WET* can be found in Figure 3.31.

$$WET_{cum}(z) = \sum_{voxel \in ray}^{z} WET(voxel) \quad \text{(Eq.3.35)}$$

For each ray, the cumulative WET_{cum} along the depth was then computed in MatRad and processed into a 3D-WET_{cum} voxel map as shown in Figure 3.32. The 3D-WET_{cum} voxel map was then used to retrieve the expected stopping position Z_{EXP} of carbon ions in the patient.
The expected stopping position Z_{EXP} of a pencil beam was defined as the depth at which the cumulative WET_{cum} along the corresponding treatment ray was equal to:

$$WET_{cum}(Z_{EXP}) = R_{water}(E) - WET_{beam\ line} - WET_{ripple filter} \quad \text{(Eq.3.36)}$$

with R_{water} the range of the pencil beam, with $WET_{beam\ line} = 1.47$ which includes the BAMS + vacuum foil[3] and with $WET_{ripple\ filter} = (0.3 + 2.7 / 2) \times RSP_{PMMA}$.

Figure 3.33 shows an example of the expected stopping positions of the pencil beams used to treat the monitored patient for a single beam energy of 192.13 MeV/u (IES20) to demonstrate the spread of the Z_{EXP} within one single IES.

[3] Dr. Bons personal communication, HIT, 2017

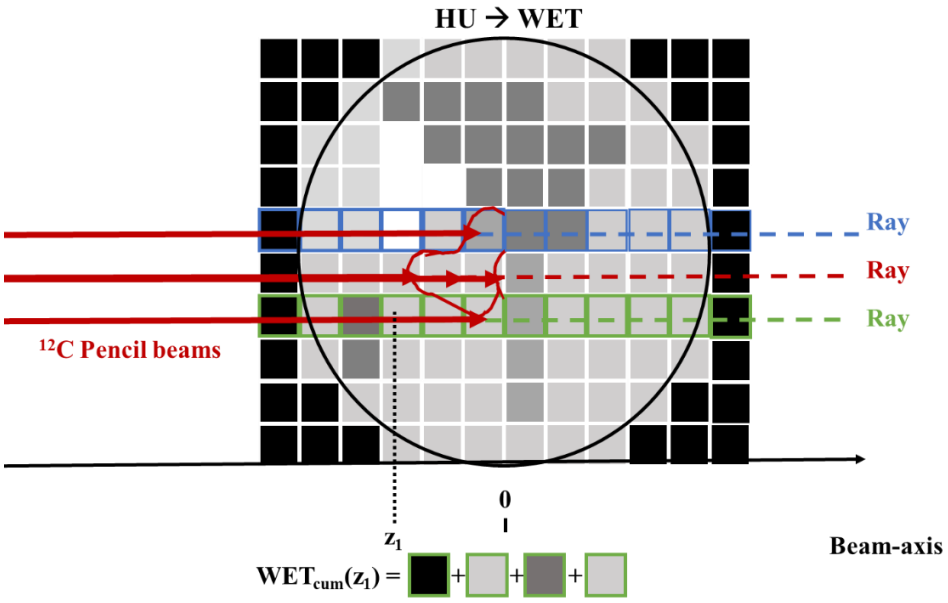

Figure 3.31: Schematic representation of carbon ion treatment rays and the determination of the cumulative WET. For each CT voxel of the irradiated volume, the HU is converted into WETs and is represented here on a grayscale. For each treatment pencil beam axis, a ray is defined as represented by the red, blue, and green dashed lines. For example, the cumulative $WET_{cum}(z)$ of the green ray is defined as the sum of the voxel WETs crossed by the ray until the depth z.

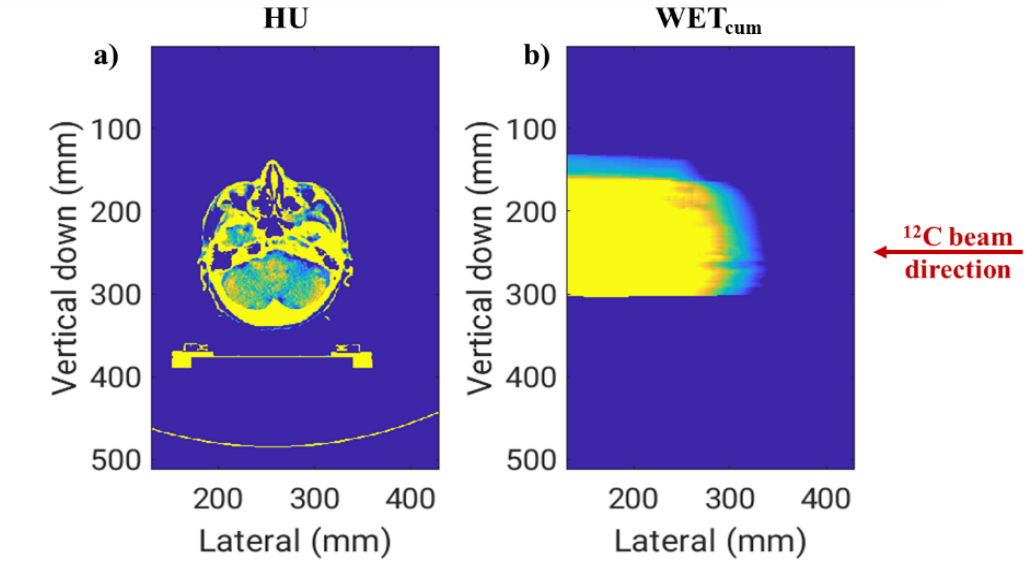

Figure 3.32: An example of a transverse view of the monitored patient's CT image in terms of Hus. a) Voxel CT HU and the corresponding extracted cumulative WET_{cum} map plotted (b) for all treatment rays used during the patient irradiation.

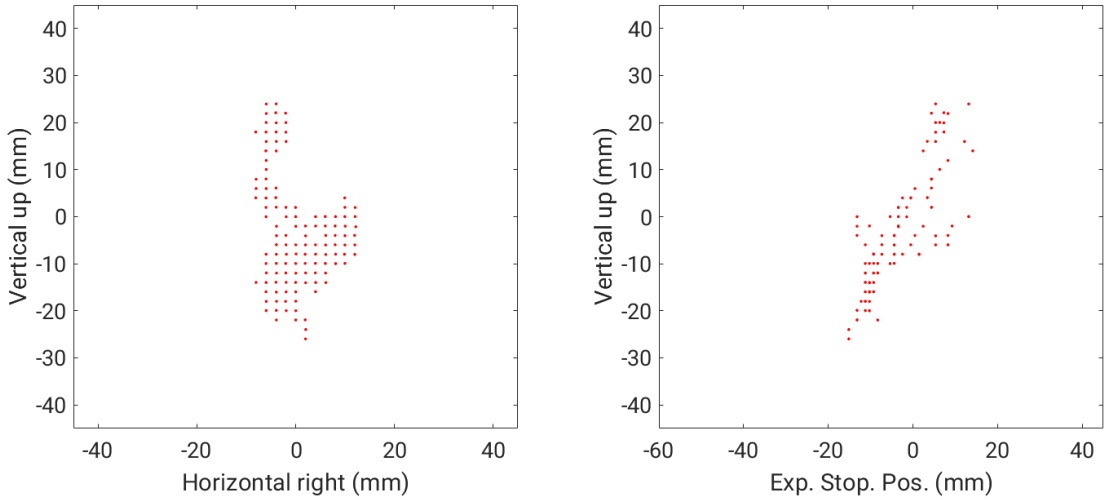

Figure 3.33: Lateral pencil beam positions (left) and their expected stopping positions along the beam axis (right) for the IES20 only. Each red point represents a pencil beam of the monitored patient treatment irradiation with an energy of 192.13 MeV/u. The expected stopping positions along the beam axis of the pencil beams of the IES20 range from -15.14 mm to +14.16 mm, and thus spread over a depth of more than 29 mm.

As seen in Figure 3.34, four longitudinal (Z_{EXP}) regions could be defined to cover the longitudinal dimension of the 73.85-cm^3-patient-tumor centered on $Z = 0$ to assess the stopping beam positions. Each carbon ion pencil beam used during the treatment plan irradiation was assigned to one of the four defined (Z_{EXP}) regions depending on its stopping position along the beam axis. As the measured secondary ion tracks were resolved on a single pencil-beam-basis, each measured secondary-ion track could be assigned to one of the four defined longitudinal (Z_{EXP}) regions depending on the pencil beam they came from.

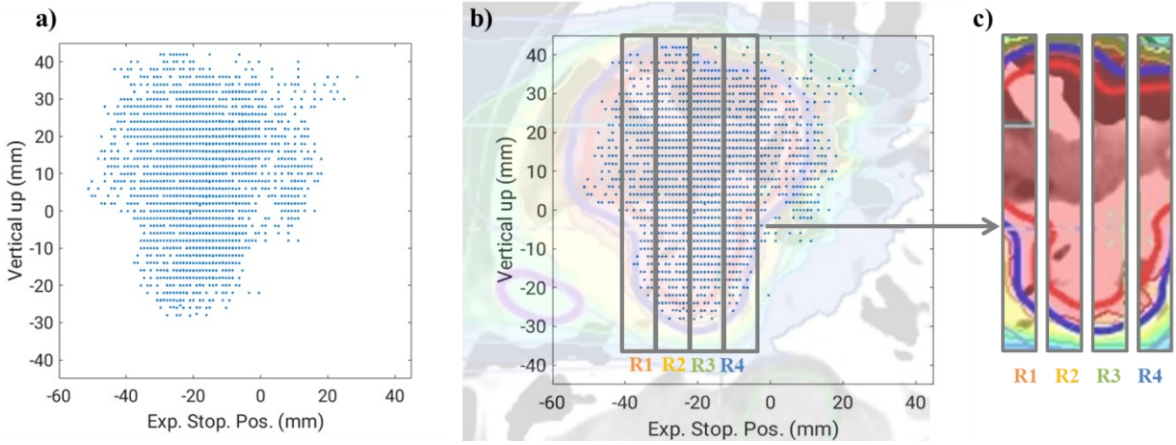

Figure 3.34: a) expected stopping positions of all pencil beams from the patient measurement (right). Each blue point represents a pencil beam from the monitored patient treatment irradiation. b)-c) show the four defined longitudinal regions in the expected stopping positions of the pencil beam overlaid with the patient treatment plan.

3.7.3. Multi-feature analysis

From each tracked secondary ion, several features can be extracted, such as the track origin depth Z, as defined in (§3.5.4.), the cluster size S_C, as defined in (Eq.3.8), and deposited energy dE/dl, as defined in (Eq.3.13).

These features were analyzed in a so-called *multi-feature analysis* to investigate which of the specific ion features convey any valuable information regarding the internal anatomy of the irradiated head model. In case a better variable than the track origin depth is found, the entire single-feature analysis in terms of that variable can be done exactly in the same way as with the track origin depth, see (§3.7.1.).

The performed analysis has been based on Fisher's combined probability test (Fisher 1936), where a new *compound variable* (X) was defined as a linear combination of several measured features (f_1, f_2, f_3, and f_4) allowing for two measured data sets to be best separated from each other. Figure 3.35 shows the new compound variable X as first defined in (Fisher 1936) for a distinction of two types of plants.

In this thesis, the multi-feature analysis was performed to first optimize the comparison and separation of each fraction data set from a reference data set. This means, for example, that for five fractions compared to a reference fraction, five equations will be found for X.

In this thesis, the main feature composing the variable X was the secondary-ion origin depth feature Z, as defined in (§3.5.4.). One or two additional normalized features, such as deposited energy dE/dl or cluster size S_C, were then linked to Z in the new compound variable X using a linear combination from one of the following equations:

$$X = 1.Z + a.\frac{dE}{dl} + b.Size \qquad \text{(Eq.3.37)}$$

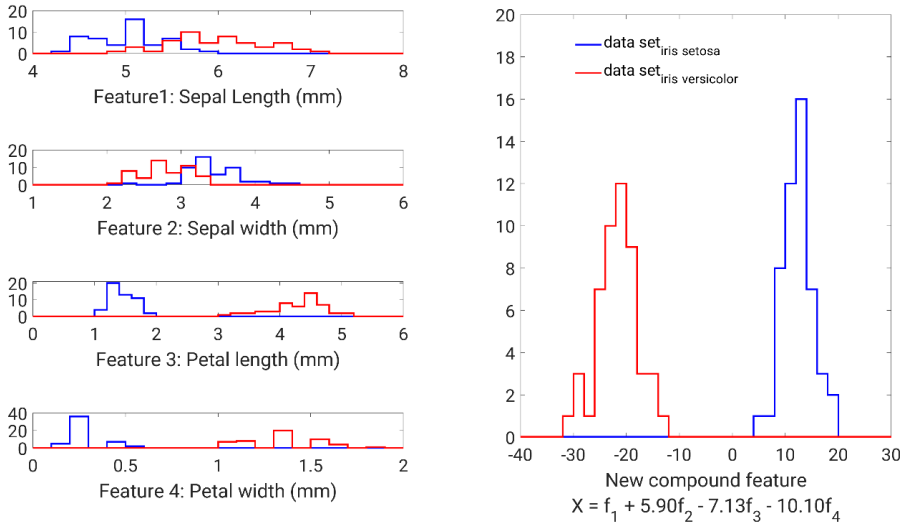

Figure 3.35: New compound variable X as a linear combination of four actual measured features, f: the sepal length, sepal width, petal length, and petal width, measured for two specific plant data sets: iris Setosa and isis Versicolor. The new compound variable X was seen to separate the two data sets better than the four input features separately.

These equations, and their *a* and *b* coefficients, can either be fixed and set as general equations identically applied to all measured data sets or they can be optimized for each specific data sets one wishes to compare.

To have an easier overview of the weighting of each feature, the different measured track features (such as secondary-ion origin position *Z* [mm], deposited energy dE_1/dl [MeV/mm], or cluster size *S* [pixel]) were normalized to the same unit, via data shift and scaling. Each measured feature f_i was thus normalized, to the secondary-ion origin position *Z* unit [mm] using:

$$f_{i_{NORMALIZED}} = \left(\frac{f_i - \mu_{f_i}}{\sigma_{f_i}}\right) \times \sigma_Z + \mu_Z \qquad \text{(Eq. 3.38)}$$

with μ_Z and μ_{fi} as the means and σ_{fi} and σ_Z as the standard deviations of the feature f_i and the feature *Z* measured respectively from a specific data set. Figure 3.36 shows how the behavior of the distribution of the deposited energy dE_1/dl of a measured data set is normalized using the secondary-ion emission profile (*Z*) as a reference.

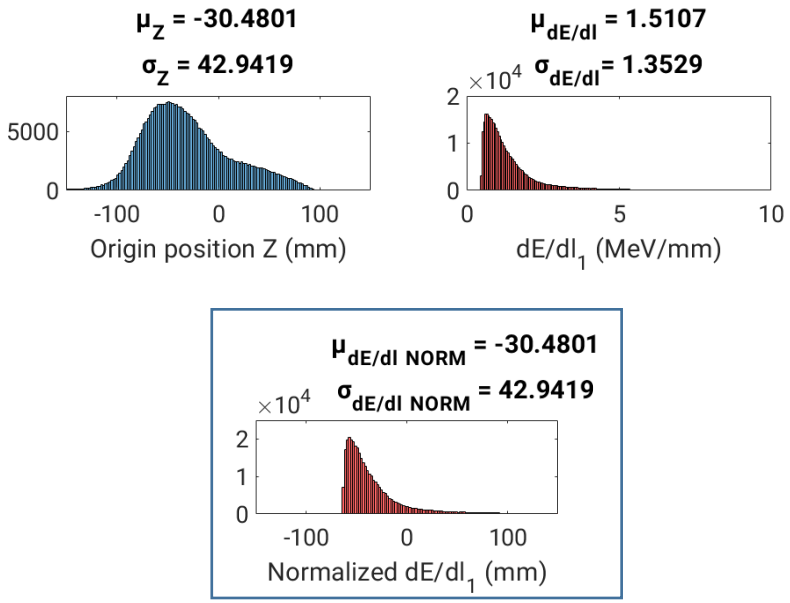

Figure 3.36: Measured secondary-ion emission profile (Z) (top left) and measured deposited energy (dE_1/dl) distribution (top right). Normalized deposited energy dE_1/dl distribution using the secondary-ion origin (*Z*) as a reference is plotted on the bottom.

4. Results

In this chapter, the thesis results are separated into five main research topics. A small summary is given for each topic separately.

(1) An investigation of the algorithms for the projected track origin analysis and their sensitivity to the actual secondary-ion origin is studied in section (§4.1.).

(2) In section (§4.2.), the capability of the developed monitoring method to detect and/or localize changes of the internal structure of the irradiated head model, mimicking inter-fractional changes, during carbon-ion radiotherapy is investigated. A so-called "single feature analysis" is employed to detect changes of different shapes, including both surface and internal changes, of different sizes and positions in the head model along the beam axis. The performance of the monitoring method is evaluated for each of the investigated types of change.

(3) In section (§4.3.), the optimal detection angle is analyzed. A compromise between good detectability and good localization of the change is studied as a function of the mini-tracker position.

(4) The potential of improvement of the method is investigated by exploiting additional secondary-ion track parameter information (e.g. deposited energy or cluster size) in section (§4.4.).

(5) The results chapter concludes with a detailed description and findings of the first clinical implementation of the developed monitoring method (§4.5.).

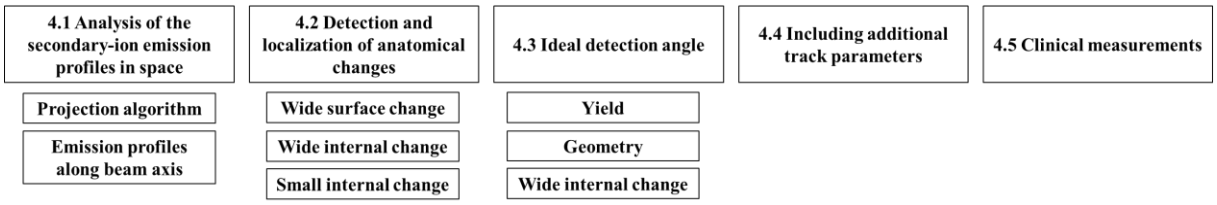

Figure 4.1: Global overview of the five topics presented in the results section of this thesis.

4.1. Analysis of the secondary-ion emission profile in space

Figure 4.2: Current topic within the five topics presented in the results section of this thesis.

This section contains results concerning the performance of the three studied track-projection algorithms in terms of detection of internal structure changes of the head model, as illustrated in Figure 4.2. This study was performed with measured experimental data. Furthermore, an MC study for investigation of the correlation of the measured track parameters and the actual origin of the secondary ion in the head model was performed.

4.1.1. Comparison of track-projection algorithms

The measured, or simulated, secondary-ion tracks can be processed with different algorithms to detect geometrical changes in the irradiated object. Here three different methods of the track-projection to the head-model volume were investigated: 2D, 2D+ and 3D+ projections, as described in section (§3.5.4.) of Materials and Methods. In this analysis, the precision of the measurement of the nuclear fragmentation point for all track-projection methods was compared for different mini-tracker positions. To do so, MC simulations mimicking the measured pre-clinical experimental setups were used to obtain the actual primary ion fragmentation point.

The measurements were performed on the homogeneous head model, see (§3.3.1.1.) of Materials and Methods. During the irradiation, secondary ions leaving the head model were measured with a mini-tracker placed at different distances d away from the tumor center and at different detection angles α with respect to the beam axis. Corresponding MC simulations (Schlechter 2021) of the setup were made with the FLUKA code as described in section (§3.4.) of Materials and Methods.

In Figure 4.3-a), the measured secondary-ion emission profiles along the beam axis, as acquired at a distance $d = 120$ mm and $\alpha = 30$ °, are plotted for each of the three track-projection methods. The corresponding simulated profiles, including the actual secondary-ion origin (fragmentation point) emission profile, are plotted in Figure 4.3-b). Comparison between true fragmentation origins and projected origins for the MC simulation is plotted in Figure 4.3-c).

The MC simulation shows that the detected secondary and tertiary-ion tracks come from a primary fragmentation that mostly happens at the entrance of the head model, around a depth of -80 mm along the beam axis (black profile in Figure 4.3-b). The experimental data and the MC simulation mimicking the experimental data show similar trends in their secondary-ion emission profiles. In both the measured and simulated emission profiles in Figure 4.3-a)-b), the two new time-dependent track-projection methods (2D+ and 3D+) better confine the measured secondary-ion production sites to the head-model volume compared to the 2D method. This is confirmed by Figure 4.3-c), and is especially visible at the entrance of the head model, where

most of the secondary ions come from. Additionally, in Figure 4.3-a)-b), the 3D+ track-projection method even better confines the measured secondary-ion production sites to the head-model volume compared to the 2D+ track-projection method as a minor shift toward the upstream direction is also visible in the 2D+ profile with respect to the 3D+ profile. This advantage of the 3D+ track-projection method over the 2D+ one is however of less importance compared to the advantage of both time-dependent track-projection methods (2D+ and 3D+) over the 2D one.

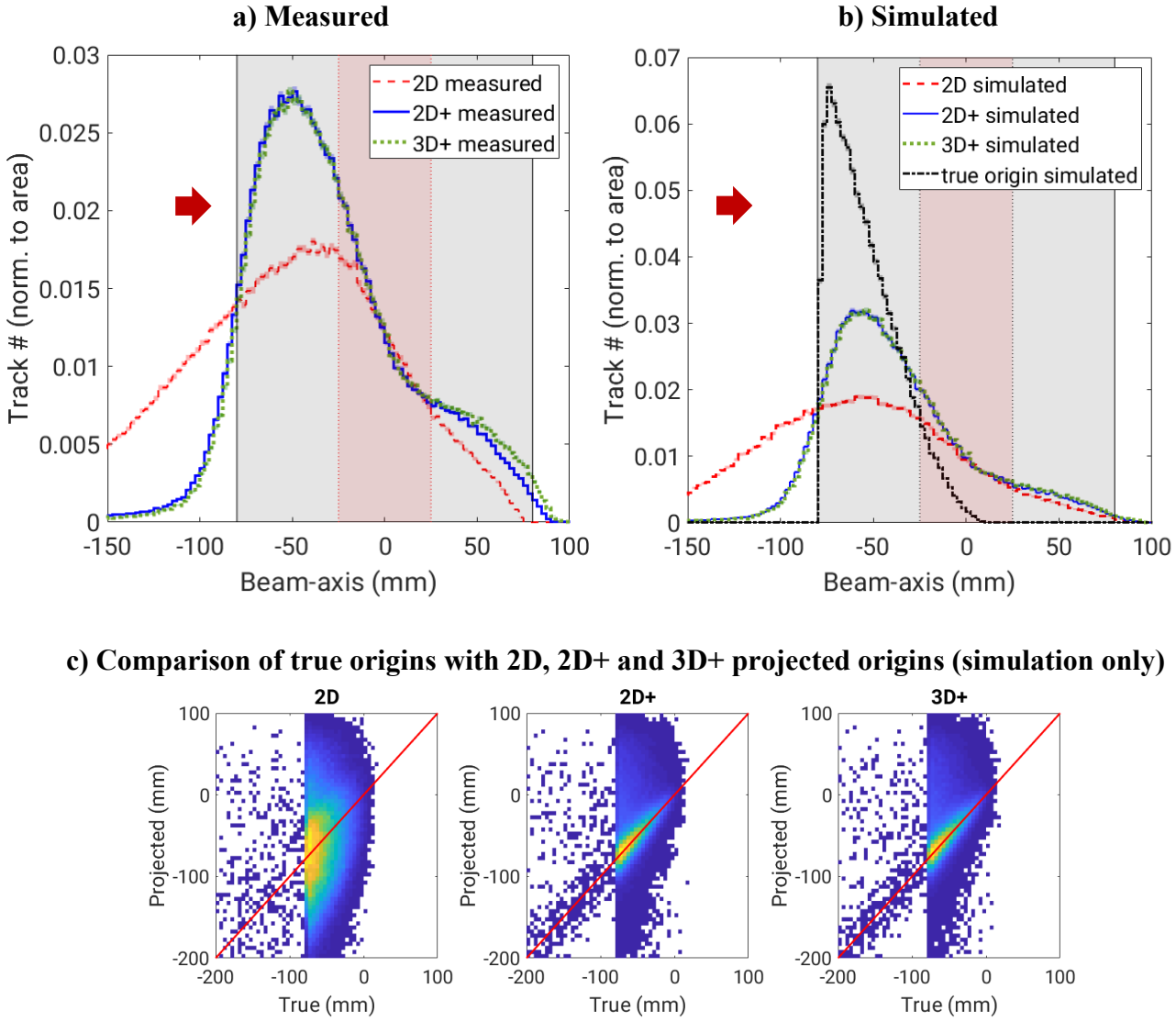

Figure 4.3: Secondary-ion emission profiles along the beam axis retrieved using 3 different projection methods as measured (a) and MC simulated (b-c) for a mini-tracker position at d = 120 mm from the tumor center and α = 30° from the beam axis. Corresponding statistical uncertainties are plotted as error bands. The 80-mm-radius PMMA cylinder volume is centered at 0 mm and represented in a) and b) by the grey area within the two vertical black lines, the 25-mm-radius tumor volume by dotted the red area within the two vertical dotted red lines. The beam enters the head model from left to right, see red arrow in a) and b).

The mean of the absolute track-by-track distance between the true primary-ion fragmentation positions and the projected secondary-ion track origins along the depth was calculated for each track-projection method in the MC simulation. These values were compared for a mini-tracker placed at the same distance to the tumor center (d = 120 mm) but at different detection angles α (10°, 20°, 30°, 40°, 50°) with respect to the beam axis. These means of the absolute track-by-track differences are plotted for each track-projection method in Figure 4.4. As shown in a previous study (Abbani 2020) at lower detector-positioning angles with respect to the beam axis, the MC simulation data contains a non-negligible fraction of the secondary ions that originate from within the beam nozzle. To discard these ions a constraint on the projected secondary-ion origin position along the beam axis (Z < - 400 mm) is applied when calculating the mean of the absolute differences (see dashed lines in Figure 4.4).
In Figure 4.4, the mean of the absolute track-by-track distance shows that both time-dependent track-projection methods, 2D+ and 3D+, better approximate the true secondary-ion track origin positions along the depth than the previously used 2D method. This is valid for all mini-tracker positions. The 3D+ projection method appears to perform even slightly better than the 2D+ one at lower detection angles. At 10°, improvements by a factor of 4 between 2D vs 2D+, and by a factor of 2.4 between 2D+ vs 3D+ can be observed. The rest of this thesis data analysis will, thus, only be performed with the time-dependent 3D+ track-projection algorithm.

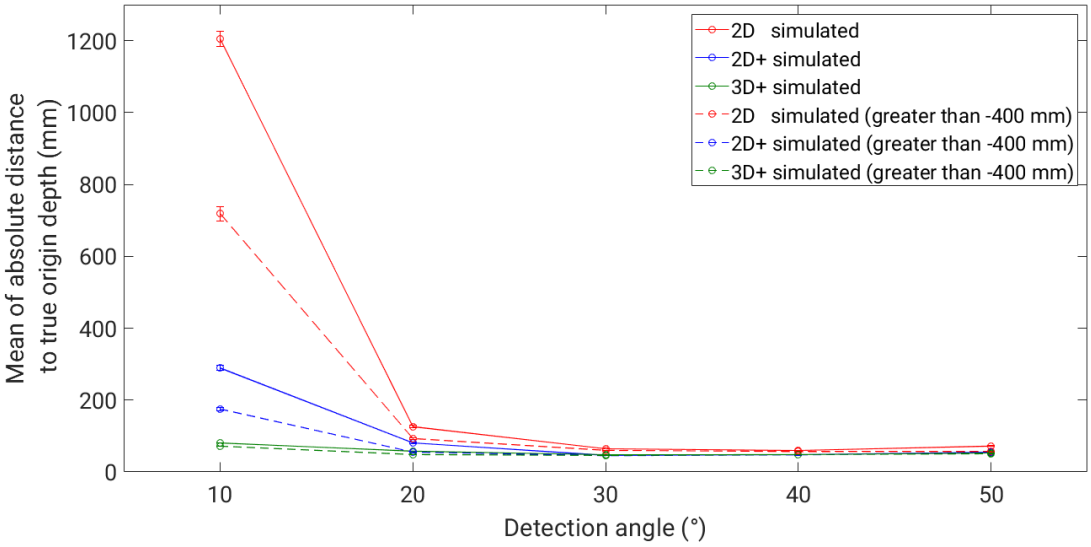

Figure 4.4: Mean of the absolute track-by-track distance for several detection angles α (°), between true and back-projected origin along the beam axis for the three investigated track-projection methods (2D, 2D+ and 3D+). Standard deviations of the mean distances are plotted as error bars. Solid lines contain all projected secondary-ion origin positions, dashed lines only contain projected secondary-ion origin positions with a position Z > -400 mm.

4.1.2. Global secondary-ion emission profiles along the beam axis

Subsequently, the profiles of the secondary-ion track origin positions along the beam axis were extracted using the 3D+ track-projection algorithm for all pre-clinical measurements performed at the Heidelberg Ion Therapy Center (HIT). In this thesis, both homogeneous and anthropomorphic head models were irradiated with clinic-like treatment plans for a 25- or 30-mm-radius spherical tumor located in their center. In both head models, the profile the track origin positions along the beam axis, as defined in section (§3.5.4.) of Materials and Methods, of the secondary ions produced during this treatment irradiation could be retrieved from the data measured at $\alpha = 30°$ with respect to the beam axis and $d = 120$ mm from the tumor center, see Figure 4.5. In the studied cases, the complexity of the irradiated head model, homogeneous or heterogeneous environment, and the target size influence the secondary-ion emission profile, but not significantly.

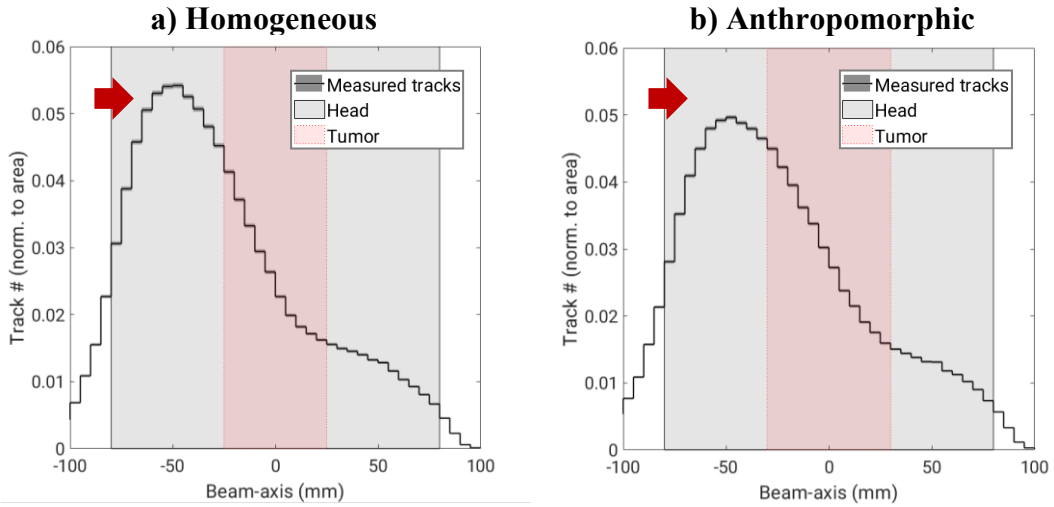

Figure 4.5: Secondary-ion emission profiles along the beam axis as measured at a detection angle of 30° with respect to the beam axis and 120 mm from the center of the homogeneous (a) and anthropomorphic (b) head models. Corresponding statistical uncertainties are plotted as error bands. The head-model volume is centered at 0 mm and represented by the grey area, the tumor volume by the red one. The beam enters the head from left to right as symbolized by the red arrow.

Subsequently, these measured emission profiles were separated into sub-profiles corresponding to the energies of the primary pencil beam, as shown in Figure 4.6 for all energy layers and in Figure 4.7 for two sets of two successive energy layers. For both treatment plans, the distance between the energy layers was 3 mm (WET). No profile could be retrieved for the lowest beam energy E1 (167.66MeV/u) of the homogeneous head-model treatment in Figure 4.7. This was due to its low amount of data, with only 8 secondary-ion tracks acquired for E1 from the homogeneous head-model treatment. As a comparison, 675 tracks were measured in E1 from the anthropomorphic head-model treatment.

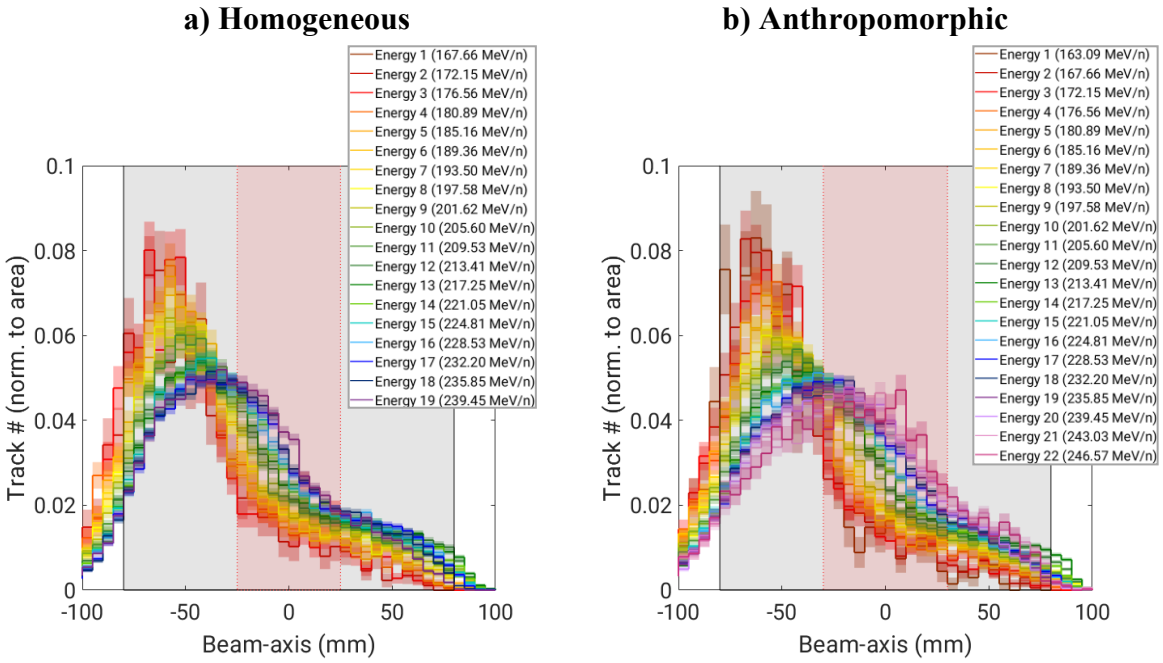

Figure 4.6: Secondary-ion origin distribution along the depth per therapeutic beam energy layers as measured at a detection angle of 30° with respect to the beam axis and 120 mm from the center of the homogeneous (a) and anthropomorphic (b) head models. The lowest beam energy E1 (167.66MeV/u) was not added to a), due to its low amount of data (only 8 secondary-ion tracks were acquired). As a comparison: 675 tracks were measured in E1 of b).

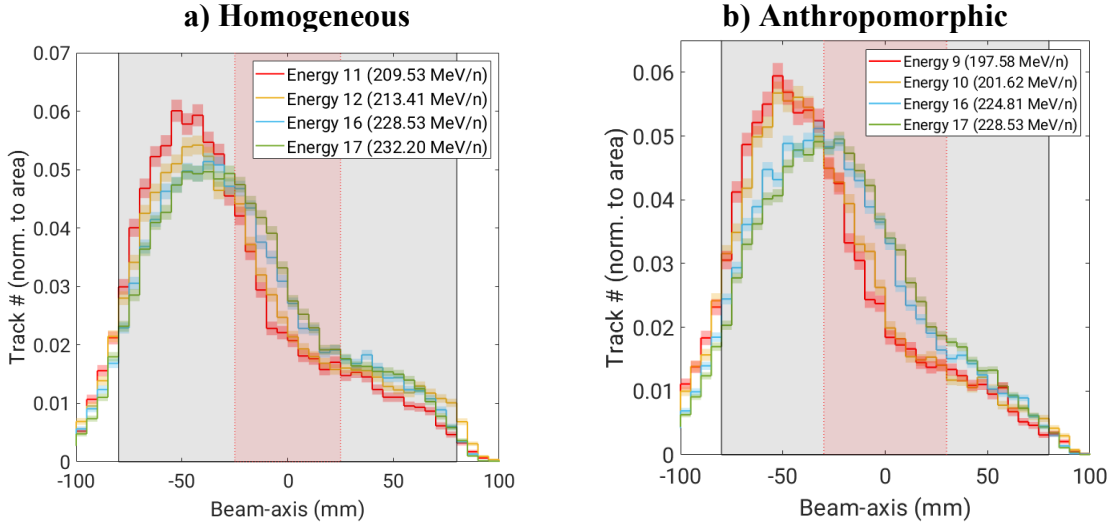

Figure 4.7: Secondary-ion emission profile along the depth per therapeutic beam energy layers as measured at a detection angle of 30° with respect to the beam axis and 120 mm from the center of the homogeneous (a) and anthropomorphic (b) head models.

4.1.3. Summary of the analysis of the secondary-ion emission profiles

In a first analysis, the precision of the different track-projection algorithms was compared for different mini-tracker positions using MC simulations mimicking simple pre-clinical measurement setups. It was found that the secondary-ion track origin positions along the depth are better approximated by the new time-dependent track-projection methods, 2D+ and 3D+, and especially by the 3D+ method for low mini-tracker detection angles.

Consequently, the profiles of the secondary-ion track origin positions along the beam axis were extracted using the 3D+ track-projection algorithm for all pre-clinical measurements performed at the HIT facility.

Additionally, measured emission profiles could be separated into sub-profiles corresponding to the energies of the primary pencil beam. It was possible for both homogeneous and anthropomorphic head models to visualize the variations in the secondary-ion emission profiles along the depth for each of the therapeutic beam energy layers used during the fraction irradiation. In both head models, low beam energies resulted in secondary ions whose emission profiles were closer to the entrance region of the head model. Larger beam energy layers resulted in secondary ions coming from deeper parts of the head model. This is clearly reflected in the plotted emission profiles.

4.2. Detection and localization of anatomical changes using secondary-ion emission profiles

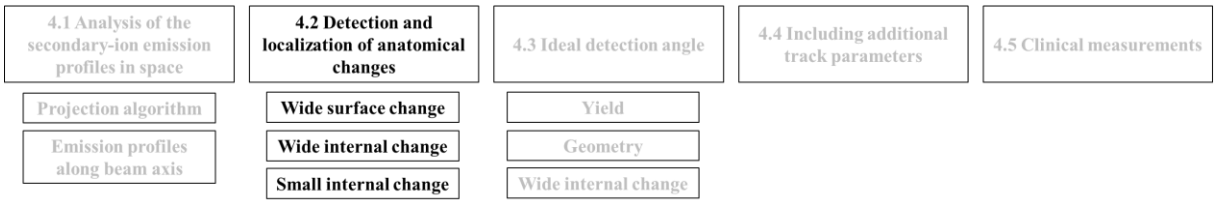

Figure 4.8: Current topic within the five topics presented in the results section of this thesis.

The overall goal of the monitoring method is to detect internal inter-fractional anatomical changes that might occur in the targeted head models in between two treatment irradiations. To this end, several clinical-like treatment irradiations of the head models with and without anatomical changes were performed, see Figure 4.8. Produced secondary ions were measured and their track distributions were compared for all irradiations, as explained in section (§3.7.1.) of Materials and Methods, to detect, quantify and localize inter-fractional changes inserted into the head models. Several changes in sizes and positions of the inter-fractional changes were investigated in this research, such as wide surface thickness (§4.2.1.), wide internal (§4.2.2.), and small internal changes (§4.2.3.).

4.2.1. Impact of wide surface changes

During radiotherapy, small inter-fractional changes at the surface of the head, corresponding to weight loss or gain, and superficial swellings, can occur. Secondary-ion tracks produced in each head model were measured first during reference fraction irradiations and compared later with tracks measured during subsequent follow-up fraction irradiations, see Figure 4.9. These follow-up fractions could either be homogeneous (head model without any surface change) or altered (head model with surface changes). To simulate such surface changes, wide (150 mm x150 mm) PMMA slabs with a thickness of +1, +2, or +3 mm (i.e. WET = +1.14, +2.19 or +3.25 mm) were positioned upstream of the irradiated homogeneous and anthropomorphic head models. Measurements were done with the mini-tracker positioned at a detection angle of 30° with respect to the beam axis and a distance of 120 mm from the tumor center.

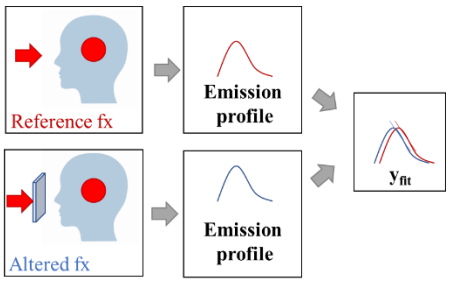

Figure 4.9: Analysis workflow for the wide surface thickness change. A comparison of the shape of the secondary-ion emission profiles measured for the reference and an altered fraction is performed. Altered fraction is measured with a small PMMA surface change placed in front of the anthropomorphic head model (light blue).

4.2.1.1 Variation of the shape of the secondary-ion emission profiles

A comparison of the secondary-ion emission profiles measured for the homogeneous (without any surface change) or the altered (with a surface change) fractions is detailed here. In particular, the impact of a +2-mm-thick surface change on the measured secondary-ion emission profile is shown for the homogeneous head model in Figure 4.10-a) and for the anthropomorphic one in Figure 4.10-b).

a) Homogeneous **b) Anthropomorphic**

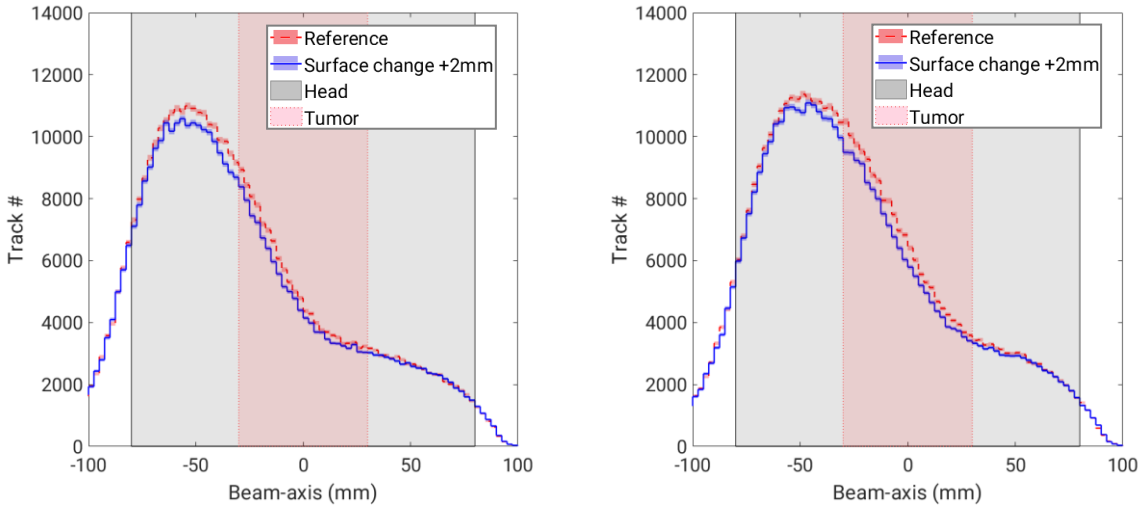

Figure 4.10: Secondary-ion emission profile along the beam axis as measured at a detection angle of 30° with respect to the beam axis and 120 mm from the tumor center for the homogeneous (a) and anthropomorphic (b) head models. The secondary-ion emission profile measured during reference fraction irradiation is plotted in red and the one measured during altered fraction irradiation (+2-mm-surface) in blue.

In both head models, the global shape of the measured secondary-ion emission profile was similar for the reference (red) and the altered fraction (blue). Both secondary-ion emission profiles – the reference one and the altered one – could be clearly differentiated considering the statistical uncertainties included in the plots. When there was a +2 mm surface change (blue), the distal falloff of the measured secondary-ion emission profile was shifted towards shallower depths and the number of measured secondary-ion tracks was reduced.

This can be explained by the fact that, when a surface change appears upstream of the head model, secondary ions are produced more upstream. Less secondary ions originated thus from deeper in the head models, leading to a shift of the distal falloff of the measured secondary-ion emission profile towards smaller depths. The inserted +2 mm surface change resulted in more material being traversed by the secondary ions. A smaller number of secondary ions could thus reach the mini-tracker and be detected, leading to a reduced number of measured secondary-ion tracks.

4.2.1.2 Quantification of the internal geometry changes based on the variations of the emission profiles

Similar to Gwosch *et a.l*, 2013 et Abbani, 2020, to quantify the impact of the inserted +1, +2, and +3mm surface changes in the measured profiles, linear fits were applied to the distal falloffs of the measured secondary-ion emission profile between 50 % and 90 % of their maximum, as detailed in section (§3.7.1.2.) of Materials and Methods. As an example, the linear fits to the distal falloffs of the measured secondary-ion emission profiles for the un-altered and the +2-mm-thick surface change are shown for the homogeneous head model in Figure 4.11-a) and for the anthropomorphic model in Figure 4.11-b).

a) Homogeneous **b) Anthropomorphic**

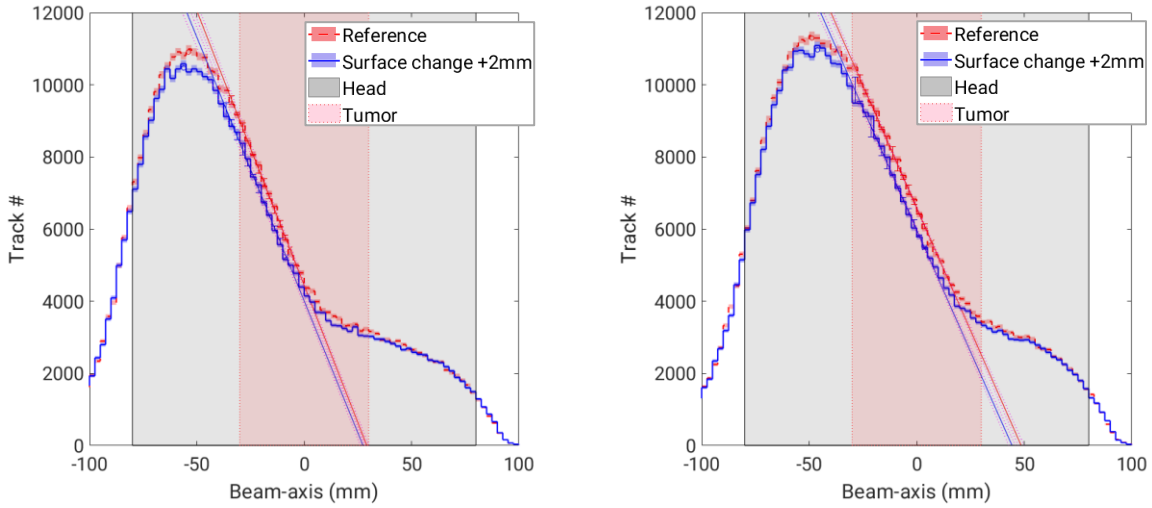

Figure 4.11: Linear fits performed to the secondary-ion emission profile as measured at a detection angle of 30° with respect to the beam axis and 120 mm from the tumor center for the (a) homogeneous and (b) anthropomorphic head models. The profiles measured during the reference fraction are plotted in red and for the altered fraction in blue. The straight lines represent the linear fit to the distal falloff of the profiles between 50 % and 90 % of their maximum. The dashed red and blue lines represent the uncertainties of the linear fits as defined in (Eq.3.20). In a) $y_{\text{fit-homo-REF}}$ = -152.1(± 4.1) x + 4442 ± 93 and $y_{\text{fit-homo-ALTERED}}$ = -146.2 (± 4.9) x + 4009 (± 124). In b) $y_{\text{fit-anthro-REF}}$ = -135.6 (± 3.6) x + 6589 ± 53 and $y_{\text{fit- anthro -ALTERED}}$ = -135.8 (± 4.4) x + 5976 (± 71)

The results of the linear fits (as defined by (Eq.3.18) $y_{fit} = a.x + b$, with x *being* the origin depth) have shown variations depending on the inserted surface changes thickness (+1, +2, and +3mm). As shown in Figure 4.12, for both head models, the found slopes a of the linear fits are constant (within its error bands) for each of the measured fractions and the surface changes. The shape of the secondary-ion emission profiles thus did not vary significantly between the reference fractions and the altered fraction. However, the ordinates to origin b are found to vary with the inserted surface change thickness. The ordinate to origin b is thus strongly correlated with the thickness of the change.

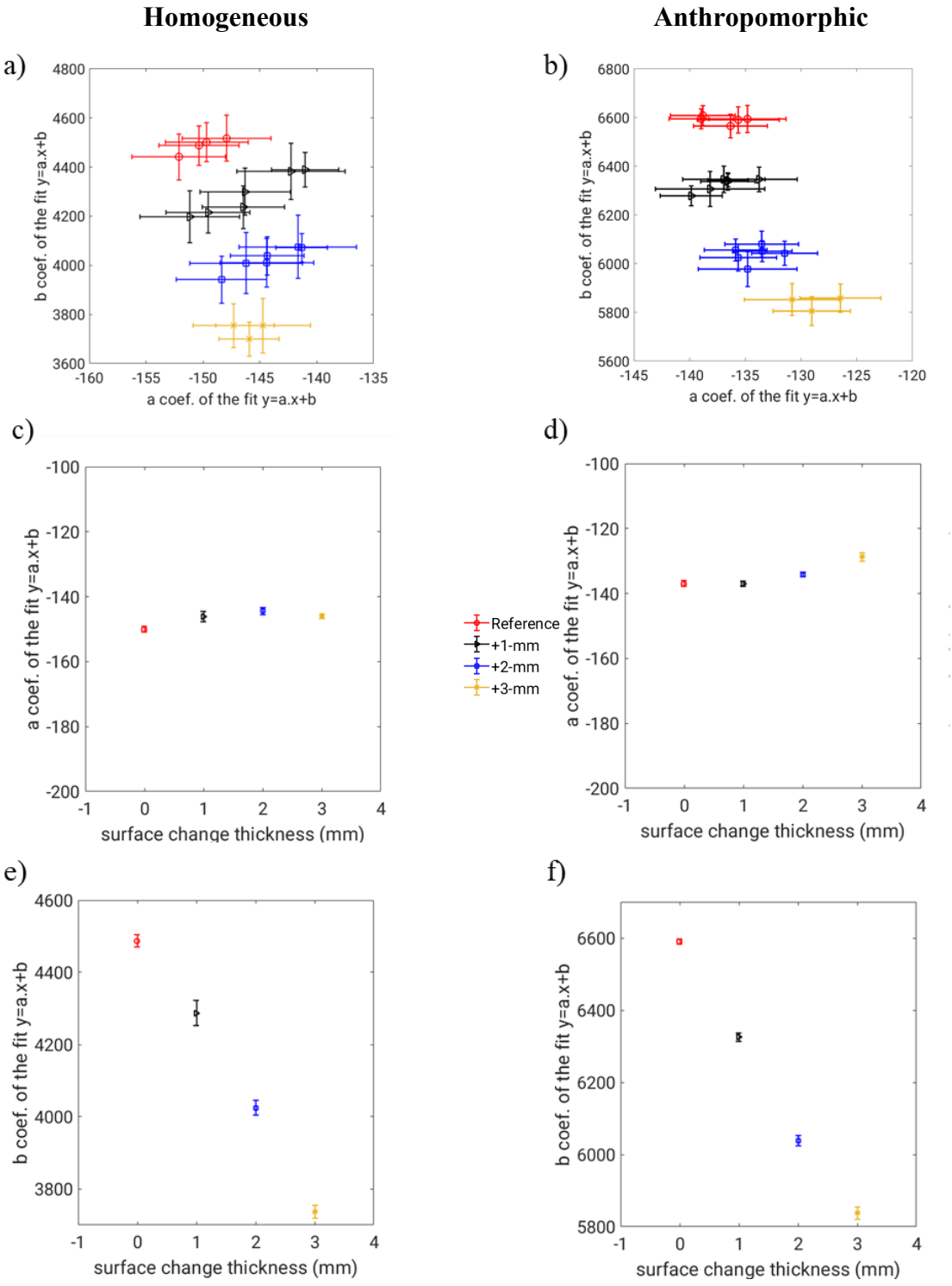

Figure 4.12: Plots of the a and b coefficients of the linear fit of the profile's distal falloff as measured at a detection angle of 30° with respect to the beam axis and 120 mm from the tumor center for the homogeneous (left) and anthropomorphic (right) head model. a-b) Each point represents a treatment fraction irradiation. Error bars represent σ_a and σ_b uncertainties of the linear fits. c-d-e-f) Plots of the mean a and mean b coefficients for each measured fraction (reference, +1, +2, or +3mm). Error bars are $\sigma/\sqrt{N}$ with N the total number of measured irradiations for each clinical-like treatment fraction.

4.2.2. Impact of wide internal changes

To simulate wide internal inter-fractional anatomical changes, wide 2-mm-thick air cavities (80 mm x 80 mm x 2 mm air slab) were positioned inside the irradiated homogeneous head model at different depths upstream and inside of the tumor volume. In the anthropomorphic head model, no such internal changes were possible. As depicted in Figure 4.13, four air cavity positions were investigated, corresponding to the front, the entrance, the middle, and the distal end of the tumor volume, i.e. centered on the four following depths respectively: [-40; -39 mm], [-22; -21 mm], [0;+1 mm] and [+18; +19 mm] along the beam axis. Here, 0 mm is set to be the room isocenter position along the beam axis, located in the middle of the head model and of the tumor volume. Negative depths are upstream of this isocenter.

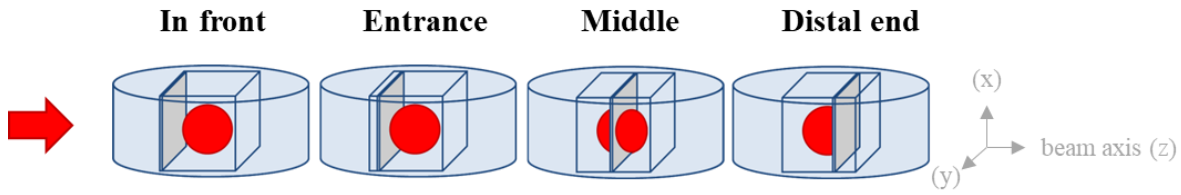

Figure 4.13: The four investigated 2-mm-thick air cavity positions in the homogeneous head model (light blue) corresponding to the front, the entrance, the middle, and the distal end of the tumor volume. This volume is represented here by the red sphere with a 25-mm-radius.

Secondary ions produced in the homogeneous head model were measured for several types of fraction irradiations by the mini-tracker positioned at a detection angle of 30° with respect to the beam axis and 120 mm from the tumor center. First, a reference fraction irradiation was measured. Then, five follow-up fractions were acquired: one homogeneous follow-up fraction (without internal change) and four heterogeneous follow-up fractions (measured with the 2-mm-thick air cavity placed at the four previously described investigated depths). As detailed in Figure 4.14, the reference fraction is compared to the follow-up fractions with and without internal changes. For this analysis, the data of 8 repetitions were summed up for each fraction. This is performed to mimic having a system of 8 mini-trackers, similar to a setup that will be used in the near future for a clinical trial with a larger patient cohort.

4.2.2.1 Variation on the shape of the secondary-ion emission profiles

The impact on the measured secondary-ion emission profile of 2-mm-thick internal air cavities positioned in front and the middle of the tumor volume in the homogeneous head model is shown in Figure 4.15-a)-b). There, the secondary-ion emission profile measured during the reference fraction irradiation (without any air cavity) is plotted in dashed black against one homogeneous fraction irradiation plotted in red (without any air cavity) and one heterogeneous fraction irradiation (with an air cavity) plotted either in green in Figure 4.15-a), or in blue in Figure 4.15-b).

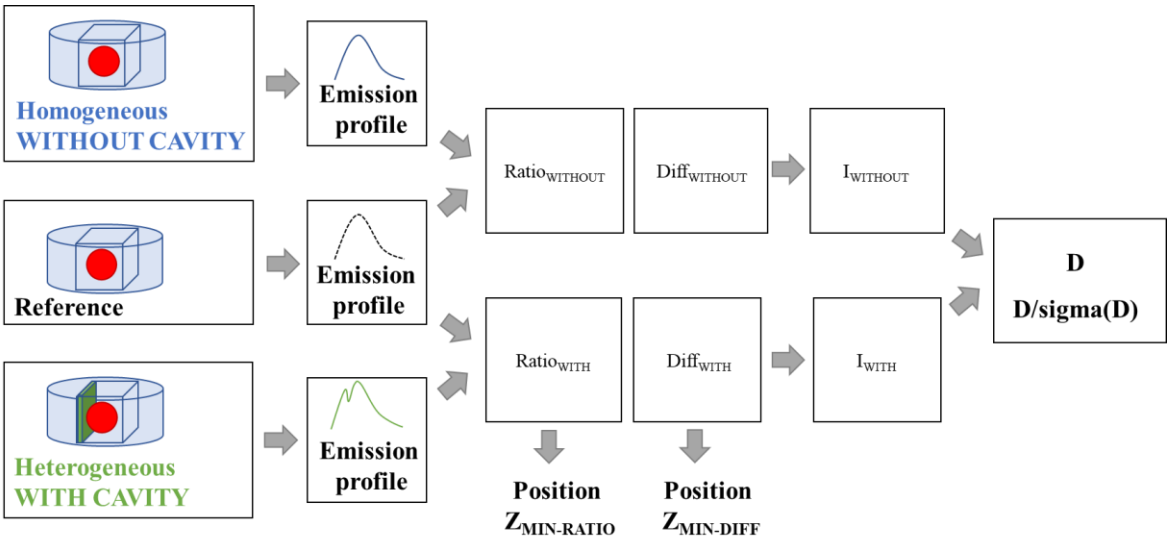

Figure 4.14 Analysis workflow for the detection and localization of a 2-mm-thick internal change. A comparison of the secondary-ion emission profiles measured for the reference fraction and a fraction without any change is performed parallelly to a comparison of the secondary-ion emission profiles measured for the reference fraction and a fraction with the change.

a) Cavity in front of tumor **b) Cavity in the middle of the tumor**

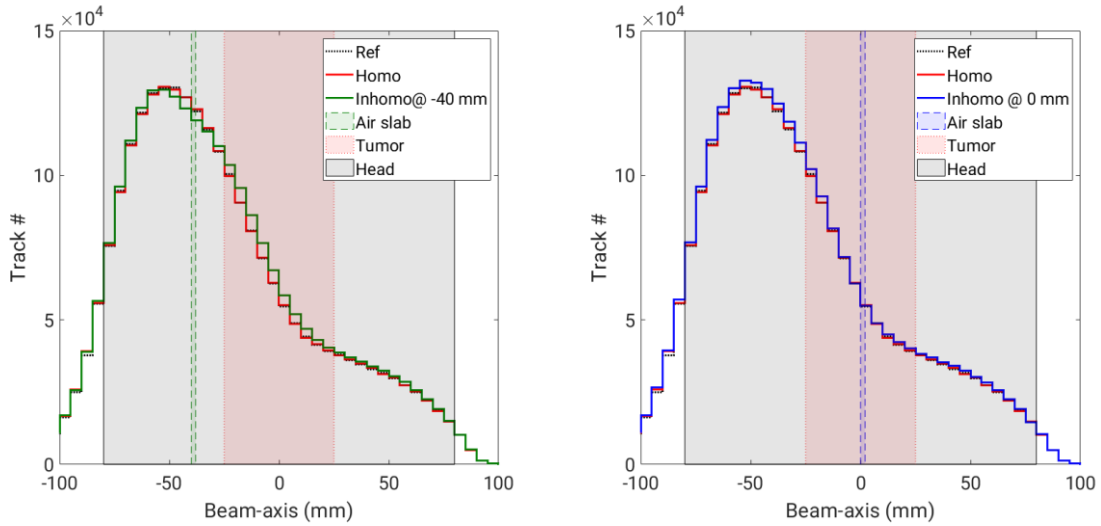

Figure 4.15: Secondary-ion emission profiles along the beam axis as measured at a detection angle of 30° with respect to the beam axis and 120 mm from the tumor center with an air cavity in front of (a) or the middle of (b) the tumor volume in the homogeneous head model. The head-model volume is centered at 0 mm along the beam axis and represented by the grey area, the tumor volume by the red one, and the inserted air cavity volume by the green or blue vertical bands. The beam enters the head model from left to right. Statistical uncertainties corresponding to an 8-fold sensitive mini-tracker area are plotted as barely visible error bands.

From Figure 4.15-a)-b), the secondary-ion emission profiles measured during the heterogeneous fractions differ significantly from the profile of the reference (dotted black) or homogeneous fractions (red) as the variations between the two curves were larger than their error bands. These error bands represent the uncertainties (1σ) based on their count statistics as defined in (Eq.3.12).
For the heterogeneous fractions, i.e. containing a 2-mm-thick air cavity, one can observe three main variations on the shapes of the secondary-ion emission profiles:

- downstream from the air cavity, the distal falloff of the heterogeneous profile was shifted towards larger depths (1).
- a dip on the heterogeneous profile was visible at the depth of the air cavity (2).
- globally the heterogeneous profile was higher than the other homogeneous profile (3).

These three main variations on the shapes of the secondary-ion emission profiles can be explained by the following:

- as the low-density air cavity replaced PMMA material, downstream for the cavity the carbon ions appeared to have crossed less material, and their range reached deeper into the head model. More secondary ions, thus, originated from deeper in the head model, leading to a distal falloff of the heterogeneous profile downstream from the air cavity shifted towards bigger depths.
- due to the lower air density, fewer secondary ions are produced in air, thus fewer secondary ions originated locally from the depth that corresponds to the air cavity location. This resulted in a dip at the location of the cavity in the heterogeneous profile.
- when an internal air cavity appeared inside the head model, less material was needed to be crossed by the secondary ions that are created upstream of the air gap, thus more ions could reach the mini-tracker and be detected, resulting in an overall higher secondary-ion emission profile for the heterogeneous fraction.

The impact on the measured secondary-ion emission profile in the case of 2-mm-thick internal air cavities positioned at different depths in the homogeneous head model was analyzed quantitatively in terms of maximal signal reduction and absolute difference in the profile shapes. For this, both ratios and differences of the measured secondary-ion emission profile as defined in (Eq.3.21) and (Eq.3.25) between the reference and heterogeneous fractions were plotted in Figure 4.16-a-b). Here both the ratio and the difference are used together as they provide complementary information regarding the absolute and relative variations induced by the inserted internal changes.
From this figure, as expected, no significant variations were visible when comparing the ratio (Figure 4.16-a)) or difference (Figure 4.16-b)) between the measured secondary-ion emission profiles of the reference fraction (without air cavity) and the homogeneous fraction (also without air cavity), plotted in both plots in dashed red.
The impact of the inserted air cavities was clearly visible in both the ratios (Figure 4.16-a)) and the differences (Figure 4.16-b)) between the measured secondary-ion emission profiles of the reference fraction (without air cavity) and of the heterogeneous fractions (with air cavity at different depths), plotted in green, yellow, blue or purple for both subplots.

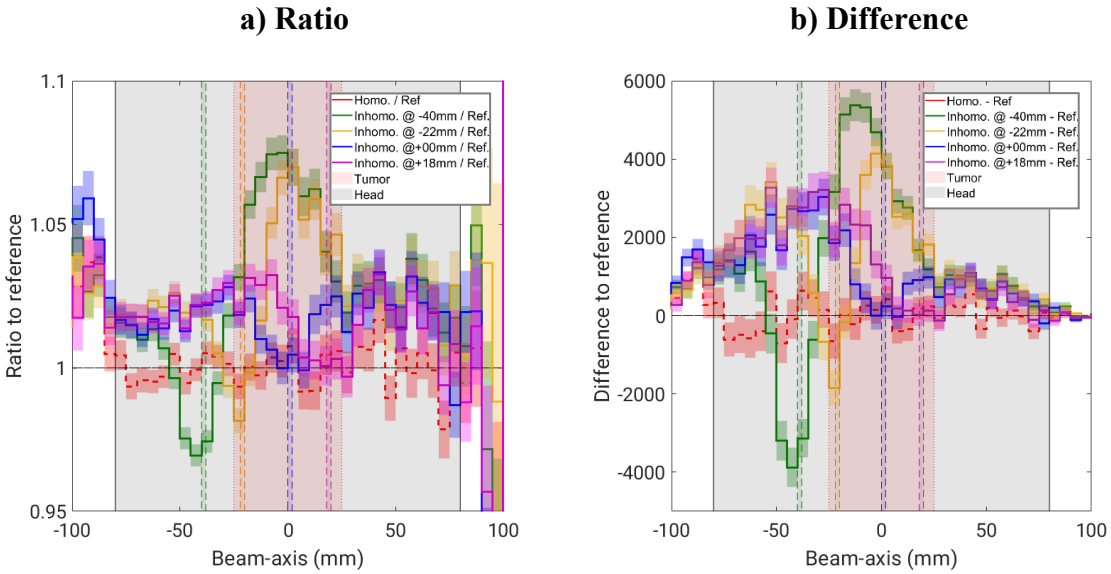

Figure 4.16: Ratios (a) and differences (b) between the measured secondary-ion emission profiles of the reference fractions versus the five follow-up fractions (with and without an air cavity). The ratio (or difference) of the reference and the homogeneous fractions is plotted in dashed red. The ratios (or differences) of the reference and the four heterogeneous fractions (with air cavity at four different depths) are plotted in green, yellow, blue, and purple, respectively. The head-model volume is centered at 0 mm along the beam axis and represented by the grey area, the tumor volume by the red one, and the inserted air cavity volume by the green or blue vertical bands. Statistical uncertainties corresponding to an 8-fold sensitive mini-tracker area are plotted as error bands.

The main three variations due to the inserted air cavity previously seen in the profile shape of Figure 4.15 (higher profile, with a dip, followed by a shift of the distal falloff towards bigger depths) can be associated here with three main variations in both the ratios and differences shapes of Figure 4.16-a)-b):

- downstream from the air cavity, an enhanced number of secondary ions in form of a peak was visible in both the ratio and difference plots (1)
- a significant dip was seen at the depth of the air cavity (2)
- the ratio and difference values were centered around higher values than 1 and zero respectively i.e. an increased in the total number of detected secondary ions (3)

The impact of the inserted air cavity was found to be visible in particular when the inserted air cavity was located upstream of the tumor, at a depth of -40 mm. For this air cavity position, a maximal signal reduction of 3.1 % ± 0.4 % is found. The maximal signal reduction is defined as the minimum value of the ratio profile along the head-model depth [-80 mm; 80 mm]. For the other three positions, the signal reduction was found to be 1.8 % ± 0.4 % when the cavity is placed at a depth of -22 mm, 0.1 % ± 0.5 % at 0 mm (isocenter) and 0.3 % ± 0.7 % at +18 mm.

4.2.2.2 Determination of the position of the change along the beam direction

A measurement of the position of the 2-mm-thick internal changes along the beam axis could be retrieved from both the ratios and differences of the measured secondary-ion emission profiles. This quantity is of interest for medical doctors to have an idea of whether the change is inside the tumor volume - which contains the highest RBE values -, or in front of it. As described in section (§3.7.1.3.) in Materials and Methods, two methods were used to approximate the air cavity position: the weighted average positions of the three minimal values induced by the air cavity in the profiles of the ratio ($Z_{MIN\text{-}RATIO}$) and of the difference ($Z_{MIN\text{-}DIFF}$). These weighted positions were computed for each investigated cavity position and are presented in Figure 4.17-a) and -b) respectively. In this figure both the positions of the $Z_{MIN\text{-}RATIO}$ (Figure 4.17-a)) and $Z_{MIN\text{-}DIFF}$ (Figure 4.17-b)) approximate the actual position of the inserted 2-mm-thick air cavity. The air cavity was found to be properly localized for all four investigated positions using the ratio and difference distributions as explained in (Eq.3.24) and (Eq.3.28) respectively. The accuracy of the localization is defined as the difference between the measured and the actual cavity position. Uncertainties on the localization of the cavity are estimated to be at maximum of the order of the bin size, i.e. 5 mm.

The accuracy ranges here:

- from 1.5 mm to 6.3 mm for the ratio analysis,
- from 2.3 mm to 5.3 mm for the difference analysis.

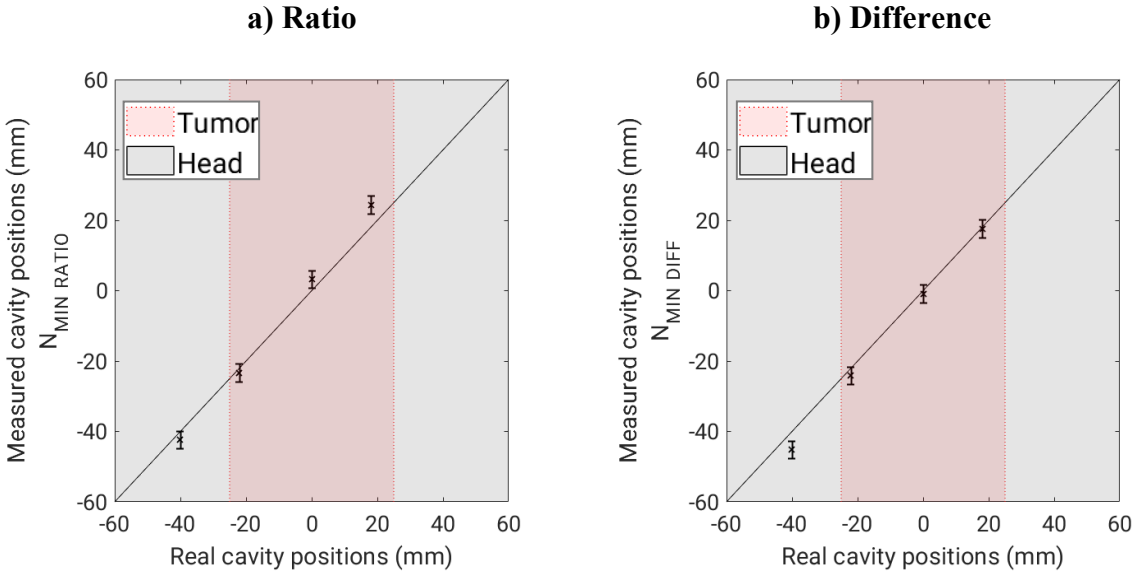

Figure 4.17: Measurement of the position of the 2-mm-thick internal changes along the beam axis for each investigated cavity position. The measured position is the weighted average position of the three minimal values induced by the air cavity in the (a) ratio and the (b) difference profiles. The error bars correspond to the statistical uncertainties on $Z_{MIN\text{-}RATIO}$ and $Z_{MIN\text{-}DIFF}$ which were estimated to be of at maximum the order of the bin size (5 mm).

4.2.2.3 Quantification of the significance of the detection

Besides the estimation of the 2-mm-thick air cavity position along the beam axis, a quantitative analysis of the detection significance of the cavity was performed. For this, as described in detail in section (§3.7.1.4.) of Materials and Methods, the integral of the absolute difference between the measured secondary-ion emission profile of a reference fraction versus follow-up fractions (with and without an air cavity) was calculated. The integrals I_{WITH} and $I_{WITHOUT}$ were determined along the entire head-model depth, i.e. from -80 mm to 80 mm, and are plotted in Figure 4.18. In red the integral value $I_{WITHOUT}$ between the reference fraction and the fraction without an air cavity is plotted. The remaining points represent the integral value I_{WITH} between the reference fraction and the fractions with an air cavity for all four investigated air cavity positions: in front (green cross), at the entrance (yellow square), in the middle (blue +), and at the distal end of the tumor (purple circle). In Figure 4.18, the integral values I_{WITH} decreased when the cavity was located deeper in the head model. Thus, the detection significance of an air-cavity decreases with increasing depth of the cavity position. For all investigated air-cavity positions, the integral value $I_{WITHOUT}$ of the absolute difference between the reference measurement and measurement without the cavity (red) was significantly lower than the integrals I_{WITH} of the absolute differences between the reference measurement and the measurements with the cavity (green, yellow, blue and purple) with respect to their error bars.

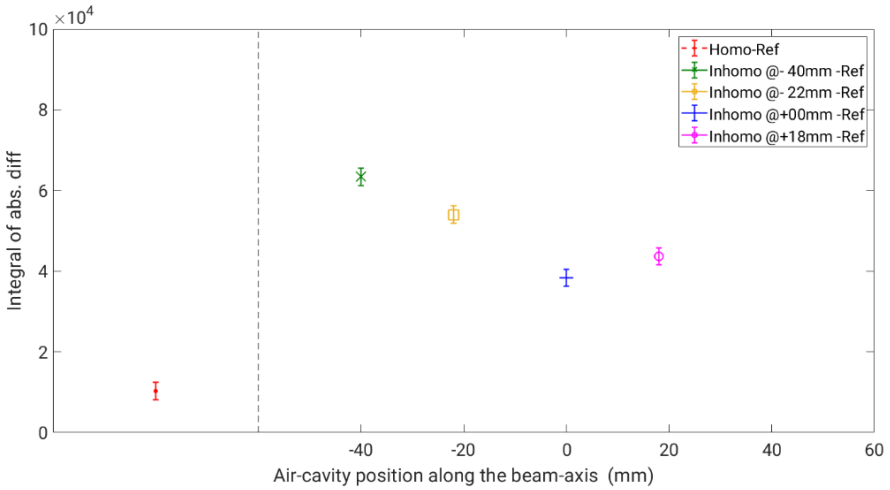

Figure 4.18: Values of the integral of the absolute difference between reference and homogeneous fractions (red) versus reference and heterogeneous fractions (green, yellow, blue, and purple). Statistical uncertainties corresponding to an 8-fold sensitive mini-tracker area are plotted as error bars.

The significance values, see D and $D/\sigma(D)$ from (Eq.3.31) and (Eq.3.33) in (§3.7.1.4.) of Materials and Methods were computed to quantitatively investigate how significant the difference in the integral values between measurement without (I_{WITH}) and with the air-cavity ($I_{WITHOUT}$) is. These *D-values* are plotted in Figure 4.19-a) and b). In this figure, D and $D/\sigma(D)$ values were found to be sufficiently large for all investigated air-cavity positions. This means that for all four air-cavity positions, the cavity was found to be detectable with a significance of at least 9 sigmas.

The detection significance was found to increase with decreasing depth of the cavity position and to reach a maximum detection significance at the entrance of the head model, where the cavity was found to be detectable with a significance of 17 sigmas.

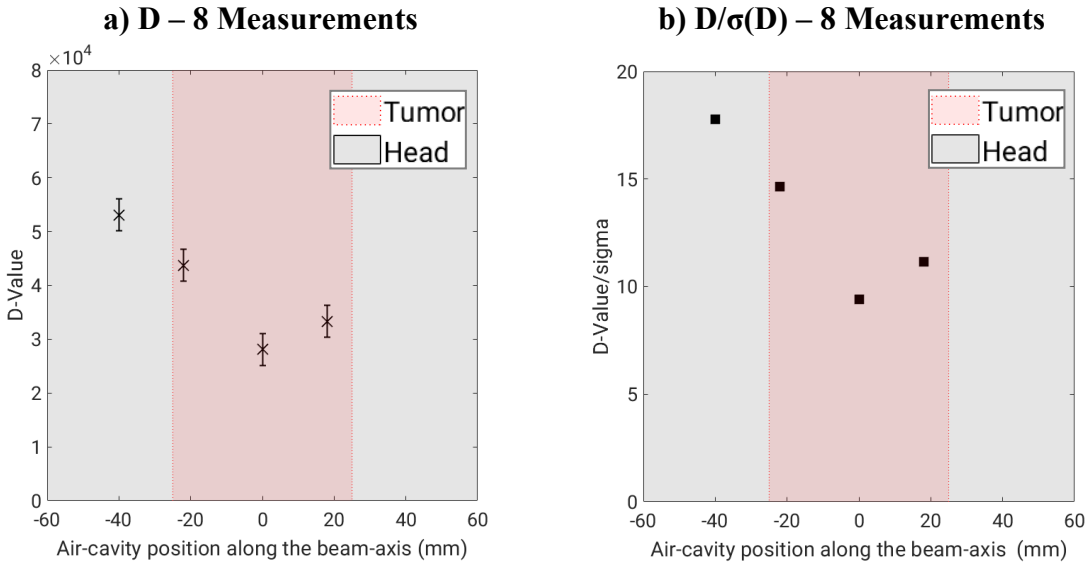

Figure 4.19: a) Detection significance $D = I_{WITH} - I_{WITHOUT}$, and b) detection significance divided by its uncertainties $D/\sigma(D)$ for all four investigated air-cavity-positions along the beam axis. The head-model volume is centered at 0 mm along the beam axis and represented by the grey area, the tumor volume by the red one. Statistical uncertainties corresponding to an 8-fold sensitive mini-tracker area are plotted as error bars.

4.2.2.4 Equivalent results with fewer statistics

So far, all presented results regarding the impact of a wide internal change were given for a statistic equivalent of having 8 mini-trackers, similar to a setup that will be used in the near future for a clinical trial with a larger patient cohort. Figure 4.20 shows the respective D and $D/\sigma(D)$ values computed for the data amount equivalent to only one mini-tracker. In this figure, the D and $D/\sigma(D)$ values were found to still be sufficiently large for all investigated air-cavity positions. This means that for all four investigated air-cavity positions, the cavity was found to be detectable with a significance of at least 3 sigmas and with a maximum detection significance at the entrance of the head model, where the cavity was found to be detectable with a significance of 6 sigmas when measuring with only one mini-tracker.

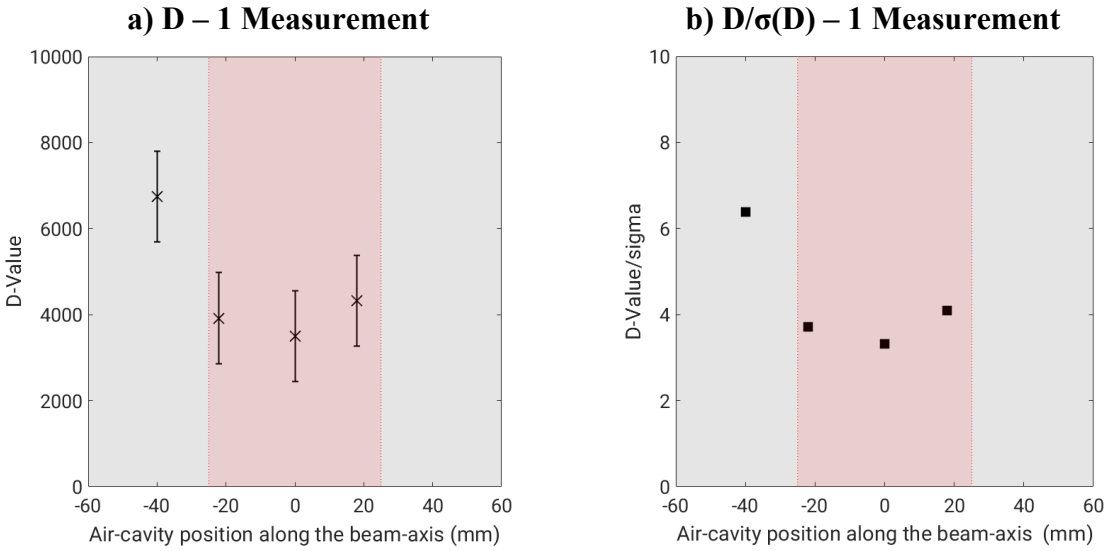

Figure 4.20: Detection significance (a) and detection significance divided by its uncertainties (b) for all four investigated air-cavity positions along the beam axis. The head-model volume is centered at 0 mm along the beam axis and represented by the grey area, the tumor volume by the red one. Statistical uncertainties corresponding to **one** mini-tracker area are plotted as error bars.

4.2.3. Impact of narrow internal changes

Changes within the irradiated patient might affect just a part of the irradiated area. To simulate such laterally narrower internal inter-fractional anatomical changes, a narrow 2-mm-thick air disc of 10-mm-diameter was positioned inside of the irradiated homogeneous head model, upstream of the tumor volume, and aligned with its center, as depicted in Figure 4.21.

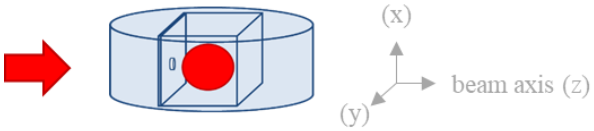

Figure 4.21: Position of the investigated 2-mm-thick air disc of 10-mm-diameter (white disk) in the homogeneous head model (light blue), positioned in front of the tumor volume, represented here by the red sphere with a 25-mm-radius.

Similar to section (§4.2.2.), secondary ions produced in the homogeneous head model were measured for three types of fraction irradiations (one reference, one homogeneous, and one heterogeneous) by the mini-tracker positioned at a detection angle of 30° with respect to the beam axis and 120 mm from the tumor center. The heterogeneous follow-up fraction was measured in this analysis with the 2-mm-thick air-disk of 10-mm-diameter placed upstream of the tumor volume. As explained in (§4.2.2.), the data of 8 repetitions were again summed up for each fraction to mimic a setup that will be used in the near future for a clinical trial with a larger patient cohort.

4.2.3.1 Variation of the shape of the secondary-ion emission profiles

Similarly, to the analysis of wide internal changes, see section (§4.2.2.), the secondary-ion emission profiles as measured during the reference fraction, the homogeneous fraction, and the heterogeneous fraction were plotted together in Figure 4.22.

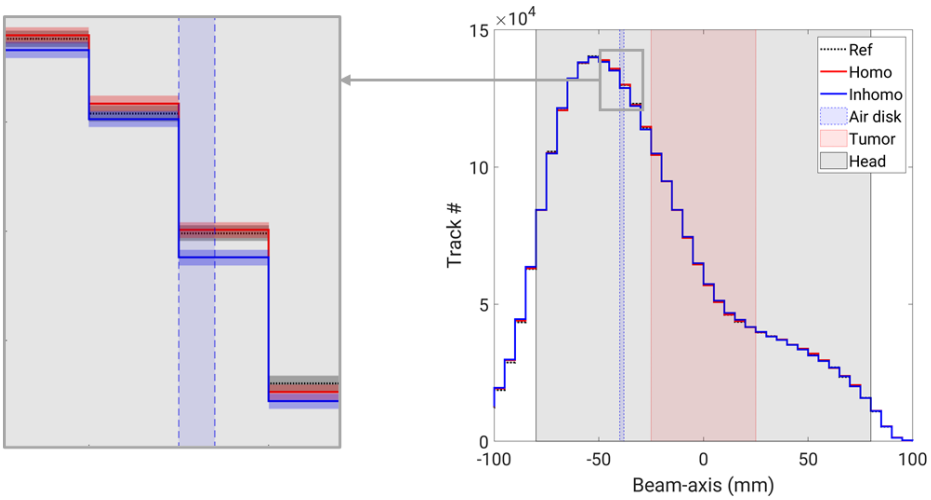

Figure 4.22: Secondary-ion emission profiles along the beam axis as measured at a detection angle of 30° and 120 mm from the tumor center with a small air disk located in front of the tumor volume in the homogeneous head model. Profile measured during the reference fraction irradiation (without any air cavity) is plotted in dashed black against one homogeneous fraction irradiation plotted in red (without any air cavity) and one heterogeneous fraction irradiation (with an air disk) plotted in blue. The head-model volume is centered at 0 mm along the beam axis and represented by the grey area, the tumor volume by the red one, and the inserted air cavity volume by the blue dashed vertical bands. Statistical uncertainties corresponding to an 8-fold sensitive mini-tracker area are plotted as barely visible error bands. The beam enters the head model from left to right.

The impact of the small air-disk on the measured secondary-ion emission profiles was investigated using the ratio (Figure 4.23-a) and the difference (Figure 4.23-b) between the measured secondary-ion emission profile of the reference fractions and the two follow-up fractions (with and without an air disk).

- The position of the weighted average position of the three minimal values induced by the air disk in the profile of the ratio, as defined by (Eq.3.24), is found to be at: $Z_{MIN\ RATIO} = -33.2 \pm 2.5$ mm.
- The position of the weighted average position of the three minimal values induced by the air disk in the profile of the difference, as defined by (Eq.3.28), is found to be at $Z_{MIN\ DIFF} = -32.5 \pm 2.5$ mm.

The accuracy of the localization is defined as the difference between the measured and the actual cavity position. Here, both the positions of the maximum signal reduction and of the minimum in the profile of the difference seem to approximate the actual position of the inserted small 2-mm-thick air disk well, with an accuracy of up to 6.5 mm. Uncertainties on the localization of the cavity are estimated to be at maximum of the order of the bin size, i.e. 5 mm.

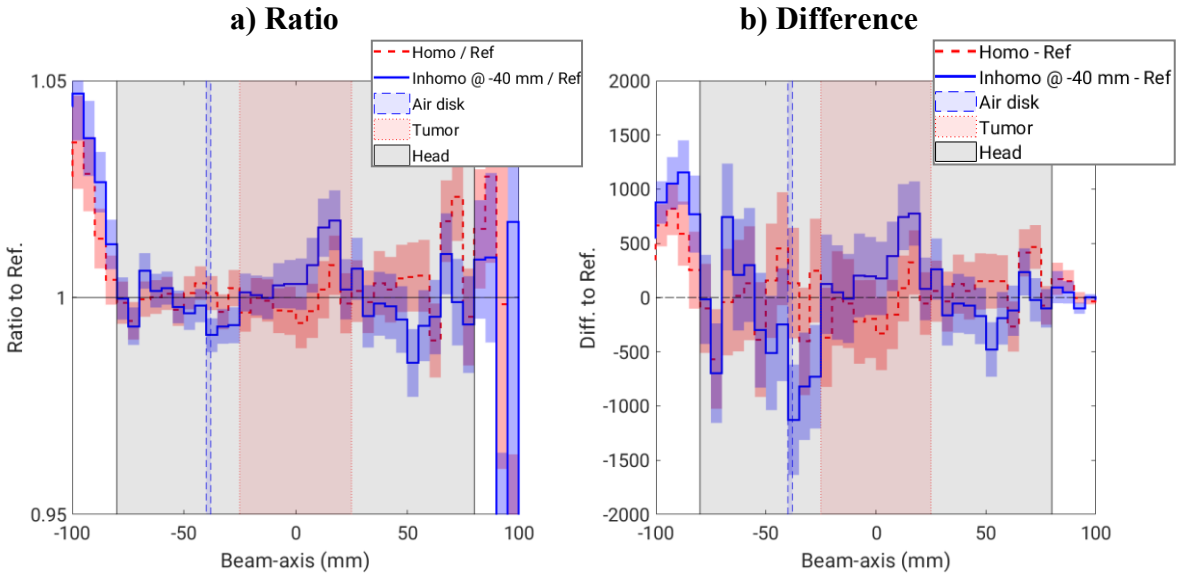

Figure 4.23: Ratios (a) and differences (b) between the measured secondary-ion emission profile of the reference fractions versus the two follow-up fractions (with and without an air disk). The ratio (or difference) between the reference and the homogeneous fractions is plotted in dashed red. The ratio (or difference) between the reference and the heterogeneous fraction (with air disk) is plotted in blue. The head-model volume is centered at 0 mm along the beam axis and represented by the grey area, the tumor volume by the red area, and the inserted air cavity volume by the blue dashed vertical band. Statistical uncertainties corresponding to an 8-fold sensitive mini-tracker area are plotted as error bands.

The integral value $I_{WITHOUT}$ of the absolute difference between the reference measurement and the measurement without the cavity (red) and the integrals I_{WITH} of the absolute differences between the reference measurement and the measurement with the cavity (blue) were plotted in Figure 4.24.

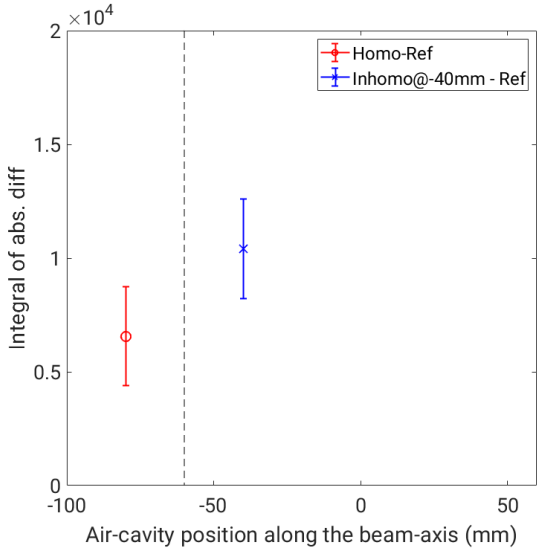

Figure 4.24: Values of the integral of the absolute difference between reference and homogeneous fractions (red) versus reference and heterogeneous fractions (blue)

The *D* and *D/σ(D)* values (see (Eq.3.31) and (Eq.3.33) for definition in (§3.7.1.4.) of Materials and Methods) were computed for the small disk and are found to be: $D = 3844 \pm 3077$ and $D/\sigma(D) = 1.2$. Unlike what was seen in section (§4.2.2.), the impact of a small air-disk (2-mm-thick disk of 10-mm-diameter laterally) was found to be less significant than the impact of a large air-cavity (2-mm-thick slab of 80 mm x 80 mm laterally) located at the same depth in the homogeneous head model. This can be explained by the fact that, due to the small lateral size of the inserted air disk (10-mm-Ø), only a few carbon-ion pencil beams have crossed the inserted small air disk. The information regarding the small air disk is thus hidden in the entire measured secondary-ion emission profile and is found to be non-significant, in contrast to the larger air cavities.

4.2.3.2 Determination of the position of the change along the beam direction and laterally

Knowing that some treatment carbon-ion pencil beams can be affected by the small inserted change independently from others, the analysis was further refined. Lateral grouping of the measured secondary ions was performed to retrieve information regarding the small air disk hidden in the entire measured secondary ion emission profile. As described in section (§3.7.2.1.) of Materials and Methods, nine lateral regions of 20 mm x 20 mm in size were defined to cover the entire lateral dimension of the tumor with a radius of 25 mm. Figure 3.30 showed how these regions are organized in a beam eye view. The central region R5 was covering the potentially affected pencil beams due to the inserted 10-mm-diameter air disk indicated by the blue circle. For each of the nine lateral regions, secondary-ion emission profiles along the beam axis as measured for the reference, the homogeneous, and the heterogeneous fractions were plotted in Figure 4.25.

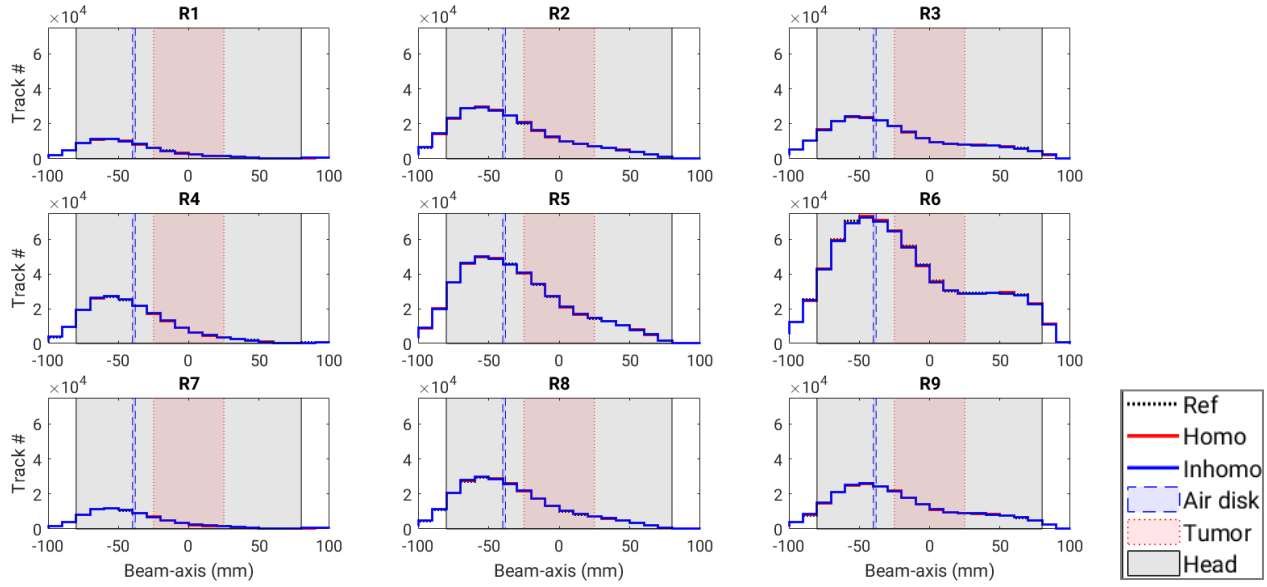

Figure 4.25: Secondary-ion emission profiles along the beam axis as measured at a detection angle of 30° and 120 mm from the tumor center with an air disk in front of the tumor volume for all nine lateral regions. Statistical uncertainties corresponding to an 8-fold sensitive mini-tracker area are plotted as barely visible error bands.

In Figure 4.25, the measured secondary-ion emission profile along the beam axis showed that most of the detected secondary-ion tracks originated from pencil beams located in regions R3, R6, and R9. On the contrary, very little originated from pencil beams located in regions R1 and R7. This can be explained by the location of the mini-tracker with respect to the defined lateral regions. Indeed, the mini-tracker is aligned with the horizontal plane ($X = 0$), thus located in the same plane as regions R4, R5, and R6. Moreover, the mini-tracker is located on the right side of the head model in the beam-eye-view, i.e. the closest to the regions R3, R6, and R9. Another explanation is that the effective angle of the detection system (mini-tracker) is lower than 30° for the pencil beams located in regions R3, R6, and R9, while being larger than 30° for regions R1, R4, and R7. Track yield with respect to angle shows an exponential relationship as it will be later presented in section (§4.3.2.1.). Therefore, pencil beams that were sent to region R6, located the closest horizontally and vertically to the mini-tracker, produced secondary ions that were the most likely to be detected by the mini-tracker. On the other hand, pencil beams that were sent to regions R1 or R7, located the farthest horizontally and vertically from the mini-tracker, produced secondary ions that were least likely to reach the mini-tracker.
Additionally, the differences between the secondary-ion emission profiles were computed for each of the nine lateral regions as seen in Figure 4.26. In this figure, the difference between the secondary-ion emission profiles for each of the nine lateral regions clearly showed the impact of the air disk on the profiles. This impact is especially visible for region R5. Region R5 was the region of interest that contains the pencil beams crossing the air disk. For this region, similar to what was observed with the air slab in section (§4.2.2.), the profile of the difference between the reference fraction and the fraction with the air-disk showed all three main characteristic variations:

- downstream from the air cavity, an enhanced number of secondary ions in form of a peak was visible (1)
- a significant dip was seen at the depth of the air cavity (2)
- the difference values were centered around higher values than zero i.e. increased the total number of detected secondary ions (3)

Some of the other lateral regions in Figure 4.26, especially regions R2 and R8, show some of these characteristic changes as well.
Region R6, as previously explained, displayed the largest difference values in Figure 4.26 due to the larger number of secondary-ion tracks detected from this region. It is not especially synonym of a large significance of the impact of the air disk. This is confirmed by Figure 4.27, where the ratio values for region R6 were seen to be centered around 1 and confirming that the large difference seen in Figure 4.26 mostly comes from the large number of detected secondary-ion tracks and not from an actual variation in the shapes of the measured profiles.

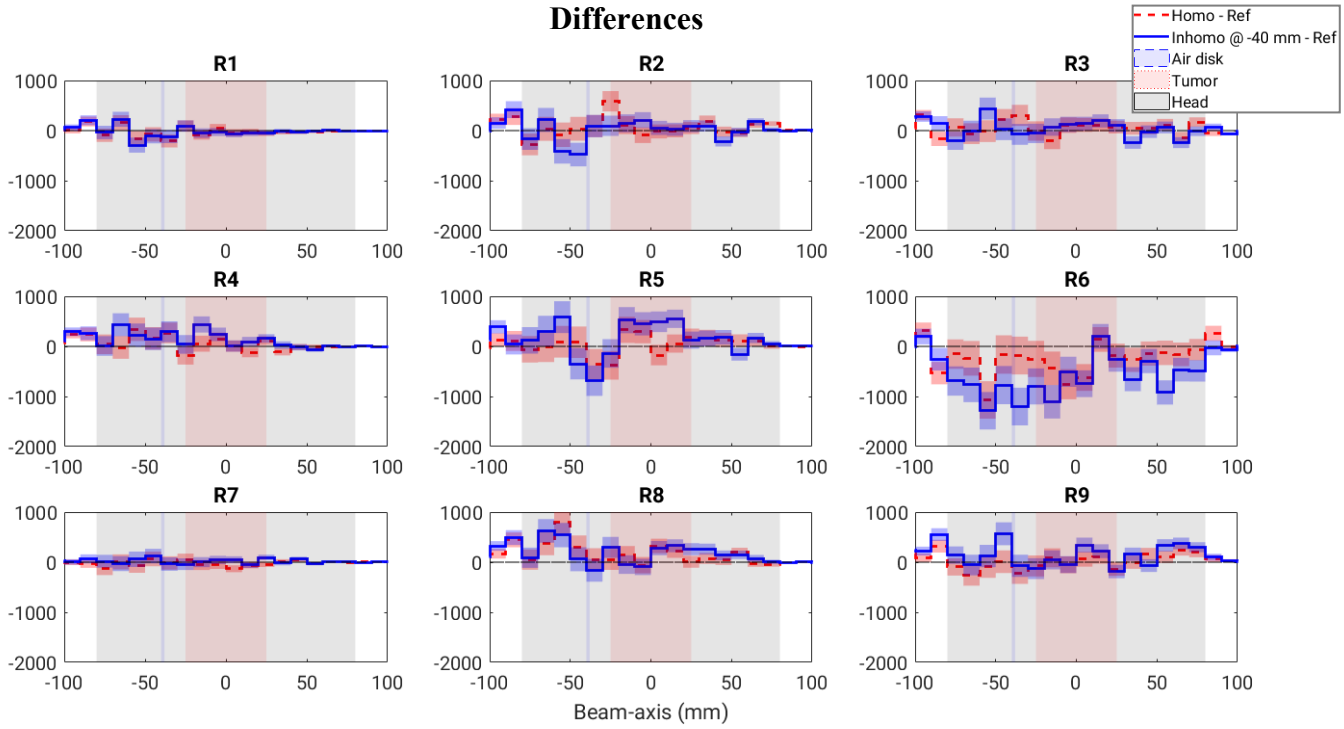

Figure 4.26: Difference between the measured secondary-ion emission profiles of the reference fractions versus the two follow-up fractions (with and without the air disk) for all nine lateral regions. Statistical uncertainties corresponding to an 8-fold sensitive mini-tracker area are plotted as error bands.

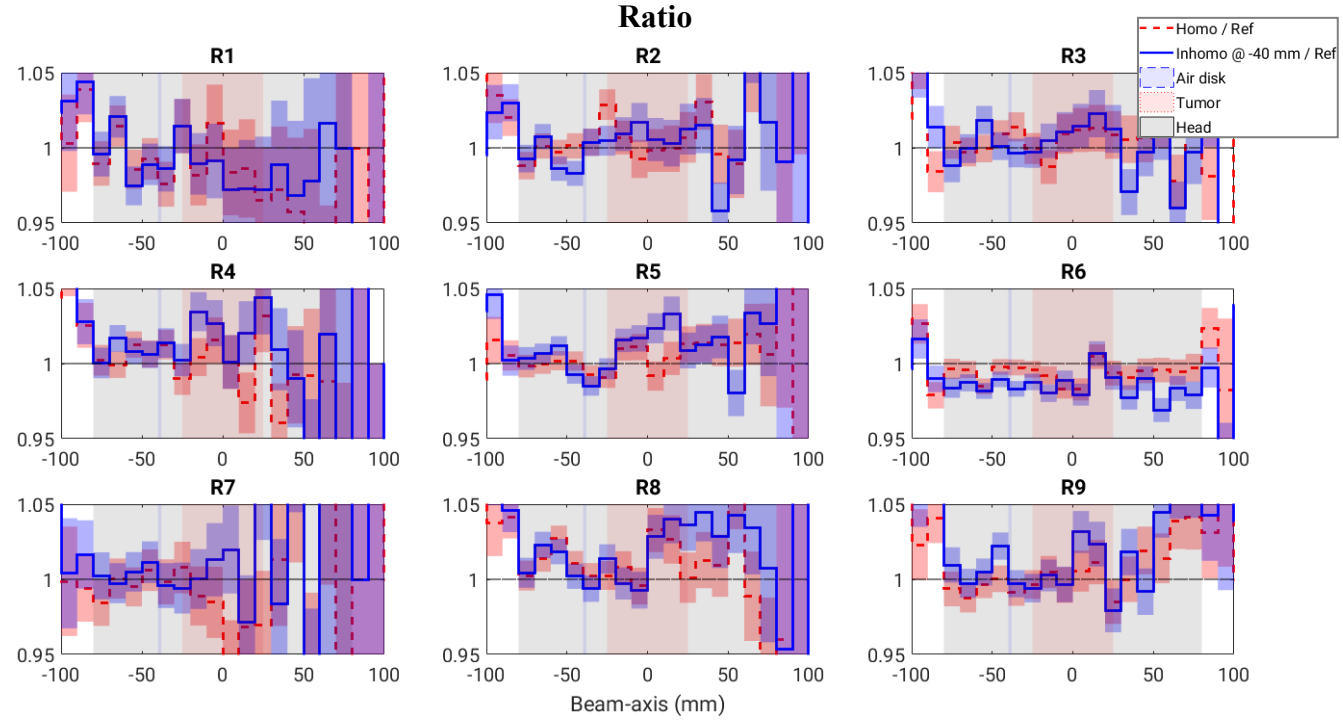

Figure 4.27: Ratio between the measured secondary-ion emission profiles of the reference fractions versus the two follow-up fractions (with and without the air disk) for all nine lateral regions. Statistical uncertainties corresponding to an 8-fold sensitive mini-tracker area are plotted as error bands.

4.2.3.3 Quantification of the significance of the detection

The integrals I_{WITH} and $I_{WITHOUT}$ of the absolute differences between reference and the two follow-up fractions (with and without air-disk) are plotted in Figure 4.28. Corresponding D and $D/\sigma(D)$ values, as defined by (Eq.3.31) and (Eq.3.33) in (§3.7.1.4.) of Materials and Methods, were calculated for each of the nine lateral regions as seen in Figure 4.29-a)-b). This figure shows that *D-values* and $D/\sigma(D)$ values computed for each of the regions were more significant for the region of interest (region R5) and the region containing most of the detected secondary-ion tracks (region R6). The found $D/\sigma(D)$ values in these two regions almost double the one calculated for the entire data set. It is observed that a narrow change that is almost non-significant ($D/\sigma(D)$ = 1.2) when considering an entire dataset can become significant by grouping the measured secondary ions laterally ($D/\sigma(D)$ = 1.9 in R5). However, the high significance in region 6 must be taken into account for the interpretation of the change detection. Additionally, it is seen that the method is sensitive to the lateral position of the change. Further investigations on the different lateral positions of the change are expected to confirm this.

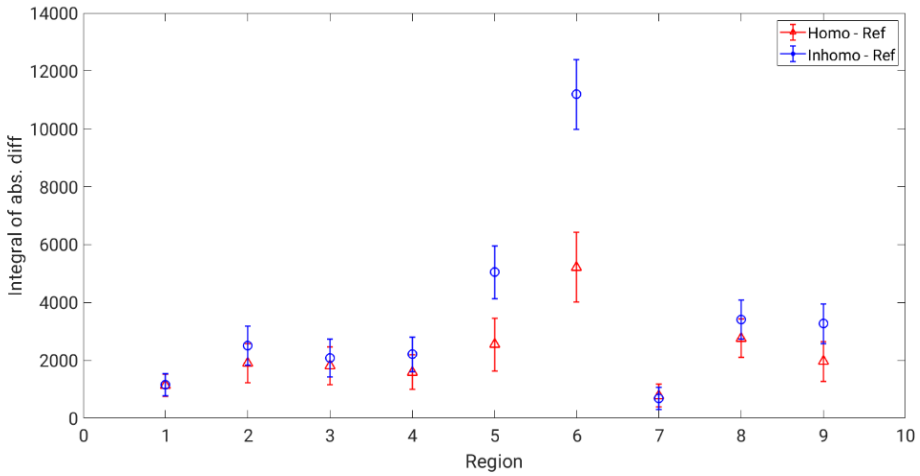

Figure 4.28: Integrals I_{WITH} (blue) and $I_{WITHOUT}$ (red) for all nine lateral regions.

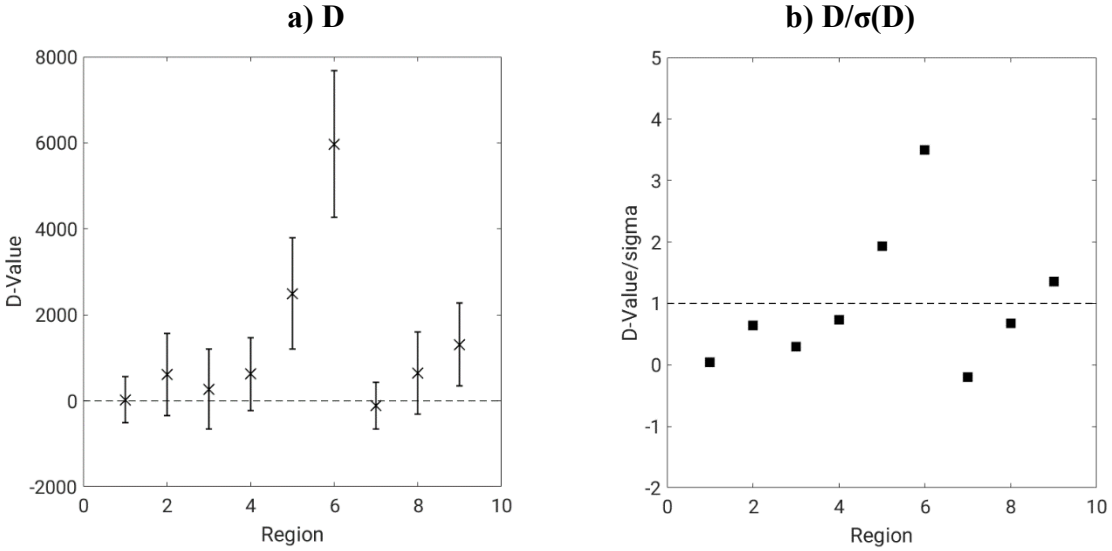

Figure 4.29: Differences of the integrals I_{WITH} and $I_{WITHOUT}$ (D-values) (a) and differences of the integrals I_{WITH} and $I_{WITHOUT}$ divided by their uncertainties ($D/\sigma(D)$-values) (b) for all nine lateral regions.

4.2.4. Summary of the detection and localization of internal changes using secondary-ion emission profiles

In the current analysis (later on called “single feature analysis” as it only uses secondary-ion emission profile information), the investigated anatomical changes contained:

- wide surface changes, modeled by a 1-,2-,3-mm-thick, and 150 mm x 150 mm wide PMMA-slabs placed upstream of the head model.
- wide internal changes, modeled by a 2-mm-thick and 80 mm x 80 mm wide air-slab placed inside the head model between the dose plateau and the distal end of the tumor.
- narrower internal changes, modeled by a 2-mm-thick and 10-mm-diameter air disk placed inside the head model.

With the developed method it was found that:

- wide surface changes down to 1 mm were detectable even for the anatomical head phantom containing structure heterogeneities similar to a real patient.
- wide internal changes of 2-mm-thickness extending over the whole lateral tumor dimension were:
    - localized for all positions with an accuracy of 1.5 to 6.3 mm for the ratio analysis and of 2.2 to 5.3 mm for the difference analysis.
    - detectable for all positions with a significance of at least 9 sigmas when using statistics of 8 mini-trackers.
    - detectable for all positions with a significance of at least 3 sigmas when using statistics of 1 mini-trackers.
- narrower internal changes, only affecting part of the pencil beams of the treatment plan were:
    - localized at the entrance of the head model with an accuracy of 6.5 mm.
    - detectable with a significance of almost 2 sigmas in the central region after grouping pencil beams laterally.

In a further analysis, a grouping of the measured data in the lateral direction was necessary to detect the narrow internal change with high enough significance, as only part of the treatment pencil beams crossed the inserted cavity. With this technique, the visualization, localization, and detection of an air cavity of only 10-mm-diameter and 2-mm-thickness was achieved. This was not feasible when considering the entire data set corresponding to the whole treatment plan. This technique makes the developed monitoring method sensitive to the lateral position of the cavity, and thus reaches the third dimension.

4.3. Analysis of the ideal detection angle

In this section, the ideal detection angle to detect internal changes is investigated, see Figure 4.30. As presented in Figure 4.31, the two main components contributing to the quality of the desired information needed for precise carbon-ion beam monitoring in-depth are the track yield and the performance of the analysis of the recorded tracks in 3D space (geometry). These two components have opposite directions and depend on the chosen detection angle.

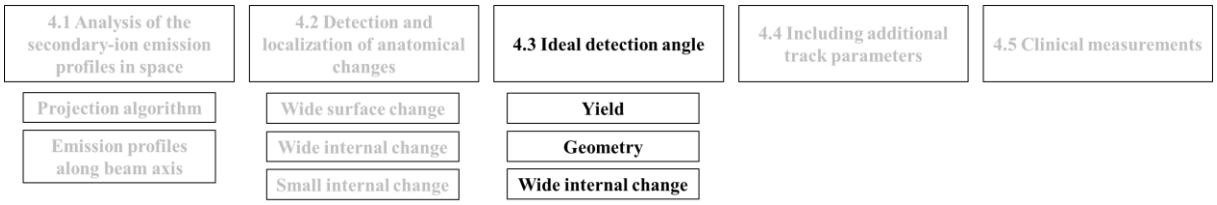

Figure 4.30: Current topic within the five topics presented in the results section of this thesis.

To investigate which mini-tracker position is the best to both detect and localize inter-fractional anatomical changes, first, a comparison of the performance of the analysis of the measured tracks (in this case the geometry of the track-projection) at different detection angles of the mini-tracker was performed and summarized in (§4.3.1. Geometry in the track-projection.). Second, the track yield was investigated as a function of the mini tracker positions in (§4.3.2.). Eventually, secondary ions produced in the homogeneous head model were measured by the mini-tracker positioned at different detection angles with respect to the beam axis and distances with respect to the tumor center. The single-feature analysis, as previously presented in (§4.2.), was then applied to each of the measured cases as a function of the mini tracker positions in (§4.3.3.).

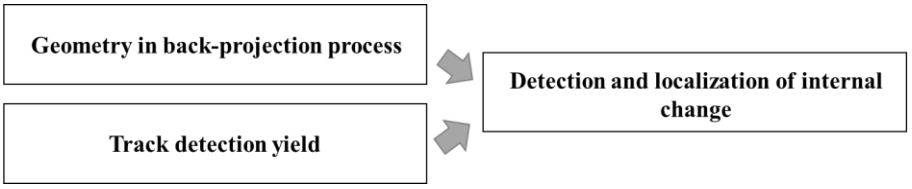

Figure 4.31: Two main opposite influences on the quality of the desired information for an ideal detection and localization of internal changes.

4.3.1. Geometry in the track-projection

Geometry uncertainties in the track-projection are directly linked to the mini-tracker position with respect to the beam axis and tumor center, as seen in Figure 4.32 and Table 4.1 for a variation of 1 pixel in the mini-tracker. At lower detection angles (10° and 20°), larger distances to the tumor center are needed to reduce the signal pile up in the mini-tracker, as explained later in section (§4.3.3.). Here it is seen that bigger detection angles lead to significantly better accuracies with respect to the track-projection geometry.

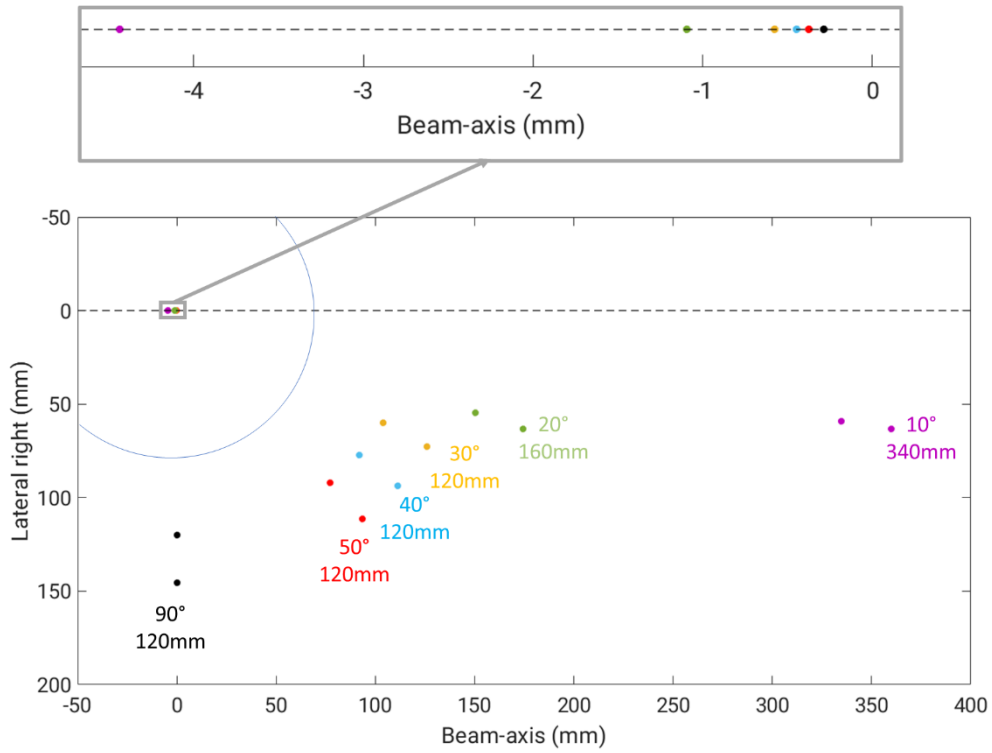

Figure 4.32: Top view of the mini-tracker positions with respect to the beam axis (dashed line) and the room isocenter (0, 0). Track-projections of the tracker center are plotted along the beam axis for each mini-tracker position considering a 1px size variation. The largest geometrical uncertainty is seen for the mini-tracker placed at 10° (purple).

Table 4.1: Geometry uncertainties on the projected track origin using 2D track-projection for the different mini-tracker positions with respect to the beam axis and distance to the isocenter.

Mini-tracker position	Projected uncertainties at the isocenter (mm)
10° 340 mm	4.4
20° 160 mm	1.1
30° 120 mm	0.6
40° 120 mm	0.4
50° 120 mm	0.4
90° 120 mm	0.3

To further investigate which mini-tracker position geometrically approximates best the measured track origin in the head model using the more complex track-projection algorithm (3D+), secondary ions produced in the homogeneous head model were simulated in MC-simulations with FLUKA (Schlechter 2021) with the mini-tracker positioned at different detection angles with respect to the beam axis. The following mini-tracker detection angles were simulated: 10°, 20°, 30°, 40°, and 50°. From these MC simulations, the mean of the absolute distances between 3D+ back-projected secondary-ion origin and true origin were computed in this work for several detection angles and plotted in Figure 4.33. This figure shows

that larger angles lead to a better accuracy with respect to the true origin's emission profile until the lack of statistics impairs it. This was expected since secondary ions are predominantly emitted in a forward-peaked direction with respect to the beam axis.

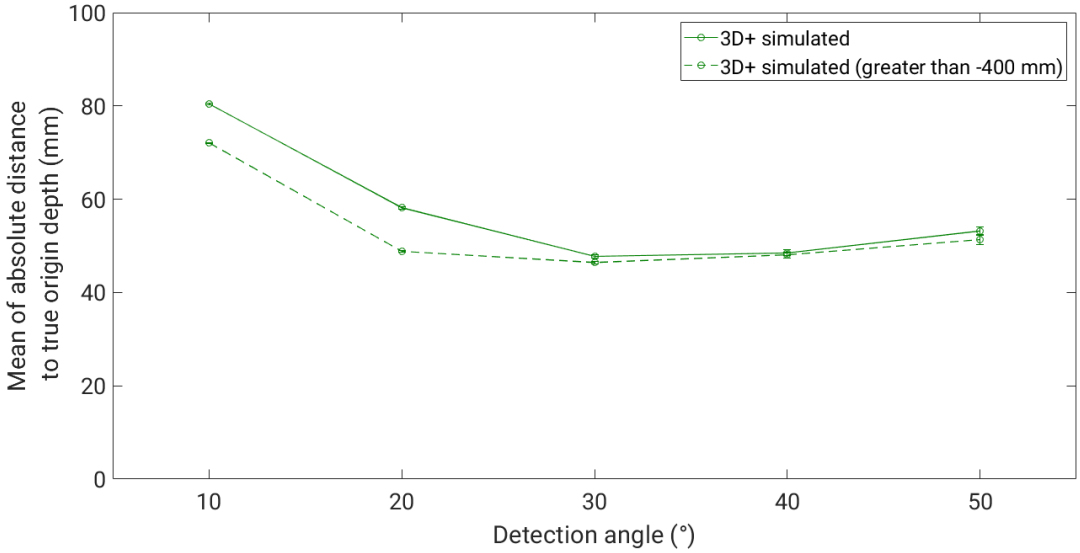

Figure 4.33: Mean of the absolute distance between back-projected secondary-ion origin and true origin for several detection angles. To exclude secondary-ion tracks created in the beam nozzle but scored by the MC-simulation, a cut on the maximal distance to true origin (> 400 mm) is applied and plotted in dashed green.

4.3.2. Achievable track yields

4.3.2.1 Track yield for different mini-tracker positions with respect to the beam axis

During the experiments at the HIT facility, both a homogeneous head-sized PMMA cylinder and an anthropomorphic Alderson head model were irradiated with clinic-like carbon-ion treatment plans of a spherical tumor located in their center, see section (§3.3.1.) of Materials and Methods. During the irradiations, secondary-ion tracks were measured with a mini-tracker positioned at different detection angles α (°) with respect to the beam axis as well as different distances d (mm) downstream of the tumor center. A distance d of 120 mm was often chosen as it is the closest clinically allowed distance to the target center while avoiding collisions with the head models. In this work, only the closest distances clinically possible were chosen to always maximize the amount of measured secondary ion tracks.

Detection track yields of full clinic-like fraction irradiations were analyzed for all investigated mini-tracker positions in both homogeneous and anthropomorphic head models, see (§3.3.1.2.) of Materials and Methods. The obtained yields and yields per solid angle are presented in Figure 4.34 and Figure 4.35. The plotted track yields represent the average track yields over the whole treatment plan.

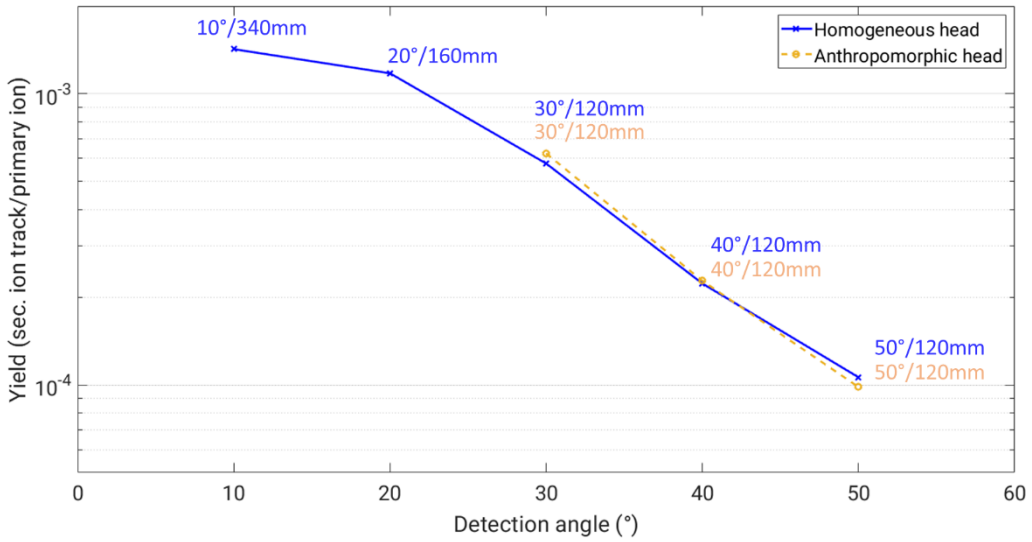

Figure 4.34: Track yields (logarithmic scale) as measured in both homogeneous and anthropomorphic head models with the mini-tracker positioned at different detection angles α (°) with respect to the beam axis and distances d (mm) from the tumor center.

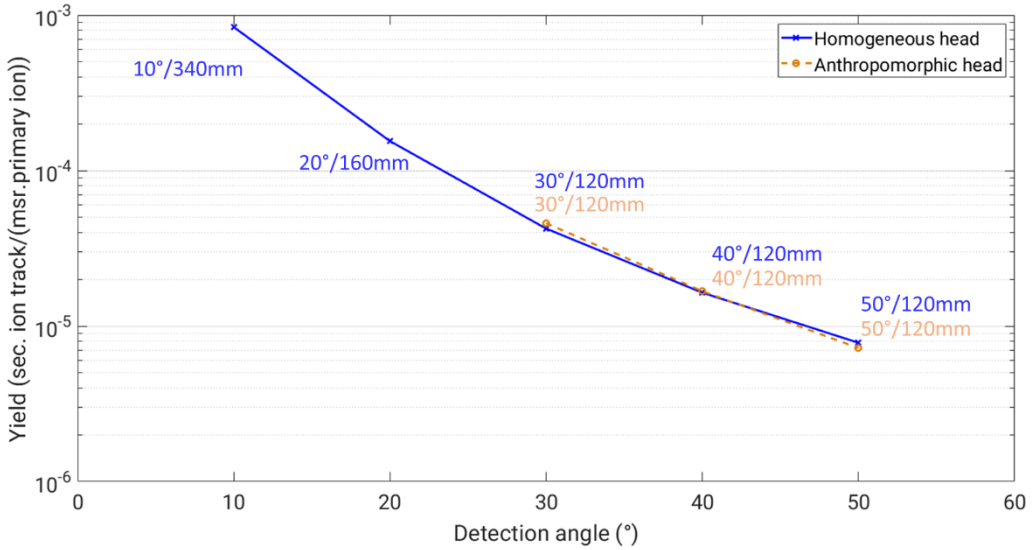

Figure 4.35: Corresponding track yield per solid angle Ω (sr^{-1}) (logarithmic scale) as measured in both homogeneous and anthropomorphic head models with the mini-tracker positioned at different detection angles α (°) with respect to the beam axis and at different distances d (mm) from the tumor center.

At low detection angles ($\alpha \leq 30°$), i.e. with the tracker closer to the beam axis, the probability of a signal pileup is higher. This is due to the forward boosted shape of the secondary-ion emission profile in the coordinate system of the treatment room (Gunzert-Marx et al. 2008), which leads to a higher ion fluence rate at low detection angles. To mitigate this effect and obtain more measurable tracks at lower detection angles, the mini-tracker had to be positioned further away from the tumor center at low detection angles. For example, instead of the usual

distance d = 120 mm, a distance of d = 340 mm was used for a detection angle of α = 10° and a distance of d = 160 mm for α = 20° (blue curve in Figure 4.34).
In both Figure 4.34 and Figure 4.35, the behavior of the track yield is similar for homogeneous and anthropomorphic head models, leaving the signal pileup at low angles and small distances in the anthropomorphic head model aside. However, a larger track yield is seen at 30° for the anthropomorphic head model, which is expected as the anthropomorphic head-model tumor has a bigger volume and as the anthropomorphic head-model radius is slightly smaller than the PMMA cylinder one. Secondary ions produced in the anthropomorphic head model have less material to cross than in the homogeneous head model and are thus more likely to be detected by the mini-tracker.
In Figure 4.34, the blue curve, which accounts for signal pileup correction, shows an almost exponential decrease of the secondary-ion track yield (with a semi-logarithmic scale) with increasing detection angles for $\alpha \geq 30°$. At lower track detection angles, (α = 10° and 20°), this behavior is not observed. Here a slighter decrease is visible. Here it has to be considered that, for these lower angles, the mini-tracker was positioned further away from the isocenter, at a distance of 340 mm and 160 mm respectively, instead of 120 mm. Thus, in addition, the track yield is expected to decrease with increasing distance to the tumor center.
To account for any distance variations between measured yields, the track yield per solid angle $Yield_{\Omega}$ was plotted in Figure 4.35. Indeed, the non-linear decrease visible in yields for lower detection angles in Figure 4.34 is no longer observed in Figure 4.35. Thus, larger distances to the tumor center allow coping with signal pileup while maintaining a high track yield. Additionally, Figure 4.35 shows an almost exponential decrease of the secondary-ion track $Yield_{\Omega}$ per detection angle. This is due to the strongly forward-peaked direction emission of secondary ions. Thus, decreasing the detection angle increases the track yield almost exponentially.

4.3.2.2 Track yield at 30° from the beam axis

As a tradeoff between high statistics and low signal pileup, secondary-ion tracks were in this work mostly measured with a mini-tracker placed at 30° with respect to the beam axis and a minimal clinical acceptable distance of 120 mm away from the tumor center. The homogeneous and anthropomorphic head models irradiated with entire clinic-like treatment plans (see section (§3.3.1.) of Materials and Methods) led to the following track yields:

- $Yield_{\text{homogeneous target}} = 5.76 \times 10^{-4}$ primary $^{-1}$
- $Yield_{\text{heterogeneous target}} = 6.24 \times 10^{-4}$ primary $^{-1}$

The track yields per solid angle $Yield_{\Omega}$ (with Ω_{120mm} = 13.6 msr) were found to be:

- $Yield_{\Omega\ \text{homogeneous target}} = 42.4 \times 10^{-3}$ primary $^{-1}$.sr^{-1}
- $Yield_{\Omega\ \text{heterogeneous target}} = 45.9 \times 10^{-3}$ primary $^{-1}$.sr^{-1}

During the irradiation of the anthropomorphic head model, 22 carbon-ion beam energies were used ranging from 163.09 to 246.57 MeV/u. This corresponds to carbon-ion ranges from 61.36 to 124.4 mm in water with an energy step of 3 mm. Figure 4.36 shows the non-normalized number of detected secondary ions for each therapeutic energy of the carbon ion beam used in the treatment of the anthropomorphic head model as measured at an angle α = 30° and a distance d = 120 mm. For low beam energies, the number of detected tracks is lower, partly due to the

lower number of primary carbon ions sent with these beam energies. But several other effects play a role in the number of detected tracks, including the total number of secondary per primary, the angular distribution of the fragmentation, and their corresponding energy-dependent scattering. It is important to note that 30° is only valid for secondary ions emitted at the isocenter. For all other secondary ions, including non-central pencil-beam positions, the effective angle is different.

The track yield per solid angle (with Ω_{120mm} = 13.6 msr) for each carbon-ion beam energy used during irradiation was measured as shown in Figure 4.37. An increasing track yield at a higher beam-energy layer is found. Therefore, low beam-energies lead to a decrease in the track yield. Overall, an increase in the statistical uncertainties of the distribution of the measured origins can be expected for shallow tumor sites, which are treated with lower beam energies. For better statistical uncertainties, centered or even deeply seated tumors are thus preferred as they are treated with higher beam energies.

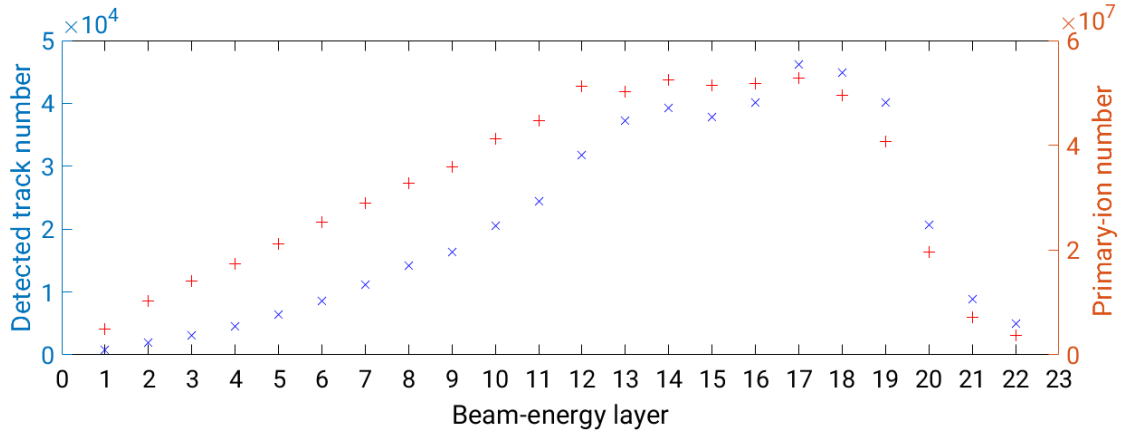

Figure 4.36: Number of detected tracks (blue crosses) and number of primary ions (red +) per therapeutic carbon-ion beam layer as measured in the anthropomorphic head model by the mini-tracker placed at a detection angle of 30° and 120 mm away from the tumor center.

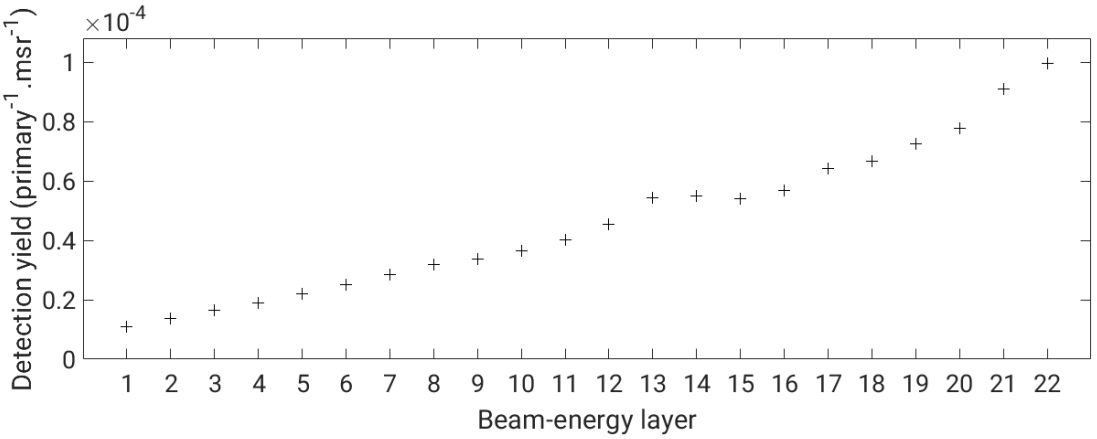

Figure 4.37: Number of detected tracks per primary ion and per solid angle covered by the detector as a function of the therapeutic carbon-ion beam energy layer as measured for the anthropomorphic head model by the mini-tracker placed at a detection angle of 30° and 120 mm away from the tumor center.

4.3.3. Impact of a wide internal change measured at different detection angles

To investigate which mini-tracker position is the best to specifically detect and localize wide inter-fractional anatomical changes, secondary ions produced in the homogeneous head model were measured by the mini-tracker positioned at different detection angles with respect to the beam axis and distances with respect to the tumor center.

The following mini-tracker detection angles and distances were investigated: 10°/340mm, 20°/160mm, 30°/120mm, 40°/120mm, and 50°/120mm. This work is also partially presented in the Bachelor thesis of A. Schlechter which was part of this thesis doctoral project.

As explained in section (§4.3.2.1.), the distances of the mini-tracker to the tumor center needed to be adapted for each detection angle to avoid the signal pileup induced by the higher fluence rate at lower angles with respect to the beam axis.

The inter-fractional anatomical changes to be detected and localized were modeled using wide 2-mm-thick air cavities (2 mm x 80 mm x 80 mm air slab) positioned inside the irradiated homogeneous head model at two different depths upstream of the tumor volume. As depicted in Figure 4.38, the two air cavity positions investigated here corresponded to an easy cavity detection position (in front of the tumor, [-40; -39 mm]) and a more challenging cavity position (in the middle of the tumor volume, centered at a depth of [0; +1 mm]). Where 0 mm was the room isocenter position, aligned with the middle of the head model and at the same time of the tumor volume. Negative depths were upstream of this isocenter.

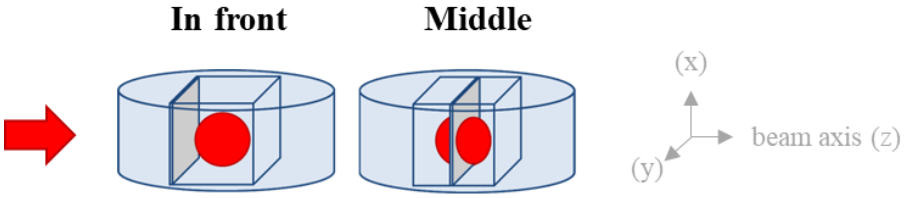

Figure 4.38: Setup used for the investigation of the different detection angles. The two investigated 2-mm-thick air cavity positions in the homogeneous head model (light blue) corresponding to the front, and the middle of the tumor volume, represented here by the red sphere with a 25-mm-radius.

First, a reference fraction irradiation was measured. Then, three follow-up fractions were acquired: one homogeneous fraction (without internal change) and two heterogeneous fractions (measured with the air cavity placed at the two investigated depths). For this analysis, the data of 8 repetitions were summed up for each fraction. This is performed to mimic having a system of 8 mini-trackers, similar to a setup that will be used in the near future for a clinical trial with a larger patient cohort.

4.3.3.1 Impact of the internal change on the shape of the secondary-ion emission profiles

The four secondary-ion emission profiles as measured during the reference fraction, the homogeneous fraction, and the two heterogeneous fractions were compared for all investigated detection angles, similarly, to the results presented in section (§4.2.2.) and section (§4.2.3.). As an example, the secondary-ion emission profiles as measured at the lowest detection angle of 20°/160mm are shown in Figure 4.39 and the one measured at the largest detection angle of 50°/120mm are shown in Figure 4.40.

Figure 4.39 and Figure 4.40 show that the impact of the air cavity on the measured secondary-ion emission profiles is globally the same at 20° and 50°. The main three variations due to the inserted air cavity previously seen at 30° in Figure 4.15, namely: (1) the higher profile with a dip (2) at the location of the cavity, followed by a shift of the distal falloff (3) towards bigger depths were also observed at 20° in Figure 4.39 and 50° in Figure 4.40.

The impact of the inserted air-cavity was investigated using the ratio and the difference between the measured secondary-ion emission profiles of the reference fractions versus the three follow-up fractions (with and without an air slab). As examples, the ratio and the difference of the secondary-ion emission profiles as measured at 20°/160mm are shown in Figure 4.41-a)-b) and the ratio and the difference of the secondary-ion emission profiles as measured at 50°/120mm are shown in Figure 4.42-a)-b).

The main three variations due to the inserted air cavity previously seen at 30° were again clearly represented by the ratio (Figure 4.41-a) and Figure 4.42-a)) and difference values (Figure 4.41-b) and Figure 4.42-b) In these figures, downstream from the air cavity an enhanced number of secondary ions in form of a peak was visible in both the ratio and difference plots (1), a dip was seen at the depth of the air-cavity (2), and the ratio and difference values measured at 20° and 50° were again centered around higher values than 1 and zero respectively (3).

However, from Figure 4.39 and Figure 4.40, it is apparent that the detection angle played an important role in the measured secondary-ion emission profiles. First of all, the detection angle impacts the overall amount of acquired data. Indeed, the lower the detection angles (i.e. the closer to the beam axis), the larger the number of measured secondary-ion tracks. This was expected due to the forward peaked distribution of the produced secondary ions. Second, the detection angle was seen to impact the shape of the secondary-ion emission profiles, especially in the region upstream of the head model (before -80 mm along the beam axis). Indeed, the lower the detection angles (i.e. the closer to the beam axis), the larger the geometrical uncertainties, as expected due to the shallow angle of the secondary ion tracks with respect to the pencil beam axis for low mini-tracker angles.

Consequently, in Figure 4.41 and Figure 4.42, the detection angle was found to play an important role in the ratio and differences between the secondary-ion emission profiles. First, the difference curve at 20° (Figure 4.41-b)) shows bigger differences than at 50° (Figure 4.42-b)). This indicates a larger number of measured secondary-ion tracks at lower detection angles. Second, the dips at the location of the cavity in the difference and the ratio-curves measured at 50° are seen to be narrower than when measured at 20°. At 20°, at least 6 bins are affected by the dip. While at 50°, only 4 bins are affected by the dip. This reflects the larger the geometrical uncertainties associated with lower detection angles (i.e. closer to the beam axis).

@ 20° 160 mm

a) Cavity in front of the tumor **b) Cavity in the middle of the tumor**

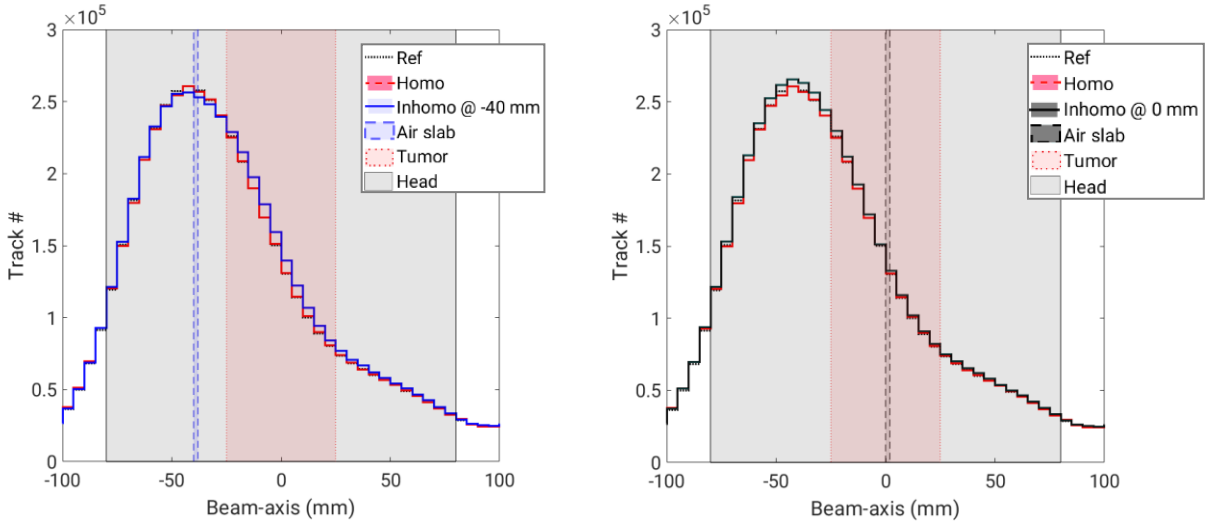

Figure 4.39: Secondary-ion emission profiles along the beam axis for fractions with and without a small air-cavity located in the front (a) or the middle (b) of the tumor volume as measured in the homogeneous head model at 20°/160mm. The head-model volume is centered at 0 mm along the beam axis and represented by the grey area, the tumor volume by the red one, and the inserted air cavity volume by the blue vertical dashed bands. The beam enters the head model from left to right. Statistical uncertainties corresponding to an 8-fold sensitive mini-tracker area are plotted as barely visible error bands.

@ 50° 120 mm

a) Cavity in front of the tumor **b) Cavity in the middle of the tumor**

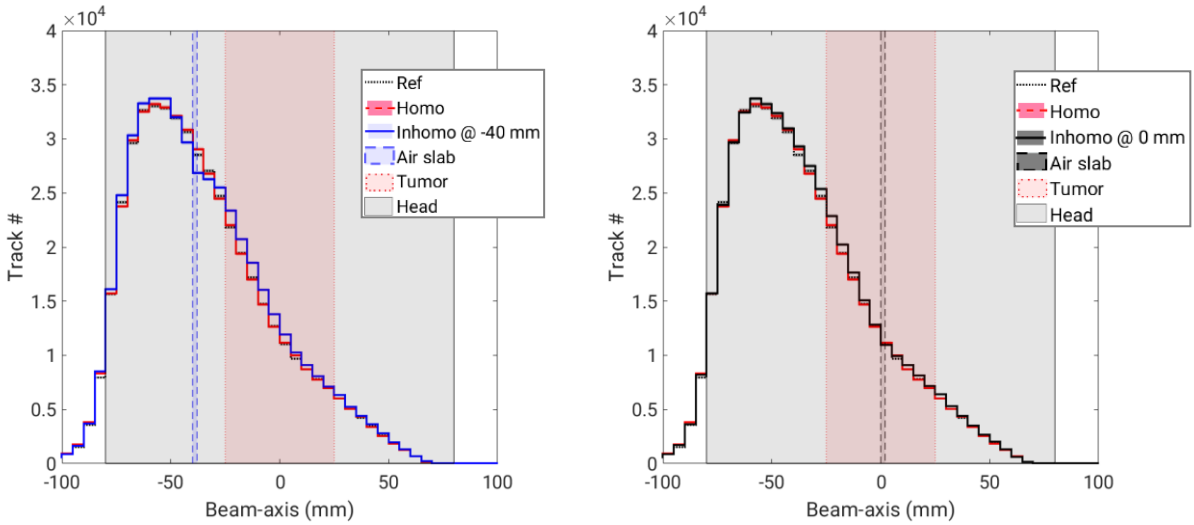

Figure 4.40: Secondary-ion emission profiles along the beam axis for fractions with and without a small air-cavity located in the front (a) or the middle (b) of the tumor volume as measured in the homogeneous head model at 50°/120mm. The head-model volume is centered at 0 mm along the beam axis and represented by the grey area, the tumor volume by the red one, and the inserted air cavity volume by the blue vertical dashed bands. The beam enters the head model from left to right. Statistical uncertainties corresponding to an 8-fold sensitive mini-tracker area are plotted as barely visible error bands.

@ 20° 160 mm

a) Ratio **b) Difference**

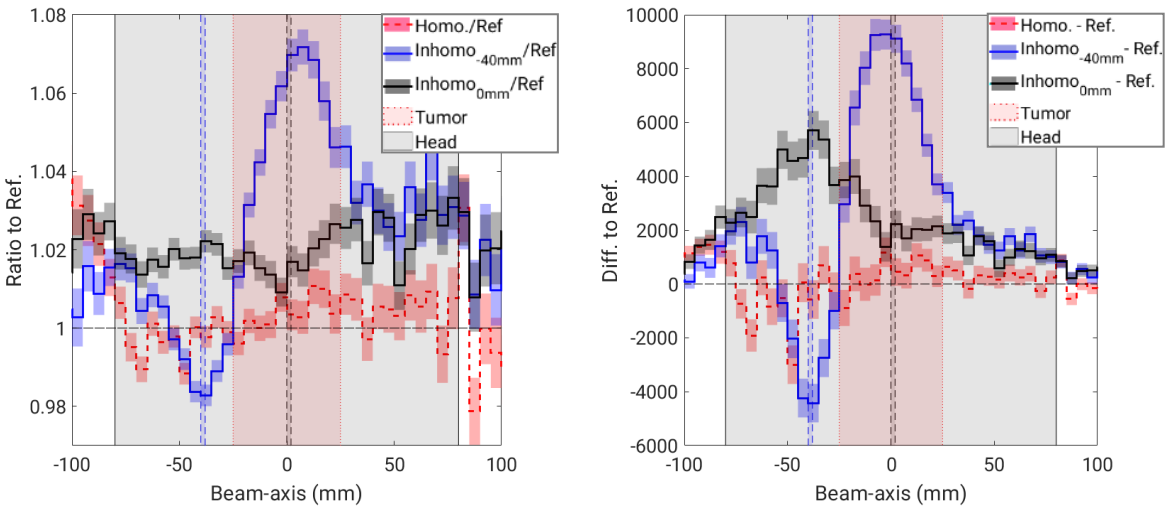

Figure 4.41: Ratios (a) and differences(b) between the secondary-ion emission profiles of the reference fractions versus the three follow-up fractions (two with and one without an air cavity) as measured at 20°/160mm. Statistical uncertainties corresponding to an 8-fold sensitive mini-tracker area are plotted as error bands.

@ 50° 120 mm

a) Ratio **b) Difference**

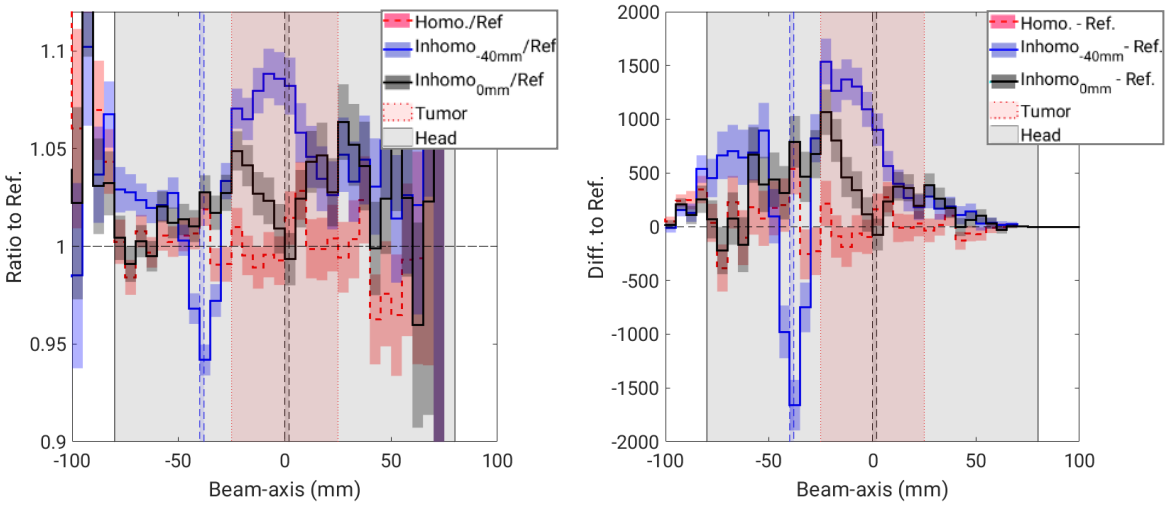

Figure 4.42: Ratios (a) and differences(b) between the secondary-ion emission profiles of the reference fractions versus the three follow-up fractions (two with and one without an air cavity) as measured at 50°/120mm. Statistical uncertainties corresponding to an 8-fold sensitive mini-tracker area are plotted as error bands.

For all investigated detection angles, the impact of the inserted air cavity was found to be particularly visible when it was located at the entrance (-40 mm depth) compared to in the middle of the tumor (0 mm depth). The maximal signal reduction at the location of the cavity is found for a detection angle of 50° in the case of the cavity located in front of the tumor. This corresponds to a signal reduction of 5.8 % ± 0.8 %. For the cavity located in the tumor, the maximal signal reduction measured at 50° is only 0.66 % ± 1.3 %.

4.3.3.2 Determination of the position of the change along the beam direction

Measurements of the position of the 2-mm-thick internal changes along the beam axis could be retrieved using both the ratios and differences by determining the position of the dip along the beam axis. These measured positions are presented in Figure 4.43-a) and -b). Both the positions of the maximum signal reduction Figure 4.43-a) and the minimum difference Figure 4.43-b) approximate the actual position of the inserted 2-mm-thick air cavity well for all investigated angles. The accuracy localization is defined as the difference between the measured and the actual cavity positions. Uncertainties on the localization of the cavity are estimated to be at maximum of the order of the bin size i.e. 5 mm.

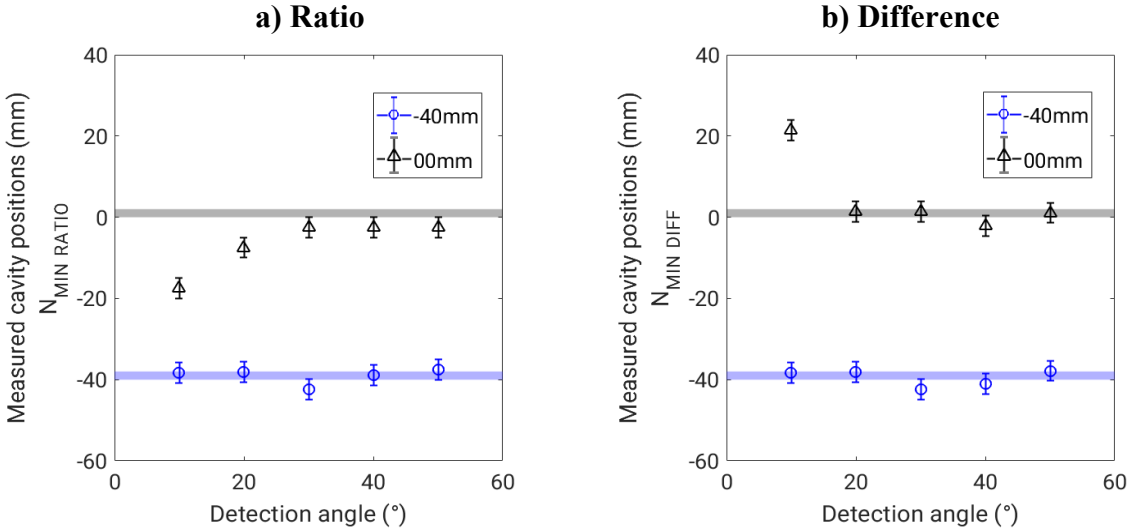

Figure 4.43: Measurement of the position of the 2-mm-thick internal changes (air slab) along the beam axis for each investigated mini-tracker position. Positions are retrieved using the weighted average position of the three minimal values in the profile of the ratio (a) and the profile of the difference (b). True cavity positions are shown with the horizontal bars. Error bars correspond to the statistical uncertainties on $Z_{MIN\text{-}RATIO}$ and $Z_{MIN\text{-}DIFF}$ which were estimated to be at maximum of the order of the bin size (5 mm).

The air cavity was properly localized with an accuracy within the bin width of the profile distribution (5 mm) for all detection angles when the air cavity was placed in front of the tumor. When the air cavity was placed deeper in the head model, it was properly localized with an accuracy below 4 mm for all detection angles except at 10° when using the profile of the difference and for all detection angles except at 10° and 20° when using the profile of the ratio. The best position accuracy was found at 50°, with an accuracy for both cavity positions below 1.2 mm from the profile difference, and below 3.5 mm from the profile ratio.

4.3.3.3 Quantification of the significance of the detection

A quantitative analysis of the detection significance of the 2-mm-thick air cavity was performed for all investigated detection angles. The integrals I_{WITH} and $I_{WITHOUT}$ determined along the entire head-model depth (i.e. from -80 mm to 80 mm) of the absolute difference between the measured secondary-ion emission profiles of the reference fractions versus follow-up fractions are plotted in Figure 4.44. In this figure, it is apparent that the integral values I_{WITH} decreased when the cavity was located deeper in the head model (0 mm air gap position, compared to -40 mm). Thus, the detection significance of an air-cavity decreases with increasing depth of the cavity position. Additionally, the integral values I_{WITH} decreased with increasing detection angles. The detection significance of the air-cavity decreases with increasing detection angles.

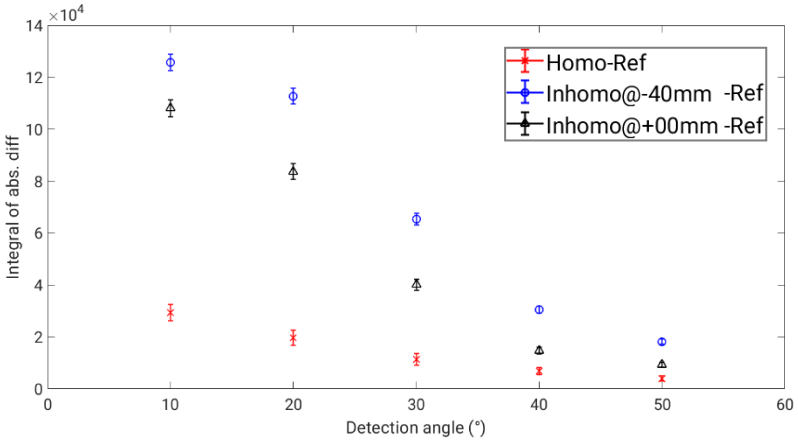

Figure 4.44 Integrals I_{WITH} (blue) and $I_{WITHOUT}$ (red) for all five investigated detection angles.

Moreover, D and $D/\sigma(D)$ were computed to investigate how significant the difference in the integral values between measurement without (I_{WITH}) and with the air-cavity ($I_{WITHOUT}$) was. See (Eq.3.31) and (Eq.3.33) for definition in section (§3.7.1.4.) of Materials and Methods. These *D-values* are plotted in Figure 4.45-a) -b).

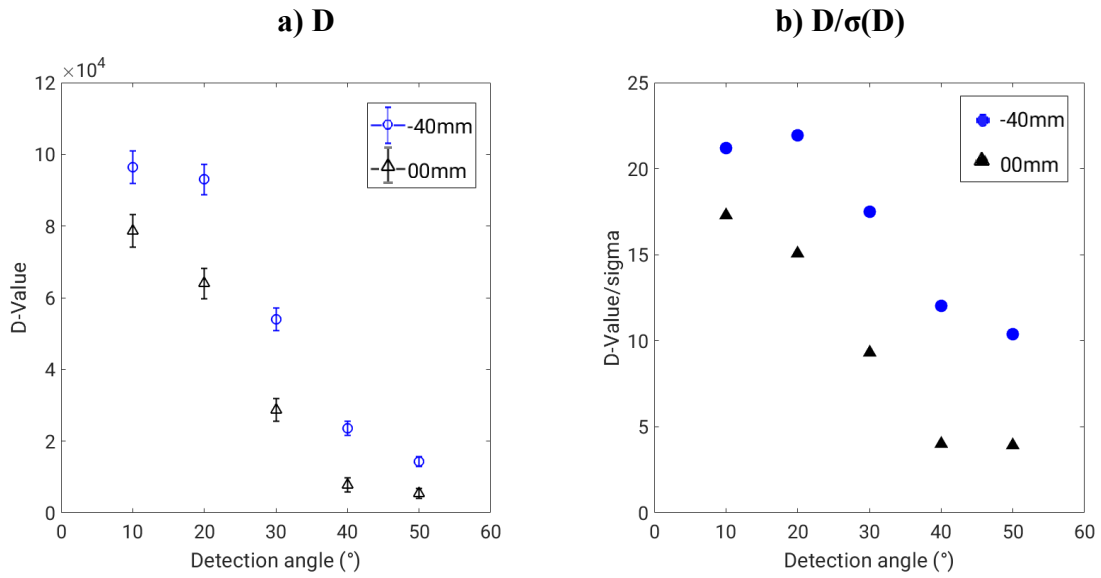

Figure 4.45: Detection significance (a) and detection significance divided by its uncertainties (b) for all five investigated detection angles.

In Figure 4.45-a) and -b), *D* and *D/σ(D)* values were found to be sufficiently large to allow significant detection of the cavity for all investigated detection angles and both cavity positions. The cavity in the middle of the tumor was found to be detectable with a significance of at least 3 sigmas, and the one in front of the tumor was found to be detectable with a significance of at least 9 sigmas (see *D/σ(D)* values in Figure 4.45-b)). At 30°, a significance similar to what was measured in (§4.2.2.) is found. The position of the mini-tracker at either 10° or 20° was found to be optimal for this setup, leading to the highest detection significance. The highest *D/σ(D)* values for cavity depths at 0 mm were measured at 10° (*D/σ(D)* = 17 sigmas). The highest *D/σ(D)* values for cavity depths at -40 mm were measured at 20° (*D/σ(D)* = 21 sigmas).

4.3.4. Summary of the ideal detection angle

The two main components contributing to the quality of the desired information needed for precise carbon-ion beam monitoring in depth are the geometrical uncertainties in the analysis of the track distribution using the track-projection method and the track yield.

From the track-projection geometry analysis using simulated secondary-ion tracks and the ground truth of the fragmentation position, it was observed that bigger detection angles lead to significantly better accuracy with respect to the primary ion fragmentation origin. The bigger the detection angle, the more accurate the track-projection is until the lack of a proper statistic impairs it.

From the measured and analyzed track yields, it was observed that the complexity of the irradiated head model, homogeneous or heterogeneous environment, does influence the track yield just in a minor way. In both head models, decreasing the distance of the mini-tracker to the tumor center or decreasing the detection angle of the mini-tracker with respect to the beam axis are the major factors influencing the track yield. Moreover, the track yield was analyzed per carbon-ion beam energy, and it was concluded that the track yield is increased for higher beam-energy layers, as these beam-energy layers exhibit a deeper range in the target, i.e. closer to the mini-tracker.

Given all the gained results, for the more accurate data analysis, which is governed by the geometry of the setup, bigger detection angles, are recommended. However, for better count statistics and, thus, for smaller uncertainties in the measured secondary-ion emission profile, monitoring of centered and deep-seated tumor measurement, measured at small detection angles, as close as possible to the beam axis; and at low distances, as close as possible to the target is recommended.

Improvements of the detection significance and localization of wide internal changes (2 mm x 80 mm x 80 mm) at the entrance (-40 mm) and deeper in the head model (0 mm) were investigated for different mini-tracker positions. No optimal detection angle was found to maximize both, the detection significance and the localization accuracy. Indeed, low detection angles (i.e. the closer to the beam axis) were found to lead to higher statistics, thus larger detection efficiency, but lead to larger geometrical uncertainties and thus to lower localization accuracy. For this setup, the best position accuracy was found at 50°, with an accuracy for both cavity positions below 1.2 mm from the profile difference, and below 3.5 mm from the profile ratio. The highest detection significances were found at lower detection angles (10° or 20°) with a detection significance of at least 21 sigmas for the cavity at -40 mm, and at least 17 sigmas for the cavity at 0 mm.

4.4. Multi-feature analysis

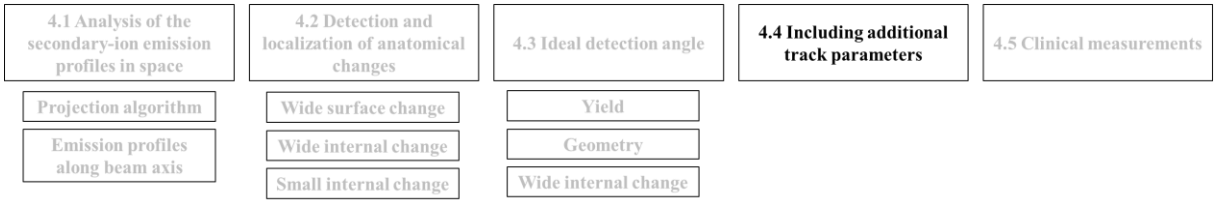

Figure 4.46: Current topic within the five topics presented in the results section of this thesis.

Results of the multi-feature analysis are presented in this chapter, see Figure 4.46. From each measured secondary-ion track, several additional features could be extracted in addition to the track origin depth (Z) information. The used additional features were the deposited energy dE/dl and cluster size S_C. These specific secondary-ion track features were investigated to analyze whether they convey any additional information regarding the internal anatomy change of the irradiated head model. The different features were combined in a single variable, to maximize the difference between the reference secondary ion emission profile and the emission profile measured when changing the internal structure. In case a better variable than the track origin depth (Z) is found, the entire single-feature analysis in terms of that variable can be performed exactly in the same way as it was presented in the above sections with the track origin depth.
The suitability of two additional variables (dE/dl and S_C) was investigated here for an improvement of the separation power of the secondary ion emission profile along the beam axis. The use of the energy loss per path of the secondary ions in the sensitive layers of the tracker is required to investigate the performance of the tracker to measure the energy deposition, as analyzed in the following section.

4.4.1. Energy deposition analysis for different detector bias voltages

In contrast to previous research with the Timepix detector (Félix-Bautista 2017; Gaa et al. 2017; Gwosch et al. 2013; Reinhart et al. 2017), the newer generation of detectors (Timepix3) used to build the mini-tracker employed in this thesis allows to simultaneously measure the time-of-arrival of the secondary ions (exploited for ion tracking) and the energy deposited by the ions in the sensitive layer of the mini-tracker. This additional information on the energy deposition was used in the above research to increase the precision of the calculation of the ion's impact on the detector by calculating an energy-weighted center of mass of the corresponding cluster measured by the mini-tracker. This information was expected to give additional valuable information on the ions measured by the mini-tracker. Partial depletion reduces saturation effects and has been shown to improve the energy deposition accuracy for ion measurements (Gehrke et al. 2017). During the experiments, the mini-tracker was thus operated at a low bias voltage (V_b = 10 V) such that both sensitive layers of the mini-tracker were partially depleted. However, this low bias voltage of 10 V applied to the silicon detectors can lead to a non-constant charge collection within the detector layer. Non-homogeneous patterns could thus be visible in the energy deposited at the surface of the partially depleted detectors.

Such a heterogeneous detector response during measurements would impair the multi-feature monitoring approach developed in this thesis. The measured deposited energy (*dE/dl*) variations might indeed not be only due to relevant changes in the patient anatomy but also due to the heterogeneous detector response. Further in-house analysis of the energy deposited on the partially depleted detector surface layers was therefore done to verify the homogeneity of the charge collection at the detector surface for the experimental setup used during this thesis specifically, as presented in section (§3.3.) of Materials and Methods. A bias voltage test was performed during the whole irradiation of a PMMA cylindrical head model with a clinic-like treatment fraction irradiation. The mini-tracker was placed 120 mm away from the tumor center, 30° with respect to the beam axis. The following five bias voltages V_b were investigated for both detector sensors: 10 V, 30 V, 40 V, 80 V, and 100 V, corresponding to depletion depths in the 300 µm silicon sensor of approximately: $d_{10V} \approx 118$ µm, $d_{30V} \approx 200$ µm, $d_{40V} \approx 231$ µm, $d_{80V} \approx 325$ µm and $d_{100V} \approx 363$ µm as calculated from (Eq.3.1). From 80 V on, the detectors were thus operated in full depletion. For each of the two detectors used in this thesis, the mean cluster energy deposition was computed for each pixel in the detector sensor as seen in Figure 4.47. This figure shows that, independently from the applied bias voltages, no clear patterns were visible in the energy deposited in the detector sensors when measuring under clinical conditions. The extracted overall mean and standard deviation of the mean energy deposition in each pixel averaged over the entire detector surface, as detailed in Table 4.2, also confirms this. A constant charge collection was therefore assumed for the experimental setup used during this thesis and a bias voltage $V_b = 10$ V was always applied.
However, in Figure 4.47, a small region positioned at the same location of both detectors (around $X = 40$ px and $Y = 25$ px in both detectors) seems to present a larger relative difference to the mean deposited cluster signal. Such a behavior located in both detectors could be due to possible radiation damages on the detector layers from direct in-beam carbon ion measurements. It is confirmed in Figure 4.48 that this region with a larger relative difference to mean deposited energy seems to have appeared over time within the course of the thesis.

Table 4.2: Overall mean and standard deviation of the mean energy deposition in each pixel averaged over the entire detector surface.

Bias Voltage V_b (V)	Detector name A07 or C07	Mean energy over detector surface (a.u.)	Std signal over detector surface (a.u.)	Pixels within 2 sigma (%)
10	A07	0.23	0.12	94
	C07	0.22	0.12	94
30	A07	0.34	0.13	96
	C07	0.33	0.14	95
40	A07	0.35	0.14	96
	C07	0.37	0.14	97
80	A07	0.41	0.15	98
	C07	0.41	0.15	97
100	A07	0.42	0.16	96
	C07	0.42	0.16	96

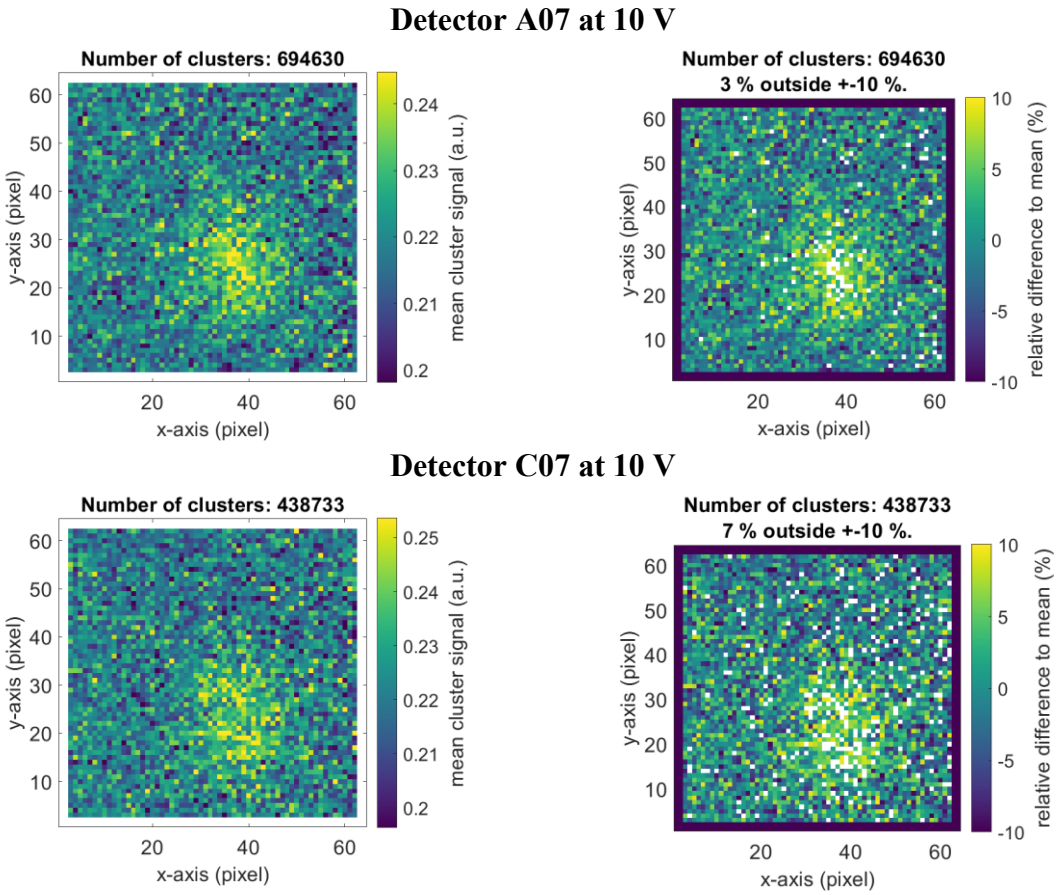

Figure 4.47: Mean energy deposition (left) of the ions in each pixel as a map of the A07 (top) and for C07 (bottom) detector surface for an applied bias voltage of 10 V. Pixels with a large relative difference to the mean are less than 7 % (see white pixels in the top right and bottom right).

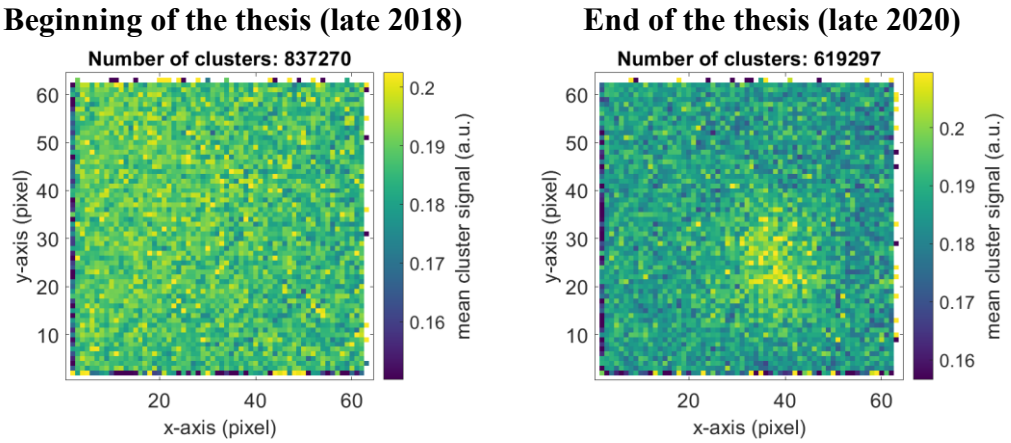

Figure 4.48: Mean energy deposition of the ions in each pixel as a map of the A07 detector surface layer over time for 10 V bias voltages. Left: at the reception of the detector (late 2018). Right: after a few years of use (late 2020).

4.4.2. Deposited energy dE/dl and origin-depth dependencies

One can expect that the energy deposited per unit path length *dE/dl* as defined in (Eq.3.13) and (Eq.3.14)) by a specific secondary ion in the sensor layers is correlated to the depth at which this ion was produced in an irradiated object. Indeed, for deeper a fragmentation location, the produced secondary ion tends to have a smaller energy, traveling slower in space and thus depositing more energy, *dE/dl*, in the sensor layer.

To verify this, secondary-ion tracks were measured during a clinic-like irradiation of an anthropomorphic head model by a mini-tracker positioned at a detection angle of 30° with respect to the beam axis, and 120 mm from the tumor center. As seen in Figure 4.49-a), the energy deposited per unit path length, *dE/dl*, by the measured secondary ion is quite similar in the first (dE_1/dl) and the second (dE_2/dl) sensitive layers of the mini-tracker. Only at a close look, there is slightly more energy deposited in the second layer ($\overline{dE_2/dl} = 1.2511$ MeV/mm) than in the first one ($\overline{dE_1/dl} = 1.4159$ MeV/mm).

To see if the energy deposited per unit path length, *dE/dl*, by a specific secondary ion in the sensor layers is correlated to the depth at which this ion was produced, a threshold of dE_1/dl = 0.9 MeV/mm was selected to separate the measured secondary-ion tracks into two sub-groups of high and low depositing energy in the front sensor layer. The secondary-ion emission profiles along the beam axis for each of the two sub-groups are plotted in Figure 4.49-b). There, the high depositing energy ions (dE_1/dl > 0.9 MeV/mm) are seen to originate from deeper in the head model, which coincides with what was previously hypothesized.

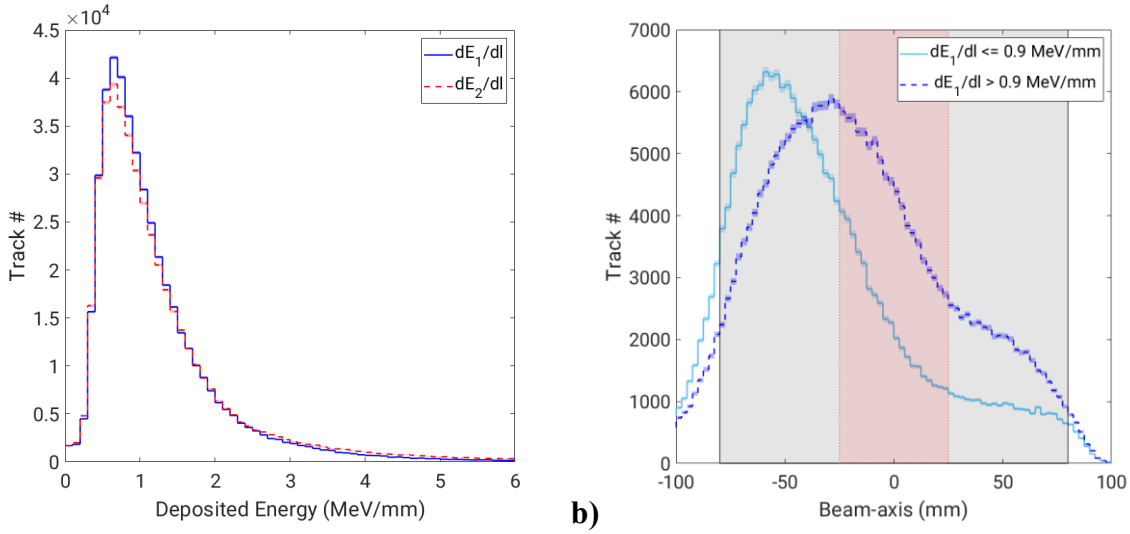

a) **b)**

Figure 4.49: (a) Distributions of *dE/dl* the energy deposited per unit path length in the two sensor layers of a mini-tracker as measured from clinic-like irradiation of an anthropomorphic head model with a mini-tracker positioned at 30° with respect to the bam axis, 120 mm from the tumor center. (b) Secondary-ion emission profiles along the beam axis for low and high energy deposited per unit path length in the front sensor layer (threshold at dE_1/dl = 0.9 MeV/mm). Corresponding statistical uncertainties are plotted as error bands. The 80-mm-radius head-model volume is centered at 0 mm and represented by the grey area, the 30-mm-radius tumor volume by the red one. The beam enters the head model from left to right.

Even though the energy deposited in the sensor layer *dE/dl* seems to be correlated to the secondary-ion track origin depth (*Z*) along the beam axis, as seen in Figure 4.49-b), no clear correlation between the secondary-ion track origin position along the beam axis and the energy deposited in either the first (dE_1/dl) or second (dE_2/dl) sensor layer of the mini-tracker was found, as shown in Figure 4.50-a)-b)-c).

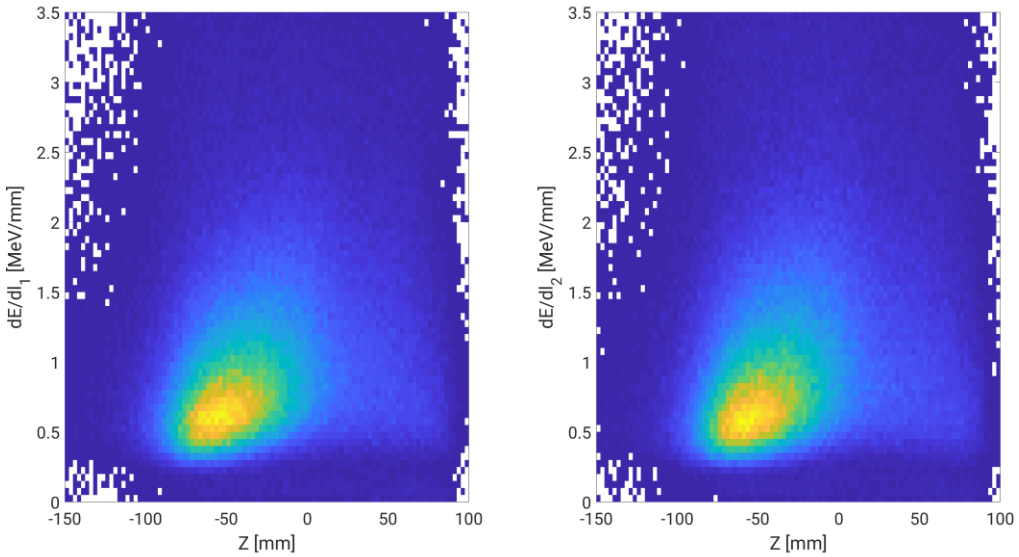

Figure 4.50: Correlation between energy deposited *dE/dl*, in sensor layer 1 and 2 and secondary-ion track origin depths (*Z*).

4.4.3. Compound variable X using several secondary-ion features

To investigate whether additional measured secondary-ion features (such as deposited energy *dE/dl* or cluster size S_C) can help to detect and to visualize anatomical changes in an irradiated head model, a linear compound variable *X* that is a linear combination of one or two of these measured features was investigated in a so-called Fisher analysis (Fisher 1936). The principle is, to build a variable that provides the best separation of the homogeneous case and the case with an anatomical change.

During this analysis, two clinic-like irradiations of an anthropomorphic head model acquired with and without a surface change of +2 mm were measured by a mini-tracker positioned at 30° with respect to the beam axis 120 mm from the tumor center. The 2-mm-thick surface changes were simulated by placing a small PMMA slab with a thickness of 2 mm upstream of the irradiated head model. The new compound variable *X* was then computed from the measured secondary-ion features to maximize the differences in *X* between two measured irradiations (with and without the surface change).

As explained in section (§3.7.3.) of Materials and Methods, the main compound of the variable *X* was set to be the secondary-ion track origin feature Z. One or two additional standardized features, (*dE/dl* or S_C), were then added to *Z* in a linear combination in the new compound variable *X* using the following formula obtained from (Eq.3.37):

$$X = 1 \times Z + a \times \frac{dE}{dl} + b \times S_C$$

The coefficients *a* (or *a&b*) of the new compound variable *X* were defined as the coefficients that maximize the differences in *X* between two measured data sets, see (§3.7.3.). These *a* (or *a* and *b*) coefficients were expected to be stable over several identical measurements. To check the reproducibility of the new compound variable *X*, the found *a* (or *a* and *b*) coefficients were thus plotted for several repeated measurements of the same clinic-like irradiation of an anthropomorphic head model. Figure 4.51 shows the *a* and *b* coefficients found for the optimization using three features.

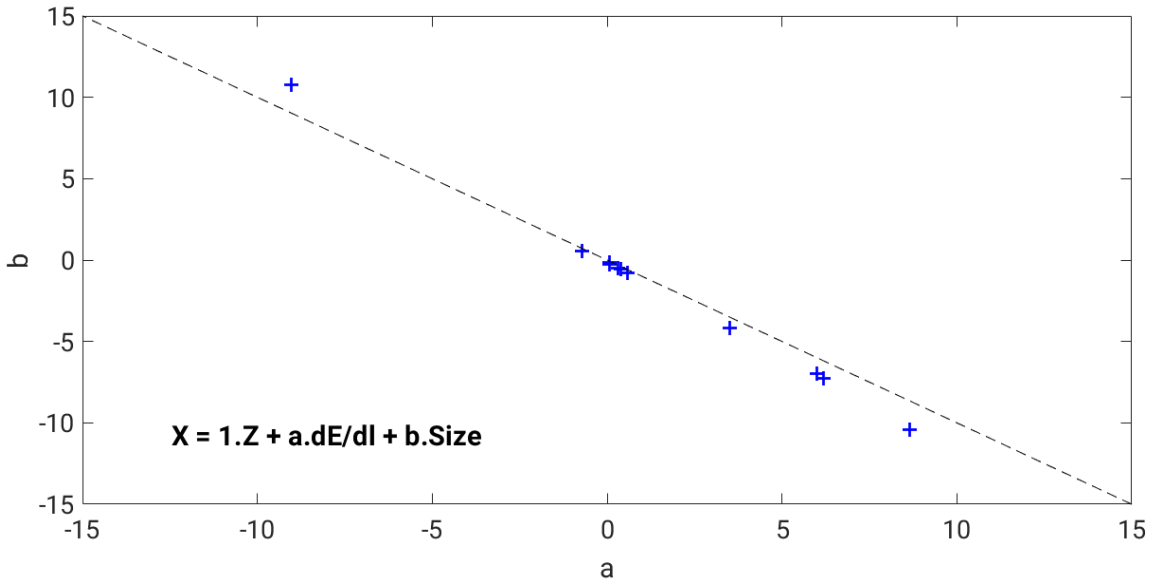

Figure 4.51: Found a and b coefficients of the new compound variable *X* using 3 features (projected origin depth *Z*, standardized energy deposited in the first sensor layer *dE/dl*, and standardized cluster size in the first sensor layer). The found variables *X* were optimized to maximize the difference in *X* between several repeated measurements of clinic-like irradiation of an anthropomorphic head model as measured by a mini-tracker positioned at 30° with respect from the beam axis, 120 mm from the tumor center with and without a surface change of 2 mm. The dashed line symbolizes the *b*=-*a* line.

In Figure 4.51, the *a* and *b* coefficients spread over a large set of values. They show, in general, a negative correlation which indicates that their contributions to the *X* variable compensate each other.

Unfortunately, for all the tested track features, no stable compound variable *X* was found, which would provide larger separation power than the measurement of the fragmentation point along the beam axis (Z). Indeed, the *a* (or *a&b*) coefficients of the new compound variable *X* were found to always strongly vary for several repeated measurements of the same setup.

4.4.4. Summary of the multi-feature analysis

To use the energy deposition of the secondary ions in the tracker layers as one of the track features, it was necessary to investigate the homogeneity of the energy deposition over both detector layers. The characterization of the energy deposition within the mini-tracker detector was performed to investigate the impact of the low bias voltages applied during the measurements presented in this thesis and it was investigated with respect to the ion charge collection. No distinct dependence of the energy deposition homogeneity over both tracker areas was found for different bias voltages. Therefore, a constant charge collection could be assumed for the mini-tracker, and measurements were always performed at a bias voltage of 10 V with partially depleted sensor layers.

A small heterogeneous region, most likely due to radiation damage was observed. This probably originates in free-in-air measurements in carbon ion beams. Therefore, it can be concluded that direct carbon ion irradiations with a high fluence should always be avoided.

From the multi-feature analysis, it was deduced that the additional investigated secondary-ion features, namely the deposited energy dE/dl, and cluster size S, do not provide improved performance of the method concerning the treatment monitoring. It was thus concluded that these features compensate each other or might not be relevant enough to detect anatomical changes in irradiated head models. Therefore, secondary-ion emission profiles along the beam axis (Z) were used alone to monitor the real patient treatment, as described in the next section. Still, it cannot be excluded that the deposited energy dE/dl and its information might be more useful for the detection of small anatomical changes if it would be measured with a higher bias voltage (and thus in a more depleted sensitive layer).

4.5. First clinical measurement during a real patient irradiation

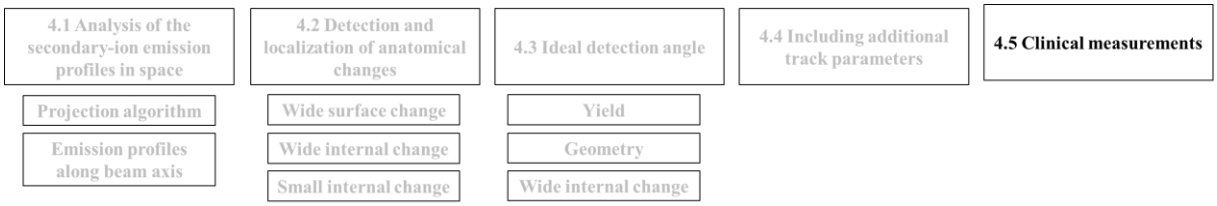

Figure 4.52: Current analysis within the five analyses presented in the results section of this thesis.

Parallel to pre-clinical investigations, and to evaluate the performance of the developed monitoring method in clinics, a first clinical measurement was performed at the Heidelberg Ion Therapy Center (HIT) during one of the fractions of a real patient treatment, see Figure 4.52.

4.5.1. Influence of the monitoring device on the beam monitoring system & beam delivery

To exclude impairment of the treatment by the constructed treatment monitoring device containing the mini-tracker and the computer hardware, the influence of the monitoring device on the beam delivery system was investigated[4] for clinical conditions. This influence test is also partly presented in (Félix-Bautista 2021).

Two influence tests were performed with the monitoring device inside the HIT treatment room:

- First, a check was performed on the influence on the beam monitoring system (BAMS). It was directly monitored in the two ionization chambers (ICs) of BAMS. The impact of the system on the ICs current offsets and thresholds was checked without any beam. If the BAMS is impacted, the measurement of the particle number is impacted too, this would have a direct influence on the radiation dose.
- Then, a check on the influence on the beam properties (beam width and position) was performed. It was monitored by two multi-wire proportional chambers (MWPCs) placed in the beam nozzle (MW1 and MW2), and by an additional MWPC placed at the isocenter (MW3), during a carbon-ion QA plan irradiation.

During these influence measurements, the signal of the BAMS was also monitored by the EtherCAT system to detect possible anomalies such as peaks or oscillations. The influence measurement results were compared with reference measurements in which the monitoring device was not located in the room. The monitoring device was operated in the same mode as used later during patient irradiation. During therapy, the monitoring device is usually positioned close to the patient's head and room isocenter (Figure 3.10 of Materials and Methods). During this influence test, the worst case was mimicked by positioning of the monitoring device as close as possible to the beam nozzle as seen in Figure 4.53.
Influence test results are presented in Table 4.3, Table 4.4, Table 4.5, and Table 4.6.

[4] with the help of Dr. M. Winter, medical physicist at the HIT facility.

Figure 4.53: Position of the monitoring device (including detectors and computer hardware) during the influence measurements of the device on the BAMS and beam delivery. These test measurements were performed in the treatment rooms H2 at the HIT facility.

4.5.1.1 Influence of the measurement setup on the beam monitoring system

The influence of the measurement setup on the BAMS can be evaluated by analyzing the measured current offsets (Table 4.3) and thresholds (Table 4.4) of the BAMS ICs. During the influence test, all measured offsets and thresholds were found to be within their tolerance. Thus, it was deducted that the monitoring device did not significant influence the BAMS.

Table 4.3: Influence on beam monitoring system: measurement of BAMS chamber offsets in the patient room, measurements 1 to 3 (M1-M3) were performed without setup in the room, measurements M4-M6 with setup in the room (courtesy of Dr. M. Winter).

Calculated Offsets (A.U.)	Range	Reference			With monitoring device			Tolerance	Significant variations
		M1	M2	M3	M4	M5	M6		
IC1	1	691	691	691	691	691	691	±3	NO
	2	690	691	691	691	691	691	±3	NO
	3	690	690	690	690	690	690	±3	NO
	4	688	688	688	688	688	687	±3	NO
IC2	1	680	680	680	680	680	680	±3	NO
	2	680	680	680	680	680	680	±3	NO
	3	680	680	680	680	680	680	±3	NO
	4	675	675	675	675	675	675	±3	NO

Table 4.4: Influence on beam monitoring system: measurement of BAMS thresholds in the patient room, measurements 1 to 3 (M1-M3) were performed without setup in the room, measurements M4-M6 with setup in the room (courtesy of Dr. M. Winter).

Thresholds (A.U.)	Range	Reference			With monitoring device			Tolerance	Significant variations
		M1	M2	M3	M4	M5	M6		
IC1	1	3	3	3	3	3	3	±1	NO
	2	9	9	9	9	9	9	±3	NO
	3	38	38	38	37	37	37	±9	NO
	4	113	111	113	113	113	114	±27	NO
IC2	1	3	3	3	3	3	3	±1	NO
	2	9	9	9	9	9	9	±3	NO
	3	38	38	38	38	38	38	±9	NO
	4	105	104	105	104	106	106	±27	NO

4.5.1.2 Influence on the beam properties (beam width and position)

The influence of the monitoring device on the beam properties can be evaluated by investigating the measured beam width (Table 4.5) and beam position (Table 4.6) as measured by the two multi-wire proportional chambers (MWPCs) placed in the beam nozzle (MW1 and MW2) and by an additional MWPC placed at the room isocenter (MW3). For the evaluation of the absolute variations in the beam position (Table 4.6), only the measured values of MW2 are relevant since it is part of the BAMS and positioned the closest to the patient compared to MW1. The values from MW3 (placed at the isocenter) are only listed for completeness.

During the influence test, all relative changes of the measured beam width and beam position were found to be non-significant (deviations of less than 10 % and less than 1 mm for the beam width and position respectively). Thus, it was deducted that the monitoring device did not influence the beam properties. The small deviations of the MW3 are not significant because the chamber position was moved between the measurements.

Table 4.5: Influence on the beam properties: relative variations (%) of the measured beam width relative to reference measurement (courtesy of Dr. M. Winter).

Beam width	MW1 (%)		MW2 (%)		MW3 (%)		Significant variations
	x	y	x	y	x	y	
Mean value	2	1	2	1	1	1	NO
Min	-1	0	-1	0	-1	0	NO
Max	8	5	8	4	2	3	NO
Std. dev.	2	1	2	1	1	1	NO

Table 4.6: Influence on the beam properties: absolute variations of beam position (mm) relative to reference measurement (max. allowed deviations of 1 mm) (courtesy of Dr. M. Winter).

Beam positions	MW1 (mm)		MW2 (mm)		MW3 (mm)		Significant variations
	x	y	x	y	x	y	
Mean value	*regulating chamber, not relevant*		0.00	-0.02	-0.05	0.24	NO
Min			-0.02	-0.07	-0.09	0.15	NO
Max			0.01	0.03	0.00	0.52	NO
Std. dev.			0.01	0.02	0.02	0.08	NO

Given Table 4.3, Table 4.4, Table 4.5, and Table 4.6, the observed variations between the IC and MWPCs measurements in terms of IC offsets, IC threshold, beam widths, and beam positions were found within the range of the usual fluctuations.
The influence measurements showed no significant influence of the monitoring device (including detectors and computer hardware) on the clinical treatment beam delivery.

4.5.2. Measured secondary-ion emission profiles

After fulfilling the safety requirements concerning its influence on the beam delivery, as well as the safety requirements concerning its electrical protection, as presented in section (§3.3.2.4.) of Materials and Methods, the monitoring device was accepted to be used during a clinical treatment delivery at the HIT facility.

4.5.2.1 Global secondary-ion emission profiles along the beam axis

For the first clinical study of the developed method, a head-and-neck patient with a tumor volume of 73.85 cm^3 treated with two fields at the angles of 5° and 330° was accessed. One fraction of the 5° field was measured using the mini-tracker positioned at 30° with respect to the beam axis, and a distance of 160 mm from the patient tumor center. The secondary-ion emission profile along the beam axis as measured behind the patient head is shown in Figure 4.54. In this figure, the secondary-ion emission profile was found to have a similar shape compared to the emission profiles found during pre-clinical measurements, such as in Figure 4.5. However, the patient distribution spreads over larger depths and has overall larger statistical uncertainty than the pre-clinical measurements, which is caused by the very shallow tumor depth, leading to the low number of acquired secondary ions per primary carbon ion pencil beam:

- $Yield_{\Omega\ Patient} = 12.1 \times 10^{-3}$ primary $^{-1}.sr^{-1}$ with $\Omega_{160mm} = 7.6$ msr.
- $Yield_{\Omega\ Alderson\ head\ phantom} = 45.9 \times 10^{-3}$ primary $^{-1}.sr^{-1}$ with $\Omega_{120mm} = 13.6$ msr.

Further quantitative comparison on the overall number of detected tracks in the patient and in the anthropomorphic head phantom is not relevant here due to the difference in the treatment field configuration, tumor shapes, and sizes, target anatomy, dose distribution, etc.

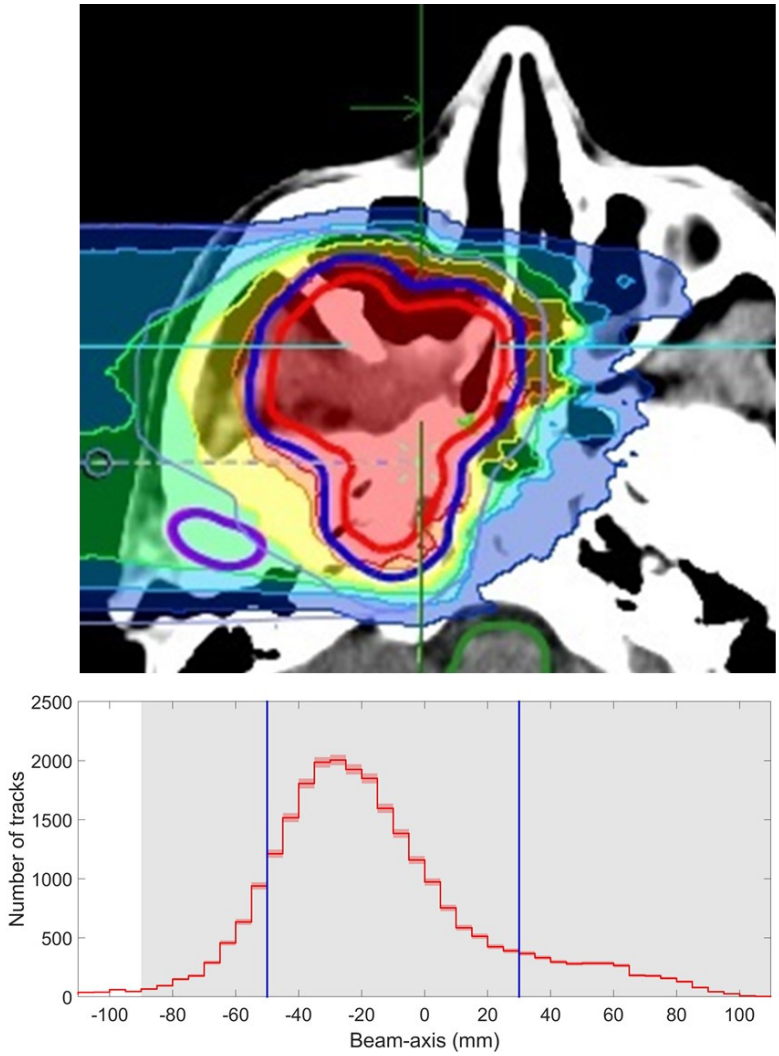

Figure 4.54: Secondary-ion emission profile along the beam axis as measured for the head of the treated patient. Corresponding statistical uncertainties are plotted as error bands. The head volume starts at -90 mm and is represented by the grey area, the tumor volume is represented by the two vertical blue lines. The beam enters the head from left to right. The treatment plan including PTV overlaid with patient CT image is plotted on top of the profile.

4.5.2.2 Secondary-ion emission profile along the beam axis per therapeutic beam energy

For the vast majority of the therapeutic beam energies of the carbon-ion beams used during the patient's fraction irradiation, it was possible to visualize the secondary-ion emission profiles along the depth, as shown in Figure 4.55 and Figure 4.56.

Due to the high heterogeneity of the tumor region, which spreads over several air cavities, bony structures, and soft tissues, no unambiguous correlation between the beam energies and the position of the secondary-ion emission profiles could be made. As seen in Figure 3.33 carbon ions of the same beam energy were found to stop at very different positions along the beam axis, i.e. with expected stopping positions (Z_{EXP}) in the patient head spreading over several centimeters in depth.

For the lowest two beam energies (E1 (95.67 MeV/u) and E2 (102.22 MeV/u) no or only a few secondary-ion tracks were measured. For the reason see section (§4.5.3.).

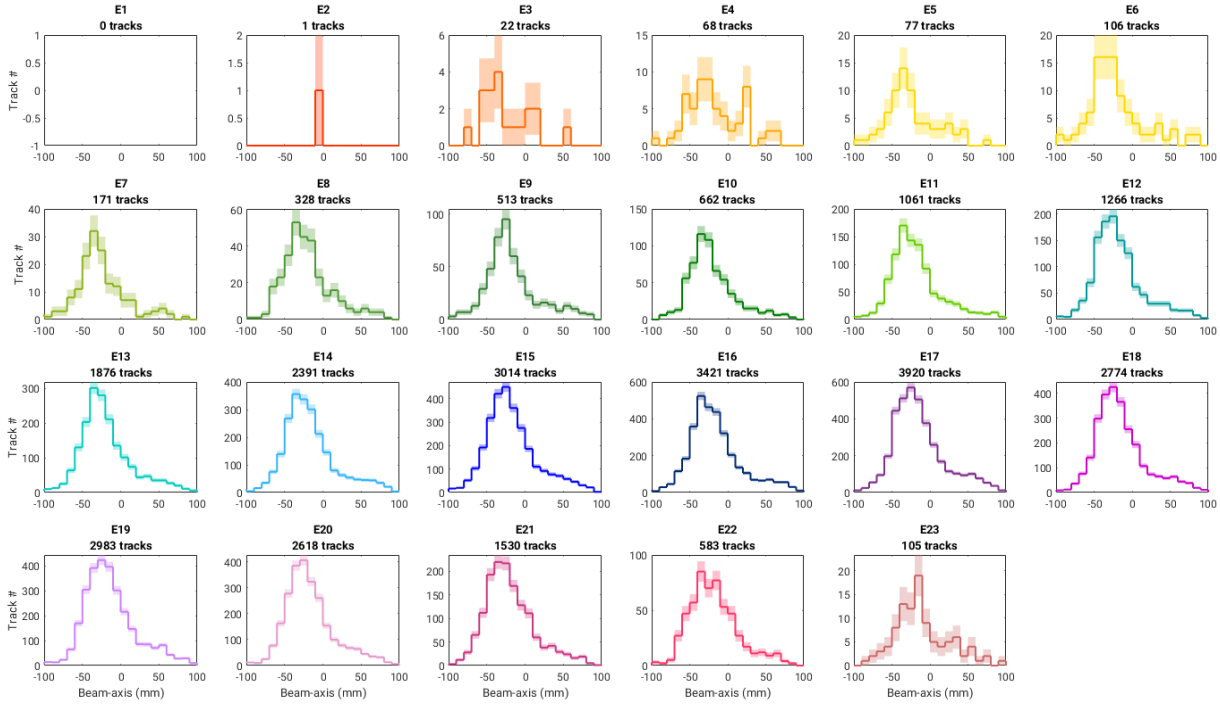

Figure 4.55: Secondary-ion emission profiles along the beam axis per all therapeutic beam energy layers as measured from the patient's head. Corresponding statistical uncertainties are plotted as error bands

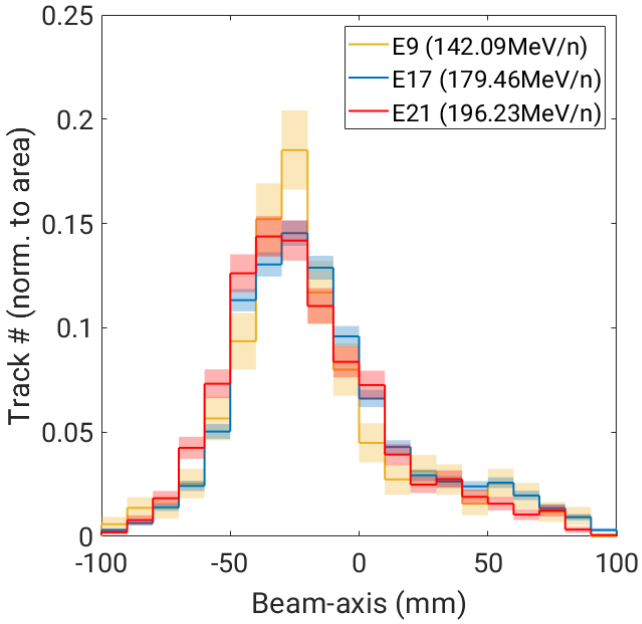

Figure 4.56: Secondary-ion emission profiles along the beam axis per therapeutic beam energy layers as measured from the patient's head for three different beam energy layers. Unlike the head model (Figure 4.6), a large overlap of each emission profile within their uncertainties is seen.

4.5.2.3 Secondary-ion emission profiles along the beam axis per expected stopping positions

Because the measured secondary ion emission profiles spread over too many centimeters in depth in the patient head, the secondary-ion origin distributions were plotted per expected stopping positions (intervals of 10 mm), to investigate the correlation of the emission profiles with the stopping positions of the pencil beams.

As detailed in section (§3.7.2.2.) of Materials and Methods, four longitudinal regions were defined in the patient's head depending on the expected stopping positions (Z_{EXP}) of the pencil beams of the treatment plan, considering the stopping power of the patient's tissue. See Figure 3.34 for the positions of these four regions overlaid with the patient treatment plan.

From these four longitudinal regions, four corresponding secondary-ion emission profiles were then established for each of the regions. As seen in Figure 4.57, clear variations in the emission profiles per expected stopping positions were visible for each of the longitudinal regions.

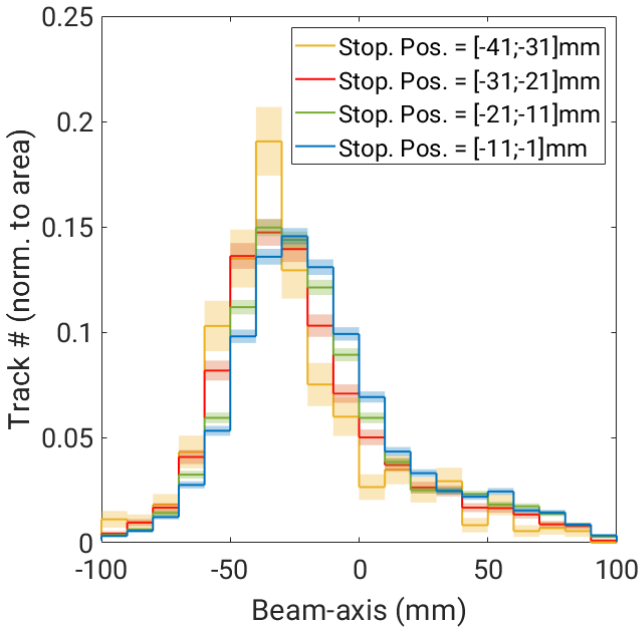

Figure 4.57: Secondary-ion emission profiles along the beam axis per expected stopping position (Z_{EXP}) of the primary carbon ions as measured from the patient's head. Corresponding statistical uncertainties are plotted as error bands. Less overlap and clear variations of the emission profiles are found.

4.5.3. Summary of the first clinical implementation

In this first clinical measurement, the developed method was investigated for the first time during a real patient treatment irradiation. It was not aimed at the detection of inter-fractional changes since only one fraction of the patient treatment was measured.

Even though the track yield was lower for this first clinical application, the measured data contained a sufficient number of tracks to allow for the establishment of secondary-ion emission profiles with reasonable statistics along the depth of the patient head for the vast majority of the therapeutic beam energies of the carbon-ion beams used during the patient's fraction irradiation. Though the first two beam energies were too small to allow for the secondary ion to have a sufficient residual range to exit the patient's head and reach the mini-tracker.

In particular, the generation of secondary-ion emission profiles of pencil-beam groups formed based on their expected stopping positions yielded profiles that could be differentiated significantly.

Considering the significantly higher track yield that is aimed for future studies with at least 10 x larger active detection area (currently planned is 14 x larger) these results are very promising. The detection of inter-fraction changes as presented in section (§4.2.) seems thus to be applicable in such a clinical setup.

Given the results presented in (§4.2.3.) and in this section, sampling a tumor volume in the lateral (X_{PB}, Y_{PB}) and the longitudinal (Z_{EXP}) dimension appears to be feasible. The combined information on the lateral and longitudinal positions of an inter-fractional change could be investigated this way. The success of such a discretization in three dimensions is, however, highly dependent on the quantity of measured data, as each region needs to contain a sufficient number of secondary ions to produce secondary-ion emission profiles that are not governed by noise only.

A lower number of secondary ions was detected in this clinical measurement compared to pre-clinical measurements (see §4.3.2.). This can be explained by three main factors: the position of the mini-tracker (1), the position of the patient tumor (2), the two-beam directions of the treatment plan (3). Each factor is detailed in the three following:

(1) As observed in section (§4.3.2.) the reduction of the track yield is impacted by the larger distance to the tumor center of this clinical measurement (d = 160 mm) compared to the pre-clinical ones (d = 120 mm). This is expected to lead to a decrease factor of ~2.

(2) As shown in the treatment plan and CT images of Figure 3.4, the very shallow position of the patient tumor as compared to the head-model tumors led to the use of lower beam energies of the carbon-ion beams. These smaller beam energies directly contributed to the lower track yield. In this measurement, the track yield was the lowest for the beam energies E2, and no secondary-ion track was detected from the smallest beam energy E1 to E6. This smallest beam energy of 95.67 MeV/u corresponds to a carbon-ion range in water of 2.4 cm (Aarhus Particle Therapy Group 2021; Lühr et al. 2012; Toftegaard et al. 2014). Produced secondary ions (mainly protons) are thus expected to have a low residual range, not enough to allow for the produced ions to leave the patient's head and reach the mini-tracker.

(3) The real patient treatment plan contained two beam directions. However, only the 5° beam direction was measured, corresponding to a fraction dose of only 0.84 Gy (RBE), less than a third of the pre-clinical treatment plan fraction doses which used 3 Gy (RBE).

5. Overall discussion

5.1. Novel algorithms for the analysis of the measured secondary-ion tracks in 3D

The previously used 2D track-projection method as presented by (Gwosch et al. 2013) and (Gaa et al. 2017) suffers from large geometrical uncertainties especially for pencil beams further away from the isocenter, see (§4.1.1.), Figure 4.4, before -80 mm along the beam axis. This is due to MCS and a so-called smearing effect, caused by the finite beam width and by projecting all secondary-ion tracks into a single plane, while they may originate from the entire irradiated head-model volume. This effect was found to significantly decrease when using projection planes of each pencil beam (in the time-dependent 2D+ method) or even by finding the closest distance between the secondary-ion track and the pencil-beam line (in the time-dependent 3D+ method).

The presented comparison of track-projection algorithms was based on MC simulations. MC simulations are, however, still known to present some limitations such as the lack of benchmarking data on fragmentation processes in the therapeutic energy range (Dedes et al. 2015). Nevertheless, the MC simulations presented here were found to be in a qualitative agreement with the measured data. Thus, conclusions on the performance of the different track-projection algorithms are assumed to be reasonable.

The profiles of the secondary-ion track origin positions along the beam axis (also called emission profiles) were extracted from the measured data using the 3D+ track-projection algorithm for all investigations in this thesis. The secondary-ion emission profiles obtained for the entire treatment irradiation (see Figure 4.5) are found to be similar in shape to former profiles presented in (Gwosch et al. 2013) and (Gaa et al. 2017). However, neither qualitative nor quantitative comparisons can be made, as the published profiles were measured for mono-energetic pencil beams only and the irradiated dose, dose rate, beam positions, and ranges, differ significantly from the investigations presented in this thesis.

5.2. Detectability of anatomical changes using secondary-ion emission profiles

The newly developed method exploiting the measured secondary-ion emission profiles was shown to enable the detection of inter-factional anatomical changes down to 2 mm, located both at the surface and inside a head model.

Several shapes and positions of internal cavities were investigated (see §4.2.4.). The thickness of the change of 2 mm is significantly thinner than previously investigated changes such as 10 mm of air (Gaa et al. 2017) or inserts of 28.5 mm (Reinhart et al. 2017) and 28 mm thicknesses (Finck et al. 2017). The 2-mm-thick change is the goal given by clinical practice. If changes of less than 2 mm in the head region would be detected, the plan would not be adapted. Larger thicknesses would exceed the currently used margin of 3 mm.

In this work the wide internal cavity dimensions were detectable at all investigated positions with at least 9 sigmas when using data corresponding to 8 mini-trackers, and with at least 3 sigmas when using the data of 1 mini-tracker. The most significant detection was found for cavities located at the entrance of the head model, where most secondary-ion tracks originate

from. Detectability is observed to further improve at low detection angles, i.e. with a mini-tracker placed close to the beam axis at 10 or 20 degrees.
The narrow internal cavity of 10 cm diameter was detectable upstream of the tumor with at least 2 sigmas when using the data amount corresponding to eight mini-trackers with the developed method using a grouping of the measured data in the lateral dimension. The grouping of pencil beams to decrease the statistical uncertainties of carbon-ion beam radiation therapy monitoring has also been investigated by (Fischetti et al. 2020) where super pencil beams of 1 cm × 1 cm × 0.6 cm volume were defined. In this thesis, the lateral dimension was subdivided into regions of 20 mm x 20 mm to find out which pencil beams were affected by the inter-fractional change of the structure.

5.3. Localization of anatomical changes using secondary-ion emission profiles

The method developed for finding out the position of the change along the beam direction enables localization of inter-factional anatomical changes located inside a head model with an accuracy below 6 mm for both the wide and the narrow 2-mm-thick air cavity, which fulfills the requirements from clinical practice.
The localization is even better for air cavities located at the entrance of the head model, allowing for accuracy of down to 1.5 mm. The accuracy is seen to improve at large detection angles, i.e. with the mini-tracker placed further from the beam axis.

5.4. Ideal detection angle

The two main components contributing to the quality of the carbon-ion beam monitoring in depth are the geometry uncertainties of the track-projection and the track yield. Both are dependent on the angular position of the tracker with respect to the beam axis. To investigate which mini-tracker position is the best to detect and localize inter-fractional anatomical changes, analyses of the track-projection geometry and the track yield were performed at different detection angles (see §4.3.1. and §4.3.2.)
From the projection geometry analysis, bigger detection angles lead to significantly better accuracies in terms of the primary ion fragmentation origin and thus to a decrease of systematical uncertainties.
The order of magnitude of the measured track *Yield*$_{\Omega}$ found in this thesis at 30° is in accordance with other published yields from other research groups. It is smaller than what was measured at 10° in (Gunzert-Marx et al. 2008) or in (Finck et al. 2017), yet larger than what was measured at larger angles 60° to 90° in (Rucinski et al. 2018) or in (Piersanti et al. 2014) and (Mattei, Bini, et al. 2017).
From the projection geometry analysis, bigger detection angles lead to significantly better accuracy with respect to the primary ion fragmentation origin.
Increasing detection angles lead to an approximately exponential decrease in the track yield. Additionally, this exponential relationship is in accordance with the track yields of secondary protons from (Gunzert-Marx et al. 2008). This decrease leads to an increase of the statistical uncertainties in the measured secondary ion emission profile, which was confirmed in the measurements of section (§4.3.3.). Therefore, to decrease statistical uncertainties, a lower detection angle, closer to the beam axis, is preferred. However, it was demonstrated that signal

pileup might impair the measured data at low detection angles or small distances to the center of the tumor. Consequently, this effect needs to be kept in mind when aiming at maximizing the track yield.

5.5. Further research

5.5.1. More complex targets, cavities, and simulations

To bring the developed monitoring method closer to clinical application, further studies with complex head models, e.g. 3D-printed, with fillable air cavities, would be valuable to investigate the capabilities of the method in more complex environments.
Additionally, more complex cavity shapes, positions, and densities should be investigated as well as controlled models of realistic clinical situations. The corresponding data on the geometries can be extracted from the therapy planning data of patients already treated.
Moreover, more complex MC-simulations should be used to investigate the developed method and its results under more realistic conditions (both more complex head models and cavities). Combining the recent work of (Abbani 2020) and (Schlechter 2021), MC-simulations of complex clinical treatment plans irradiating altered anthropomorphic head models are expected to give valuable insight into the capabilities of the developed method to detect small intra-fractional changes under several different realistic conditions.
A basic prerequisite for such research is a sufficient benchmarking of secondary ion emission profiles, which are dependent on the fragmentation models incorporated in the simulations.

5.5.2. Larger and multi-angle detection systems

Several types of tracking detectors have been used for ion beam range monitoring. These detector types include scintillating fiber detectors (Bisogni 2019; Rucinski et al. 2018; Traini et al. 2019), CMOS monolithic active pixel detector (Finck et al. 2017; Henriquet et al. 2012; Reidel et al. 2019), or hybrid pixelized silicon semiconductor detectors (Félix-Bautista 2017; Gaa et al. 2017; Gwosch et al. 2013). Compared to other detector types, the Timepix3 hybrid pixelized silicon detector used for this thesis offers versatile setups where a 2-cm^2-module is sufficient to acquire enough data to produce secondary-ion emission profiles used for the detection and the localization of internal anatomical changes.
The developed method was seen to rely on sufficient data acquisition to provide meaningful results with reasonable statistics. Most of the experimental results presented in the result sections (§4.2.2.) and (§4.2.3.) were achieved using eight repetitions of the same fraction irradiations. Future studies should investigate larger sensitive areas of the tracker to uncover the full potential of the monitoring method. To this end, larger sensitive sizes of the tracker can be constructed by using two sensors side-by-side in a 2x1 sensor surface, or four sensors in a 2x2 sensor surface, as already simulated and studied in (Abbani 2020). It was found that doubling the detection area (2x1 sensor surface) increased the track yield by up to three times. Quadrupling the detection area (2x2 sensor surface) increased the track yield by up to six times. First experimental investigations using a newer generation of mini-trackers with a 2x1 sensor surface are in progress within the scope of the work towards a clinical application of the method at DKFZ.

Moreover, simultaneous track detection using several mini-trackers placed at different angles would be of interest to reach both, sufficient detectability and localization of the changes in clinical conditions. For this, the combined results of section (§4.3.) and of (Schlechter 2021), pave the way to such simultaneous detections. A mini-tracker placed at low detection angles exhibiting lower statistical uncertainties will increase the detectability of any inter-fractional changes inside the patient's head. Simultaneous measurements at larger detection angles will permit localization of this detected change along the depth of the head.
In general: since the secondary emission is not isotropic (like PET or prompt gammas), a wise positioning of the tracker is of the highest importance.

5.5.3. Improving the analysis of the measured track distributions

In this thesis, the method included all measured secondary-ion tracks regardless of their direction. However, a selection of specific measured tracks considering, for example, the distance between the track and the primary beam axis could potentially lead to further improvements of the method. The bigger this distance, the larger the influence of multiple Coulomb scattering (MCS) on the secondary ion on its way through the head is assumed. Therefore, selecting tracks with only a small distance to the primary beam axis could improve the performance of the monitoring method.
The advantage of Timepix3's simultaneous measurements of secondary ion time of arrival and energy deposition was not fully investigated for track selection to enhance the performance of the method. So far, variations in the secondary-ion emission profile along the beam axis (Z), have mostly been used alone to monitor carbon-ion beam delivery in patients or patient models (Gaa et al. 2017; Gwosch et al. 2013; Traini et al. 2017). However, additional measured secondary-ion features, such as deposited energy dE/dl and cluster size S_C, were investigated here to analyze if these features convey relevant information to complement monitor carbon-ion beam delivery in patients (see §4.4.). It was concluded that these additional features might compensate each other or might not be relevant enough to detect anatomical changes in irradiated head models. A more precise measurement of the deposited energy dE/dl, which could be achieved using a higher bias voltage of the detector, might be more useful in the analysis to detect and track small anatomical changes. A possible improvement of the precision of the developed monitoring method can be reached by including the energy information conveyed by the secondary ions outgoing the patient body during the treatment using a calorimeter; measuring the total energy of the detected secondary ions.
Besides, the acquired data allow extracting more cluster parameters of the detected ions than just the cluster size investigated in this thesis. This source of information should be closely investigated in the future.
This monitoring method could be used in the future for online longitudinal pencil-beam monitoring if online access to the pencil beam lateral positions is possible and if fast online data evaluation is developed on respectively fast computational devices.
Given section (§4.2.3.2.) and (§4.5.2.3.), simultaneous sampling of a tumor volume in both lateral (XY) dimension but also the longitudinal (Z_{EXP}) dimension became technically feasible. Such a sampling of the tumor volume in sub-cubes, also called "super pencil beams" in (Fischetti et al. 2020), is expected to allow for a better understanding of where anatomical

changes are located in an irradiated volume. However, the success of such a discretization in three dimensions is highly dependent on the quantity of measured data, as each region needs to contain a sufficient number of secondary ions to derive secondary-ion emission profiles from, which are not governed by noise only.

5.6. Clinical implementation and rationales

PET-based monitoring techniques were (and are) implemented in clinics, however not on a wide scale. These techniques are still bound to inherent PET limitations such as biological washouts and traveled distances by positrons. Currently, no secondary-ion-based monitoring techniques are routinely used in clinics yet. The first results of a secondary-ion-based monitoring technique on a clinical trial were recently published (Fischetti et al. 2020). In this study, secondary ions were used to monitor potential inter-fractional changes in the anatomy of three treated patients. For one patient, a clear change was visible in the shape of the measured secondary emission profile. This change was correlated with an actual change of the anatomy in the patient (as seen in their re-evaluation CT). No details were given on the dimension of the visualized change. Further refinement of the method is ongoing to evaluate the sensitivity of the method to detect inter-fractional changes.

The first clinical implementation within this thesis, as detailed in section (§4.5.), combined with (Félix-Bautista 2021), shows that the developed method allows for simultaneous independent measurements of the lateral and longitudinal positions of carbon-ion pencil beams in a patient and could be implemented into clinics directly.

As discussed in section (§4.5.), the method was successfully implemented in a clinical workflow and is thus ready to be evaluated in a bigger clinical study on a larger group of patients.

Lastly, for a clinical application of the method, clinical action thresholds should be defined considering the measured impact of the detected inter-fractional change on the dose delivery and its position with respect to OARs.

The global aim of this thesis was to investigate and further develop a monitoring method for carbon ion radiotherapy based on secondary-ion measurement and tracking from patient's head and under clinical conditions. Within this thesis, secondary-ion emission profiles were measured and analyzed to detect and localize small anatomical changes in patient-head models. The final purpose of this thesis was to demonstrate the applicability of the monitoring of carbon-ion pencil beam delivery in real patient treatment by designing a patient-friendly measurement setup and integrating it into a clinical workflow. Within the frame of this thesis, first patient measurements for carbon-ion pencil beam monitoring using secondary-ion tracking were performed at the Heidelberg Ion Therapy center, HIT, paving the way to a clinical application of the whole method.

6. Summary

The advantages of carbon-ion pencil beam radiotherapy imply an increased sensitivity of the dose distribution in the patient to any changes in the patient geometry, such as internal anatomical changes or patient misalignment. This can lead to a deterioration of the dose distribution within the patient. Monitoring methods of the internal patient's dose distribution for carbon-ion beam radiotherapy are therefore of great importance to early detect possible under- or over-dosage in the patient, eventually, reduce the tumor safety margins applied around targeted tumor volumes and thus decrease the delivered dose in healthy tissues. Up to now, several non-invasive *in-vivo* ion-beam monitoring methods have been developed. These are mostly based on the detection of different kinds of secondary radiation, such as annihilation-photons from β+ emitters, prompt photons, or prompt charged nuclear fragments, emitted from a patient during the treatment delivery. These secondary radiations are the results of nuclear interactions of the primary treatment beam with the irradiated tissue. They potentially carry valuable information about the primary treatment beam range, position, or intensity in the patient. However, so far none of the monitoring methods has reached sufficient maturity for a wide application in clinical routine.

This thesis aimed to develop methods for detection and localization of therapy-relevant geometry variations of 2 mm in head models, mimicking possible inter-fractional changes on the surface or inside patients' heads. In contrast to previous research which concentrated on single stationary pencil beams, this thesis was focused on entire therapy-like treatment plans composed of thousands of single pencil beams with low numbers of primary-ions and irradiated under clinic-like conditions in terms of dose, dose rate, and tumor volume.

In this thesis, methods were based on the detection and tracking of charged secondary nuclear fragments (secondary ions) emitted from the patient during carbon ion radiotherapy delivery. Subsequently, methods for analysis and interpretation of the measured secondary-ion paths (tracks) were developed. The developed radiation detection methods exploited the capabilities of a novel mini-tracker, based on the Timepix3 technology developed at CERN and positioned behind the patient. The deadtime-free data acquisition enabled a gapless recording of all impacting secondary ion tracks. Moreover, it enabled synchronization of the data with the beam application monitoring system, and thus assign each measured secondary ion with its respective pencil beam, opening entirely new research possibilities.

The experiments were performed at the Heidelberg Ion-Beam Therapy Center (HIT), closely mimicking clinic-like conditions. Single fields of carbon-ion treatment plans with a prescribed fraction dose of 3 Gy (RBE) were used to simulate treatments of spherical tumor volumes in the used head models. Two types of head models were used: a homogeneous plastic cylinder and an anthropomorphic head phantom composed of real bones and tissue-equivalent materials. Secondary ions exiting the head models during irradiation were detected with a mini-tracker composed of two small (2cm^2) parallel Timepix3 detectors placed downstream of the head with a certain angle with respect to the beam axis. Inter-fractional changes were modeled by adding or removing 2-mm-thick slabs positioned in front or inside the targeted head models.

Within the thesis, it was demonstrated that the developed method for the analysis of the measured track distributions, taking into account the actual time-dependent position of the pencil beam, approximated the measured position of the secondary ion creation in the head model significantly better than the methods developed up to now. By using this method, surface changes down to 1 mm were found to be detectable even for the anatomical head phantom. Internal changes of 2-mm-thickness extending over the whole lateral tumor dimension (wide changes) were found to be detectable for all investigated positions between the dose plateau

and the distal end of the tumor. The significance was at least 3 standard deviations for a single mini-tracker and of at least 9 standard deviations when using 8 mini-trackers at 30°, as it is planned for the future. Correct localization of all the studied changes was achieved within 6.3 mm of their actual position. This is sufficient to provide information to the clinicians about the part of the dose distribution which is affected. The detection of 2-mm-thick changes affecting only a part of the tumor (narrow changes), required the development of a new method based on the additional information on the lateral pencil beam positions. With this technique, internal 2-mm-thick changes as small as 10 mm in diameter placed in front of the tumor, were demonstrated to be detectable with a significance of almost 2 standard deviations. This technique makes the developed monitoring method sensitive to the lateral position of the cavity and thus reaches the third dimension. Positions of the mini-tracker closer to the beam axis were found to provide higher detection efficiencies due to the larger amount of data, but also lead to larger geometrical uncertainties and lower localization accuracies. At larger angles, the accuracy of the change localization was found to be better. For future measurements, multi-angle detection systems are recommended to maximize both detectability and localization accuracy. Finally, the applicability of the monitoring of carbon-ion pencil beam delivery in a real patient treatment was demonstrated by designing a patient-friendly measurement system that was shown to be safely used in a clinical environment. After investigating the influence of the developed system on the beam delivery, and with the fulfillment of all clinical and safety requirements, the integration of this system into the clinical workflow of the HIT facility was achieved. With this detection system, the first measurement of a real patient irradiation fraction was performed. The amount of measured data was sufficient to determine a secondary-ion emission profile along the depth of the patient's head. And a differentiation between pencil beams with a 1 cm range difference was demonstrated.

In conclusion, this thesis presents novel methods for carbon ion treatment monitoring of external and internal patient geometry changes in the head based on secondary ion tracking, allowing detection changes down to the clinically desired 2 mm. The designed monitoring system was proven to be well incorporable into a clinical workflow. Thus, the presented work paves the way towards monitoring inter-fractional changes along the beam direction during carbon-ion beam therapy and builds the basis for the upcoming clinical trial at the HIT facility.

Zusammenfassung

Die Vorteile der Kohlenstoffionentherapie implizieren eine erhöhte Empfindlichkeit der Dosisverteilung im Patienten gegenüber jeglichen Veränderungen der Patientengeometrie, wie z. B. Interne anatomische Veränderungen oder fehler in der Patientenpositionierung. Dies kann zu einer Verschlechterung der Dosisverteilung im Patienten führen. Methoden zur Überwachung der Dosisverteilung im Patienten für die Strahlentherapie mit Kohlenstoffionen sind daher von großer Bedeutung, um eine mögliche Unter- oder Überdosierung im Patienten früh zu erkennen und ggf. die Sicherheitssäume um das Tumorvolumen zu reduzieren und damit die abgegebene Dosis im gesunden Gewebe zu verringern. Bislang wurden mehrere nicht-invasive *in-vivo* Überwachungsmethoden für die Ionenstrahltherapie entwickelt. Diese basieren größtenteils auf der Detektion verschiedener Arten von Sekundärstrahlung, wie Annihilationsphotonen von β+-Emittern, prompte Gammastrahlung oder prompte geladene Kernfragmente, die während der Behandlung von einem Patienten emittiert werden. Diese Sekundärstrahlungen sind das Ergebnis von Kernwechselwirkungen des primären Behandlungsstrahls mit dem bestrahlten Gewebe. Sie tragen potenziell wertvolle Informationen über die Reichweite, Position oder Intensität des primären Behandlungsstrahls im Patienten. Bislang hat jedoch keine der Überwachungsmethoden eine ausreichende Reife für eine breite Anwendung in der klinischen Routine erreicht.

Ziel dieser Arbeit war es, Methoden zur Detektion und Lokalisierung von therapierelevanten Geometrievariationen von 2 mm im Kopf des Patienten zu entwickeln. Solche Variationen, die mögliche interfraktionelle Veränderungen an der Oberfläche oder im Inneren des Kopfes darstellen, wurden anhand von Kopfmodellen untersucht. Im Gegensatz zu früheren Untersuchungen, die sich auf einzelne stationäre Stiftstrahlen konzentrierten, wurden in dieser Arbeit ganze Behandlungspläne berücksichtigt, die aus tausenden von einzelnen Stiftstrahlen mit geringer Primärionenanzahl zusammengesetzt sind und unter klinikähnlichen Bedingungen in Bezug auf Dosis, Dosisleistung und Tumorvolumen appliziert wurden.

Methoden zur Detektion und Verfolgung von geladenen sekundären Kernfragmenten (Sekundär-Ionen) wurden entwickelt, die während der Bestrahlung mit Kohlenstoffionen vom Patienten emittiert werden. Darauf aufbauend wurden Methoden zur Analyse und Interpretation der gemessenen Sekundärionenbahnen (*Tracks*) entwickelt. Die entwickelten Detektionsmethoden nutzen die Möglichkeiten eines neuartigen *Mini-Trackers*, der auf der am CERN entwickelten Timepix3-Technologie basiert und hinter dem Patienten positioniert wurde. Die totzeitfreie Datenerfassung ermöglicht eine lückenlose Aufzeichnung aller auftreffenden Sekundärionenbahnen. Darüber hinaus ermöglicht sie eine Synchronisation der Daten mit dem Strahlenapplikations- und Überwachungssystem und damit die Zuordnung jedes gemessenen Sekundärions zu seinem jeweiligen Stiftstrahl, was neue Forschungsmöglichkeiten eröffnet.

Die Experimente wurden am Heidelberger Ionenstrahl-Therapiezentrum (HIT) durchgeführt und haben die klinischen Bedingungen widergespiegelt. Es wurden Einzelfelder von Kohlenstoffionen-Behandlungsplänen mit einer Fraktionsdosis von 3 Gy (RBW) verwendet, um Behandlungen von sphärischen Tumorvolumina in den verwendeten Kopfmodellen zu simulieren. Es wurden zwei Arten von Kopfmodellen verwendet: ein homogener Kunststoffzylinder und ein anthropomorphes Kopfphantom, das aus echten Knochen und gewebeäquivalenten Materialien besteht. Die während der Bestrahlung aus den Kopfmodellen austretenden Sekundärionen wurden mit einem *Mini-Tracker* detektiert, der aus zwei kleinen (2 cm^2) parallelen Timepix3-Detektoren bestand, die in einem bestimmten Winkel zur Strahlachse hinter dem Kopf platziert wurden. Interfraktionelle Änderungen wurden durch Hinzufügen oder Entfernen von 2-mm-dicken Platten modelliert, die vor oder innerhalb der bestrahlten Kopfmodelle positioniert wurden.

Im Rahmen der Arbeit konnte gezeigt werden, dass die entwickelte Methode zur Analyse der gemessenen Bahnverteilungen unter Berücksichtigung der tatsächlichen zeitabhängigen Position des Stiftstrahls die gemessene Position des Sekundärionenursprungs im Kopfmodell deutlich besser approximiert als die bisher entwickelten Methoden. Mit dieser Methode konnten selbst für das anthropomorphe Kopfphantom Oberflächenveränderungen bis zu 1 mm nachgewiesen werden. Veränderungen innerhalb des Phantoms von 2 mm Dicke, die sich über die gesamte laterale Tumorausdehnung erstrecken (breite Veränderungen), wurden für alle untersuchten Positionen zwischen dem Dosisplateau und dem distalen Ende des Tumors nachgewiesen. Die Signifikanz lag bei mindestens 3 Standardabweichungen für einen einzelnen *Mini-Tracker* und bei mindestens 17 Standardabweichungen bei Verwendung von 8 *Mini-Trackern*, wie es für die Zukunft vorgesehen ist. Eine Lokalisierung aller untersuchten Veränderungen wurde innerhalb von 5 mm gegenüber ihrer tatsächlichen Positionen erreicht. Dies ist ausreichend, um den Ärzten Informationen über den Teil der Dosisverteilung zu geben, der von den Änderungen betroffen ist. Die Erkennung von 2-mm-dicken Veränderungen, die nur einen Teil des Tumors betreffen (schmale Veränderungen), erforderte die Entwicklung einer neuen Methode, die auf den zusätzlichen Informationen über die lateralen Stiftstrahlpositionen basiert. Mit dieser Technik konnten interne Veränderungen von 2 mm Dicker mit einem Durchmesser von nur 10 mm, die vor dem Tumor platziert wurden, mit einer Signifikanz von fast 2 Standardabweichungen nachgewiesen werden. Diese Technik macht unsere Überwachungsmethode empfindlich für die laterale Position der Kavität und macht sie somit dreidimensional. Es wurde festgestellt, dass die Positionen des *Mini-Trackers*, die eine kleineren Winkel zur Strahlachse haben, aufgrund der größeren an *Tracks* eine höhere Detektionseffizienz bieten, aber auch zu größeren geometrischen Unsicherheiten und geringeren Lokalisierungsgenauigkeiten führen. Bei größeren Winkeln wurde festgestellt, dass die Genauigkeit der Lokalisierung der anatomischen Veränderungen besser ist. Für zukünftige Messungen werden Detektionsssysteme, die mehrere Winkel abdecken, empfohlen, um sowohl die Detektionseffizienz als auch die Lokalisierungsgenauigkeit zu maximieren. Schließlich wurde die Anwendbarkeit der Überwachung in einer realen Patientenbehandlung mit Kohlenstoffionen durch den Entwurf eines patientenfreundlichen Messsystems demonstriert, das sich als sicher einsetzbar in der klinischen Umgebung erwies. Nach Untersuchung des Einflusses des entwickelten Systems auf die Strahlapplikation und nach Erfüllung aller klinischen und sicherheitstechnischen Anforderungen wurde die Integration dieses Systems in den klinischen Arbeitsablauf der HIT-Einrichtung erzielt. Mit diesem Detektionssystem wurde eine erste Messung einer Bestrahlungsfraktion eines realen Patienten durchgeführt. Die Menge der gemessenen Teilchenbahnen war ausreichend, um ein Sekundärionen-Emissionsprofil entlang der Strahlachse innerhalb des Patientenkopfes zu bestimmen. Außerdem wurde eine Differenzierung zwischen Stiftstrahlen mit einem Reichweiteunterschied von 1 cm demonstriert.

Zusammenfassend wird in dieser Arbeit eine neuartige Methode zur Überwachung der externen und internen Geometrieveränderungen des Patientenkopfes bei der Kohlenstoffionen-Behandlung auf der Basis der Sekundärionendetektion vorgestellt, die es ermöglicht, Veränderungen bis hinab zu den klinisch gewünschten 2 mm zu erkennen. Das entworfene Überwachungssystem hat sich als gut integrierbar in einen klinischen Arbeitsablauf erwiesen. Somit ebnet die vorgestellte Arbeit den Weg zur Überwachung von interfraktionellen Veränderungen der Kohlenstoffionentherapie in der Tiefe und bildet die Grundlage für die kommende klinische Studie am HIT.

7. Bibliography

Aarhus Particle Therapy Group. (2021). **Electronic Stopping Power**. Retrieved July 4, 2021 URL: https://apps.alldbx.de/apps/5da938a6bb9f246e81416791/ [date accessed: July 4, 2021].

Abbani, N. (2020). **Simulation Analysis for the Monitoring of Carbon-Ion Beam Radiotherapy inside Patient Models**. Medical Faculty Mannheim, University of Heidelberg, Germany.

Adeberg, S., Akbaba, S., Lang, K., Held, T., Verma, V., Nikoghosyan, A., Bernhardt, D., Münter, M., Freier, K., Plinkert, P., Hauswald, H., Herfarth, K., Rieken, S., Debus, J., and Jensen, A. D. (2020). **The Phase 1/2 ACCEPT Trial: Concurrent Cetuximab and Intensity Modulated Radiation Therapy with Carbon Ion Boost for Adenoid Cystic Carcinoma of the Head and Neck**. Int J Radiat Oncol Biol Phys 106(1):167–73. doi: 10.1016/j.ijrobp.2019.09.036.

Amaldi, U., Hajdas, W., Iliescu, S., Malakhov, N., Samarati, J., Sauli, F., and Watts, D. (2010). **Advanced Quality Assurance for CNAO**. Nucl Instrum Methods Phys Res A 617(1–3):248–49. doi: 10.1016/j.nima.2009.06.087.

Bangert, M., Wahln, L., Abbani, N., Stadler, A., Neishabouri, A., Bennan, A., Doerner, E., Pezzano, Wieser, H.-P., Gabryś, H., Charton, L., Handrack, J., and Mescher, H. (2020). **E0404/MatRad: Blaise v2.10.0**. Retrieved May 11, 2021 URL: https://zenodo.org/record/3879616 [date accessed: May 11, 2021].

Battistoni, G., Cerutti, F., Fassò, A., Ferrari, A., Muraro, S., Ranft, J., Roesler, S., and Sala, P. R. (2007). **The FLUKA Code: Description and Benchmarking**. Pp. 31–49 in AIP Conference Proceedings. Vol. 896. AIP.

Battistoni, G., Collamati, F., De Lucia, E., Faccini, R., Marafini, M., Mattei, I., Muraro, S., Paramatti, R., Patera, V., Pinci, D., Rucinski, A., Russomando, A., Sarti, A., Sciubba, A., Solfaroli Camillocci, E., Toppi, M., Traini, G., and Voena, C. (2017). **Design of a Tracking Device for On-Line Dose Monitoring in Hadrontherapy**. Nucl Instrum Methods Phys Res A 845:679–83. doi: 10.1016/j.nima.2016.05.095.

Bethe, H. (1932). **Bremsformel Für Elektronen Relativistischer Geschwindigkeit**. Zeitschrift Für Physik 76(5–6):293–99. doi: 10.1007/BF01342532.

Bethe, H. A. (1953). **Molière's Theory of Multiple Scattering**. Physical Review 89(6):1256–66. doi: 10.1103/PhysRev.89.1256.

Bhandari, V., Patel, P., Gurjar, O. P., and Gupta, K. L. (2014). **Impact of Repeat Computerized Tomography Replans in the Radiation Therapy of Head and Neck Cancers**. Journal of Medical Physics 39(3):164–68. doi: 10.4103/0971-6203.139005.

Bimbot, R., Geissel, H., Paul, H., Schinner, A., Sigmund, P., Wambersie, A., DeLuca, P. M., and Seltzer, S. M. (2005). **Stopping of Ions Heavier than Helium**. Journal of Applied Physics 5(1).

Bisogni, M. (2019). **The INSIDE Bimodal System for Range Monitoring in Particle Therapy toward Clinical Validation**. Nuclear Instruments and Methods in Physics Research, Section A: Accelerators, Spectrometers, Detectors and Associated Equipment 936:73–74.

Bloch, F. (1933). **Zur Bremsung Rasch Bewegter Teilchen Beim Durchgang Durch Materie**. Ann Phys 408(3):285–320. doi: 10.1002/andp.19334080303.

Böhlen, T. T., Brons, S., Dosanjh, M., Ferrari, A., Fossati, P., Haberer, T., Patera, V., and Mairani, A. (2012). **Investigating the Robustness of Ion Beam Therapy Treatment Plans to Uncertainties in Biological Treatment Parameters**. Phys Med Biol 57(23):7983–8004. doi: 10.1088/0031-9155/57/23/7983.

Böhlen, T. T., Cerutti, F., Chin, M. P. W., Fassò, A., Ferrari, A., Ortega, P. G., Mairani, A., Sala, P. R., Smirnov, G., and Vlachoudis, V. (2014). **The FLUKA Code: Developments and Challenges for High Energy and Medical Applications**. Nuclear Data Sheets 120:211–14. doi: 10.1016/j.nds.2014.07.049.

Bragg, W. H., and Kleeman, R. (1904). **On the Ionization Curves of Radium**. The London, Edinburgh, and Dublin Philosophical Magazine and Journal of Science 8(48):726–38. doi: 10.1080/14786440409463246.

Bray, F., Ferlay, J., Soerjomataram, I., Siegel, R. L., Torre, L. A., and Jemal, A. (2018). **Global Cancer Statistics 2018: GLOBOCAN Estimates of Incidence and Mortality Worldwide for 36 Cancers in 185 Countries**. CA Cancer J Clin 68(6):394–424. doi: 10.3322/caac.21492.

Burigo, L., Pshenichnov, I., Mishustin, I., and Bleicher, M. (2014). **Microdosimetry Spectra and RBE of 1H, 4He, 7Li and 12C Nuclei in Water Studied with Geant4**. Nucl Instrum Methods Phys Res B 320:89–99. doi: 10.1016/j.nimb.2013.10.018.

Chu, W. T., Ludewigt, B. A., and Renner, T. R. (1993). **Instrumentation for Treatment of Cancer Using Proton and Light-Ion Beams**. Review of Scientific Instruments 64(8):2055–2122.

Combs, S. E., Burkholder, I., Edler, L., Rieken, S., Habermehl, D., Jäkel, O., Haberer, T., Haselmann, R., Unterberg, A., Wick, W., and Debus, J. (2010). **Randomised Phase I/II Study to Evaluate Carbon Ion Radiotherapy versus Fractionated Stereotactic Radiotherapy in Patients with Recurrent or**

Progressive Gliomas: The CINDERELLA Trial. BMC Cancer 10. doi: 10.1186/1471-2407-10-533.

Combs, S. E., Edler, L., Burkholder, I., Rieken, S., Habermehl, D., Jäkel, O., Haberer, T., Unterberg, A., Wick, W., Debus, J., and Haselmann, R. (2010). **Treatment of Patients with Atypical Meningiomas Simpson Grade 4 and 5 with a Carbon Ion Boost in Combination with Postoperative Photon Radiotherapy: The MARCIE Trial**. BMC Cancer 10. doi: 10.1186/1471-2407-10-615.

Combs, S. E., Ellerbrock, M., Haberer, T., Habermehl, D., Hoess, A., Jäkel, O., Jensen, A., Klemm, S., Münter, M., Naumann, J., Nikoghosyan, A., Oertel, S., Parodi, K., Rieken, S., and Debus, J. (2010). **Heidelberg Ion Therapy Center (HIT): Initial Clinical Experience in the First 80 Patients**. Acta Oncol 49(7):1132–40. doi: 10.3109/0284186X.2010.498432.

Combs, S. E., Jäkel, O., Haberer, T., and Debus, J. (2010). **Particle Therapy at the Heidelberg Ion Therapy Center (HIT) - Integrated Research-Driven University-Hospital-Based Radiation Oncology Service in Heidelberg, Germany**. Radiotherapy and Oncology 95(1):41–44.

Combs, S. E., Kessel, K. A., Herfarth, K., Jensen, A., Oertel, S., Blattmann, C., Ecker, S., Hoess, A., Martin, E., Witt, O., Jäkel, O., Kulozik, A. E., and Debus, J. (2012). **Treatment of Pediatric Patients and Young Adults with Particle Therapy at the Heidelberg Ion Therapy Center (HIT): Establishment of Workflow and Initial Clinical Data**. Radiation Oncology 7(1). doi: 10.1186/1748-717X-7-170.

Combs, S. E., Kessel, K., Habermehl, D., Haberer, T., Jäkel, O., and Debus, J. (2013). **Proton and Carbon Ion Radiotherapy for Primary Brain Tumors and Tumors of the Skull Base**. Acta Oncol 52(7):1504–9. doi: 10.3109/0284186X.2013.818255.

Combs, S. E., Kieser, M., Rieken, S., Habermehl, D., Jäkel, O., Haberer, T., Nikoghosyan, A., Haselmann, R., Unterberg, A., Wick, W., and Debus, J. (2010). **Randomized Phase II Study Evaluating a Carbon Ion Boost Applied after Combined Radiochemotherapy with Temozolomide versus a Proton Boost after Radiochemotherapy with Temozolomide in Patients with Primary Glioblastoma: The CLEOPATRA Trial**. BMC Cancer 10. doi: 10.1186/1471-2407-10-478.

Dal Bello, R., Magalhaes Martins, P., Brons, S., Hermann, G., Kihm, T., Seimetz, M., and Seco, J. (2020). **Prompt Gamma Spectroscopy for Absolute Range Verification of 12C Ions at Synchrotron-Based Facilities**. Phys Med Biol 65(9):95010. doi: 10.1088/1361-6560/ab7973.

Dauvergne, D., Battaglia, M., Montarou, G., and Testa, E. (2009). **New Methods of Real-Time Control Imaging for Ion Therapy**. Pp. 154–60 in 1st NIRS-ETOILE symposium.

Dedes, G., and Parodi, K. (2015). **Monte Carlo Simulations of Particle Interactions with Tissue in Carbon Ion Therapy**. Int J Part Ther 2(3):447–58. doi: 10.14338/ijpt-15-00021.

Draeger, E., Mackin, D., Peterson, S., Chen, H., Avery, S., Beddar, S., and Polf, J. C. (2018). **3D Prompt Gamma Imaging for Proton Beam Range Verification**. Physics in Medicine and Biology 63(3). doi: 10.1088/1361-6560/aaa203.

Enghardt, W., Crespo, P., Fiedler, F., Hinz, R., Parodi, K., Pawelke, J., and Pönisch, F. (2004). **Charged Hadron Tumour Therapy Monitoring by Means of PET**. Pp. 284–88 in Nucl Instrum Methods Phys Res A. Vol. 525. North-Holland.

Everett, D. B., Fleming, J. S., Todd, R. W., and Nightingale, J. M. (1977). **Gamma-Radiation Imaging System Based on the Compton Effect**. Proceedings of the Institution of Electrical Engineers 124(11):995–1000. doi: 10.1049/piee.1977.0203.

Fano, U. (1963). **Penetration of Protons, Alpha Particles, and Mesons**. Annu Rev Nucl Sci 13(1):1–66. doi: 10.1146/annurev.ns.13.120163.000245.

Fattori, G., Riboldi, M., Scifoni, E., Krämer, M., Pella, A., Durante, M., Ronchi, S., Bonora, M., Orecchia, R., and Baroni, G. (2014). **Dosimetric Effects of Residual Uncertainties in Carbon Ion Treatment of Head Chordoma**. Radiotherapy and Oncology 113(1):66–71. doi: 10.1016/j.radonc.2014.08.001.

Félix-Bautista, R. (2017). **Monitoring of a Clinic-like C-12 Treatment by Means of Secondary Ions: First Study**. Medical Faculty Heidelberg, Pontificia Universidad Católica de Chile and Heidelberg University.

Félix-Bautista, R. (2021). **Monitoring of Lateral Positions of Therapeutic Carbon-Ion Pencil Beams Using Secondary Ion Tracking**. Combined Faculty for the Natural Sciences and Mathematics, University of Heidelberg, Germany.

Félix-Bautista, R., Gehrke, T., Ghesquiere-Diérickx, L., Reimold, M., Amato, C., Turecek, D., Jakubek, J., Ellerbrock, M., and Martišiková, M. (2019). **Experimental Verification of a Non-Invasive Method to Monitor the Lateral Pencil Beam Position in an Anthropomorphic Phantom for Carbon-Ion Radiotherapy**. Phys Med Biol 64(17). doi: 10.1088/1361-6560/ab2ca3.

Félix-Bautista, R., Ghesquière-Diérickx, L., Marek, L., Granja, C., Soukup, P., Turecek, D., Kelleter, L., Brons, S., Ellerbrock, M., Jäkel, O., Gehrke, T., and Martišíková, M. (2021). **Quality Assurance Method for Monitoring of Lateral Pencil Beam Positions in Scanned Carbon-ion Radiotherapy Using Tracking of Secondary Ions**. Medical Physics. doi: 10.1002/mp.15018.

Ferrari, A., Sala, P. R., Fasso, A., and Ranft, J. (2005). **FLUKA: A Multi-Particle Transport Code**. CERN Yellow Report. doi: 10.2172/877507.

Ferrero, V., Bisogni, M. G., Camarlinghi, N., Fiorina, E., Giraudo, G., Morrocchi, M., Pennazio, F., Sportelli, G., Wheadon, R., and Cerello, P. (2018). **Double-Field Hadrontherapy Treatment Monitoring With the INSIDE In-Beam PET Scanner: Proof of Concept**. IEEE Trans Radiat Plasma Med Sci 2(6):588–93. doi: 10.1109/trpms.2018.2870478.

Finck, C., Karakaya, Y., Reithinger, V., Rescigno, R., Baudot, J., Constanzo, J., Juliani, D., Krimmer, J., Rinaldi, I., Rousseau, M., Testa, E., Vanstalle, M., and Ray, C. (2017). **Study for Online Range Monitoring with the Interaction Vertex Imaging Method**. Physics in Medicine and Biology 62(24):9220–39. doi: 10.1088/1361-6560/aa954e.

Fischetti, M., Baroni, G., Battistoni, G., Bisogni, G., Cerello, P., Ciocca, M., De Maria, P., De Simoni, M., Di Lullo, B., Donetti, M., Dong, Y., Embriaco, A., Ferrero, V., Fiorina, E., Franciosini, G., Galante, F., Kraan, A., Luongo, C., Magi, M., Mancini-Terracciano, C., Marafini, M., Malekzadeh, E., Mattei, I., Mazzoni, E., Mirabelli, R., Mirandola, A., Morrocchi, M., Muraro, S., Patera, V., Pennazio, F., Schiavi, A., Sciubba, A., Solfaroli Camillocci, E., Sportelli, G., Tampellini, S., Toppi, M., Traini, G., Valle, S. M., Vischioni, B., Vitolo, V., and Sarti, A. (2020). **Inter-Fractional Monitoring of 12 C Ions Treatments: Results from a Clinical Trial at the CNAO Facility**. Scientific Reports 10(1). doi: 10.1038/s41598-020-77843-z.

Fisher, R. A. (1936). **THE USE OF MULTIPLE MEASUREMENTS IN TAXONOMIC PROBLEMS**. Ann Eugen 7(2):179–88. doi: 10.1111/j.1469-1809.1936.tb02137.x.

FLUKA. (2018). **FLUKA 2011 Online Manual**. 1–347. Retrieved July 4, 2021 URL: http://www.fluka.org/content/manuals/fluka2011.manual [date accessed: July 4, 2021].

Fossati, P., Molinelli, S., Matsufuji, N., Ciocca, M., Mirandola, A., Mairani, A., Mizoe, J., Hasegawa, A., Imai, R., Kamada, T., Orecchia, R., and Tsujii, H. (2012). **Dose Prescription in Carbon Ion Radiotherapy: A Planning Study to Compare NIRS and LEM Approaches with a Clinically-Oriented Strategy**. Phys Med Biol 57(22):7543–54. doi: 10.1088/0031-9155/57/22/7543.

Gaa, T., Reinhart, M., Hartmann, B., Jakubek, J., Soukup, P., Jäkel, O., and Martišíková, M. (2017). **Visualization of Air and Metal Inhomogeneities in Phantoms Irradiated by Carbon Ion Beams Using Prompt Secondary Ions**. Physica Medica 38:140–47. doi: 10.1016/j.ejmp.2017.05.055.

Gehrke, T., Burigo, L., Arico, G., Berke, S., Jakubek, J., Turecek, D., Tessonnier, T., Mairani, A., and Martišíková, M. (2017). **Energy Deposition Measurements of Single 1H, 4He and 12C Ions of Therapeutic Energies in a Silicon Pixel Detector**. Journal of Instrumentation 12(4). doi: 10.1088/1748-0221/12/04/P04025.

Golnik, C., Hueso-González, F., Müller, A., Dendooven, P., Enghardt, W., Fiedler, F., Kormoll, T., Roemer, K., Petzoldt, J., Wagner, A., and Pausch, G. (2014). **Range Assessment in Particle Therapy Based on Prompt γ-Ray Timing Measurements**. Physics in Medicine and Biology 59(18):5399–5422. doi: 10.1088/0031-9155/59/18/5399.

Greilich, S. (2017). **Tools to Measure and Improve the Microscopic Energy Deposition in Ion Beam Therapy - Habilitation Thesis Heidelberg University**. Habilitation at the Medical Faculty.

Gunzert-Marx, K., Iwase, H., Schardt, D., and Simon, R. S. (2008). **Secondary Beam Fragments Produced by 200 MeV U-1 12C Ions in Water and Their Dose Contributions in Carbon Ion Radiotherapy**. New Journal of Physics 10. doi: 10.1088/1367-2630/10/7/075003.

Gwosch, K., Hartmann, B., Jakubek, J., Granja, C., Soukup, P., Jäkel, O., and Martišíková, M. (2013). **Non-Invasive Monitoring of Therapeutic Carbon Ion Beams in a Homogeneous Phantom by Tracking of Secondary Ions**. Physics in Medicine and Biology 58(11):3755–73. doi: 10.1088/0031-9155/58/11/3755.

Haberer, T., Becher, W., Schardt, D., and Kraft, G. (1993). **Magnetic Scanning System for Heavy Ion Therapy**. Nucl Instrum Methods Phys Res A 330(1–2):296–305. doi: 10.1016/0168-9002(93)91335-K.

Hanahan, D., and Weinberg, R. A. (2000). **The Hallmarks of Cancer Review Evolve Progressively from Normalcy via a Series of Pre**. Cell 100:57–70.

Hanahan, D., and Weinberg, R. A. (2011). **Hallmarks of Cancer: The next Generation**. Cell 144(5):646–74.

Henriquet, P., Testa, E., Chevallier, M., Dauvergne, D., Dedes, G., Freud, N., Krimmer, J., Létang, J. M., Ray, C., Richard, M. H., and Sauli, F. (2012). **Interaction Vertex Imaging (IVI) for Carbon Ion Therapy Monitoring: A Feasibility Study**. Phys Med Biol 57(14):4655–69. doi: 10.1088/0031-9155/57/14/4655.

Highland, V. L. (1975). **Some Practical Remarks on Multiple Scattering**. Nuclear Instruments and Methods 129(2):497–99. doi: 10.1016/0029-554X(75)90743-0.

Hueso-González, F., Rabe, M., Ruggieri, T. A., Bortfeld, T., and Verburg, J. M. (2018). **A Full-Scale Clinical Prototype for Proton Range Verification Using Prompt Gamma-Ray Spectroscopy**. Physics in Medicine and Biology 63(18):185019. doi: 10.1088/1361-6560/aad513.

ICRU 85. (2011). **ICRU Report 85: Fundamental Quantities and Units for Ionizing Radiation**. Journal of the ICRU 11(1). doi: 10.1093/rpd/ncs077.

ICRU 93. (2016). **ICRU Report 93: Operational Quantities for External Radiation Exposure**. Journal of the ICRU Vol 16(No 1–2). doi: 10.1177/0146645315624341.

Jäkel, O. (2020). **Physical Advantages of Particles: Protons and Light Ions**. Br J Radiol 93(1107):20190428. doi: 10.1259/bjr.20190428.

Jäkel, O., Hartmann, G. H., Karger, C. P., Heeg, P., and Rassow, J. (2000). **Quality Assurance for a Treatment Planning System in Scanned Ion Beam Therapy**. Medical Physics 27(7):1588–1600. doi: 10.1118/1.599025.

Jäkel, O., Jacob, C., Schardt, D., Karger, C. P., and Hartmann, G. H. (2001). **Relation between Carbon Ion Ranges and X-Ray CT Numbers**. Medical Physics 28(4):701–3. doi: 10.1118/1.1357455.

Jäkel, O., Krämer, M., Karger, C. P., and Debus, J. (2001). **Treatment Planning for Heavy Ion Radiotherapy: Clinical Implementation and Application**. Phys Med Biol 46(4):1101–16. doi: 10.1088/0031-9155/46/4/314.

Jakubek, J. (2009a). **Energy-Sensitive X-Ray Radiography and Charge Sharing Effect in Pixelated Detector**. Nucl Instrum Methods Phys Res A 607(1):192–95. doi: 10.1016/j.nima.2009.03.148.

Jakubek, J. (2009b). **Energy-Sensitive X-Ray Radiography and Charge Sharing Effect in Pixelated Detector**. Nucl Instrum Methods Phys Res A 607(1):192–95. doi: 10.1016/j.nima.2009.03.148.

Jakubek, J. (2011). **Precise Energy Calibration of Pixel Detector Working in Time-over-Threshold Mode**. in Nucl Instrum Methods Phys Res A. Vol. 633.

Jakůbek, J. (2009). **Semiconductor Pixel Detectors and Their Applications in Life Sciences**. Journal of Instrumentation 4(3). doi: 10.1088/1748-0221/4/03/P03013.

Jakubek, J., Cejnarova, A., Holy, T., Pospisil, S., Uher, J., and Vykydal, Z. (2008). **Pixel Detectors for Imaging with Heavy Charged Particles**. Nucl Instrum Methods Phys Res A 591(1):155–58. doi: 10.1016/j.nima.2008.03.091.

Jensen, A. D., Krauss, J., Potthoff, K., Desta, A., Habl, G., Mavtratzas, A., Windemuth-Kiesselbach, C., Debus, J., and Münter, M. W. (2011). **Phase II Study of Induction Chemotherapy with TPF Followed by Radioimmunotherapy with Cetuximab and Intensity-Modulated Radiotherapy (IMRT) in Combination with a Carbon Ion Boost for Locally Advanced Tumours of the Oro-, Hypopharynx and Larynx - TPF-C-HIT**. BMC Cancer 11. doi: 10.1186/1471-2407-11-182.

Jensen, A. D., Nikoghosyan, A. V., Lossner, K., Haberer, T., Jäkel, O., Münter, M. W., and Debus, J. (2015). **COSMIC: A Regimen of Intensity Modulated Radiation Therapy plus Dose-Escalated, Raster-Scanned Carbon Ion Boost for Malignant Salivary Gland Tumors: Results of the Prospective Phase 2 Trial**. Pp. 37–46 in Int J Radiat Oncol Biol Phys. Vol. 93. Elsevier Inc.

Jensen, A. D., Nikoghosyan, A. V, Windemuth-Kieselbach, C., Debus, J., and Münter, M. W. (2011). **Treatment of Malignant Sinonasal Tumours with Intensity-Modulated Radiotherapy (IMRT) and Carbon Ion Boost (C12)**. BMC Cancer 11. doi: 10.1186/1471-2407-11-190.

Jensen, A. D., Winter, M., Kuhn, S. P., Debus, J., Nairz, O., and Münter, M. W. (2012). **Robotic-Based Carbon Ion Therapy and Patient Positioning in 6 Degrees of Freedom: Setup Accuracy of Two Standard Immobilization Devices Used in Carbon Ion Therapy and IMRT**. Radiation Oncology 7(1). doi: 10.1186/1748-717X-7-51.

Jiang, H., and Paganetti, H. (2004). **Adaptation of GEANT4 to Monte Carlo Dose Calculations Based on CT Data**. Medical Physics 31(10):2811–18. doi: 10.1118/1.1796952.

Karger, C. P. (2021). **Therapy Course at the German Cancer Research Center (DKFZ)**.

Kraan, A. C. (2015). **Range Verification Methods in Particle Therapy: Underlying Physics and Monte Carlo Modelling**. Front Oncol 5(JUN). doi: 10.3389/fonc.2015.00150.

Krimmer, J., Angellier, G., Balleyguier, L., Dauvergne, D., Freud, N., Herault, J., Létang, J. M., Mathez, H., Pinto, M., and Testa, E. (2017). **A Cost-Effective Monitoring Technique in Particle Therapy via Uncollimated Prompt Gamma Peak Integration**. Physics 110(15). doi: 10.1063/1.4980103ï.

Krimmer, J., Dauvergne, D., Létang, J. M., and Testa. (2018). **Prompt-Gamma Monitoring in Hadrontherapy: A Review**. Nucl Instrum Methods Phys Res A 878:58–73.

Kurosawa, S., Kubo, H., Ueno, K., Kabuki, S., Iwaki, S., Takahashi, M., Taniue, K., Higashi, N., Miuchi, K., Tanimori, T., Kim, D., and Kim, J. (2012). **Prompt Gamma Detection for Range Verification in Proton Therapy**. Curr Appl Phys 12(2):364–68. doi: 10.1016/j.cap.2011.07.027.

Leo, W. R., and Haase, D. G. (1990). **Techniques for Nuclear and Particle Physics Experiments**. American Journal of Physics 58(12):1216–17. doi: 10.1119/1.16209.

Llopart, X. (2014). **Timepix3 Manual v1.9 2/3/2014**. 1–72.

Lomax, M. E., Folkes, L. K., and O'Neill, P. (2013). **Biological Consequences of Radiation-Induced DNA Damage: Relevance to Radiotherapy**. Clinical Oncology 25(10):578–85. doi: 10.1016/j.clon.2013.06.007.

Lühr, A., Toftegaard, J., Kantemiris, I., Hansen, D. C., and Bassler, N. (2012). **Stopping Power for Particle Therapy: The Generic Library LibdEdx and Clinically Relevant Stopping-Power Ratios for Light Ions**. Int J Radiat Biol 88(1–2):209–12. doi: 10.3109/09553002.2011.595877.

Malouff, T. D., Mahajan, A., Krishnan, S., Beltran, C., Seneviratne, D. S., and Trifiletti, D. M. (2020). **Carbon Ion Therapy: A Modern Review of an Emerging Technology**. Front Oncol 10(February):1–13. doi: 10.3389/fonc.2020.00082.

Marek, L. (2020). **Directional and Spectrometric Mapping of Secondary Radiation Induced during Hadron**

Radiotherapy with Miniaturized Particle Trackers. Faculty of Nuclear Sciences and Physical Engineering, Department of Physics, Czech Technical University, Prague, Czech Republic.

Martišíková, M., Hartmann, B., Gwosch, K., Jakubek, J., Granja, C., and Jäkel, O. (2012). **Study of the Capabilities of the Timepix Detector for Ion Beam Radiotherapy Applications**. Pp. 4324–28 in IEEE Nucl Sci Symp Conf Rec.

Mattei, I., Battistoni, G., Collini, F., De Lucia, E., Durante, M., Fiore, S., La Tessa, C., Mancini-Terracciano, C., Marafini, M., Mirabelli, R., Muraro, S., Paramatti, R., Piersanti, L., Rucinski, A., Russomando, A., Sarti, A., Schuy, C., Sciubba, A., Solfaroli Camillocci, E., Toppi, M., Traini, G., Valle, S. M., Vanstalle, M., and Patera, V. (2017). **Addendum: Measurement of Charged Particle Yields from PMMA Irradiated by a 220 MeV/u 12 C Beam**. Phys Med Biol 62(21):8483–94. doi: 10.1088/1361-6560/aa8b35.

Mattei, I., Bini, F., Collamati, F., De Lucia, E., Frallicciardi, P. M., Iarocci, E., Mancini-Terracciano, C., Marafini, M., Muraro, S., Paramatti, R., Patera, V., Piersanti, L., Pinci, D., Rucinski, A., Russomando, A., Sarti, A., Sciubba, A., Solfaroli Camillocci, E., Toppi, M., Traini, G., Voena, C., and Battistoni, G. (2017). **Secondary Radiation Measurements for Particle Therapy Applications: Prompt Photons Produced by 4He, 12C and 16O Ion Beams in a PMMA Target**. Phys Med Biol 62(4):1438–55. doi: 10.1088/1361-6560/62/4/1438.

Mein, S., Klein, C., Kopp, B., Magro, G., Harrabi, S., Karger, C. P., Haberer, T., Debus, J., Abdollahi, A., Dokic, I., and Mairani, A. (2020). **Assessment of RBE-Weighted Dose Models for Carbon Ion Therapy Toward Modernization of Clinical Practice at HIT: In Vitro, in Vivo, and in Patients**. Int J Radiat Oncol Biol Phys 108(3):779–91. doi: 10.1016/j.ijrobp.2020.05.041.

Min, C. H., Kim, C. H., Youn, M. Y., and Kim, J. W. (2006). **Prompt Gamma Measurements for Locating the Dose Falloff Region in the Proton Therapy**. Appl Phys Lett 89(18):183517. doi: 10.1063/1.2378561.

Mohamad, O., Sishc, B. J., Saha, J., Pompos, A., Rahimi, A., Story, M. D., Davis, A. J., and Kim, D. W. N. (2017). **Carbon Ion Radiotherapy: A Review of Clinical Experiences and Preclinical Research, with an Emphasis on DNA Damage/Repair**. Cancers 9(6).

Moini, J., and Piran, P. (2020). **Histophysiology**. Pp. 1–49 in Functional and Clinical Neuroanatomy. Elsevier.

Moliere, G. (1948). **Theorie Der Streuung Schneller Geladener Teilchen II Mehrfach-Und Vielfachstreuung1**. Z Nat Forsch A J Phys Sci 3(2):78–97. doi: 10.1515/zna-1948-0203.

Muraro, S., Battistoni, G., Collamati, F., De Lucia, E., Faccini, R., Ferroni, F., Fiore, S., Frallicciardi, P., Marafini, M., Mattei, I., Morganti, S., Paramatti, R., Piersanti, L., Pinci, D., Rucinski, A., Russomando, A., Sarti, A., Sciubba, A., Solfaroli-Camillocci, E., Toppi, M., Traini, G., Voena, C., and Patera, V. (2016). **Monitoring of Hadrontherapy Treatments by Means of Charged Particle Detection**. Front Oncol 6(AUG).

Nikoghosyan, A. V, Karapanagiotou-Schenkel, I., Münter, M. W., Jensen, A. D., Combs, S. E., and Debus, J. (2010). **Randomised Trial of Proton vs. Carbon Ion Radiation Therapy in Patients with Chordoma of the Skull Base, Clinical Phase III Study HIT-1-Study**. BMC Cancer 10:607. doi: 10.1186/1471-2407-10-607.

Nikoghosyan, A. V, Rauch, G., Münter, M. W., Jensen, A. D., Combs, S. E., Kieser, M., and Debus, J. (2010). **Randomised Trial of Proton vs. Carbon Ion Radiation Therapy in Patients with Low and Intermediate Grade Chondrosarcoma of the Skull Base, Clinical Phase III Study**. BMC Cancer 10:606. doi: 10.1186/1471-2407-10-606.

Nishio, T., Ogino, T., Nomura, K., and Uchida, H. (2006). **Dose-Volume Delivery Guided Proton Therapy Using Beam on-Line PET System**. Medical Physics 33(11):4190–97. doi: 10.1118/1.2361079.

Paganetti, H. (2012). **Range Uncertainties in Proton Therapy and the Role of Monte Carlo Simulations**. Physics in Medicine and Biology 57(11):R99.

Parodi, K. (2016). **On- and off-Line Monitoring of Ion Beam Treatment**. Nucl Instrum Methods Phys Res A 809:113–19. doi: 10.1016/j.nima.2015.06.056.

Parodi, K., Mairani, A., Brons, S., Hasch, B. G., Sommerer, F., Naumann, J., Jäkel, O., Haberer, T., and Debus, J. (2012). **Monte Carlo Simulations to Support Start-up and Treatment Planning of Scanned Proton and Carbon Ion Therapy at a Synchrotron-Based Facility**. Phys Med Biol 57(12). doi: 10.1088/0031-9155/57/12/3759.

Parodi, K., Paganetti, H., Shih, H. A., Michaud, S., Loeffler, J. S., DeLaney, T. F., Liebsch, N. J., Munzenrider, J. E., Fischman, A. J., Knopf, A., and Bortfeld, T. (2007). **Patient Study of In Vivo Verification of Beam Delivery and Range, Using Positron Emission Tomography and Computed Tomography Imaging After Proton Therapy**. Int J Radiat Oncol Biol Phys 68(3):920–34. doi: 10.1016/j.ijrobp.2007.01.063.

Parodi, K., and Polf, J. C. (2018). **In Vivo Range Verification in Particle Therapy**. Pp. e1036–50 in Medical Physics. Vol. 45. John Wiley and Sons Ltd.

Piersanti, L., Bellini, F., Bini, F., Collamati, F., De Lucia, E., Durante, M., Faccini, R., Ferroni, F., Fiore, S., Iarocci, E., La Tessa, C., Marafini, M., Mattei, I., Patera, V., Ortega, P. G., Sarti, A., Schuy, C., Sciubba, A., Vanstalle, M., and Voena, C. (2014). **Measurement of Charged Particle Yields from PMMA Irradiated by a 220 MeV/u 12C Beam**. Physics in Medicine and Biology 59(7):1857–72. doi: 10.1088/0031-

9155/59/7/1857.

Podgorsak, E. B. (2005). **Review of Radiation Oncology Physics: A Handbook for Teachers and Students**.

PTCOG. (2017). **Particle Therapy Patient Statistics (per End of 2017)**. Particle Therapy Co-Operative Group (June). Retrieved February 9, 2021 URL: http://www.ptcog.ch/archive/patient_statistics/Patientstatistics-updateMar2014.pdf [date accessed: February 9, 2021].

PTCOG. (2019). **PTCOG - Patient Statistics**. Particle Therapy Co-Operative Group. Retrieved March 9, 2021 URL: https://www.ptcog.ch/index.php/ptcog-patient-statistics [date accessed: March 9, 2021].

PTCOG. (2021a). **PTCOG - Facilities in Operation**. Particle Therapy Co-Operative Group. Retrieved February 9, 2021 URL: http://www.ptcog.ch/index.php/facilities-in-operation [date accessed: February 9, 2021].

PTCOG. (2021b). **PTCOG - Facilities under Construction**. Particle Therapy Co-Operative Group. Retrieved February 9, 2021 URL: https://www.ptcog.ch/index.php/facilities-under-construction [date accessed: February 9, 2021].

Rackwitz, T., and Debus, J. (2019). **Clinical Applications of Proton and Carbon Ion Therapy**. Seminars in Oncology 46(3):226–32. doi: 10.1053/j.seminoncol.2019.07.005.

Reidel, C. A., Finck, C., Schuy, C., Rovituso, M., and Weber, U. (2019). **Alignment Procedure of Silicon Pixel Detectors for Ion-Beam Therapy Applications**. Nuclear Instruments and Methods in Physics Research, Section A: Accelerators, Spectrometers, Detectors and Associated Equipment 931:142–50. doi: 10.1016/j.nima.2019.03.042.

Reimold, M. (2018). **Monitoring of Carbon Ion Pencil Beams in a Homogeneous PMMA Phantom Using Timepix3 Detectors**. Department of physics and astronomy, University of Heidelberg, Germany.

Reinhart, A. M., Spindeldreier, C. K., Jakubek, J., and Martišíková, M. (2017). **Three Dimensional Reconstruction of Therapeutic Carbon Ion Beams in Phantoms Using Single Secondary Ion Tracks**. Physics in Medicine and Biology 62(12):4884–96. doi: 10.1088/1361-6560/aa6aeb.

Rieken, S., Habermehl, D., Haberer, T., Jaekel, O., Debus, J., and Combs, S. E. (2012). **Proton and Carbon Ion Radiotherapy for Primary Brain Tumors Delivered with Active Raster Scanning at the Heidelberg Ion Therapy Center (HIT): Early Treatment Results and Study Concepts**. Radiation Oncology 7(1). doi: 10.1186/1748-717X-7-41.

Rietzel, E., Schardt, D., and Haberer, T. (2007). **Range Accuracy in Carbon Ion Treatment Planning Based on CT-Calibration with Real Tissue Samples**. Radiation Oncology 2(1). doi: 10.1186/1748-717X-2-14.

Rossi, L., Fischer, P., Rohe, T., and Wermes, N. (2005). **Pixel Detector: From Fundamentals to Applications**. Springer.

Rucinski, A., Battistoni, G., Collamati, F., De Lucia, E., Faccini, R., Frallicciardi, P. M., Mancini-Terracciano, C., Marafini, M., Mattei, I., Muraro, S., Paramatti, R., Piersanti, L., Pinci, D., Russomando, A., Sarti, A., Sciubba, A., Solfaroli Camillocci, E., Toppi, M., Traini, G., Voena, C., and Patera, V. (2018). **Secondary Radiation Measurements for Particle Therapy Applications: Charged Particles Produced by 4He and 12C Ion Beams in a PMMA Target at Large Angle**. Physics in Medicine and Biology 63(5). doi: 10.1088/1361-6560/aaa36a.

Sakthivel, V., Ganesh, K. M., McKenzie, C., Boopathy, R., and Selvaraj, J. (2019). **Second Malignant Neoplasm Risk after Craniospinal Irradiation in X-Ray-Based Techniques Compared to Proton Therapy**. Australas Phys Eng Sci Med 42(1):201–9. doi: 10.1007/s13246-019-00731-y.

Schardt, D. (2007). **Tumor Therapy with High-Energy Carbon Ion Beams**. Nuclear Physics A 787(1-4 SPEC. ISS.):633–41. doi: 10.1016/j.nuclphysa.2006.12.097.

Schardt, D., Elsässer, T., and Schulz-Ertner, D. (2010). **Heavy-Ion Tumor Therapy: Physical and Radiobiological Benefits**. Reviews of Modern Physics 82(1):383–425.

Schlechter, A. (2021). **Monitoring of Carbon Ion Radiotherapy Using Track Distributions of Secondary Ions at Different Detection Angles**. University of Heidelberg.

Schlegel, W, and Bille, J. (2002). **Medizinische Physik 2**. edited by Wolfgang Schlegel and Josef Bille. Berlin, Heidelberg: Springer Berlin Heidelberg.

Schneider, W., Bortfeld, T., and Schlegel, W. (2000). **Correlation between CT Numbers and Tissue Parameters Needed for Monte Carlo Simulations of Clinical Dose Distributions**. Phys. Med. Biol. 459(4500):459–459.

Schulz-Ertner, D., Nikoghosyan, A., Didinger, B., Münter, M., Jäkel, O., Karger, C. P., and Debus, J. (2005). **Therapy Strategies for Locally Advanced Adenoid Cystic Carcinomas Using Modern Radiation Therapy Techniques**. Cancer 104(2):338–44. doi: 10.1002/cncr.21158.

Serber, R. (1947). **Nuclear Reactions at High Energies**. Physical Review 72(11):1114–15. doi: 10.1103/PhysRev.72.1114.

El Shafie, R. A., Czech, M., Kessel, K. A., Habermehl, D., Weber, D., Rieken, S., Bougatf, N., Jäkel, O., Debus, J., and Combs, S. E. (2018). **Evaluation of Particle Radiotherapy for the Re-Irradiation of Recurrent Intracranial Meningioma**. Radiation Oncology 13(1). doi: 10.1186/s13014-018-1026-x.

Shakirin, G., Braess, H., Fiedler, F., Kunath, D., Laube, K., Parodi, K., Priegnitz, M., and Enghardt, W. (2011).

Implementation and Workflow for PET Monitoring of Therapeutic Ion Irradiation: A Comparison of in-Beam, in-Room, and off-Line Techniques. Phys Med Biol 56(5):1281–98. doi: 10.1088/0031-9155/56/5/004.

Spieler, H. (2005). **Semiconductor Detector Systems**. OUP Oxford,.

Sze, S. M., and Ng, K. k. (2007). **Physics of Semiconductor Devices**. John Wiley & Sons, Ltd.

Takagi, M., Demizu, Y., Nagano, F., Terashima, K., Fujii, O., Jin, D., Mima, M., Niwa, Y., Katsui, K., Suga, M., Yamashita, T., Akagi, T., Sakata, K. ichi, Fuwa, N., and Okimoto, T. (2018). **Treatment Outcomes of Proton or Carbon Ion Therapy for Skull Base Chordoma: A Retrospective Study**. Radiation Oncology 13(1). doi: 10.1186/s13014-018-1173-0.

Toftegaard, J., Lühr, A., Sobolevsky, N., and Bassler, N. (2014). **Improvements in the Stopping Power Library LibdEdx and Release of the Web GUI Dedx.Au.Dk**. P. 12003 in Journal of Physics: Conference Series. Vol. 489. Institute of Physics Publishing.

Traini, G., Battistoni, G., Bollella, A., Collamati, F., De Lucia, E., Faccini, R., Ferroni, F., Frallicciardi, P. M., Mancini-Terracciano, C., Marafini, M., Mattei, I., Miraglia, F., Muraro, S., Paramatti, R., Piersanti, L., Pinci, D., Rucinski, A., Russomando, A., Sarti, A., Sciubba, A., Senzacqua, M., Solfaroli-Camillocci, E., Toppi, M., Voena, C., and Patera, V. (2017). **Design of a New Tracking Device for On-Line Beam Range Monitor in Carbon Therapy**. Physica Medica 34:18–27. doi: 10.1016/j.ejmp.2017.01.004.

Traini, G., Mattei, I., Battistoni, G., Bisogni, M. G., De Simoni, M., Dong, Y., Embriaco, A., Fischetti, M., Magi, M., Mancini-Terracciano, C., Marafini, M., Mirabelli, R., Muraro, S., Patera, V., Schiavi, A., Sciubba, A., Solfaroli Camillocci, E., Valle, S. M., and Sarti, A. (2019). **Review and Performance of the Dose Profiler, a Particle Therapy Treatments Online Monitor**. Physica Medica 65(June):84–93. doi: 10.1016/j.ejmp.2019.07.010.

Uhl, M., Edler, L., Jensen, A. D., Habl, G., Oelmann, J., Röder, F., Jäckel, O., Debus, J., and Herfarth, K. (2014). **Randomized Phase II Trial of Hypofractionated Proton versus Carbon Ion Radiation Therapy in Patients with Sacrococcygeal Chordoma-the ISAC Trial Protocol**. Radiation Oncology 9(1). doi: 10.1186/1748-717X-9-100.

UniversitätsKlinikum Heidelberg. (2021a). **ACCO-Studie**. Retrieved February 9, 2021 URL: https://www.klinikum.uni-heidelberg.de/radiologische-klinik/radioonkologie-und-strahlentherapie/forschung/acco-studie

UniversitätsKlinikum Heidelberg. (2021b). **Indikationen**. Retrieved February 9, 2021 URL: https://www.klinikum.uni-heidelberg.de//interdisziplinaere-zentren/heidelberger-ionenstrahl-therapiezentrum-hit/fuer-aerzte/indikationen

UniversitätsKlinikum Heidelberg. (2021c). **Klinische Studien Im HIT**. Retrieved February 9, 2021 URL: https://www.klinikum.uni-heidelberg.de/kliniken-institute/interdisziplinaere-zentren/heidelberger-ionenstrahl-therapiezentrum-hit/fuer-aerzte/klinische-studien

UniversitätsKlinikum Heidelberg. (2021d). **Universitätsklinikum Heidelberg: Behandlungsverfahren**. Retrieved February 10, 2021 URL: https://www.klinikum.uni-heidelberg.de/interdisziplinaere-zentren/heidelberger-ionenstrahl-therapiezentrum-hit/leistungsspektrum [date accessed: February 10, 2021].

UniversitätsKlinikum Heidelberg. (2021e). **Universitätsklinikum Heidelberg: OSCAR Studie**. Retrieved June 1, 2021 URL: https://www.klinikum.uni-heidelberg.de/en/radiologische-klinik/radioonkologie-und-strahlentherapie/forschung/oscar-studie

Vlachoudis, V. (2009). **Flair: A Powerful but User Friendly Graphical Interface for FLUKA**. Pp. 790–800 in American Nuclear Society - International Conference on Mathematics, Computational Methods and Reactor Physics 2009, M and C 2009. Vol. 2.

Vogin, G., Wambersie, A., Koto, M., Ohno, T., Uhl, M., Fossati, P., Balosso, J., Pötter, R., Beuve, M., Combs, S. E., Magrin, G., Mayer, R., Mock, U., Sarrut, D., and Schreiner, T. (2019). **A Step towards International Prospective Trials in Carbon Ion Radiotherapy: Investigation of Factors Influencing Dose Distribution in the Facilities in Operation Based on a Case of Skull Base Chordoma**. Radiation Oncology 14(1). doi: 10.1186/s13014-019-1224-1.

Weber, U., and Kraft, G. (1999). **Design and Construction of a Ripple Filter for a Smoothed Depth Dose Distribution in Conformal Particle Therapy**. Phys Med Biol 44(11):2765–75. doi: 10.1088/0031-9155/44/11/306.

Weber, U., and Kraft, G. (2009). **Comparison of Carbon Ions versus Protons**. Cancer Journal 15(4):325–32.

WHO. (2019). **International Statistical Classification of Diseases and Related Health Problems, 10th Revision ICD-10**. World Health Organization. Retrieved July 4, 2021 URL: https://icd.who.int/browse10/2019/en [date accessed: July 4, 2021].

Wieser, H. P., Cisternas, E., Wahl, N., Ulrich, S., Stadler, A., Mescher, H., Muller, L. R., Klinge, T., Gabrys, H., Burigo, L., Mairani, A., Ecker, S., Ackermann, B., Ellerbrock, M., Parodi, K., Jakel, O., and Bangert, M. (2017). **Development of the Open-Source Dose Calculation and Optimization Toolkit MatRad**. Medical Physics 44(6):2556–68. doi: 10.1002/mp.12251.

Wild, C., Weiderpass, E., and Stewart, B. (2020). **World Cancer Report: Cancer Research for Cancer Prevention**.
Wilson, R. R. (1946). **Radiological Use of Fast Protons.** Radiology 47(5):487–91. doi: 10.1148/47.5.487.

8. Personal Contributions

This project was part of the carbon-ion radiotherapy monitoring project and the InViMo project.

Personal publications:

- R Félix-Bautista, **L Ghesquière-Diérickx**, L. Marek, C. Granja, P. Soukup, D. Turecek, M. Ellerbrock, T Gehrke, and M Martišíková, 2021, "Quality assurance method for monitoring of lateral pencil beam positions in scanned carbon-ion radiotherapy using tracking of secondary ions" Medical Physics
- R Félix-Bautista,T Gehrke, **L Ghesquière-Diérickx**, M Reimold, C Amato, D Turecek, J Jakubek, M Ellerbrock and M Martišíková, 2019, "Experimental verification of a non-invasive method to monitor the lateral pencil beam position in an anthropomorphic phantom for carbon-ion radiotherapy", Physics in Medicine & Biology, Volume 64, Number 17

Conference proceedings:

- **L. Ghesquière-Diérickx**, R. Félix-Bautista, A. Schlechter, T. Gehrke, L. Kelleter, M. Winter, P. Soukup, D. Turecek and M. Martišíková. **Poster:** "Detection of patient anatomical changes during carbon-ion radiotherapy using secondary ion tracking". 22st IWORID (online) 2021
- **L.M.H. Ghesquiere-Dierickx**, A. Schechter, R. Felix-Bautista, L. Kelleter, G. Echner, M. Winter, T. Gehrke, M. Martišíková. **Poster:** "Detection of 2 mm air cavities in a head phantom using secondary-ion tracking during clinic-like carbon-ion irradiations". 59th PTCOG (online) 2021
- **L. Ghesquière-Diérickx**, R. Félix-Bautista, T. Gehrke, J. Jakubek, M. Winter6, M. Ellerbrock, M. Martišíková. **Poster:** "Towards a clinical application of carbon ion beam monitoring along depth using detection and tracking of prompt secondary charged particles. IEEE - Nuclear Science Symposium - Medical Imaging Conference, (Boston, USA) 2020
- **L. Ghesquière-Diérickx**, R. Félix-Bautista, T. Gehrke, J. Jakubek, E. Echner, A. Hoess, M. Winter, M. Ellerbrock, O. Jäkel, and M. Martišíková. **Talk:** "Towards a clinical application of carbon-ion pencil beam monitoring in depth using prompt secondary-ion detection and tracking". Online Particle Therapy Co-Operative Group PTCOG Conference (online) 2020
- **L. Ghesquière-Diérickx**, R. Félix-Bautista, T. Gehrke, D. Turecek, J. Jakubek, M. Ellerbrock, M. Martišíková. **Talk:** "Measurement of energy loss of secondary charged particles in carbon-ion beam therapy range monitoring using TPX3 Detectors". 21st IWORID (Chania, GR) 2019
- **L Ghesquière-Diérickx**. **Talk:** "Range monitoring of carbon-ion pencil beam radiotherapy", Pizza and talk" at the German Cancer Research Center, (Heidelberg, DE) 2019

- **L.M.H. Ghesquiere-Dierickx**, R. Felix Bautista, T. Gehrke, M. Ellerbrock, M. Martisikova. **Poster:** "Range monitoring for carbon-ion radiotherapy using prompt secondary ion detection and tracking". Ph.D. Poster Presentation at the DKFZ (Heidelberg, DE) 2019
- **L.M.H. Ghesquiere-Dierickx**, R. Felix Bautista, T. Gehrke, M. Ellerbrock, J. Jakubek, D. Turecek, M. Martisikova. **Poster:** "Measurement of energy loss of secondary charged particles for 12C-ion pencil-beam radiotherapy monitoring". 58th annual PTCOG (Manchester, UK) 2019
- **L.M.H. Ghesquiere-Dierickx**, R. Felix Bautista, T. Gehrke, M. Ellerbrock, and M. Martisikova. **Poster:** "Energy deposition of secondary ions for carbon-ion radiotherapy monitoring". 3rd Heidelberg Symposium on Novel Techniques in Ion Beam Radiotherapy (Heidelberg, DE). 2018

Curriculum Vitae

PERSONAL INFORMATION

Name:	Laura, Marie, Hélène, GHESQUIÈRE-DIÉRICKX
Date of Birth:	10.10.1993
Place of Birth:	Versailles, France
Nationality:	French

UNIVERSITY

Mai 2018 Present-day	Doctoral studies in Medical Physics (Dr. sc. hum) Medical Faculty, Heidelberg University, *Heidelberg, Germany*
Sept. 2015 Oct. 2017	MSc in Biomedical Engineering Mechanical, Maritime and Materials Engineering Faculty, TU Delft, *Delft, the Netherlands*
Sept. 2014 Oct. 2017	MSc in General Engineering "Diplome d'Ingénieur de l'Ecole Centrale Marseille" Ecole Centrale Marseille*, Marseille, France*
Sept. 2014 Sept. 2011	BSc equivalence in General Engineering École Centrale Marseille*, Marseille, France* and "Classe préparatoire aux Grandes Écoles", Lycée Masséna, *Nice, France*

PROFESSIONAL EXPERIENCE

Mai 2018 Present-day	Doctoral project, German Cancer Research Center (DKFZ) *Heidelberg, Germany*
Dec. 2019 Feb. 2021	QA assistant, Heidelberg Ion Therapy Center (HIT) *Heidelberg, Germany*
Feb 2017 Oct. 2017	R&D engineer (MSc Thesis project) Leiden University Medical Center (LUMC) *Leiden, the Netherlands*
Jul. 2017 Dec. 2017	Deputy Director and Management intern, Median Technologies *Nice, France*
Mai 2017 Jul. 2017	Research assistant, LAI, INSERM *Marseille, France*

Acknowledgments

First of all, I would like to express my deepest appreciation to Prof. Dr. Oliver Jäkel for giving me the opportunity to work on this doctoral project in the Department of Medical Physics in Radiation Oncology, for supporting my research while always providing good guidance and insight on my results.
My exceptional gratitude is dedicated to Dr. Maria Matisikova, for being the daily supervisor for my doctoral project. I thank her for her unlimited support in making it all possible but most importantly for creating within our research group such a nice and friendly atmosphere.
I would also like to extend my sincere thanks to my dissertation reviewers and thesis committee. Many thanks to Prof. Dr. Dr. Jürgen Debus for being one of the two second-reviewers of this doctoral thesis, Dr. Andrea Mairani for being part of my DKFZ Thesis Advisory Committee, and a reviewer of this doctoral thesis, and to Prof. Dr. Christian Karger for being part of my DKFZ Thesis Advisor Committee.
Regarding technical and scientific support, I must also thank the HIT facility, Dr. Stephan Brons, Dr. Marcus Winter, and Dr. Malte Ellerbrock for their valuable support, their treatment plans, and for allowing me to perform my experiments in both the cave and the patient room. Many thanks to Gernot Echner, Armin Runz, and the entire E040 workshop for their help manufacturing my experimental and clinical setups. I would like to also acknowledge the assistance and technical support provided by Dr. Jan Jakubek and everyone at ADVACAM regarding the Timepix3 detectors.
My exceptional gratitude is dedicated to my colleagues and friends Dr. Tim Gehrke, and Dr. Renato Felix Bautista, for their contribution to the amazing team spirit of the group and their incredible support throughout the entire journey of my three-year-long Ph.D. I would additionally like to thank Dr. Laurent Kelleter, who even though join our research group more recently, managed on providing great guidance and support to this work. Similarly, I express my gratitude to all former and current members of the E0406 group, as well as all members of the whole E040 department for the incredible time we spent together during meetings, over lunch, or coffee breaks we had in the past years.
Lastly, on a more personal note, I cannot begin to express my thanks and love to Timon for his daily emotional support and to my family and friends for always believing in me even from far away and giving me the energy and affection much needed to go through these three intense years.

To all of you: Merci !

Eidesstattliche Versicherung (Affidavit)

1. Bei der eingereichten Dissertation zu dem Thema
   .....
   handelt es sich um meine eigenständig erbrachte Leistung.

2. Ich habe nur die angegebenen Quellen und Hilfsmittel benutzt und mich keiner unzulässigen Hilfe Dritter bedient. Insbesondere habe ich wörtlich oder sinngemäß aus anderen Werken übernommene Inhalte als solche kenntlich gemacht.

3. Die Arbeit oder Teile davon habe ich bislang nicht an einer Hochschule des In- oder Auslands als Bestandteil einer Prüfungs- oder Qualifikationsleistung vorgelegt.

4. Die Richtigkeit der vorstehenden Erklärungen bestätige ich.

5. Die Bedeutung der eidesstattlichen Versicherung und die strafrechtlichen Folgen einer unrichtigen oder unvollständigen eidesstattlichen Versicherung sind mir bekannt. Ich versichere an Eides statt, dass ich nach bestem Wissen die reine Wahrheit erklärt und nichts verschwiegen habe.

Ort und Datum Unterschrift